



IntechOpen

**Nonlinear Optics**  
Novel Results in Theory and Applications

*Edited by Boris I. Lembrikov*





---

# Nonlinear Optics - Novel Results in Theory and Applications

*Edited by Boris I. Lembrikov*

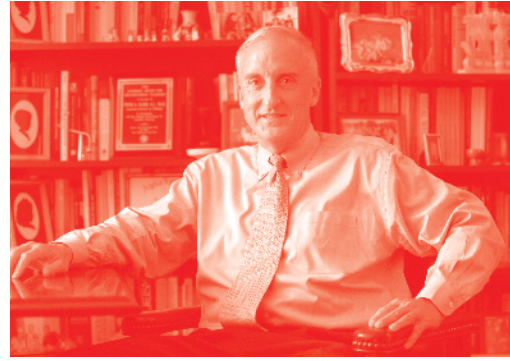
Published in London, United Kingdom

---



## IntechOpen





*Supporting open minds since 2005*



Nonlinear Optics – Novel Results in Theory and Applications

<http://dx.doi.org/10.5772/intechopen.77311>

Edited by Boris I. Lembrikov

#### Contributors

Ariel Flores, Orlando Díaz-Hernaández, Roberto Arceo, Gerardo J. Escalera-Santos, Sergio Mendoza-Vazquez, Elizeth Ramírez-Álvarez, Christian I. Enriquez Flores, Evgeny Kuzin, Gabino Torres-Vega, Luigi Sirleto, Maria Antonietta Ferrara, Dhruva Biswas, Padma Nilaya, Jing Huang, Sergey Chefranov, Artem S. Chefranov, Alice Bernard, Jean-Michel Gérard, Giuseppe Leo, Ivan Favero, Boris I. Lembrikov

© The Editor(s) and the Author(s) 2019

The rights of the editor(s) and the author(s) have been asserted in accordance with the Copyright, Designs and Patents Act 1988. All rights to the book as a whole are reserved by INTECHOPEN LIMITED. The book as a whole (compilation) cannot be reproduced, distributed or used for commercial or non-commercial purposes without INTECHOPEN LIMITED's written permission. Enquiries concerning the use of the book should be directed to INTECHOPEN LIMITED rights and permissions department ([permissions@intechopen.com](mailto:permissions@intechopen.com)).

Violations are liable to prosecution under the governing Copyright Law.



Individual chapters of this publication are distributed under the terms of the Creative Commons Attribution 3.0 Unported License which permits commercial use, distribution and reproduction of the individual chapters, provided the original author(s) and source publication are appropriately acknowledged. If so indicated, certain images may not be included under the Creative Commons license. In such cases users will need to obtain permission from the license holder to reproduce the material. More details and guidelines concerning content reuse and adaptation can be found at <http://www.intechopen.com/copyright-policy.html>.

#### Notice

Statements and opinions expressed in the chapters are those of the individual contributors and not necessarily those of the editors or publisher. No responsibility is accepted for the accuracy of information contained in the published chapters. The publisher assumes no responsibility for any damage or injury to persons or property arising out of the use of any materials, instructions, methods or ideas contained in the book.

First published in London, United Kingdom, 2019 by IntechOpen

eBook (PDF) Published by IntechOpen, 2019

IntechOpen is the global imprint of INTECHOPEN LIMITED, registered in England and Wales,

registration number: 11086078, The Shard, 25th floor, 32 London Bridge Street

London, SE19SG – United Kingdom

Printed in Croatia

British Library Cataloguing-in-Publication Data

A catalogue record for this book is available from the British Library

Additional hard and PDF copies can be obtained from [orders@intechopen.com](mailto:orders@intechopen.com)

Nonlinear Optics – Novel Results in Theory and Applications

Edited by Boris I. Lembrikov

p. cm.

Print ISBN 978-1-78985-163-2

Online ISBN 978-1-78985-164-9

eBook (PDF) ISBN 978-1-83962-009-6

# We are IntechOpen, the world's leading publisher of Open Access books Built by scientists, for scientists

4,000+

Open access books available

116,000+

International authors and editors

120M+

Downloads

151

Countries delivered to

Our authors are among the  
Top 1%

most cited scientists

12.2%

Contributors from top 500 universities



WEB OF SCIENCE™

Selection of our books indexed in the Book Citation Index  
in Web of Science™ Core Collection (BKCI)

Interested in publishing with us?  
Contact [book.department@intechopen.com](mailto:book.department@intechopen.com)

Numbers displayed above are based on latest data collected.  
For more information visit [www.intechopen.com](http://www.intechopen.com)





# Meet the editor



Dr. Boris I. Lembrikov is a senior lecturer at the Holon Institute of Technology (HIT), Holon, Israel. He is a co-author of the book *Electrodynamics of Magneto-active Media*. He has published 44 papers in peer-reviewed international scientific journals, 15 chapters in scientific books, and 36 papers in conference proceedings. He is the editor of two books. Dr. Lembrikov's fields of research interest are nonlinear optics, optical communications, quantum dot lasers and optical amplifiers, and plasmonics.



# Contents

<b>Preface</b>	<b>XIII</b>
<b>Section 1</b> Introduction	<b>1</b>
<b>Chapter 1</b> Introductory Chapter: Nonlinear Optical Phenomena <i>by Boris I. Lembrikov</i>	<b>3</b>
<b>Section 2</b> Mathematical Methods of Nonlinear Optical Phenomena Analysis	<b>13</b>
<b>Chapter 2</b> Nonlinear Schrödinger Equation <i>by Jing Huang</i>	<b>15</b>
<b>Chapter 3</b> Three Solutions to the Nonlinear Schrödinger Equation for a Constant Potential <i>by Gabino Torres Vega</i>	<b>35</b>
<b>Chapter 4</b> Hydrodynamic Methods and Exact Solutions in Application to the Electromagnetic Field Theory in Medium <i>by Sergey G. Chefranov and Artem S. Chefranov</i>	<b>53</b>
<b>Section 3</b> Optical Generation Processes	<b>71</b>
<b>Chapter 5</b> Polarization Properties of the Solitons Generated in the Process of Pulse Breakup in Twisted Fiber Pumped by ns Pulses <i>by Ariel Flores Rosas, Orlando Díaz Hernández, Roberto Arceo, Gerardo J. Escalera Santos, Sergio Mendoza Vázquez, Elizeth Ramírez Álvarez, Christian I. Enriquez Flores and Evgeny Kuzin</i>	<b>73</b>
<b>Chapter 6</b> Towards Enhancing the Efficiency of Nonlinear Optical Generation <i>by Padma Nilaya J. and Dhruba J. Biswas</i>	<b>89</b>

<b>Section 4</b>	
Nonlinear Optical Processes in Micro- and Nanostructures	107
<b>Chapter 7</b>	109
Widely Tunable Quantum-Well Laser: OPO Diode Around 2 $\mu\text{m}$ Based on a Coupled Waveguide Heterostructure <i>by Alice Bernard, Jean-Michel Gérard, Ivan Favero and Giuseppe Leo</i>	
<b>Chapter 8</b>	127
Stimulated Raman Scattering in Micro- and Nanophotonics <i>by Maria Antonietta Ferrara and Luigi Sirleto</i>	

# Preface

Nonlinear optics is one of the most important and rapidly developing fields of modern physics related to the nonlinear interaction between light and matter. Generally, all media are optically nonlinear. However, these nonlinearities are very weak. For this reason, nonlinear optical phenomena had been first observed experimentally in the early 1960s after the invention of the laser as a source of coherent and sufficiently strong optical radiation. Typical nonlinear optical effects are sum and difference frequency harmonics generation, higher harmonic generation, self-focusing of light beams, self-phase modulation of optical pulses, soliton formation and propagation, stimulated light scattering, four-wave mixing, nonlinear dynamics of lasers and optical amplifiers, etc. The theoretical analysis of nonlinear optical effects is based on the simultaneous solution of Maxwell's equations and the equations of motion of a medium excited by optical waves. Such an approach results in a system of nonlinear differential equations, which is typically solved by using the slowly varying envelope approximation (SVEA). Nonlinear optical effects are widely used in modern optical communications and optical signal processing. These applications require novel theoretical and experimental investigations in nonlinear optics.

The objective of this book is to discuss novel results concerning both theoretical analysis and experimental observation of optical pulse generation and stimulated light scattering in optical fibers and nanostructures.

The book consists of eight chapters divided into four sections. Section 1 is an introduction. In Chapter 1, the basic equations and theoretical approach to the analysis of nonlinear optical phenomena are summarized. Essential nonlinear optical effects are briefly reviewed. The contents of Chapter 1 should facilitate an understanding of the following sections.

Section 2 consists of three chapters. In this section, novel results in mathematical methods of nonlinear optical effects analysis are presented. In Chapter 2, novel methods of the nonlinear Schrödinger equation (NLSE) solution for optical pulse propagation in optical fibers are presented. Fiber losses, higher-order dispersion coefficients, noise, and different modulation formats are taken into account. In Chapter 3, three novel solutions of NLSE are introduced. They represent the nonlinear superposition of real and complex exponential and trigonometric functions. In Chapter 4, a new theory of Vavilov–Cherenkov radiation (VCR) is presented.

Section 3 consists of two chapters. In this section, nonlinear effects related to optical pulse generation are discussed. In Chapter 5, nonlinear effects that accompany nanosecond pulse generation in optical fibers are investigated theoretically and experimentally. In Chapter 6, methods of nonlinear optical generation efficiency enhancement are demonstrated experimentally.

Section 4 consists of two chapters where the peculiarities of nonlinear optical phenomena in micro- and nanostructures are studied. In Chapter 7, the design of the tunable quantum well (QW) laser based on waveguide heterostructure is proposed. In Chapter 8, experimental results for stimulated Raman scattering (SRS) in micro- and nanophotonics are reviewed.

**Dr. Boris I. Lembrikov**  
Holon Institute of Technology (HIT), Holon, Israel

---

Section 1

# Introduction

---



# Introductory Chapter: Nonlinear Optical Phenomena

*Boris I. Lembrikov*

## 1. Introduction

The number of publications concerning different aspects of nonlinear optics is enormous and hardly observable. We briefly discuss in this chapter the fundamental nonlinear optical phenomena and methods of their analysis. Nonlinear optics is related to the analysis of the nonlinear interaction between light and matter when the light-induced changes of the medium optical properties occur [1, 2]. The nonlinear optical effects are weak, and their observation became possible only after the invention of lasers which provide a highly coherent and intense radiation [2]. A typical nonlinear optical process consists of two stages. First, the intense coherent light induces a nonlinear response of the medium, and then the modified medium influences the optical radiation in a nonlinear way [1]. The nonlinear medium is described by a system of the dynamic equations including the optical field. The optical field itself is described by Maxwell's equations including the nonlinear polarization of the medium [1, 2]. All media are essentially nonlinear; however, the nonlinear coupling coefficients are usually very small and can be enhanced by the sufficiently strong optical radiation [1, 2]. For this reason, to a first approximation, light and matter can be considered as a system of uncoupled oscillators, and the nonlinear terms are some orders of magnitude smaller than the linear ones [2]. Nevertheless, the nonlinear effects can be important in the long-time and long-distance limits [2]. Generally, the light can be considered as a superposition of plane waves  $A \exp i \left[ (\vec{k} \cdot \vec{r}) - \omega t \right]$  where  $\vec{k}$ ,  $\omega$ ,  $\vec{r}$ ,  $t$  are the wave vector, angular frequency, radius vector in the space, and time, respectively [1, 2]. The medium oscillators can be electronic transitions, molecular vibrations and rotations, and acoustic waves [2]. Typically, only a small number of linear and nonlinear oscillator modes are important that satisfy the resonance conditions [1–3]. In such a case, the optical fields can be represented by a finite sum of discrete wave packets  $\vec{E}(\vec{z}, t)$  given by [1–3]

$$\vec{E}(\vec{z}, t) = \frac{1}{2} [A(\vec{z}, t) \exp i(kz - \omega t) + c.c.] \quad (1)$$

where *c.c.* stands for the complex conjugate and  $A(\vec{z}, t)$  is the slowly varying envelope (SVE) such that [1–3]

$$\left| \frac{\partial^2 A}{\partial z^2} \right| \ll \left| k \frac{\partial A}{\partial z} \right|; \quad \left| \frac{\partial^2 A}{\partial t^2} \right| \ll \left| \omega \frac{\partial A}{\partial t} \right| \quad (2)$$

Here we for the sake of definiteness consider the one-dimensional case. The evolution of the waves (1) is described by the system of the coupled equations in the

so-called SVE approximation (SVEA) when the higher-order derivatives of the SVE can be neglected according to conditions (2) [1–3]. The typical nonlinear optical phenomena are self-focusing, self-trapping, sum- and difference-frequency generation, harmonic generation, parametric amplification and oscillation, stimulated light scattering (SLS), and four-wave mixing (FWM) [1].

During the last decades, optical communications and optical signal processing have been rapidly developing [1–4]. In particular, the nonlinear optical effects in optical waveguides and fibers became especially important and attracted a wide interest [1–4]. The nonlinear optical interactions in the waveguide devices have been investigated in detail in Ref. [3]. Nonlinear fiber optics as a separate field of nonlinear optics has been reviewed in Ref. [4]. The self-phase modulation (SPM), cross-phase modulation (XPM), FWM, stimulated Raman scattering (SRS), stimulated Brillouin scattering (SBS), pulse propagation, and optical solitons in optical fibers have been considered in detail [4]. Silicon photonics, i.e., integrated optics in silicon, also attracted a wide interest due to the highly developed silicon technology which permits the combination of the photonic and electronic devices on the same Si platform [5]. The nonlinear optical phenomena in Si nanostructures such as quantum dots (QD), quantum wells (QW), and superlattices had been discussed [6]. It has been shown that the second harmonic generation (SHG) in silicon nanostructures is possible despite the centrosymmetric structure of Si crystals [6].

Nonlinear dynamics in complex optical systems such as solid-state lasers, CO<sub>2</sub> lasers, and semiconductor lasers is caused by the light-matter interaction [7]. Under certain conditions, the nonlinear optical processes in such optical complex systems result in instabilities and transition to chaos [7].

In this chapter we briefly describe the basic nonlinear optical phenomena. The detailed analysis of these phenomena may be found in [1–7] and references therein. The chapter is constructed as follows. Maxwell's equations for a nonlinear medium and nonlinear optical susceptibilities are considered in Section 2. The mechanisms and peculiarities of the basic nonlinear effects mentioned above are discussed in Section 3. Conclusions are presented in Section 4.

## 2. Maxwell's equations for a nonlinear medium and nonlinear optical susceptibilities

All electromagnetic phenomena are described by macroscopic Maxwell's equations for the electric and magnetic fields  $\vec{E}(\vec{r}, t)$  and  $\vec{H}(\vec{r}, t)$  [1–8]. They have the form [4]

$$\nabla \cdot \vec{B} = 0 \quad (3)$$

$$\nabla \cdot \vec{D} = \rho_{free} \quad (4)$$

$$\nabla \times \vec{E} = -\frac{\partial \vec{B}}{\partial t} \quad (5)$$

$$\nabla \times \vec{H} = \vec{J} + \frac{\partial \vec{D}}{\partial t} \quad (6)$$

Here  $\rho_{free}$  is the free charge density consisting of all charges except the bound charges inside atoms and molecules;  $\vec{J}$  is the current density; the electric induction is given by  $\vec{D} = \epsilon_0 \vec{E} + \vec{P}$ ; the magnetic induction (magnetic flux density) has the

form  $\vec{B} = \mu_0 \vec{H} + \vec{M}$ ;  $\epsilon_0, \mu_0$  are the free space permittivity and permeability, respectively; and  $\vec{P}, \vec{M}$  are the induced electric and magnetic polarizations, respectively. For nonmagnetic media  $\vec{M} = 0$ . Equations (3)–(6) describe the vectors averaged over the volumes which contain many atoms but have linear dimensions smaller than substantial variations of the applied electric field [8]. Combining Eqs. (3)–(6) we obtain the wave equation for the light propagation in a medium. It has the form [1–8]

$$\nabla \times \nabla \times \vec{E} + \frac{1}{c^2} \frac{\partial^2 \vec{E}}{\partial t^2} = -\mu_0 \frac{\partial^2 \vec{P}}{\partial t^2} \quad (7)$$

Here  $c$  is the free space light velocity. The polarization  $\vec{P}$  is a complicated nonlinear function of  $\vec{E}$  [1]. In the general nonlinear case, the polarization  $\vec{P}$  as a function of the electric field  $\vec{E}$  can be expanded into a power series of  $\vec{E}$  as follows [1, 2]:

$$\begin{aligned} \frac{1}{\epsilon_0} P_j(\vec{r}, t) = & \int_{-\infty}^{\infty} \chi_{jk}^{(1)}(\vec{r} - \vec{r}', t - t') E_k(\vec{r}', t') d\vec{r}' dt' \\ & + \int_{-\infty}^{\infty} \chi_{jkl}^{(2)}(\vec{r} - \vec{r}_1, t - t_1; \vec{r} - \vec{r}_2, t - t_2) E_k(\vec{r}_1, t_1) E_l(\vec{r}_2, t_2) d\vec{r}_1 dt_1 d\vec{r}_2 dt_2 \\ & + \int_{-\infty}^{\infty} \chi_{jklm}^{(3)}(\vec{r} - \vec{r}_1, t - t_1; \vec{r} - \vec{r}_2, t - t_2; \vec{r} - \vec{r}_3, t - t_3) E_k(\vec{r}_1, t_1) E_l(\vec{r}_2, t_2) \\ & \times E_m d\vec{r}_1 dt_1 d\vec{r}_2 dt_2 d\vec{r}_3 dt_3 + \dots \end{aligned} \quad (8)$$

Here,  $\chi^{(1)}(\vec{r}, t)$  is the linear susceptibility;  $\chi^{(n)}(\vec{r}, t)$ ,  $n > 1$  is  $n$ th-order nonlinear susceptibility [1]. Suppose that the electric field is a group of monochromatic plane waves given by [1]

$$\vec{E}(\vec{r}, t) = \sum_n \vec{E}_{0n}(\vec{k}_n, \omega_n) \exp \left[ i(\vec{k}_n \cdot \vec{r}) - i\omega_n t \right] \quad (9)$$

Then, the Fourier transform of the nonlinear polarization (1) yields [1]

$$\vec{P}(\vec{k}, \omega) = \vec{P}^{(1)}(\vec{k}, \omega) + \vec{P}^{(2)}(\vec{k}, \omega) + \vec{P}^{(3)}(\vec{k}, \omega) + \dots \quad (10)$$

where

$$\begin{aligned} P_j^{(1)}(\vec{k}, \omega) &= \chi_{jk}^{(1)}(\vec{k}, \omega) E_k(\vec{k}, \omega); \\ P_j^{(2)}(\vec{k}, \omega) &= \chi_{jkl}^{(2)}(\vec{k} = \vec{k}_n + \vec{k}_m, \omega = \omega_n + \omega_m) E_k(\vec{k}_n, \omega_n) E_l(\vec{k}_m, \omega_m); \\ P_j^{(3)}(\vec{k}, \omega) &= \chi_{jklm}^{(3)}(\vec{k} = \vec{k}_n + \vec{k}_m + \vec{k}_p, \omega = \omega_n + \omega_m + \omega_p) \\ &\times E_k(\vec{k}_n, \omega_n) E_l(\vec{k}_m, \omega_m) E_s(\vec{k}_p, \omega_p) \end{aligned} \quad (11)$$

and

$$\begin{aligned}
 & \chi^{(n)}(\vec{k} = \vec{k}_1 + \vec{k}_2 + \dots + \vec{k}_n; \omega = \omega_1 + \omega_2 + \dots + \omega_n) \\
 &= \int_{-\infty}^{\infty} \chi^{(n)}(\vec{r} - \vec{r}_1, t - t_1; \dots; \vec{r} - \vec{r}_n, t - t_n) \\
 & \quad \times \exp \left\{ -i \left[ \left( \vec{k}_1 \cdot (\vec{r} - \vec{r}_1) \right) - \omega_1(t - t_1) + \dots + \left( \vec{k}_n \cdot (\vec{r} - \vec{r}_n) \right) - \omega_n(t - t_n) \right] \right\} \\
 & \quad \times d\vec{r}_1 dt_1 \dots d\vec{r}_n dt_n
 \end{aligned} \tag{12}$$

The linear and nonlinear optical properties of a medium are described by the linear and nonlinear susceptibilities (12), and the  $n$ th-order nonlinear optical effects in such a medium can be obtained theoretically from Maxwell's Eqs. (3)–(6) with the polarization determined by Eq. (8) [1]. We do not present here the analytical properties of the nonlinear susceptibilities which are discussed in detail in Ref. [1].

In some simple cases, the nonlinear susceptibilities can be evaluated by using the anharmonic oscillator model [1, 8]. It is assumed that a medium consists of  $N$  classical anharmonic oscillators per unit volume [1]. Such an oscillator may describe an electron bound to a core or an infrared-active molecular vibration [1]. The equation of motion of the oscillator in the presence of an applied electric field with the Fourier components at frequencies  $\pm\omega_1, \pm\omega_2$  is given by [1]

$$\frac{d^2x}{dt^2} + \Gamma \frac{dx}{dt} + \omega_0^2 x + ax^2 = \frac{q}{m} [E_1(e^{-i\omega_1 t} + e^{i\omega_1 t}) + E_2(e^{-i\omega_2 t} + e^{i\omega_2 t})] \tag{13}$$

Here  $x$  is the oscillator displacement;  $\Gamma$  is the decay factor;  $\omega_0$  is the oscillator frequency;  $q, m$  are the oscillator charge and mass, respectively; and the anharmonic term  $ax^2$  is small and can be considered as a perturbation in the successive approximation series given by [1, 8]

$$x = x^{(1)} + x^{(2)} + x^{(3)} + \dots \tag{14}$$

The nonlinear terms become essential when the electromagnetic power is large enough in such a way that a medium response cannot be considered linear anymore [8]. We limit our analysis with quadratic and cubic nonlinearities proportional to  $x^2$  and  $x^3$ , respectively [1–8]. The induced electric polarization  $P$  can be expressed by using the solutions (13) and (14) as follows:  $P = Nqx$  [1]. In general case, the microscopic expressions for nonlinear susceptibilities of a medium are calculated by using the quantum mechanical approach. In particular, the density matrix formalism is a powerful and convenient tool for such calculations [1, 2, 7, 8].

### 3. Nonlinear optical effects

Electromagnetic waves in a medium interact through the nonlinear polarization (8) [1]. Typically, a nonlinear optical effect that occurs due to such an interaction is described by the coupled wave equations of the type (7) with the nonlinear susceptibilities (12) as the coupling coefficients [1]. In general case, the coupled wave method can also include waves other than electromagnetic [1]. For instance, in the case of SBS process, the acoustic waves are taken into account, and in the case of

SRS process, the molecular vibrations are typically considered [1, 2, 4]. The coupled wave equations are usually solved by using SVEA (2) [1]. In this section, we discuss some important nonlinear optical phenomena caused by the quadratic and cubic susceptibilities  $\chi^{(2)}$  and  $\chi^{(3)}$ , respectively. It should be noted that  $\chi^{(2)} = 0$  in the electric dipole approximation for a medium with inversion symmetry [1].

We start with the sum-frequency, difference-frequency, and second harmonic generation. These phenomena are based on the wave mixing by means of the quadratic susceptibility  $\chi^{(2)}$ . The three coupled waves are  $\vec{E}(\omega_1)$ ,  $\vec{E}(\omega_2)$ , and  $\vec{E}(\omega_3)$  where  $\omega_3 = \omega_1 + \omega_2$  in the cases of sum-frequency [1]. The second-order nonlinear polarization with a sum-frequency  $\omega_3$  in such a case has the form [1]

$$P_j^{(2)}(\omega_3 = \omega_1 + \omega_2) = \epsilon_0 \chi_{jkl}^{(2)}(\omega_3 = \omega_1 + \omega_2) E_k(\omega_1) E_l(\omega_2) \quad (15)$$

Similarly, in the case of the difference-frequency generation, we obtain [1]

$$P_j^{(2)}(\omega_2 = \omega_3 - \omega_1) = \epsilon_0 \chi_{jkl}^{(2)}(\omega_2 = \omega_3 - \omega_1) E_k(\omega_3) E_l^*(\omega_2) \quad (16)$$

where the asterisk means the complex conjugation. Consider the particular case of equal frequencies  $\omega_1 = \omega_2 = \omega$ . In such a case, the nonlinear polarization (15) has the form  $P_j^{(2)}(\omega_3 = 2\omega)$ , and the second harmonic generation (SHG) takes place [1]. The efficient nonlinear wave mixing can occur only under the phase-matching conditions. The phase mismatch  $\Delta k$  between the coupled waves is caused by the refractive index dispersion  $n(\omega_i)$ . The collinear phase matching  $\Delta k = 0$  can be realized in the medium with an anomalous dispersion or in the birefringent crystals [1]. The detailed analysis of the sum-frequency generation, difference-frequency generation, and SHG in different configurations may be found in [1, 3, 6]. It can be shown that the efficient sum-frequency generation can be realized under the following conditions [1]. The nonlinear optical crystal without the inversion symmetry or with the broken inversion symmetry should have low absorption at the interaction frequencies  $\omega_{1,2,3}$  and a sufficiently large quadratic susceptibility  $\chi^{(2)}$  and should allow the collinear phase matching. The particular phase-matching direction and the coupled wave polarizations should be chosen in order to optimize the effective nonlinear susceptibility  $\chi_{eff}^{(2)}$ . The length of the nonlinear crystal must provide the required conversion efficiency. The efficient SHG can be realized with the single-mode laser beams focused into the nonlinear optical crystal [1].

Sum-frequency generation, difference-frequency generation, and SHG can be also carried out in the waveguide nonlinear optical devices [3]. Typically, a thin film of a nonlinear material such as ZnO and ZnS, ferroelectric materials LiNbO<sub>3</sub> and LiTaO<sub>3</sub>, and III-V semiconductor materials GaAs and AlAs can be used as a waveguiding layer [3]. The output power  $P^{(2\omega)}(L)$  of the second harmonic (SH) mode under the no-pump depletion approximation is given by [3]

$$P^{(2\omega)}(L) = \left(P_0^{(\omega)}\right)^2 k^2 L^2 \left(\frac{\sin \Delta L}{\Delta L}\right)^2 \quad (17)$$

where  $2\Delta = \beta^{(2\omega)} - (2\beta^{(\omega)} + K)$ ;  $K = 2\pi/\lambda$ ;  $P_0^{(\omega)}$  is the input pump power;  $k$  is the coupling constant;  $L$  is the device length;  $\Delta$  is the phase mismatch;  $\lambda$  is the pump wavelength;  $\beta^{(\omega)}$ ,  $\beta^{(2\omega)}$  are the propagation constants of the pump and SH waves, respectively; and  $\Lambda$  is the period of the quasi-phase matching (QPM) grating. Waveguide SHG devices can be used in optical signal processing such as laser

printer, laser display, optical memory, short pulse, multicolor, and ultraviolet light generation [3].

Consider the nonlinear optical effects related to the cubic susceptibility  $\chi^{(3)}$ . These phenomena are much weaker than the second-order ones. However, they can exist in centrosymmetric media where  $\chi^{(2)} = 0$  and may be strongly pronounced under the high enough optical intensity pumping. We briefly discuss self-focusing, SPM, third harmonic generation (THG), SBS, SRS, and FWM.

Self-focusing is an induced lens effects caused by the self-induced wavefront distortion of the optical beam propagating in the nonlinear medium [1]. In such a medium, a refractive index  $n$  has the form [1]

$$n = n_0 + \Delta n(|E|^2) \quad (18)$$

Here  $n_0$  is the refractive index of the unperturbed medium,  $\Delta n(|E|^2)$  is the optical field-induced refractive index change, and  $E$  is the optical beam electric field. Typically, the field-induced refractive index change can be described as  $\Delta n = n_2|E|^2$  like in the case of the so-called Kerr nonlinearity [1, 3]. If  $\Delta n > 0$ , the central part of the optical beam with a higher intensity has a larger refractive index than the beam edge. Consequently, the central part of the beam travels at a smaller velocity than the beam edge. As a result, the gradual distortion of the original plane wavefront of the beam occurs, and the beam appears to focus by itself [1]. The self-focusing results in the local increase of the optical power in the central part of the beam and possible optical damage of transparent materials limiting the high-power laser performance [1].

SPM is also caused by the positive refractive index change (18). It is the temporal analog of self-focusing which leads to the spectral broadening of optical pulses [4]. In optical fibers, for short pulses and sufficiently large fiber length  $L_f$ , the combined effect of the group velocity dispersion (GVD) and SPM should be taken into account [4]. The GVD parameter  $\beta_2$  is given by [4]

$$\beta_2 = \frac{1}{c} \left( 2 \frac{dn}{d\omega} + \omega \frac{d^2n}{d\omega^2} \right) \quad (19)$$

In the normal-dispersion regime when  $\beta_2 > 0$ , the combined effect of the SPM and GVD leads to a pulse compression. In the opposite case of the anomalous-dispersion regime  $\beta_2 < 0$ , SPM and GVD under certain conditions can be mutually compensated [4]. In such a case, the pulse propagates in the optical fiber as an optical soliton, i.e., a solitary wave which does not change after mutual collisions [4]. The solitons are described with the nonlinear Schrödinger equation (NLS) which can be solved with the inverse scattering method [4]. The fundamental soliton solution  $u(\xi, \tau)$  has the form [4]

$$u(\xi, \tau) = \eta [\cosh(\eta\tau)]^{-1} \exp(i\eta^2\xi/2) \quad (20)$$

Here  $\eta$  is the soliton amplitude;  $\tau = (t - \beta_1 z)/T_0$ ;  $\xi = z/L_D$ ;  $\beta_1 = 1/v_g$ ;  $v_g$  is the light group velocity in the optical fiber;  $L_D$  is the dispersion length; and  $T_0$  is the initial width of the incident pulse. The optical solitons can propagate undistorted over long distances, and they can be applied in fiber-optic communications [4].

Consider now THG. Unlike SHG, it is always allowed [1]. The third harmonic  $\vec{E}(3\omega)$  is caused by the third-order nonlinear polarization given by [1, 2]

$$P_j^{(3)}(3\omega) = \varepsilon_0 \chi_{jklm}^{(3)}(3\omega) E_k(\omega) E_l(\omega) E_m(\omega) \quad (21)$$

The cubic susceptibility  $|\chi^{(3)}|$  is usually small compared to the  $|\chi^{(2)}|$  [1]. For this reason, the laser intensity required for the efficient THG is limited by the optical damage in crystals [1]. The phase matching for the THG is difficult to achieve which results in low efficiency of the THG process [1, 4]. THG can be realized in highly nonlinear optical fibers where the phase matching can be accomplished [4].

SBS is a nonlinear optical effect related to parametric coupling between light and acoustic waves [1]. It is described by the coupled wave equation (7) for the coupled counterpropagating light waves  $\vec{E}_{1,2}(\omega_{1,2})$  and the acoustic wave equation for the mass density variation  $\Delta\rho(\omega_a = \omega_1 - \omega_2)$  [1, 2, 4]. The nonlinear coupling between light and acoustic waves is caused by the electrostrictive pressure

$p \sim \rho_0 \frac{\partial \varepsilon_r}{\partial \rho} \left( \vec{E}_1(\omega_1) \cdot \vec{E}_2^*(\omega_2) \right)$  where  $\rho_0$ ,  $\varepsilon_r$  are the equilibrium medium mass density and permittivity, respectively. The acoustic wave enhanced by the interacting pump and signal (Stokes) wave modulates the mass density of the medium which in turn modulates the refractive index [1, 3, 4]. For the typical values of the attenuation coefficient and the acoustic frequency shift of about 5 GHz, the acoustic wave excitation is overdamped, and the signal Stokes wave  $\vec{E}_2(\omega_2)$  would grow in the backward direction  $-z$  under the conditions that  $\text{Im} \chi_B^{(3)} > 0$ ,  $\omega_1 \gg \omega_a = \omega_1 - \omega_2 > 0$ , and the optical gain is larger than the optical wave damping constant [1]. The pumping wave  $\vec{E}_1(\omega_1)$  is decaying in the forward direction  $z$  [1]. SBS has been successfully demonstrated in optical fibers, and the SBS gain in a fiber can be used for the amplification of the weak signal with the frequency shift equal to the acoustic frequency  $\omega_a$  [4]. Brillouin fiber amplifiers may be used for applications where the selective amplification is needed [4].

Consider now the SRS process. SRS can be described in the framework of the quantum mechanics as a two-photon process where one photon with energy  $\hbar\omega_1(\vec{k}_1)$  is absorbed by the system and another photon with energy  $\hbar\omega_2(\vec{k}_2)$  is emitted [1]. The system itself makes a transition from the initial state with the energy  $E_i$  to the final state with the energy  $E_f$ , and the energy conservation takes place:  $\hbar(\omega_1 - \omega_2) = E_f - E_i$  [1].

In the framework of the coupled wave description, SRS is a third-order parametric generation process where the optical pump wave  $\vec{E}_1(\omega_1)$  generates a Stokes wave  $\vec{E}_2(\omega_2)$  and a material excitation wave [1]. The nonlinear polarization  $\vec{P}^{(3)}(\omega_{1,2})$  related to SRS in such a case takes the form [1, 2]

$$\vec{P}^{(3)}(\omega_1) = \varepsilon_0 \chi_{R1}^{(3)} |E_2|^2 \vec{E}_1(\omega_1), \quad \vec{P}^{(3)}(\omega_2) = \varepsilon_0 \chi_{R2}^{(3)} |E_1|^2 \vec{E}_2(\omega_2) \quad (22)$$

where  $\chi_{R1,2}^{(3)}$  are the third-order Raman susceptibilities coupling the optical waves and providing SRS process [1]. They can be evaluated by using the quantum mechanical methods [1]. Typically, the material excitation wave in the SRS process is considered as molecular vibrations or optical phonons [1, 2, 4]. The specific feature of SRS is the so-called Stokes-anti-Stokes coupling [1, 2]. Indeed, the mixing of the pump wave with the frequency  $\omega_1$  and the Stokes wave with the frequency  $\omega_2$  results in the generation of the anti-Stokes wave  $\vec{E}_a(\omega_a = 2\omega_1 - \omega_2)$  at the anti-Stokes frequency  $\omega_a = 2\omega_1 - \omega_2 > \omega_1$  [1]. Consequently, the coupled wave analysis of SRS should include the equations for the pump wave, Stokes wave, anti-Stokes

wave, and the material excitation wave [1, 2]. The analysis of this problem can be found in Refs. [1, 2]. Usually, the anti-Stokes wave is attenuated [2]. SRS in optical fibers can be used for the development of Raman fiber lasers and Raman fiber amplifiers [4].

FWM is the nonlinear process with four interacting electromagnetic waves [1]. FWM is a third-order process caused by the third-order nonlinear susceptibility  $\chi^{(3)}$ . It can be easily observed by using the high-intensity lasers, and it has been demonstrated experimentally [1]. FWM is a complicated nonlinear phenomenon because it exhibits different nonlinear effects for different combinations of the coupled wave frequencies, wave vectors, and polarizations. The analysis of FWM is based on the general theory of optical wave mixing [1, 2, 4]. For three input pump waves with frequencies  $\omega_{1,2,3}$ , the singly resonant, doubly resonant, and triply resonant cases can occur [1]. They correspond to the situations when one, two, or three input frequencies or their algebraic sums approach medium transition frequencies [1]. In such cases the third-order susceptibility  $\chi^{(3)}$  can be divided into a resonant part  $\chi_R^{(3)}$  and a nonresonant part  $\chi_{NR}^{(3)}$  [1]. The FWM process has some important applications. Due to the wide range of the mixed frequencies, FWM can be used for the generation of the waves from the infrared up to ultraviolet range [1]. For instance, the parametric amplification can be realized when two strong pump waves amplify two counterpropagating weak waves [1]. The frequency degenerate FWM occurs when the frequencies of the four waves are the same. It is used for the creation of a phase-conjugated wave with respect to one of the coupled waves [2]. In such a case, the phase of the output wave is complex conjugate to the phase of the input wave [1, 2]. FWM in optical fibers can be used for signal amplification, phase conjugation, wavelength conversion, pulse generation, and high-speed optical switching [4].

#### **4. Conclusions**

We briefly discussed the fundamentals of nonlinear optics. The nonlinear optical phenomena are caused by the interaction between light and matter. Generally, all media are nonlinear. However, optical nonlinearity is extremely weak, and the observation of the nonlinear optical effects became possible only after invention of lasers as the sources of the strong enough coherent optical radiation. The nonlinear optical processes are described by Maxwell's equations with the nonlinear polarization of the medium. The coupled equations for the interacting electromagnetic and material waves are usually solved by using SVEA. Typically, the second- and third-order polarizations are considered. The nonlinear polarization and the optical field in the medium are related by the nonlinear susceptibilities which in general case can be evaluated by the quantum mechanical methods. In some simple cases, the classical model of anharmonic oscillator also can be used. We briefly discussed the fundamental nonlinear phenomena related to the second- and third-order susceptibilities. The former exists only in the media without the inversion symmetry, while the latter exists in any medium.

The typical nonlinear optical phenomena related to the second-order susceptibility are the sum-frequency generation, difference-frequency generation, and SHG. The typical nonlinear optical phenomena related to the third-order susceptibility are self-focusing, SPM, optical soliton formation and propagation, different types of SLS such as SBS and SRS, and FWM. SBS involves the acoustic waves. SRS involves the material excitations such as molecular vibrations. We also discussed some peculiarities of nonlinear optical processes in optical fibers. The nonlinear optical effects are widely used in optical communications and optical signal processing.

## **Author details**

Boris I. Lembrikov  
Department of Electrical Engineering and Electronics, Holon Institute of  
Technology (HIT), Holon, Israel

\*Address all correspondence to: [borisle@hit.ac.il](mailto:borisle@hit.ac.il)

## **IntechOpen**

---

© 2019 The Author(s). Licensee IntechOpen. This chapter is distributed under the terms of the Creative Commons Attribution License (<http://creativecommons.org/licenses/by/3.0>), which permits unrestricted use, distribution, and reproduction in any medium, provided the original work is properly cited. 

## **References**

[1] Shen YR. *The Principles of Nonlinear Optics*. Hoboken, New Jersey, USA: Wiley; 2003. 563 p. ISBN: 0-471-43080-3

[2] Moloney JV, Newell AC. *Nonlinear Optics*. Boulder, Colorado, USA: Westview Press; 2004. 436 p. ISBN: 0-8133-4118-3

[3] Suhara T, Fujimura M. *Waveguide Nonlinear-Optic Devices*. Berlin, Heidelberg, Germany: Springer; 2003. 321 p. ISBN: 3-540-01527-2

[4] Agrawal G. *Nonlinear Fiber Optics*. London, New York: Academic Press; 2013. 629 p. ISBN: 978-0-12397-023-7

[5] Reed GT, Knights AP. *Silicon Photonics*. Chichester, England: Wiley; 2004. 255 p. ISBN: 0-470-87034-6

[6] Aktsipetrov OA, Baranova IM, Evtyukhov KN. *Second Order Non-Linear Optics of Silicon and Silicon Nanostructures*. Boca Raton, FL, USA: CRC Press; 2016. 581 p. ISBN: 978-1-4987-2415-9

[7] Otsuka K. *Nonlinear Dynamics in Optical Complex Systems*. Dordrecht, The Netherlands: Kluwer Academic Publishers; 1999. 295 p. ISBN: 07923-6132-6

[8] Meystre P, Sargent M III. *Elements of Quantum Optics*. Berlin, Heidelberg, New York: Springer; 1998. 432 p. ISBN: 3-540-64220-X

---

Section 2

Mathematical Methods of  
Nonlinear Optical  
Phenomena Analysis

---



# Nonlinear Schrödinger Equation

*Jing Huang*

## Abstract

Firstly, based on the small-signal analysis theory, the nonlinear Schrödinger equation (NLSE) with fiber loss is solved. It is also adapted to the NLSE with the high-order dispersion terms. Furthermore, a general theory on cross-phase modulation (XPM) intensity fluctuation which adapted to all kinds of modulation formats (continuous wave, non-return-to-zero wave, and return-zero pulse wave) is presented. Secondly, by the Green function method, the NLSE is directly solved in the time domain. It does not bring any spurious effect compared with the split-step method in which the step size has to be carefully controlled. Additionally, the fourth-order dispersion coefficient of fibers can be estimated by the Green function solution of NLSE. The fourth-order dispersion coefficient varies with distance slightly and is about  $0.002 \text{ ps}^4/\text{km}$ ,  $0.003 \text{ ps}^4/\text{nm}$ , and  $0.00032 \text{ ps}^4/\text{nm}$  for SMF, NZDSF, and DCF, respectively. In the zero-dispersion regime, the higher-order nonlinear effect (higher than self-steepening) has a strong impact on the short pulse shape, but this effect degrades rapidly with the increase of  $\beta_2$ . Finally, based on the traveling wave solution of NLSE for ASE noise, the probability density function of ASE by solving the Fokker-Planck equation including the dispersion effect is presented.

**Keywords:** small-signal analysis, Green function, traveling wave solution, Fokker-Planck equation, nonlinear Schrödinger equation

## 1. Introduction

The numerical simulation and analytical models of nonlinear Schrödinger equation (NLSE) play important roles in the design optimization of optical communication systems. They help to understand the underlying physics phenomena of the ultrashort pulses in the nonlinear and dispersion medium.

The inverse scattering [1], variation, and perturbation methods [2] could obtain the analytical solutions under some special conditions. These included the inverse scattering method for classical solitons [3], the dam-break approximation for the non-return-to-zero pulses with the extremely small chromatic dispersion [4], and the perturbation theory for the multidimensional NLSE in the field of molecular physics [5]. When a large nonlinear phase was accumulated, the Volterra series approach was adopted [6]. With the assumption of the perturbations, the NLSE with varying dispersion, nonlinearity, and gain or absorption parameters was solved in [7]. In [8], the generalized Kantorovitch method was introduced in the extended NLSE. By introducing Rayleigh's dissipation function in Euler-Lagrange equation,

the algebraic modification projected the extended NLSE as a frictional problem and successfully solved the soliton transmission problems [9].

Since the numerical computation of solving NLSE is a huge time-consuming process, the fast algorithms and efficient implementations, focusing on (i) an accurate numerical integration scheme and (ii) an intelligent control of the longitudinal spatial step size, are required.

The finite differential method [10] and the pseudo-spectral method [11] were adopted to increase accuracy and efficiency and suppress numerically induced spurious effects. The adaptive spatial step size-controlling method [12] and the predictor-corrector method [13] were proposed to speed up the implementation of split-step Fourier method (SSFM). The cubic (or higher order) B-splines were used to handle nonuniformly sampled optical pulse profiles in the time domain [14]. The Runge-Kutta method in the interaction picture was applied to calculate the effective refractive index, effective area, dispersion, and nonlinear coefficients [15].

Recently, the generalized NLSE, taking into account the dispersion of the transverse field distribution, is derived [16]. By an inhomogeneous quasi-linear first-order hyperbolic system, the accurate simulations of the intensity and phase for the Schrödinger-type pulse propagation were obtained [17]. It has been demonstrated that modulation instability (MI) can exist in the normal GVD regime in the higher-order NLSE in the presence of non-Kerr quintic nonlinearities [18].

In this chapter, several methods to solve the NLSE will be presented: (1) The small-signal analysis theory and split-step Fourier method to solve the coupled NLSE problem, the MI intensity fluctuation caused by SPM and XPM, can be derived. Furthermore, this procedure is also adapted to NLSE with high-order dispersion terms. The impacts of fiber loss on MI gain spectrum can be discussed. The initial stage of MI can be described, and then the whole evolution of MI can also be discussed in this way; (2) the Green function to solve NLSE in the time domain. By this solution, the second-, third-, and fourth-order dispersion coefficients is discussed; and (3) the traveling wave solution to solve NLSE for ASE noise and its probability density function.

## 2. Small-signal analysis solution of NLSE for MI generation

### 2.1 Theory for continuous wave

The NLSE governing the field in nonlinear and dispersion medium is

$$\frac{\partial u}{\partial z} + \beta_1 \frac{\partial u}{\partial t} + \frac{i}{2} \beta_2 \frac{\partial^2 u}{\partial t^2} + \frac{\alpha}{2} u = i\gamma \left[ |u|^2 + 2|u'|^2 \right] u \quad (1)$$

where  $\beta_1$  and  $\beta_2$  are the dispersions,  $\gamma$  is the nonlinear coefficient, and  $\alpha$  is the fiber loss. In the frequency domain, the solution is

$$u(z + dz, \omega) = \exp(dz\hat{D}) \exp(dz\hat{N})u(z, \omega) \quad (2)$$

where  $\hat{D} = \frac{i}{2}\omega^2\beta_2 + i\omega\beta_1 - \frac{\alpha}{2}$  and  $\hat{N} = i\gamma \left[ |u|^2 + i2|u'|^2 \right]$  [19] (**Figure 1**).

Usually, the field amplitudes can be written as

$$u(z, \omega) = \sqrt{P(z, \omega)} \exp[i\phi(z, \omega)] \quad (3)$$

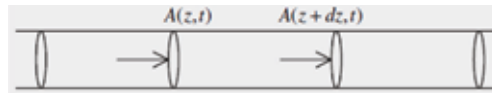


**Figure 1.** Schematic illustration of medium.  $u(z, t)$  and  $u(z + dz, t)$  correspond to the field amplitudes at  $z$  and  $z + dz$ , respectively.

$\phi(z, \omega)$  is caused by the nonlinear effect, and  $\phi(z, \omega) = \int_0^z \gamma [P(z, \omega) + 2P'(z, \omega)] dz$  [3].

$u(z + dz, \omega)$  (is)

$$\begin{aligned} u(z + dz, \omega) &= \exp(dz\hat{D}) \sqrt{P(z, \omega)} \exp\{i\phi(z, \omega) + i\gamma[P + 2P']dz\} \\ &= e^{-adz/2} \exp(\beta_1\omega dz) \exp(\beta_2/2\omega^2 dz) \sqrt{P(z, \omega)} e^{i\phi(z+dz, \omega)} \quad (4) \\ &= \sqrt{P(z + dz, \omega)} \exp[i\phi(z + dz, \omega)] \end{aligned}$$

Assuming:  $P(z, \omega) = \langle P(z) \rangle + \Delta P(z, \omega)$

$\langle P(z) \rangle$  is the average signal intensity.  $\Delta P(z, \omega)$  is the noise or modulation term.

There is [20]  $\langle P(z) \rangle \Delta P(z, \omega)$

The amplitude  $\sqrt{P(z, \omega)}$  can be regarded as

$$\sqrt{P(z, \omega)} \approx \sqrt{\langle P(z) \rangle} \left( 1 + \frac{\Delta P(z, \omega)}{2P(z)} \right) \quad (5)$$

The small-signal theory implies that the frequency modulation or noise  $\dot{\phi}(z + dz, \omega) = \frac{d\phi(z+dz, \omega)}{dt}$  is small enough. Finally ([21])

$$\begin{aligned} P(z + dz, \omega) &= \langle P(z) \rangle + 2e^{-adz/2} \times \\ &\quad \text{Re} \left\{ \langle P(z) \rangle \exp(i\omega\beta_1 dz + i\omega^2\beta_2 dz) \left[ \frac{\Delta P(z, \omega)}{2\langle P(z) \rangle} + i\phi(z + dz, \omega) \right] \right\} \quad (6) \end{aligned}$$

The operation  $\exp(i\omega\beta_1 dz + i\omega^2\beta_2 dz)$  can be split into its real and imaginary parts:

$$\exp(i\omega\beta_1 dz + i\omega^2\beta_2 dz) = \cos(\omega\beta_1 dz + \omega^2\beta_2 dz) + i \sin(\omega\beta_1 dz + \omega^2\beta_2 dz) \quad (7)$$

The modulation or noise  $\Delta P(z + dz, \omega)$  is  $\Delta P(z + dz, \omega) \approx P(z + dz, \omega) - \langle P(z) \rangle$   
 So

$$\begin{aligned} P(z + dz, \omega) &= e^{-adz/2 - i\omega\beta_1 dz} \\ &\quad \left[ \cos\left(\frac{1}{2}\beta_2\omega^2 dz\right) \Delta P(z, \omega) + \sin\left(\frac{1}{2}\beta_2\omega^2 dz\right) 2\langle P(z) \rangle \phi(z + dz, \omega) \right] \quad (8) \end{aligned}$$

And

$$\left( \frac{\Delta P(z + dz, \omega)}{2\langle P(z) \rangle} \right) = e^{-adz/2 - i\omega\beta_1 dz} e^{i\gamma[\langle P(z) \rangle + 2\langle P'(z) \rangle] dz} \varphi(z + dz, \omega) \quad (9)$$

$$\begin{pmatrix} \cos\left(\frac{1}{2}\beta_2\omega^2 dz\right) & -\sin\left(\frac{1}{2}\beta_2\omega^2 dz\right) \\ \sin\left(\frac{1}{2}\beta_2\omega^2 dz\right) & \cos\left(\frac{1}{2}\beta_2\omega^2 dz\right) \end{pmatrix} \begin{pmatrix} \frac{\Delta P(z, \omega)}{2\langle P(z) \rangle} \\ \varphi(z, \omega) \end{pmatrix}$$

When only intensity modulation is present and no phase modulation exists, the transfer function  $\cos\left(\frac{1}{2}\beta_2\omega^2 dz\right)$  is obtained. The 3 dB cutoff frequency corresponds to  $\frac{1}{2}\beta_2\omega^2 dz = \pi/4$  in [22, 23]. This treatment is also adaptable to the case that only the nonlinear phase (frequency) modulation is present; then, the intensity modulation  $\Delta P(z + dz, \omega)$  due to FM-IM conversion is given as

$$\Delta P(z + dz, \omega) = 2\langle P(z) \rangle e^{-adz/2 - i\omega\beta_1 dz} \sin\left(\frac{1}{2}\beta_2 dz \omega^2\right) \varphi(z + dz, \omega) \quad (10)$$

This is in very good agreement with [24] for small-phase modulation index. Even for large modulation index  $\frac{1}{2}\beta_2\omega^2 dz = \pi/2$ , the difference is within 0.5 dB. Eq. (10) does not include a Bessel function, so it is simpler than that in [24].

Obviously, the above process can be used to treat NLSE with higher-order dispersion ( $\beta_3, \beta_4$ ) [25]. Similarly, the result in Eq. (10) will include  $\omega^3$  and  $\omega^4$ .

The corresponding MI gain  $g_{MI}$  in the side bands of  $\omega_0$  (the frequency of signal) is given by

$$g_{MI}(z, \omega) = \frac{|\Delta P(z + dz, \omega) - \Delta P(z, \omega)|}{\langle P(z) \rangle dz}$$

$$= 2e^{-adz/2 - i\omega\beta_1 dz} \sin\left(\frac{1}{2}\beta_2 dz \omega^2\right) \left\{ \gamma \int_z^{z+dz} [P(z, \omega) + 2P'(z, \omega)] dz \right\} / dz \quad (11)$$

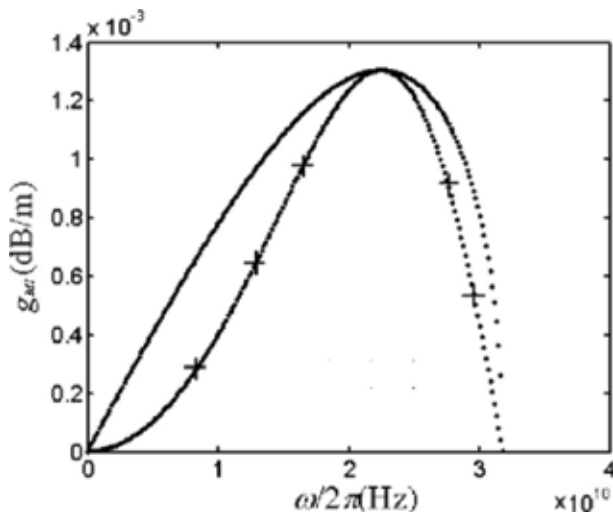


**Figure 2.** MI gain spectra. +++ result of small-signal analysis. — result of perturbation approach. The parameters are  $P_0 = 10$  dBm,  $\beta_2 = 15$  ps<sup>2</sup>/km,  $\lambda = 1550$  nm,  $a = 0.21$  dB/km,  $\gamma = 0.015$  W<sup>-1</sup>/m, and  $z = 0$  m.

**Figure 2** shows a comparison of the gain spectra between Eq. (11) and [6] for the case  $\langle P(z) \rangle / \langle P'(z) \rangle = 1$ . The maximum frequency modulation index caused by dispersion corresponds to  $\frac{1}{2}\beta_2\omega^2 dz = \pi$  [22, 23], and the maximum value of the sideband is  $\omega_c = \sqrt{4\gamma\langle P(z) \rangle / |\beta_2|}$ , so the choice of  $dz$  satisfies  $\frac{1}{2}\beta_2\omega^2 dz = \pi$ , which makes Eq. (11) have the same frequency regime as [26]. In **Figure 2**, the curves are different but have the same maximum value of  $g_{MI}$ . In practice, researchers generally utilize the maximum value of  $g_{MI}$  to estimate the amplified noises and SNR [3]. The result of small-signal analysis in **Figure 2** has a phase delay of around  $\omega_0$ . Compared with the experiment result of [27], the reason is taking the fiber loss into account, the gain spectrum exhibits a phase delay close to  $\omega_0$ , and the curve descends a little [27]. Fiber loss results in the difference of  $g_{MI}$  between the small-signal analysis method and the perturbation approach.

## 2.2 The general theory on cross-phase modulation (XPM) intensity fluctuation

For the general case of two channels, the input optical powers are denoted by  $P(t), P'(t)$ , respectively [28]. Only in the first walk-off length, the nonlinear interaction (XPM) is taken into account; in the remaining fibers, signals are propagated linearly along the fibers, and dispersion acts on the phase-modulated signal resulting in intensity fluctuation. According to [4], the whole length  $L$  is separated into two parts  $0 < z < L_{wo}$  and  $L_{wo} < z < L$ ;  $L_{wo}$  is the walk-off length,  $L_{wo} = \Delta t / (D\Delta\lambda)$ .  $\Delta t$  is the edge duration of the carrier wave,  $D$  is the dispersion coefficient, and  $\Delta\lambda$  is the wavelength spacing between the channels. By the small-signal analysis, the phase modulation in channel 1 originating in  $dz$  at  $z$  can be expressed as

$$d\phi_{XPM}(z, t) = \gamma 2P'(z, t - z\beta_1') e^{-az} dz \quad (12)$$

This phase shift is converted to an intensity fluctuation through the group velocity dispersion (GVD) from  $z$  to the receiver. So, at the fiber output, the intensity fluctuation originating in  $dz$  in the frequency domain is given by [29].

$$\begin{aligned} dP_{XPM}(z, \omega) &= 2[e^{i\omega z\beta_1} P(z, \omega)] \otimes \left\{ e^{-a(L-z)} \cdot e^{i\omega\beta_1(L-z)} \sin[b(L-z)] d\phi_{XPM}(z, \omega) \right\} \\ &= 4\gamma [e^{i\omega z\beta_1} P(z, \omega)] \otimes \left\{ e^{-a(L-z)} \cdot e^{-az} \cdot e^{i\omega\beta_1'z} \cdot e^{i\omega\beta_1(L-z)} P'(z, \omega) \sin[b(L-z)] \right\} dz \end{aligned} \quad (13)$$

$\otimes$  representing the convolution operation  $b = \omega^2 D \lambda^2 / (4\pi c)$ , where  $c$  is the speed of light. At the fiber output, the XPM-induced intensity fluctuation is the integral of Eq. (13) with  $z$  ranging from 0 to  $L$ :

$$\begin{aligned} P_{XPM} &= \int_0^L dP_{XPM}(z, \omega) dz \\ &= \int_0^L 4\gamma [e^{i\omega z\beta_1} P(z, \omega)] \otimes \left\{ e^{-a(L-z)} \cdot e^{-az} \cdot e^{i\omega\beta_1'z} \cdot e^{i\omega\beta_1(L-z)} P'(z, \omega) \sin[b(L-z)] \right\} dz \end{aligned} \quad (14)$$

The walk-off between co-propagating waves is regulated by the convolution operation.

### 3. Green function method for the time domain solution of NLSE

#### 3.1 NLSE including the resonant and nonresonant cubic susceptibility tensors

From Maxwell's equation, the field in fibers satisfies

$$\nabla^2 \vec{E} - \frac{1}{c^2} \frac{\partial^2 \vec{E}}{\partial t^2} = -u_0 \frac{\partial^2 \vec{P}_L}{\partial t^2} - u_0 \frac{\partial^2 \vec{P}_{NL}}{\partial t^2} \quad (15)$$

$$\begin{aligned} \vec{P}_L(\vec{r}, t) &= \varepsilon_0 \int_{-\infty}^{+\infty} \chi^{(1)}(t-t') \vec{E}(\vec{r}, t') dt' \\ &= \varepsilon_0 \int_{-\infty}^{+\infty} \chi^{(1)}(\omega) \vec{E}(\vec{r}, \omega) \exp(i\omega t) d\omega \end{aligned} \quad (16)$$

$$\chi^{(1)}(\omega) = \int_{-\infty}^{+\infty} d\tau \chi^{(1)}(\tau) \exp(-j\omega\tau) \quad (17)$$

where  $\vec{E}$  is the vector field and  $\chi^{(1)}$  is the linear susceptibility.  $\vec{P}_L$  and  $\vec{P}_{NL}$  represent the linear and nonlinear induced fields, respectively [30]. The cubic susceptibility tensor including the resonant and nonresonant terms is

$$\chi^{(3)}(\omega) = \chi_{NR}^{(3)} + \chi_R^{(3)}(\omega) \quad (18)$$

There are

$$\begin{aligned} \vec{P}_{NL,NR}(\vec{r}, t) &= \varepsilon_0 \iiint_{\infty} dt_1 dt_2 dt_3 \chi_{NR}^{(3)}(t_1, t_2, t_3) : \vec{E}(\vec{r}, t-t_1) \cdot \vec{E}(\vec{r}, t-t_2) \cdot \vec{E}(\vec{r}, t-t_3) \\ &= \varepsilon_0 \iiint_{\infty} d\omega_1 d\omega_2 d\omega_3 \chi_{NR}^{(3)}(-\omega_1 - \omega_2 - \omega_3; \omega_1 + \omega_2 + \omega_3) \\ &\quad \vec{E}(\vec{r}, t_1) \cdot \vec{E}(\vec{r}, t_2) \cdot \vec{E}(\vec{r}, t_3) \exp(j\omega t) \delta(\omega - \omega_1 - \omega_2 - \omega_3) \end{aligned} \quad (19)$$

$$\begin{aligned} \chi_{NR}^{(3)}(-\omega_1 - \omega_2 - \omega_3; \omega_1 + \omega_2 + \omega_3) &= \iiint_{\infty} dt_1 dt_2 dt_3 \chi_{NR}^{(3)}(t_1, t_2, t_3) \\ &\quad \exp(-j\omega_1 t_1 - j\omega_2 t_2 - j\omega_3 t_3) \end{aligned} \quad (20)$$

$$\begin{aligned} \vec{P}_{NL,R}(\vec{r}, t) &= \varepsilon_0 \iiint_{\infty} dt_1 dt_2 dt_3 \chi_R^{(3)}(t, t_1, t_2, t_3) : \vec{E}(\vec{r}, t-t_1) \cdot \vec{E}(\vec{r}, t-t_2) \cdot \vec{E}(\vec{r}, t-t_3) \\ &= \varepsilon_0 \iiint_{\infty} d\omega_1 d\omega_2 d\omega_3 \chi_R^{(3)}(t, -\omega_1 - \omega_2 - \omega_3; \omega_1 + \omega_2 + \omega_3) \\ &\quad \vec{E}(\vec{r}, t_1) \cdot \vec{E}(\vec{r}, t_2) \cdot \vec{E}(\vec{r}, t_3) \exp(j\omega t) \delta(\omega - \omega_1 - \omega_2 - \omega_3) \end{aligned} \quad (21)$$

$$\begin{aligned} \chi_R^{(3)}(t) &= \frac{1}{\sqrt{2\pi}} \int_{-\infty}^{+\infty} \frac{a}{\omega - (\omega_1 + \omega_2 + \omega_3) + i\Gamma} e^{-i\omega t} d\omega \\ &= -\sqrt{\frac{\pi}{2}} a \left( 1 + \frac{\Gamma}{|\Gamma|} \right) e^{-|\Gamma|t + i(\omega_1 + \omega_2 + \omega_3)t - i\frac{\pi}{2}} \end{aligned} \quad (22)$$

$\Gamma$  and  $a$  are the attenuation and absorption coefficients, respectively [31].

Repeating the process of [3]

$E = F(x, y)A(z, t) \exp(i\beta z)$ , there is

$$\frac{\partial A}{\partial z} + \frac{i}{2}\beta_2 \frac{\partial^2 A}{\partial t^2} - \frac{1}{6}\beta_3 \frac{\partial^3 A}{\partial t^3} = -\frac{a}{2}A + i\frac{3k_0}{8nA_{eff}}\chi_{NR}^{(3)}|A|^2A + \frac{ik_0g(\omega_0)[1-if(\omega_0)]}{2nA_{eff}}A \int_{-\infty}^t \chi_R^{(3)}(t-\tau)|A(\tau)|^2d\tau \quad (23)$$

$k_0 = \omega_0/c$ , where  $\omega_0$  is the center frequency.  $A_{eff}$  is the effective core area.  $n$  is the refractive index. The last term is responsible for the Raman scattering, self-frequency shift, and self-steepening originating from the delayed response:

$$f(\omega_1 + \omega_2 + \omega_3) = \frac{2(\omega_1 + \omega_2 + \omega_3)(1 - |\Gamma|)}{-2(\omega_1 + \omega_2 + \omega_3)^2 - 2|\Gamma| + |\Gamma|^2} \quad (24)$$

$$g(\omega_1 + \omega_2 + \omega_3) = \left[ -2(\omega_1 + \omega_2 + \omega_3)^2 - 2|\Gamma| + |\Gamma|^2 \right] \quad (25)$$

where  $g(\omega_1 + \omega_2 + \omega_3)$  is the Raman gain and  $f(\omega_1 + \omega_2 + \omega_3)$  is the Raman non-gain coefficients.

### 3.2 The solution by Green function

The solution has the form

$$A(z, t) = \varphi(t)e^{-iEz} \quad (26)$$

Then, there is

$$\frac{1}{2}\beta_2 \frac{\partial^2 \phi}{\partial t^2} + \frac{i}{6}\beta_3 \frac{\partial^3 \phi}{\partial t^3} - \frac{3k_0}{8nA_{eff}}\chi_{NR}^{(3)}|\phi|^2\phi - \frac{k_0g(\omega_s)[1-if(\omega_s)]}{2nA_{eff}}\phi \int_{-\infty}^{+\infty} \chi_R^{(3)}(t-\tau)|\phi(\tau)|^2d\tau = E\phi \quad (27)$$

Let

$$\hat{H}_0(t) = \frac{1}{2}\beta_2 \frac{\partial^2}{\partial t^2} + \frac{i}{6}\beta_3 \frac{\partial^3}{\partial t^3} \quad (28)$$

$$\hat{V}(t) = \frac{-3k_0}{8nA_{eff}}\chi_{NR}^{(3)}|\phi| - \frac{k_0g(\omega_s)[1-if(\omega_s)]}{2nA_{eff}} \int_{-\infty}^{+\infty} \chi_R^{(3)}(t-\tau)|\phi(\tau)|^2d\tau \quad (29)$$

and taking the operator  $\hat{V}(t)$  as a perturbation item, we first solve the eigen equation  $-\sum_{n=2}^k \frac{i^n}{n!}\beta_n \frac{\partial^n \varphi}{\partial T^n} = E\varphi$ .

$$\frac{1}{2}\beta_2 \frac{\partial^2 \phi}{\partial T^2} + \frac{i}{6}\beta_3 \frac{\partial^3 \phi}{\partial T^3} = E\phi \quad (30)$$

Assuming  $E = 1$ , we get the corresponding characteristic equation:

$$-\frac{1}{2}\beta_2 r^2 + \frac{\beta_3}{6} r^3 = E \quad (31)$$

Its characteristic roots are  $r_1, r_2, r_3$ . The solution can be represented as

$$\phi = c_1\phi_1 + c_2\phi_2 + c_3\phi_3 \quad (32)$$

where  $\phi_m = \exp(ir_mt)$ ,  $m = 1, 2, 3$  and  $c_1, c_2, c_3$  are determined by the initial pulse. The Green function of (30) is

$$(E - \hat{H}_0(t))G_0(t, t') = \delta(t - t') \quad (33)$$

By the construction method, it is

$$G_0(t, t') = \begin{cases} a_1\phi_1 + a_2\phi_2 + a_3\phi_3, & t > t' \\ b_1\phi_1 + b_2\phi_2 + b_3\phi_3, & t < t' \end{cases} \quad (34)$$

At the point  $t = t'$ , there are

$$a_1\phi_1(t') + a_2\phi_2(t') + a_3\phi_3(t') = b_1\phi_1(t') + b_2\phi_2(t') + b_3\phi_3(t') \quad (35)$$

$$a_1\phi_1'(t') + a_2\phi_2'(t') + a_3\phi_3'(t') = b_1\phi_1'(t') + b_2\phi_2'(t') + b_3\phi_3'(t') \quad (36)$$

$$a_1\phi_1''(t') + a_2\phi_2''(t') + a_3\phi_3''(t') - b_1\phi_1''(t') - b_2\phi_2''(t') - b_3\phi_3''(t') = -6i/\beta_3 \quad (37)$$

Let  $b_1 = b_2 = b_3 = 0$ , then

$$a_1 = \frac{\varphi_2\dot{\varphi}_3 - \dot{\varphi}_2\varphi_3}{W(t')}, a_2 = \frac{\varphi_3\dot{\varphi}_1 - \dot{\varphi}_3\varphi_1}{W(t')}, a_3 = \frac{\varphi_1\dot{\varphi}_2 - \dot{\varphi}_1\varphi_2}{W(t')} \quad (38)$$

$$W(t') = \begin{vmatrix} \phi_1 & \phi_2 & \phi_3 \\ \phi_1^{(1)} & \phi_2^{(1)} & \phi_3^{(1)} \\ \phi_1^{(2)} & \phi_2^{(2)} & \phi_3^{(2)} \end{vmatrix} \quad (39)$$

Finally, the solution of (27) can be written with the eigen function and Green function:

$$\begin{aligned} \varphi(t) &= \varphi(t) + \int G_0(t, t')V(t')\varphi(t')dt' \\ &= \varphi(t) + \int G_0(t, t', E)V(t')\phi(t')dt' + \int dt'G_0(t, t', E)V(t') \int G_0(t', t'', E)V(t'')\varphi(t'')dt'' \\ &= \varphi(t) + \int G_0(t, t', E)V(t')\phi(t')dt' + \int dt'G_0(t, t', E)V(t') \int G_0(t', t'', E)V(t'')\phi(t'')dt'' + \dots \\ &\quad + \underbrace{\int dt'G_0(t, t')V(t') \int G_0(t', t'')V(t'')dt'' \dots \int G_0(t^l, t^{l+1})V(t^{l+1})\varphi(t^{l+1})dt^{l+1}}_{\text{times } l} \end{aligned} \quad (40)$$

The accuracy can be estimated by the last item of (40). The algorithm is plotted in **Figure 3**.

### 3.3 Estimation of the fourth-order dispersion coefficient $\beta_4$

The NLSE governing the wave's transmission in fibers is

$$\frac{\partial u}{\partial z} + \frac{i}{2}\beta_2 \frac{\partial^2 u}{\partial t^2} - \frac{1}{6}\beta_3 \frac{\partial^3 u}{\partial t^3} - i\gamma \exp(-2\alpha z) \left[ |u|^2 u + is \frac{\partial |u|^2}{\partial t} u + is |u|^2 \frac{\partial u}{\partial t} \right] = 0 \quad (41)$$

where  $s$  is the self-steepening parameter. In the frequency domain, its solution is

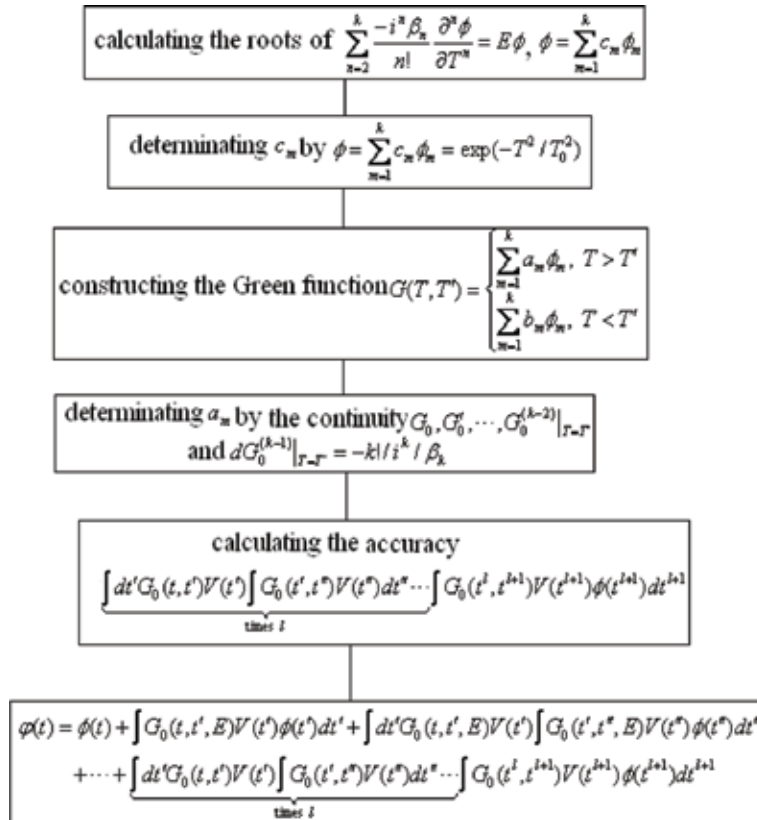


**Figure 3.**  
 The Green algorithm for solving NLSE.

$$u(z + dz, \omega) = \exp(dz\hat{D}) \exp(dz\hat{N})u(z, \omega) \quad (42)$$

where  $\hat{D} = \frac{i}{2}\omega^2\beta_2 - \frac{i}{6}\omega^3\beta_3$ ,  $\hat{N} = \Gamma\{i\gamma \exp(-2\alpha z) [ |u|^2 + is\frac{\partial|u|^2}{\partial t} + is|u|^2\frac{\partial}{\partial t} ]\}$ , and  $\Gamma$  represents the Fourier transform [32]. Let  $\hat{L} = \frac{\partial}{\partial z} - \hat{D} - \hat{N}$  and  $\hat{L}G(z, z', \omega) = \delta(z - z')$ ; we obtain the Green function

$$G(z, z', \omega) = \frac{1}{2\pi} \int_{-\infty}^{+\infty} \frac{\exp[-ik(z - z')]}{ik - \hat{D} - \hat{N}} dk \quad (43)$$

Constructing the iteration  $\beta_3 = \beta_3^0 + \delta\beta_3$ ,  $u(z, \omega) = u^0(z, \omega) + \delta u(z, \omega)$ , then there is

$$\delta u(z, \omega) = \int G(z, z', \omega) Z(z', \omega, \delta\beta_3(z'), u^0(z', \omega)) dz' \quad (44)$$

where  $Z(z', \omega, \delta\beta_3(z'), u^0(z', \omega)) = -\frac{i}{6}\delta\beta_3(z')\omega^3 u^0(z', \omega)$  and  $u^0(z', \omega, \beta_3^0)$  is determined by (42).

The minimum value of  $\delta u(z, \omega)$  satisfies  $\partial\delta u(z, \omega)/\partial\omega = 0$ ,  $R[\partial^2\delta u(z, \omega)/\partial\omega^2] > 0$ , so

$$\delta\beta_3 = \exp \left[ \int_{-\infty}^{+\infty} \left( -\frac{1}{G} \frac{\partial G}{\partial\omega} - \frac{3}{\omega} - \frac{1}{u^0} \frac{\partial u^0}{\partial\omega} \right) d\omega \right] \quad (45)$$

Next, we take the higher-order nonlinear effect into account. Constructing another iteration related to  $\delta\gamma : \gamma = \gamma^0 + \delta\gamma$ ,  $u(z, \omega) = u^0(z, \omega) + \delta u(z, \omega)$  and repeating the above process, we get

$$\delta\gamma \approx \exp \left[ \int_{-\infty}^{+\infty} \left( -\frac{1}{G} \frac{\partial G}{\partial \omega} - \frac{3is}{1-3is\omega} - \frac{1}{u^0} \frac{\partial u^0}{\partial \omega} \right) d\omega \right] \quad (46)$$

Now, we can simulate the pulse shape affected by high-order dispersive and nonlinear effects. Assume  $L_D = t_0^2/|\beta_2|$  and

$$u(0, t) = \int_{-\infty}^{+\infty} u(0, \omega) \exp(-i\omega t) d\omega = u_0 \exp(-t^2/t_0^2/2).$$

Firstly, we see what will be induced by the above items  $\delta\beta_3$  and  $\delta\gamma$ . To extrude their impact, we choose the other parameters to be small values in **Figures 4** and **5**. The deviation between the red and the black lines in **Figure 4(a)** indicates the impact of  $\delta\beta_3$  and  $\delta\gamma$ ; that is, they induce the pulse's symmetrical split. This split does not belong to the SPM-induced broadening oscillation spectral or  $\beta_3$ -induced oscillation in the tailing edge of the pulse, because here  $\gamma$  is very small and  $\beta_3 = 0$  [3]. The self-steepening effect attributing to  $is \partial(|u|^2 u)/\partial t$  is also shown explicitly in the black line. When we reduce the  $s$  value to 0.0001 in (b), the split pulse's symmetry is improved.

Is the pulse split in **Figure 4(a)** caused by  $\delta\beta_3$  or  $\delta\gamma$ ? The red lines in **Figure 5** describe the evolution of pulse affected by the very small second-order dispersion and nonlinear (including self-steepening) coefficients. Here,  $\delta\beta_3$  induces the pulse's symmetrical split, and the maximum peaks of split pulse alter and vary from the spectral central to the edge and to the central again. Therefore, its effect is equal to that of the fourth-order dispersion  $\beta_4$  [33, 34, 3].

From the deviation between the red and black lines in **Figure 5**, we can also detect the impact of  $\delta\gamma$ . It only accelerates the pulse's split when the self-steepening effect is ignored ( $s = 0$  in **Figure 5(a)**). This is similar to the self-phase modulation-broadening spectral and oscillation. The high nonlinear  $\gamma$  accelerating pulse's split is validated in [35, 36]. If  $s \neq 0$  (**Figure 5(b)**),  $\delta\gamma$  simultaneously leads to the split pulse's redshift.

Generally, we do not take  $\delta\gamma$  into account, so we should clarify in which case it creates impact. Compared (c) with (b) in **Figure 5**, the red lines change little means that  $\delta\beta_3$  has a tiny relationship with  $\gamma$ . But with the increase of  $\gamma$  (**Figure 5(c)**), the

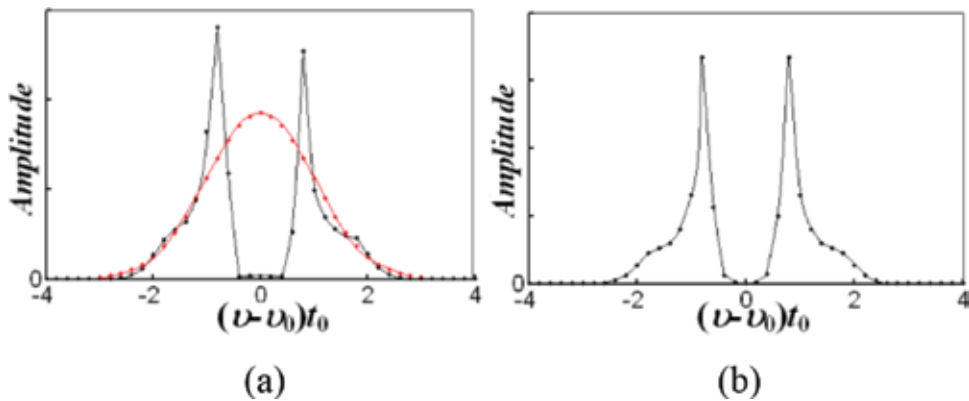


**Figure 4.** The pulse shapes with and without  $\delta\beta_3$  and  $\delta\gamma$ . The red line: without  $\delta\beta_3$  and  $\delta\gamma$ ; the black line: with  $\delta\beta_3$  and  $\delta\gamma$ .  $\nu = \omega/2\pi$ ,  $\beta_3^0 = 0$  (ps<sup>3</sup>/km),  $\gamma = 1.3 \times 10^{-2}$  (/km/W),  $t_0 = 80$ (fs),  $z = 3.7 \times t_0^2/|\beta_2|$ ,  $\beta_2 = -21.7/150$ (ps<sup>2</sup>/km),  $u_0 = |\beta_2|/\gamma/t_0^2$ . (a)  $s = 0.01$  and (b)  $s = 0.0001$ .

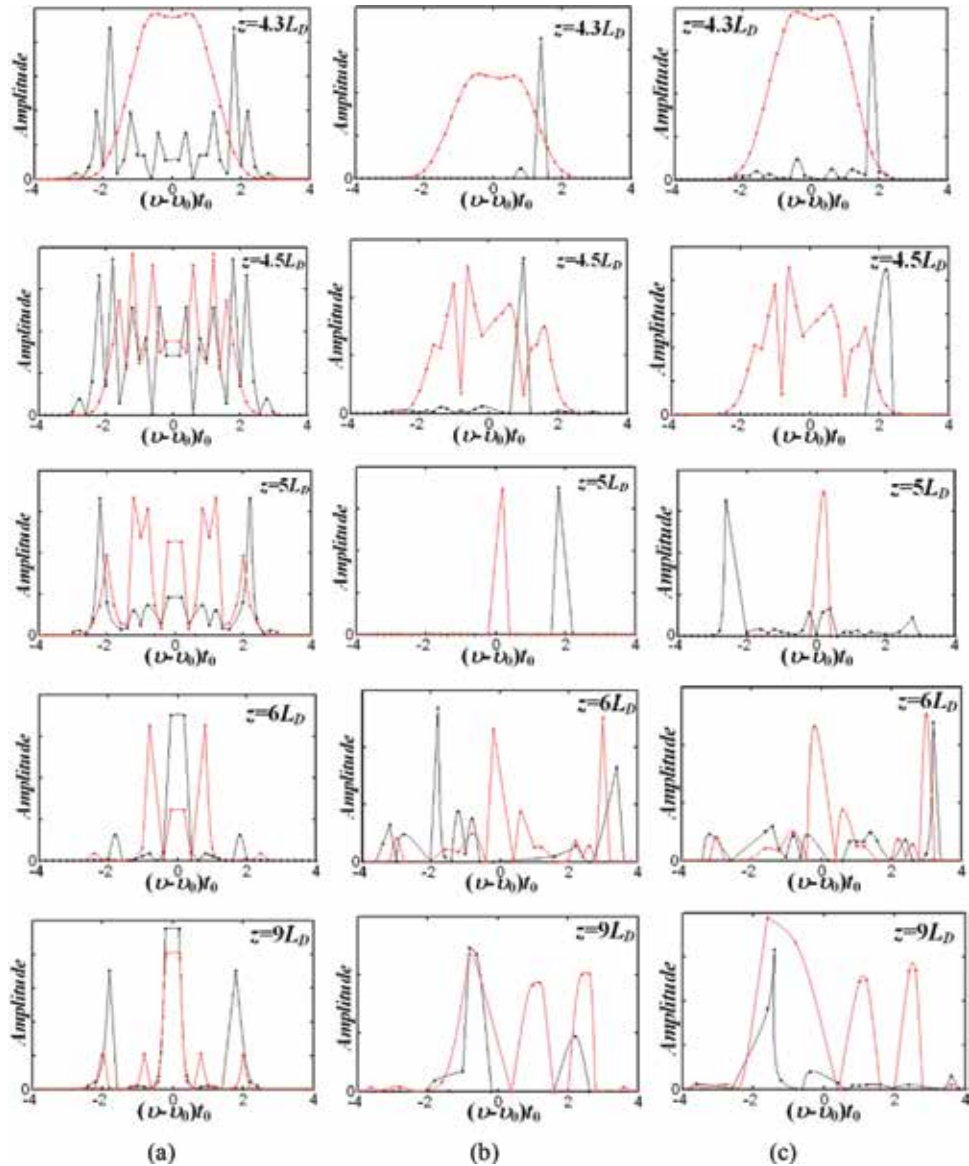


**Figure 5.** The evolutions of pulse. The red line: without  $\delta\gamma$ ; the black line: with  $\delta\beta_3$  and  $\delta\gamma$ . (a)  $s = 0$ ,  $\gamma = 1.3 \times 10^{-4}$  (/km/W); (b)  $s = 0.01$ ,  $\gamma = 1.3 \times 10^{-4}$  (/km/W); (c)  $s = 0.01$ ,  $\gamma = 1.3$  (/km/W). Other parameters are the same as **Figure 4**.

split pulse's redshift is strengthened, so  $\delta\gamma$  has a relationship with  $\gamma$ . In **Figure 6**, the pulse is not split until  $z = 9 L_D$ , and the black line with  $\delta\gamma$  is completely overlapped by the red line without  $\delta\gamma$ , so the high second-order dispersion  $\beta_2$  results in the impact of  $\delta\gamma$  covered and the impact of  $\delta\beta_3$  weakened. Therefore, only in the zero-dispersion regime,  $\delta\gamma$  should be taken into account in the simulation of pulse shape.

So, we can utilize  $\delta\beta_3$  to determine the fourth-order dispersion coefficient  $\beta_4$ . Fiber parameters are listed in **Table 1**. The process is shown in **Figure 7**, and the dispersion operator including  $\beta_4$  is  $\hat{D} = \frac{1}{2}\omega^2\beta_2 - \frac{i}{6}\omega^3\beta_3 + \frac{i}{24}\omega^4\beta_4$ .

**Table 2** is the average of  $\beta_4$ . They are different from those determined by FWM or MI where  $\beta_4$  is related to power and broadening frequency [35, 36]. By our method, the fourth-order dispersion is also a function of distance, and every type of

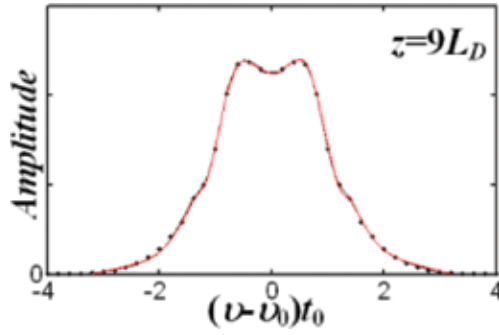


**Figure 6.** The pulse shapes with and without  $\delta\gamma$ .  $\beta_2 = -21.7(\text{ps}^2/\text{km})$ ,  $s = 0.01$ ,  $\gamma = 1.3$  ( $/\text{km}/\text{W}$ ). Other parameters are the same as **Figure 5**.

	$a$ (dB/km)	$\gamma$ (/km/W)	$s$	$\beta_2$ ( $\text{ps}^2/\text{km}$ )	$\beta_3$ ( $\text{ps}^3/\text{km}$ )
DCF	0.59	5.5	0.01	110	0.1381
NZDSF	0.21	2.2	0.01	-5.6	0.115
SMF	0.21	1.3	0.01	-21.7	-0.5

**Table 1.** Fiber parameters.

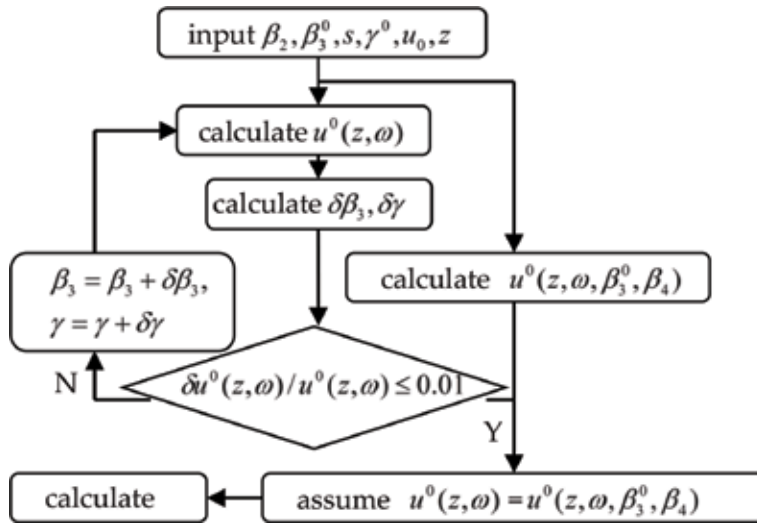


**Figure 7.** The process of calculating  $\beta_4$ .

	$Z = 1.5L_D$	$Z = 5L_D$	$Z = 50L_D$
DCF	0.0003	0.00035	0.00032
NZDSF	0.0022	0.003	0.0032
SMF	0.0012	0.002	0.0025

Units ( $\text{ps}^4/\text{km}$ ).

**Table 2.** The average.

fibers has its special average  $\beta_4$  which reveals the characteristic of fibers. These values are similar to those experiment results in highly nonlinear fibers [35, 36]. Although we take the higher-order nonlinear effect  $\delta\gamma$  into account which upgrades the pulse's symmetrical split and redshift, the items is  $\partial(|u|^2u)/\partial t$  and  $i\delta\gamma \exp(-2\alpha z)|u|^2u$  have a very tiny contribution to  $\beta_4$ , only  $10^{-26}$  ps<sup>4</sup>/km quantity order for the typical SMF. Here, the impact of  $\delta\gamma$  is hidden by the relative strong  $\beta_2$ .

## 4. Traveling wave solution of NLSE for ASE noise

### 4.1 The in-phase and quadrature components of ASE noise

The field including the complex envelopes of signal and ASE noise is:

$$U(z, t) = \sum_{l=1}^N [u_l(z, t) + A_l(z, t)] \exp(-i\omega_l t) \quad (47)$$

where  $u_l(z, t)$  and  $A_l(z, t)$  are the complex envelopes of signal and ASE noise, respectively [37, 38].  $N$  is the channel number. ASE noise generated in erbium-doped fiber amplifiers (EDFAs) is  $A_l(0, t) = A_{lR}(0, t) + iA_{lI}(0, t)$ ,  $A_{lR}(0, t)$  and  $A_{lI}(0, t)$  are statistically real independent stationary white Gaussian processes, and  $\langle A_{lR}(0, t + \tau)A_{lR}^*(0, t) \rangle = \langle A_{lI}(0, t + \tau)A_{lI}^*(0, t) \rangle = n_{sp}h\nu_l(G_l - 1)\Delta\nu_l\delta(\tau)$ . In the complete inversion case,  $n_{sp} = 1$ .  $h$  is the Planck constant.  $G_l$  is the gain for channel  $l$ .

Substituting Eq. (47) into (1), we can get the equation that  $A_l(z, t)$  satisfies:

$$i \frac{\partial A_l(z, t)}{\partial z} = \frac{\beta_2}{2} \left( -\omega_l^2 + \frac{\partial^2}{\partial t^2} - i2\omega_l \frac{\partial}{\partial t} \right) A_l(z, t) - \gamma(z) \exp(-2\alpha z) \left| \sum_{j=1}^N u_j(z, t) + A_j(z, t) \right|^2 A_l(z, t) \quad (48)$$

So, the in-phase and quadrature components of ASE noise obey:

$$\frac{\partial A_{lR}(z, t)}{\partial z} = -\beta_2\omega_l \frac{\partial A_{lR}(z, t)}{\partial t} + \frac{1}{2}\beta_2 \frac{\partial^2 A_{lI}(z, t)}{\partial t^2} - \frac{1}{2}\beta_2\omega_l^2 A_{lI} - \gamma \exp(-2\alpha z) \left| \sum_{j=1}^N u_j(z, t) + A_j(z, t) \right|^2 A_{lI} \quad (49)$$

$$\frac{\partial A_{lI}(z, t)}{\partial z} = -\beta_2\omega_l \frac{\partial A_{lI}(z, t)}{\partial t} - \frac{1}{2}\beta_2 \frac{\partial^2 A_{lR}(z, t)}{\partial t^2} + \frac{1}{2}\beta_2\omega_l^2 A_{lR}(z, t) + \gamma \exp(-2\alpha z) \left| \sum_{j=1}^N u_j(z, t) + A_j(z, t) \right|^2 A_{lR} \quad (50)$$

We now seek their traveling wave solution by taking [37]  $A_{lR} = \phi(\xi)$ ,  $A_{lI} = \varphi(\xi)$ , and  $\xi = t - cz$ .

Then, (49) and (50) are converted into

$$\phi'(\beta_2\omega_l - c) = - \left[ \frac{1}{2}\beta_2\omega_l^2 + \gamma \exp(-2\alpha z) \left| \sum_{j=1}^N u_j(z, t) + A_j(z, t) \right|^2 \right] \varphi + \frac{1}{2}\beta_2\varphi'' \quad (51)$$

$$\phi'(\beta_2\omega_l - c) = \left[ \frac{1}{2}\beta_2\omega_l^2 + \gamma \exp(-2\alpha z) \left| \sum_{j=1}^N u_j(z, t) + A_j(z, t) \right|^2 \right] \phi - \frac{1}{2}\beta_2\phi'' \quad (52)$$

(52) is differentiated to  $\xi$

$$\phi''(\beta_2\omega_l - c) = \left[ \frac{1}{2}\beta_2\omega_l^2 + \gamma \exp(-2\alpha z) \left| \sum_{j=1}^N u_j(z, t) + A_j(z, t) \right|^2 \right] \phi' - \frac{1}{2}\beta_2\phi''' \quad (53)$$

Replacing  $\phi'$  and  $\phi'''$  in (53) with (51) and the differential of (51), there are

$$\begin{aligned} \phi''(\beta_2\omega_l - c)^2 = & - \left[ \frac{1}{2}\beta_2\omega_l^2 + \gamma \exp(-2\alpha z) \left| \sum_{j=1}^N u_j(z, t) + A_j(z, t) \right|^2 \right]^2 \phi + \\ & \beta_2 \left[ \frac{1}{2}\beta_2\omega_l^2 + \gamma \exp(-2\alpha z) \left| \sum_{j=1}^N u_j(z, t) + A_j(z, t) \right|^2 \right] \phi'' + \frac{1}{4}\beta_2^2\phi^{(4)} \end{aligned} \quad (54)$$

From (51) and (54), we can easily obtain

$$\varphi = B \left\{ \left[ \beta_2\omega_l^2/2 + \gamma \exp(-2\alpha z) \left| \sum_{j=1}^N u_j(z, t) + A_j(z, t) \right|^2 \right] \cos k\xi + \beta_2k^2/2 \cdot \cos k\xi \right\} / (\beta_2\omega_l - c) / k \quad (55)$$

$$\varphi = B \sin k\xi \quad (56)$$

and

$$B = A_{IR}(0, t)(\beta_2\omega_l - c)k / \left\{ \left[ \beta_2\omega_l^2/2 + \gamma \exp(-2\alpha z) \left| \sum_{j=1}^N u_j(z, t) + A_j(z, t) \right|^2 \right] \cos kt + \beta_2k^2/2 \cdot \cos kt \right\} \quad (57)$$

$$c = \pm \left\{ \beta_2^2k^2/4 + \left[ \beta_2\omega_l^2/2 + \gamma \exp(-2\alpha z) \left| \sum_{j=1}^N u_j(z, t) + A_j(z, t) \right|^2 \right] / k^2 + \beta_2^2\omega_l^2/2 + \gamma\beta_2 \exp(-2\alpha z) \left| \sum_{j=1}^N u_j(z, t) + A_j(z, t) \right|^2 \right\}^{1/2} + \beta_2\omega_l \quad (58)$$

$$k = \arcsin(A_{II}(0, t)/B)/t \quad (59)$$

In the above calculation process,  $B$ ,  $c$ , and  $k$  should be regarded as constants, and  $A_{IR}$ ,  $A_{II}$  are the functions of the solo variable  $\xi$ , respectively.

## 4.2 Probability density function of ASE noise

Because  $A_{IR}$  and  $A_{II}$  have been solved, the time differentials of (49) and (50) can be calculated. Thus, the stochastic differential equations (ITO forms) around  $A_{IR}$  and  $A_{II}$  are

$$\frac{\partial A_{IR}(z, t)}{\partial z} = f(A_{IR}(z, t)) + g(A_{IR}(z, t))A_{IR, z=0} \quad (60)$$

$$\frac{\partial A_{II}(z, t)}{\partial z} = f'(A_{II}(z, t)) + g'(A_{II}(z, t))A_{II, z=0} \quad (61)$$

Here,

$$f(A_{IR}(z, t)) = \beta_2 k \omega_l \sqrt{B \frac{\beta_2 \omega_l^2 / 2 + \gamma \exp(-2\alpha z) \left| \sum_{j=1}^N u_j(z, t) + A_j(z, t) \right|^2 + \beta_2 k^2 / 2}{(\beta_2 \omega_l - c)k}} - A_{IR}^2(z, t)} \quad (62)$$

$$g(A_{IR}(z, t)) = -\frac{(\beta_2 \omega_l - c)k}{A_{IR, z=0}} \sqrt{B \frac{\beta_2 \omega_l^2 / 2 + \gamma \exp(-2\alpha z) \left| \sum_{j=1}^N u_j(z, t) + A_j(z, t) \right|^2 + \beta_2 k^2 / 2}{(\beta_2 \omega_l - c)k}} - A_{IR}^2(z, t)} \quad (63)$$

$$f'(A_{II}(z, t)) = -\beta_2 k \omega_l \sqrt{B^2 - A_{II}^2(z, t)} \quad (64)$$

$$g'(A_{II}(z, t)) = \frac{(\beta_2 \omega_l - c)k}{BA_{II, z=0}} \sqrt{B^2 - A_{II}^2(z, t)} \quad (65)$$

Now, they can be regarded as the stationary equations, and we can gain their probabilities according to Sections (7.3) and (7.4) in [39]. By solving the corresponding Fokker-Planck equations of (60) and (61), the probabilities of ASE noise are

$$p_{IR} = \frac{C}{[g(A_{IR})]^2} \exp \left[ 2 \int_{-\infty}^{A_{IR}} \frac{f(s)}{[g(s)]^2} ds \right] \quad (66)$$

$$p_{II} = \frac{C'}{[g'(A_{II})]^2} \exp \left[ 2 \int_{-\infty}^{A_{II}} \frac{f'(s)}{[g'(s)]^2} ds \right] \quad (67)$$

$C, C'$  are determined by  $\int_{-\infty}^{+\infty} p dp = 1$ . Compared with [40], these probabilities of ASE noise take dispersion effect into account. This is the first time that the p.d.f. of ASE noise simultaneously including dispersion and nonlinear effects is presented.

(66) and (67) are efficient in the models of Gaussian and correlated non-Gaussian processes as our (49) and (50). Obviously, the Gaussian distribution has been distorted. They are no longer symmetrical distributions, and both have phase shifts consistent with [40], and as its authors have expected that “if the dispersion

effect was taken into account, the asymmetric modulation side bands occur.” The reasons are that item  $-i\beta_2\omega_l \frac{\partial}{\partial t} A_l(z, t)$  in (48) brings the phase shift and item  $\frac{\beta_2}{2} \frac{\partial^2}{\partial t^2} A_l(z, t)$  brings the expansion and induces the side bands, the self-phase modulation effects, and the cross-phase modulation effects. Their synthesis impact is amplified by (66) and (67) and results in the complete non-Gaussian distributions.

## 5. Conclusion

NLSE is solved with small-signal analyses for the analyses of MI, and it can be broadened to all signal formats. The equation can be solved by introducing the Green function in the time domain, and it is used as the tool for the estimations of high-order dispersion and nonlinear coefficients. For the conventional fibers, SMF, NZDSF, and DCF, the higher-order nonlinear effect contribution to  $\beta_4$  can be neglected. This can be deduced that each effect has less impact for another coefficient's estimation. The Green function can also be used for the solving of 3 + 1 dimension NLSE.

By the traveling wave methods, the p.d.f. of ASE noise can be obtained, and it provides a method for the calculation of ASE noise in WDM systems. So, the properties of MI, pulse fission, coefficient value, and ASE noise's probability density function are also discussed for demonstrations of the theories.

## Author details

Jing Huang

Physics Department, South China University of Technology, Guangzhou, China

\*Address all correspondence to: [jhuang@scut.edu.cn](mailto:jhuang@scut.edu.cn)

## IntechOpen

© 2018 The Author(s). Licensee IntechOpen. This chapter is distributed under the terms of the Creative Commons Attribution License (<http://creativecommons.org/licenses/by/3.0>), which permits unrestricted use, distribution, and reproduction in any medium, provided the original work is properly cited. 

## References

- [1] Hasegawa A, Matsumoto M, Kattan PI. *Optical Solitons in Fibers*. 3rd ed. New York: Springer-Verlag; 2000
- [2] Brandt-Pearce M, Jacobs I, Shaw JK. Optimal input Gaussian pulse width for transmission in dispersive nonlinear fiber. *Journal of the Optical Society of America B*. 1999;**16**:1189-1196. DOI: 10.1364/JOSAB.16.001189
- [3] Agrawal GP. *Nonlinear Fiber Optics*. 4th ed. San Diego, CA: Academic; 2007
- [4] Kodama Y, Wabnitz S. Analytical theory of guiding center nonreturn to zero and return to zero signal transmission in normally dispersive nonlinear optical fibers. *Optics Letters*. 1995;**20**:2291-2293. DOI: 10.1364/OL.20.002291
- [5] Surján PR, Ángyán J. Perturbation theory for nonlinear time-independent Schrödinger equations. *Physical Review A—Physical Review Journals*. 1983;**28**: 45-48. DOI: 10.1103/PhysRevA.28.45
- [6] Peddanarappagari KV, Brandt-Pearce M. Volterra series transfer function of single-mode fibers. *Journal of Lightwave Technology*. 1997;**15**: 2232-2241. DOI: 10.1109/50.643545
- [7] Serkin VN, Hasegawa A. Novel soliton solutions of the nonlinear Schrödinger equation model. *Physical Review Letters*. 2000;**85**:4502-4505. DOI: 10.1103/PhysRevLett.85.4502
- [8] Cerda SC, Cavalcanti SB, Hickmann JM. A variational approach of nonlinear dissipative pulse propagation. *European Physical Journal D*. 1998;**1**:313-316. DOI: 10.1007/s100530050
- [9] Roy S, Bhadra SK. Solving soliton perturbation problems by introducing Rayleigh's dissipation function. *Journal of Lightwave Technology*. 2008;**26**: 2301-2322. DOI: 10.1109/JLT.2008.922305
- [10] Chang Q, Jia E, Suny W. Difference schemes for solving the generalized nonlinear Schrodinger equation. *Journal of Computational Physics*. 1999;**148**: 397-415. DOI: 10.1006/jcph.1998.6120
- [11] Bosco G, Carena A, Curri V, Gaudio R, Poggiolini P, Benedetto S. Suppression of spurious tones induced by the split-step method in fiber systems simulation. *IEEE Photonics Technology Letters*. 2000;**12**:489-491. DOI: 10.1109/68.841262
- [12] Sinkin V, Holzlohner R, Zweck J, Menyuk CR. Optimization of the split-step Fourier method in modeling optical-fiber communication systems. *Journal of Lightwave Technology*. 2003;**21**:61-68. DOI: 10.1109/JLT.2003.808628
- [13] Liu X, Lee B. A fast method for nonlinear Schrodinger equation. *IEEE Photonics Technology Letters*. 2003;**15**: 1549-1551. DOI: 10.1109/LPT.2003.818679
- [14] Premaratne M. Numerical simulation of nonuniformly time-sampled pulse propagation in nonlinear fiber. *Journal of Lightwave Technology*. 2005;**23**:2434-2442. DOI: 10.1109/JLT.2005.850770
- [15] Dabas B, Kaushal J, Rajput M, Sinha RK. Nonlinear pulse propagation in chalcogenide As<sub>2</sub>Se<sub>3</sub> glass photonic crystal fiber using RK4IP method. *Applied Optics*. 2011;**50**:5803-5811. DOI: 10.1364/AO.50.005803
- [16] Pedersen MEV, Ji C, Chris X, Rottwitt K. Transverse field dispersion in the generalized nonlinear Schrodinger equation: Four wave mixing in a higher order mode fiber.

- Journal of Lightwave Technology. 2013; **31**:3425-3431. DOI: 10.1109/JLT.2013.2283423
- [17] Deiterding R, Glowinski R, Oliver H, Poole S. A reliable split-step Fourier method for the propagation equation of ultra-fast pulses in single-mode optical fibers. Journal of Lightwave Technology. 2013;**31**:2008-2017. DOI: 10.1109/JLT.2013.2262654
- [18] Choudhuri A, Porsezian K. Impact of dispersion and non-Kerr nonlinearity on the modulational instability of the higher-order nonlinear Schrodinger equation. Physical Review A. 2012;**85**: 033820. DOI: 10.1103/PhysRevA.85.033820
- [19] Huang J, Yao J. Small-signal analysis of cross-phase modulation instability in lossy fibres. Journal of Modern Optics. 2005;**52**:1947-1955. DOI: 10.1080/09500340500106717
- [20] Wang J, Petermann K. Small signal analysis for dispersive optical fiber communication systems. Journal of Lightwave Technology. 1992;**10**:96. DOI: 10.1109/50.108743
- [21] Huang W, Hong J. A coupled-mode analysis of modulation instability in optical fibers. Journal of Lightwave Technology. 1992;**10**:156-162. DOI: 10.1109/50.120570
- [22] Meslener GJ. Chromatic dispersion induced distortion of modulated monochromatic light employing direct detection. IEEE Journal of Quantum Electronics. 1984. DOI: QE-20:1208-1216. DOI:10.1109/JQE.1984.1072286
- [23] Koyama F, Suematsu Y. Analysis of dynamic spectral width of dynamic-single-mode (DSM) lasers and related transmission bandwidth of single-mode fibers. IEEE Journal of Quantum Electronics. 1985. DOI: QE-21:292-297. DOI:10.1109/JQE.1985.1072653
- [24] Rchraplyvy A, Tkach RW, Buhl LL, Alferness RC. Phase modulation to amplitude modulation conversion of CW laser light in optical fibres. Electronics Letters. 1988;**22**:409-412. DOI: 10.1049/el:19860279
- [25] Grudihin AB, Dianov EM, Korobkin DV, Prokhorov AM, Serkin VN. Decay of femtosecond pulses in single-mode fiber-optic waveguides. JETP Letters. 1987;**46**:221-225
- [26] Agrawal GP, Baldeck PL, Alfano RR. Modulation instability induced by cross-phase modulation in optical fibers. Physical Review A. 1989;**39**:3406-3413. DOI: 10.1103/PhysRevA.39.3406
- [27] Ciaramella E, Tamburrini M. Modulation instability in long amplified links with strong dispersion compensation. IEEE Photonics Technology Letters. 1999;**11**:1608-1610. DOI: 10.1109/ 68.806862
- [28] Huang J, Yao J. Analysis of cross-phase modulation in WDM systems. Journal of Modern Optics. 2005;**52**: 1819-1825. DOI: 10.1080/09500340500092016
- [29] Cartaxo AVT. Impact of modulation frequency on crossphase modulation effect in intensity modulation-direct detection WDM systems. IEEE Photonics Technology Letters. 1998;**10**: 1268-1270. DOI: 10.1109/68.705612
- [30] Huang J, Yao J, Degang X. Green function method for the time domain simulation of pulse propagation. Applied Optics. 2014;**53**(16):-20
- [31] Shen YR. The Principles of Nonlinear Optics. Hoboken, NJ: John Wiley & Sons, Inc; 1984
- [32] Huang J, Yao J. Estimation of the fourth-order dispersion coefficient  $\beta_4$ . Chinese Optics Letters. 2012;**10**: 101903-101903. DOI: 10.3788/COL201210.101903

- [33] Capmany J, Pastor D, Sales S, Ortega B. Effects of fourth-order dispersion in very high-speed optical time-division multiplexed transmission. *Optics Letters*. 2002;27:960-962. DOI: 10.1364/OL.27.000960
- [34] Igarashi K, Saito S, Kishi M, Tsuchiya M. Broad-band and extremely flat super-continuum generation via optical parametric gain extended spectrally by fourth-order dispersion in anomalous-dispersion-flattened fibers. *IEEE Journal of Selected Topics in Quantum Electronics*. 2002;8:521-526. DOI: 10.1109/JSTQE.2002.1016355
- [35] Gholami F, Chavez Boggio JM, Moro S, Alic N, Radic S. Measurement of ultra-low fourth order dispersion coefficient of nonlinear fiber by distant low-power FWM. *IEEE Photonics Society Summer Topical Meeting Series*. 2010;2010:162-163. DOI: 10.1109/PHOSST.2010.5553630
- [36] Marhic ME, Wong KK-Y, Kazovsky LG. Wide-band tuning of the gain spectra of one-pump fiber optical parametric amplifiers. *IEEE Journal of Selected Topics in Quantum Electronics*. 2004;10:1133-1141. DOI: 10.1109/JSTQE.2004.835298
- [37] Gui M, Jing H. Statistical analyses of ASE noise. *Optics and Photonics Journal*. 2017;7:160-169. DOI: 10.4236/opj.2017.710016
- [38] Nichel J, Schurmann HW, Serov VS. Some elliptic travelling wave solution to the Nonikov-Vesela equation. In: *Proceedings of the International Conference on Days on Diffraction*, DD2005; 2005, 28–01; 2005. pp. 177-186
- [39] Primak S, Kontorovich V, Lyandres V. *Stochastic Method and Their Applications to Communications*. Chichester, UK: John Wiley & Sons; 2004. Chap. 7. DOI:10.1002/0470021187
- [40] Dlubek MP, Phillips AJ, Larkins EC. Nonlinear evolution of Gaussian ASE noise in ZMNL fiber. *Journal of Lightwave Technology*. 2008;26:891-898. DOI: 10.1109/JLT.2008.917373



# Three Solutions to the Nonlinear Schrödinger Equation for a Constant Potential

*Gabino Torres Vega*

## Abstract

We introduce three sets of solutions to the nonlinear Schrödinger equation for the free particle case. A well-known solution is written in terms of Jacobi elliptic functions, which are the nonlinear versions of the trigonometric functions  $\sin$ ,  $\cos$ ,  $\tan$ ,  $\cot$ ,  $\sec$ , and  $\csc$ . The nonlinear versions of the other related functions like the real and complex exponential functions and the linear combinations of them is the subject of this chapter. We also illustrate the use of these functions in Quantum Mechanics as well as in nonlinear optics.

**Keywords:** new nonlinear exponential-like functions, superpositions of nonlinear functions, nonlinear optics, nonlinear quantum mechanics

## 1. Introduction

Since the nonlinear Schrödinger equation appears in many fields of physics, including nonlinear optics, thus, there is interest in finding its solutions, in particular, its eigenfunctions. A set of eigenfunctions, for the free particle, is given in terms of Jacobi's elliptic functions [1–4], which are real periodic functions, and they have been used in order to find the eigenstates of the particle in a box [5, 6] and in a double square well [7].

Jacobi's elliptic functions are needed in subjects like the description of pulse narrowing nonlinear transmission lines [8].

Interestingly, there is a way to linearly superpose Jacobi's elliptic functions by means of adding constant terms to their arguments [3]. So, we ask ourselves if there are other ways to achieve nonlinear superposition of nonlinear functions.

Besides, the linear equation has complex solutions with a current density flux different from zero, and we expect that the nonlinear equation should also have this type of solutions at least for small nonlinear interaction.

In this chapter, we introduce three other sets of functions which are also solutions to the Gross-Pitaevskii equation; they all are nonlinear superpositions of functions. The modification of the elliptic functions allows us to consider the nonlinear equivalent of the linear superposition of exponential, real and complex, and trigonometric functions found in nonrelativistic linear quantum mechanics.

The functions we are about to introduce can be used, for instance, in the case of a free Bose-Einstein condensate reflected by a potential barrier. One might be able to further analyze nonlinear tunneling [7] and nonlinear optics phenomena with the help of these functions.

## 2. Nonlinear complex exponential functions

The definitions of the functions and their properties are similar to those used in Jacobi's elliptic functions [1, 2, 4]. Let us start with the definition of our complex exponential nonlinear functions:

$$\text{cnc}(u, \alpha) = a e^{ix} + b e^{-ix}, \quad \text{snc}(u, \alpha) = a e^{ix} - b e^{-ix}, \quad (1)$$

$$\text{dnc}(u, \alpha) = \sqrt{1 - \alpha |\text{cnc}(u, \alpha)|^2}, \quad \text{ncc}(u, \alpha) = \frac{1}{\text{cnc}(u, \alpha)}, \quad (2)$$

$$\text{nsc}(u, \alpha) = \frac{1}{\text{snc}(u, \alpha)}, \quad \text{ndc}(u, \alpha) = \frac{1}{\text{dnc}(u, \alpha)}, \quad (3)$$

$$\text{tac}(u, \alpha) = \frac{\text{snc}(u, \alpha)}{\text{cnc}(u, \alpha)}, \quad \text{coc}(u, \alpha) = \frac{\text{cnc}(u, \alpha)}{\text{snc}(u, \alpha)}. \quad (4)$$

where  $\alpha, a, b \in \mathbb{R}$ , and they are such that  $\alpha < 1/\max[(a \pm b)^2]$ . With these choices, the function dnc is always positive, and we do not have to worry about branch points in the relation between the variables  $x$  and  $u$ . The variables  $u$  and  $x$  are related as

$$u = \int_0^x \frac{dt}{\sqrt{1 - \alpha |\text{cnc}(t, \alpha)|^2}}. \quad (5)$$

A plot of these functions is found in **Figure 1** for a particular set of values of the parameters. These functions behave like the usual superposition of complex exponential functions ( $\alpha = 0$ ), changing behavior as the value of  $\alpha$  increases until

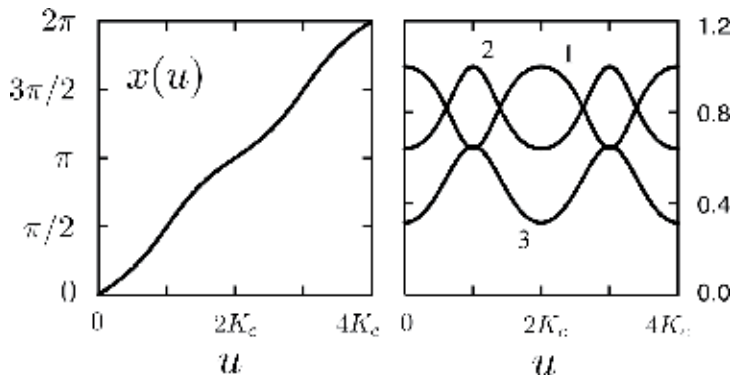


**Figure 1.** Nonlinear complex exponential functions with  $a = 0.1$ ,  $b = 0.9$ , and  $\alpha = 0.9$ . The curves correspond to 1,  $|\text{cnc}(u, \alpha)|^2$ ; 2,  $|\text{snc}(u, \alpha)|^2$ ; and 3,  $\text{dnc}(u, \alpha)$ .

it reaches the soliton value,  $\alpha = 1/\max[(a \pm b)^2]$ . The functions become concentrated around the origin for the soliton value of  $\alpha$ .

The quarter period of these functions is defined as

$$Kc = \int_0^{\pi/2} \frac{dt}{\sqrt{1 - \alpha|\text{cnc}(t, \alpha)|^2}}. \quad (6)$$

If we call

$$n_0 = a^2 + b^2, \quad n_1 = 1 - 2\alpha(a^2 + b^2), \quad (7)$$

$$n_2 = 1 - \frac{3}{2}\alpha(a^2 + b^2), \quad n_3 = 1 - \alpha(a^2 + b^2), \quad (8)$$

$$n_4 = 1 - \frac{\alpha}{2}(a^2 + b^2), \quad n_5 = 1 + \frac{\alpha}{2}(a^2 + b^2), \quad (9)$$

$$n_6 = 1 + \alpha(a^2 + b^2), \quad n_7 = 1 + \frac{3}{2}\alpha(a^2 + b^2), \quad (10)$$

the squares of the nonlinear functions are written as

$$\text{cnc}^2(u, \alpha) - \text{snc}^2(u, \alpha) = 4ab, \quad (11)$$

$$|\text{cnc}(u, \alpha)|^2 + |\text{snc}(u, \alpha)|^2 = 2n_0, \quad (12)$$

$$\text{dnc}^2(u, \alpha) = 1 - \alpha|\text{cnc}(u, \alpha)|^2 \quad (13)$$

$$= n_1 + \alpha|\text{snc}(u, \alpha)|^2, \quad (14)$$

$$\text{tac}^2(u, \alpha) = 1 - 4ab \text{ncc}^2(u, \alpha), \quad (15)$$

$$\text{coc}^2(u, \alpha) = 1 + 4ab \text{nsc}^2(u, \alpha). \quad (16)$$

Some derivatives of these functions are

$$\text{cnc}'(u, \alpha) = i \text{snc}(u, \alpha) \text{dnc}(u, \alpha), \quad (17)$$

$$\text{snc}'(u, \alpha) = i \text{cnc}(u, \alpha) \text{dnc}(u, \alpha), \quad (18)$$

$$\text{dnc}'(u, \alpha) = \alpha \Im\{\text{cnc}^*(u, \alpha) \text{snc}(u, \alpha)\}, \quad (19)$$

$$\text{ncc}'(u, \alpha) = -i \text{tac}(u, \alpha) \text{ncc}(u, \alpha) \text{dnc}(u, \alpha), \quad (20)$$

$$\text{nsc}'(u, \alpha) = -i \text{coc}(u, \alpha) \text{nsc}(u, \alpha) \text{dnc}(u, \alpha), \quad (21)$$

$$\text{ndc}'(u, \alpha) = -\alpha \text{ndc}^2(u, \alpha) \Im\{\text{cnc}^*(u, \alpha) \text{snc}(u, \alpha)\}, \quad (22)$$

$$\text{tac}'(u, \alpha) = i[1 + \text{tac}^2(u, \alpha)] \text{dnc}(u, \alpha) \quad (23)$$

$$\text{coc}'(u, \alpha) = -i4ab \text{nsc}^2(u, \alpha) \text{dnc}(u, \alpha), \quad (24)$$

where  $\Im$  indicates to take the imaginary part of the quantity.

We also have that the derivative of the inverse functions is given by

$$\frac{d}{dy} \text{cnc}^{-1}(y) = \pm \frac{i}{\sqrt{(y^2 - 4ab)(1 - \alpha|y|^2)}}, \quad (25)$$

$$\frac{d}{dy} \text{snc}^{-1}(y) = \pm \frac{i}{\sqrt{(4ab + y^2)(n_1 + \alpha|y|^2)}}, \quad (26)$$

$$\frac{d}{dy} \text{ncc}^{-1}(y) = \pm \frac{i}{y\sqrt{(1 - 4aby^2)(1 - \alpha/|y|^2)}}, \quad (27)$$

$$\frac{d}{dy} \text{nsc}^{-1}(y) = \pm \frac{i}{y\sqrt{(1 + 4aby^2)(n_1 + \alpha/|y|^2)}}. \quad (28)$$

Now, the second derivatives are as follows

$$\text{cnc}''(u, \alpha) = [2\alpha |\text{cnc}(u, \alpha)|^2 - n_6 \text{cnc}(u, \alpha) - 2\alpha ab \text{cnc}^*(u, \alpha), \quad (29)$$

$$\begin{aligned} \text{snc}''(u, \alpha) = & \left( [3\alpha(a^2 + b^2) - 1] - 2\alpha |\text{snc}(u, \alpha)|^2 \right) \\ & \text{snc}(u, \alpha) - 2\alpha ab \text{snc}^*(u, \alpha), \end{aligned} \quad (30)$$

$$\text{dnc}''(u, \alpha) = 2[\text{dnc}^2(u, \alpha) - \alpha n_0] \text{dnc}(u, \alpha), \quad (31)$$

$$\text{ncc}''(u, \alpha) = n_6 \text{ncc}(u, \alpha) - 2\alpha \text{cnc}^*(u, \alpha) + 2\alpha ab \text{ncc}^2(u, \alpha) \text{cnc}^*(u, \alpha), \quad (32)$$

$$\begin{aligned} \text{nsc}''(u, \alpha) = & (n_3 + 8abn_1 \text{nsc}^2(u, \alpha)) \text{nsc}(u, \alpha) \\ & - \alpha [1 + 10ab \text{nsc}^2(u, \alpha)] \text{nsc}^*(u, \alpha), \end{aligned} \quad (33)$$

$$\begin{aligned} \text{ndc}''(u, \alpha) = & 2\alpha^2 \text{ndc}^3(u, \alpha) (\Im \text{cnc}(u, \alpha) \text{snc}(u, \alpha))^2 \\ & + 2\alpha(a^2 + b^2) \text{ndc}(u, \alpha), \end{aligned} \quad (34)$$

$$\begin{aligned} \text{tac}''(u, \alpha) = & [1 + \text{tac}^2(u, \alpha)] \\ & \left\{ \alpha [2\text{tac}(u, \alpha) + i \Im \text{tac}(u, \alpha)] |\text{cnc}(u, \alpha)|^2 - 2\text{tac}(u, \alpha) \right\}, \end{aligned} \quad (35)$$

$$\begin{aligned} \text{coc}''(u, \alpha) = & 2[1 - \text{coc}^2(u, \alpha)] \text{coc}(u, \alpha) \text{dnc}^2(u, \alpha) \\ & - 2\alpha ab \left[ \frac{\text{cnc}^*(u, \alpha)}{\text{cnc}(u, \alpha)} - \frac{\text{snc}^*(u, \alpha)}{\text{snc}(u, \alpha)} \right] \text{coc}(u, \alpha). \end{aligned} \quad (36)$$

The first three of the above equations can be thought of as modifications of the Gross-Pitaevskii equation, which allows for solutions of the form  $\text{cnc}(u, \alpha)$ ,  $\text{snc}(u, \alpha)$ , and  $\text{dnc}(u, \alpha)$ . However, when  $a$  or  $b$  vanishes, we get the Gross-Pitaevskii form.

With these results at hand, we can see that the probability current densities associated with  $\text{cnc}(u, \alpha)$  and  $\text{snc}(u, \alpha)$  are given by

$$\begin{aligned} j_c(u) = & \text{Re} \left\{ \text{cnc}^*(u, \alpha) \left[ -i \frac{d}{du} \text{cnc}(u, \alpha) \right] \right\} \\ = & (a^2 - b^2) \text{dnc}(u, \alpha), \end{aligned} \quad (37)$$

$$\begin{aligned} j_s(u) = & \text{Re} \left\{ \text{snc}^*(u, \alpha) \left[ -i \frac{d}{du} \text{snc}(u, \alpha) \right] \right\} \\ = & (a^2 - b^2) \text{dnc}(u, \alpha), \end{aligned} \quad (38)$$

respectively. The nonlinear term causes that the quantum flux be no longer constant (as is the case for linear interaction) but modulated by  $\text{dnc}(u, \alpha)$  instead.

The differential equations for cnc ( $u, \alpha$ ) and snc ( $u, \alpha$ ) would have the Gross-Pitaevskii equation form if any of  $\alpha, a$ , or  $b$  becomes zero or when  $a = b$  (which is the case of real functions, i.e., Jacobi's functions). The case of  $\alpha, a$ , or  $b$  zero corresponds to the cases when there is no nonlinear interaction or when there is total reflection or only transmission in a quantum system.

## 2.1 The potential step

A straight forward application of the functions introduced in this section is the finding of the eigenfunctions of the Gross-Pitaevskii equation for a step potential:

$$V(u) = \begin{cases} 0, & \text{when } u < 0, \\ V_0, & \text{when } u \geq 0, \end{cases} \quad (39)$$

and a chemical potential  $\mu$  larger than the potential height  $V_0$ . The Gross-Pitaevskii equation is written as

$$\frac{d^2\psi(u)}{du^2} + \frac{2ML^2}{\hbar^2}(\mu - V_0) \psi(u) - \frac{2ML^2}{\hbar^2 A^2} NU_0 |\psi(u)|^2 \psi(u) = 0, \quad (40)$$

where  $\psi(u)$  is the unnormalized eigenfunction for the Bose-Einstein condensate (BEC),  $M$  is the mass of a single atom,  $N$  is the number of atoms in the condensate,  $U_0 = 4\pi\hbar^2 a/M$  characterizes the atom-atom interaction,  $a$  is the scattering length,  $L$  is a scaling length,  $A$  is the integral of the magnitude squared of the wave function,  $u$  is a dimensionless length,  $\mu$  is the chemical potential, and  $V_0$  is an external constant potential.

For  $u < 0$  (we call it the region I,  $V_0 = 0$ ), we use the cnc function with  $a = 1$ , i.e.,

$$\psi_I(u, \alpha) = \text{cnc}(k_I u, \alpha_I), \quad (41)$$

with parameters

$$k_I^2 = \frac{2ML^2\mu}{\hbar^2 [1 + \alpha_I(a^2 + b^2)]}, \quad (42)$$

$$\alpha_I = \frac{ML^2 NU_0}{\hbar^2 A^2 k_I^2} \quad (43)$$

From these equations, we obtain

$$\alpha_I = \frac{NU_0}{2\mu A^2 - NU_0(a^2 + b^2)}, \quad (44)$$

and

$$\mu = \frac{\hbar^2 k_I^2}{2ML^2} + \frac{NU_0}{2A^2} (a^2 + b^2). \quad (45)$$

This last result for  $\mu$  is in agreement with the conjecture formulated by D'Agosta et al. in Ref. [9], with the last term being the self-energy of the condensate, which is independent of  $k_I$ .

For  $u > 0$ , we use the nonlinear plane wave ( $a = T, b = 0$ )

$$\psi_{II}(u) = \text{cnc}(k_{II} u, \alpha_{II}), \quad (46)$$

with

$$1 + \alpha_{II}T^2 = \frac{2ML^2}{\hbar^2 k_{II}^2}(\mu - V_0), \quad \frac{2ML^2 NU_0}{\hbar^2 A^2 k_{II}^2} = 2\alpha_{II}, \quad (47)$$

i.e.,

$$\mu = V_0 + \frac{\hbar^2 k_{II}^2}{2ML^2} + \frac{NU_0}{2A^2} T^2, \quad k_{II}^2 = \frac{2ML^2(\mu - V_0)}{\hbar^2(1 + \alpha_{II}T^2)}. \quad (48)$$

By combining the expressions for the  $\alpha$ s in both regions, we find that

$$\alpha_I k_I^2 = \alpha_{II} k_{II}^2, \quad (49)$$

and since the chemical potential should be the same on both regions, we also get

$$V_0 = \frac{\hbar^2(k_I^2 - k_{II}^2)}{2ML^2} + \frac{NU_0}{2A^2}(a^2 + b^2 - T^2). \quad (50)$$

The equal flux condition results in

$$k_I(a^2 - b^2) = k_{II}T^2. \quad (51)$$

Now, equating the functions and their derivatives at  $u = 0$ , we find two relations for the parameters:

$$a + b = T, \quad (52)$$

$$(a - b)k_I \sqrt{1 - \alpha_I(a + b)^2} = Tk_{II} \sqrt{1 - \alpha_{II}T^2}, \quad (53)$$

i.e.,

$$\frac{k_{II}}{k_I} = \frac{(a - b)}{(a + b)} \sqrt{\frac{1 - \alpha_I(a + b)^2}{1 - \alpha_I(a + b)^2 k_I^2 / k_{II}^2}}. \quad (54)$$

We show these values in **Figure 2**. We observe a behavior similar to the linear system; when  $\mu \gg V_0$  ( $k_{II} \rightarrow k_I$ ), which means very high energies, the step is just a small perturbation on the evolution of the wave.

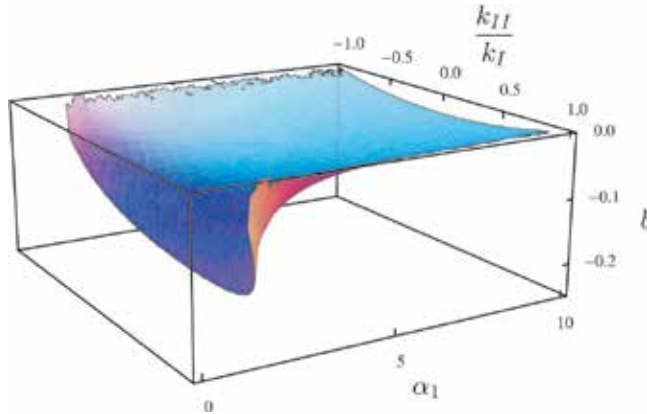


**Figure 2.** A three-dimensional plot of the values of  $k_{II}/k_I$  for the potential step. Dimensionless units.

### 3. Nonlinear superposition of trigonometric functions

A second set of nonlinear functions is the nonlinear version of the superposition of trigonometric functions, which is the subject of this section. We only mention some results; more details are found in Ref. [10].

Let us consider the change of variable from  $\theta$  to  $u$  defined by the Jacobian

$$\text{dna}(u) = \frac{d\theta}{du} = \sqrt{1 + \frac{\alpha}{2}(a^2 - b^2) \cos(2\theta) + \alpha ab \sin(2\theta)}, \quad (55)$$

where  $\alpha, a, b \in \mathbb{R}$ , and  $|\alpha| < 4|ab|/(a^2 + b^2)^2$ , a plot of  $4|ab|/(a^2 + b^2)^2$ , is shown in **Figure 3**. Thus, the relationship between  $\theta$  and  $u$  is

$$u = \int_0^\theta \frac{d\theta}{\sqrt{1 + \frac{\alpha}{2}(a^2 - b^2) \cos(2\theta) + \alpha ab \sin(2\theta)}}. \quad (56)$$

We also define the nonlinear functions

$$\text{sna}(u) := a \sin(\theta) - b \cos(\theta), \quad (57)$$

$$\text{cna}(u) := a \cos(\theta) + b \sin(\theta), \quad (58)$$

$$\text{osa}(u) := \frac{1}{\text{sna}(u)}, \quad \text{oca}(u) := \frac{1}{\text{cna}(u)}, \quad \text{oda}(u) := \frac{1}{\text{dna}(u)}, \quad (59)$$

$$\text{csa}(u) := \frac{\text{cna}(u)}{\text{sna}(u)}, \quad \text{sca}(u) := \frac{\text{sna}(u)}{\text{cna}(u)}, \quad \text{dsa}(u) := \frac{\text{dna}(u)}{\text{sna}(u)}, \quad (60)$$

$$\text{dca}(u) := \frac{\text{dna}(u)}{\text{cna}(u)}, \quad \text{sda}(u) := \frac{\text{sna}(u)}{\text{dna}(u)}, \quad \text{cda}(u) := \frac{\text{cna}(u)}{\text{dna}(u)}. \quad (61)$$

A plot of these functions can be found in **Figure 4**, for a set of values of  $\alpha, a, b$ . The algebraic relationships between the above functions are

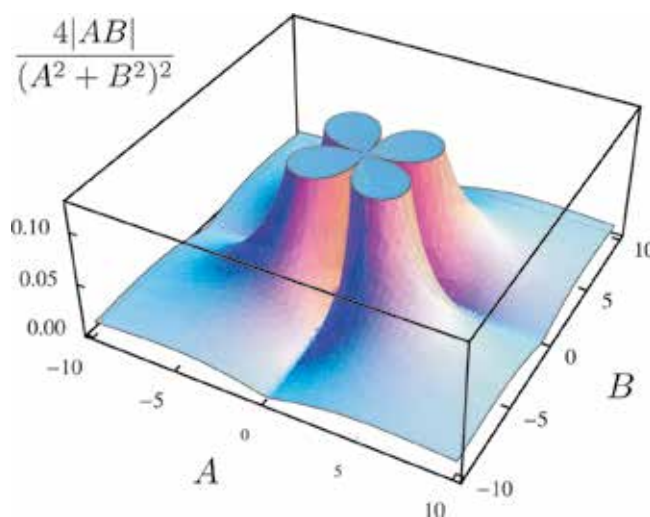


**Figure 3.**  
 Three-dimensional plot of  $4|ab|/(a^2 + b^2)^2$ .

$$a^2 + b^2 = \text{sna}^2(u) + \text{cna}^2(u), \quad (62)$$

$$\text{dna}^2(u) = 1 - \frac{\alpha}{2} (\text{sna}^2(u) - \text{cna}^2(u)) \quad (63)$$

$$= n_4 + \alpha \text{cna}^2(u) \quad (64)$$

$$= n_5 - \alpha \text{sna}^2(u), \quad (65)$$

$$\text{sda}^2(u) = n_0 \text{oda}^2(u) - \text{cda}^2(u), \quad (66)$$

$$1 - \text{oda}^2(u) = \frac{\alpha}{2} [\text{cda}^2(u) - \text{sda}^2(u)], \quad (67)$$

$$1 + \alpha \text{sda}^2(u) = n_5 \text{oda}^2(u), \quad (68)$$

$$1 - \alpha \text{cda}^2(u) = n_4 \text{oda}^2(u), \quad (69)$$

$$\text{sca}^2(u) = n_0 \text{oca}^2(u) - 1, \quad (70)$$

$$\text{dca}^2(u) = n_4 \text{oca}^2(u) + \alpha, \quad (71)$$

$$\text{csa}^2(u) = n_0 \text{osa}^2(u) - 1. \quad (72)$$

The derivatives of these functions are

$$\text{sna}'(u) = \text{cna}(u) \text{dna}(u), \quad (73)$$

$$\text{cna}'(u) = -\text{sna}(u) \text{dna}(u), \quad (74)$$

$$\text{dna}'(u) = -\alpha \text{sna}(u) \text{cna}(u), \quad (75)$$

$$\text{osa}'(u) = -\text{cna}(u) \text{dna}(u) \text{osa}^2(u), \quad (76)$$

$$\text{oca}'(u) = \text{sna}(u) \text{dna}(u) \text{oca}^2(u), \quad (77)$$

$$\text{oda}'(u) = \alpha \text{cna}(u) \text{sna}(u) \text{oda}^2(u). \quad (78)$$

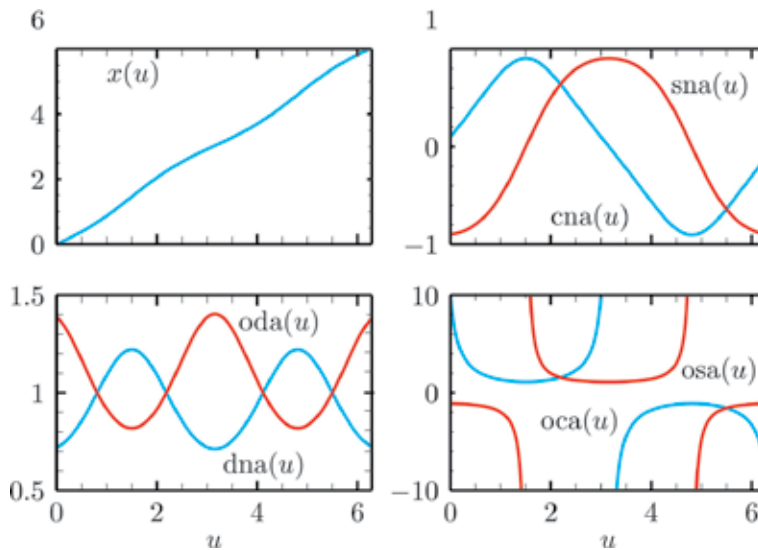


**Figure 4.** Plots of the nonlinear functions for  $a = 0.1$ ,  $b = 0.9$ , and  $\alpha = 1.2$ . Note that the functions  $\text{cna}$  and  $\text{sna}$  have different shapes, and, thus, they are not just the other function shifted by some amount.

Another property is the eliminant equation, also known as energy or Liapunov function,

$$[\text{sna}'(u)]^2 + n_7 \text{sna}^2(u) - \alpha \text{sna}^4(u) = n_0 n_5, \quad (79)$$

$$[\text{cna}'(u)]^2 + n_2 \text{cna}^2(u) + \alpha \text{cna}^4(u) = n_0 n_4, \quad (80)$$

$$[\text{dna}'(u)]^2 - 2 \text{dna}^2(u) + \text{dna}^4(u) = -n_4 n_5, \quad (81)$$

$$[\text{osa}'(u)]^2 + n_7 \text{osa}^2(u) - n_0 n_5 \text{osa}^4(u) = \alpha, \quad (82)$$

$$[\text{oca}'(u)]^2 + n_2 \text{oca}^2(u) - n_0 n_4 \text{oca}^4(u) = -\alpha, \quad (83)$$

$$[\text{oda}'(u)]^2 - 2 \text{oda}^2(u) + n_4 n_5 \text{oda}^4(u) = -1. \quad (84)$$

Second derivatives of the functions lead to the differential equations similar to the Gross-Pitaevskii nonlinear differential equation. For sna, cna, and dna, we have that

$$\text{sna}''(u) + n_7 \text{sna}(u) - 2\alpha \text{sna}^3(u) = 0, \quad (85)$$

$$\text{cna}''(u) + n_2 \text{cna}(u) + 2\alpha \text{cna}^3(u) = 0, \quad (86)$$

$$\text{dna}''(u) + 2 \text{dna}(u) [\text{dna}^2(u) - 1] = 0, \quad (87)$$

$$\text{osa}''(u) + n_7 \text{osa}(u) - 2n_0 n_5 \text{osa}^3(u) = 0, \quad (88)$$

$$\text{oca}''(u) + n_2 \text{oca}(u) - 2n_0 n_4 \text{oca}^3(u) = 0, \quad (89)$$

$$\text{oda}''(u) - 2 \text{oda}(u) + 2n_4 n_5 \text{oda}^3(u) = 0. \quad (90)$$

Quarter period of these functions is defined as

$$\text{Ka}(\alpha, a, b) = \int_0^{\pi/2} \frac{dt}{\sqrt{1 + \alpha(a^2 - b^2) \cos(2t)/2 + \alpha ab \sin(2t)}}. \quad (91)$$

A plot of  $\text{Ka}(\alpha, a, b)$  can be found in **Figure 5** for  $\alpha = 1.2$ .

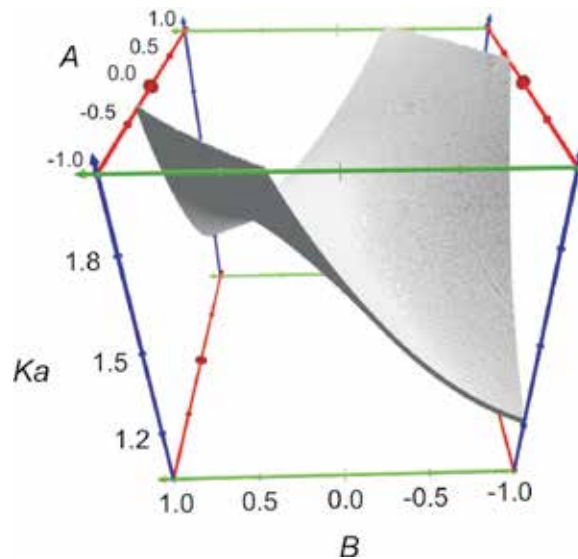


**Figure 5.** Some of the values of nonlinear quarter period  $\text{Ka}(\alpha, a, b)$ , for  $\alpha = 1.2$ .

The derivatives of the inverse functions are

$$\frac{d}{dy} \text{sna}^{-1}(y) = \frac{\pm 1}{\sqrt{(n_0 - y^2)(n_5 - \alpha y^2)}}, \quad (92)$$

$$\frac{d}{dy} \text{cna}^{-1}(y) = \frac{\pm 1}{\sqrt{(n_0 - y^2)(n_4 + \alpha y^2)}}, \quad (93)$$

$$\frac{d}{dy} \text{dna}^{-1}(y) = \frac{\pm 1}{\sqrt{(n_5 - y^2)(y^2 - n_4)}}, \quad (94)$$

$$\frac{d}{dy} \text{osa}^{-1}(y) = \frac{\pm 1}{\sqrt{(n_0 y^2 - 1)(n_5 y^2 - \alpha)}}, \quad (95)$$

$$\frac{d}{dy} \text{oca}^{-1}(y) = \frac{\pm 1}{\sqrt{(n_0 y^2 - 1)(n_4 y^2 + \alpha)}}, \quad (96)$$

$$\frac{d}{dy} \text{oda}^{-1}(y) = \frac{\pm 1}{\sqrt{(n_5 y^2 - 1)(1 - n_4 y^2)}}. \quad (97)$$

Then, as expected, we can see that these functions also invert the same integrals that Jacobi's functions invert.

We also introduce the integral

$$Ea(u) = \int_0^u dv \text{dna}^2(v) \quad (98)$$

$$= n_5 u - \alpha \int_0^u dv \text{sna}^2(v) \quad (99)$$

$$= n_4 u + \alpha \int_0^u dv \text{cna}^2(v), \quad (100)$$

which resembles Jacobi's elliptic integral of the second kind. This function is shown in **Figure 6**, for a set of values of the parameters.

This is the minimum set of properties for these functions. Fortunately, we can still introduce another set of nonlinear functions.

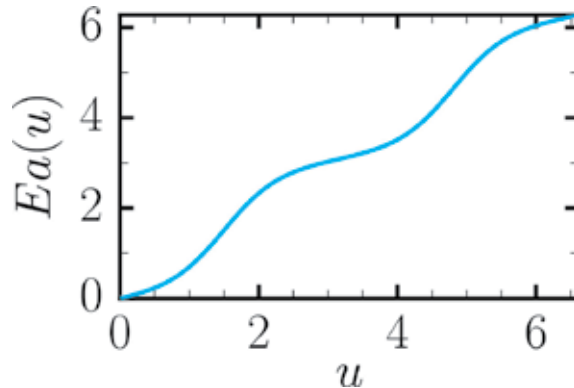


**Figure 6.** Plot of  $Ea(u)$  for  $A = 0.1$ ,  $B = 0.9$ , and  $\alpha = 1.2$ .

#### 4. Nonlinear exponential-like functions

It is possible to define still another set of nonlinear functions inspired on Jacobi's elliptic functions [11]. Let us consider the following set of nonlinear functions of exponential type:

$$pn(u) = e^x, \quad mn(u) = e^{-x}, \quad fn(u) = a e^x + b e^{-x}, \quad (101)$$

$$gn(u) = a e^x - b e^{-x}, \quad rn(u) = \sqrt{1 + m(a e^x - b e^{-x})^2}, \quad (102)$$

$$nf(u) = \frac{1}{fn(u)}, \quad ng(u) = \frac{1}{gn(u)}, \quad nr(u) = \frac{1}{rn(u)}, \quad (103)$$

with  $u$  and  $x$  related as

$$u = \int_0^x \frac{dt}{\sqrt{1 + m(a e^t - b e^{-t})^2}}, \quad (104)$$

where  $a, b \in \mathbb{R}$  and  $m > 0$ . The required values of  $a, b, m$  causes that the radical is positive and then there is no need to consider branching points.

Note that  $rn(u) \neq rn(-u)$ , and, then,  $mn(u)$  is not the mirror image of  $pn(u)$ , i.e.,  $mn(u) \neq pn(-u)$  unless  $a = b$ . A plot of these functions is found in **Figure 7** for a set of values of the parameters  $a, b$ , and  $m$ . The values of  $a$  and  $b$  are related to the mirror symmetry between the functions  $pn(u)$  and  $mn(u)$ , being  $b = a$  the more symmetric case (which would be the case of Jacobi's elliptic functions with complex arguments). The value of  $m$  causes that these functions decay or increase more rapidly with respect to the regular exponential functions. The domain of these functions is finite unless  $m = 0$ ; in fact, increasing the magnitude of  $x$  beyond, for instance,  $\ln(10^4/2a\sqrt{m})$ , does not increase the magnitude of  $u$  significantly. One can extend the domain of these functions by setting the value of the function to zero

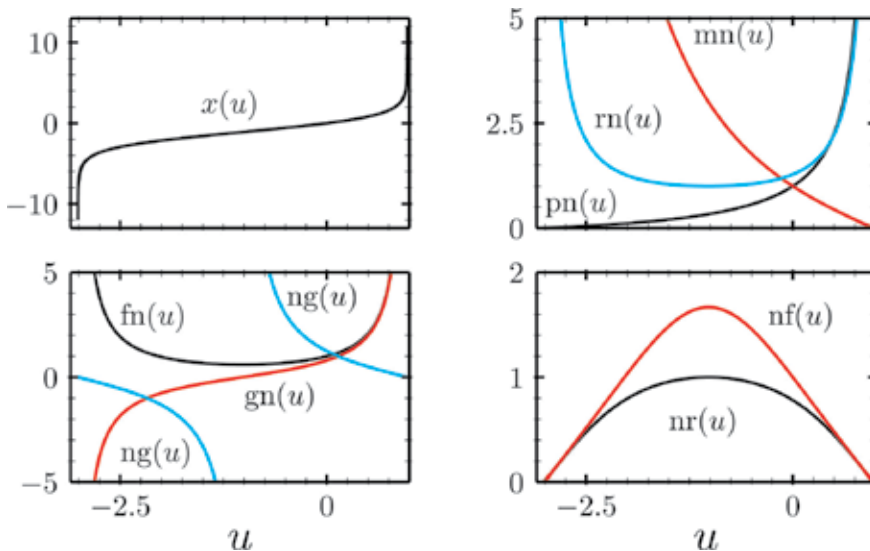


**Figure 7.**  
 Nonlinear exponential-like functions for  $m = 1$ ,  $a = 0.1$ , and  $b = 0.9$ .

or infinity for larger  $|u|$ , making them nonperiodic functions on the real axes. We also note that some of these functions are actually bounded.

We can verify easily the following properties which are similar to those for the elliptic functions. The square of these functions are related as

$$4ab = \text{fn}^2(u) - \text{gn}^2(u), \quad (105)$$

$$\text{rn}^2(u) - 1 = m \text{gn}^2(u) = m [\text{fn}^2(u) - 4ab] \quad (106)$$

$$\text{fn}(u)\text{gn}(u) = a^2\text{pn}^2(u) - b^2\text{mn}^2(u), \quad (107)$$

$$\text{fn}^2(u) + \text{gn}^2(u) = 2[b^2 \text{mn}^2(u) + a^2 \text{pn}^2(u)], \quad (108)$$

whereas the derivatives of them are

$$\text{pn}'(u) = \text{pn}(u) \text{rn}(u), \quad \text{mn}'(u) = -\text{mn}(u) \text{rn}(u), \quad (109)$$

$$\text{fn}'(u) = \text{gn}(u) \text{rn}(u), \quad \text{gn}'(u) = \text{fn}(u) \text{rn}(u), \quad (110)$$

$$\text{rn}'(u) = m \text{fn}(u) \text{gn}(u), \quad \text{nf}'(u) = -\text{gn}(u) \text{nf}^2(u) \text{rn}(u), \quad (111)$$

$$\text{ng}'(u) = -\text{fn}(u) \text{ng}^2(u) \text{rn}(u), \quad \text{nr}'(u) = -m \text{fn}(u) \text{gn}(u) \text{nr}^2(u). \quad (112)$$

As we can see from these derivatives, the rate of increase or decrease of the functions is modulated by the  $\text{rn}$  function; it would be the same as that for the usual exponential functions for the case  $m = 0$ .

We also have that

$$\frac{d \text{pn}^{-1}(y)}{dy} = \frac{1}{\sqrt{y^2 + m(a y^2 - b)^2}}, \quad (113)$$

$$\frac{d \text{mn}^{-1}(y)}{dy} = -\frac{1}{\sqrt{y^2 + m(a - b y^2)^2}}, \quad (114)$$

$$\frac{d \text{fn}^{-1}(y)}{dy} = \pm \frac{1}{\sqrt{(y^2 - 4ab)(c_2 + m y^2)}}, \quad (115)$$

$$\frac{d \text{gn}^{-1}(y)}{dy} = \frac{1}{\sqrt{(y^2 + 4ab)(1 + m y^2)}}, \quad (116)$$

$$\frac{d \text{rn}^{-1}(y)}{dy} = \pm \frac{1}{\sqrt{(1 - y^2)(c_2 - y^2)}}, \quad (117)$$

$$\frac{d \text{nf}^{-1}(y)}{dy} = -\frac{1}{\sqrt{(1 - 4ab y^2)[c_2 y^2 + m]}}, \quad (118)$$

$$\frac{d \text{ng}^{-1}(y)}{dy} = -\frac{1}{\sqrt{(1 + 4ab y^2)(y^2 + m)}}, \quad (119)$$

$$\frac{d \text{nr}^{-1}(y)}{dy} = -\frac{1}{\sqrt{(1 - y^2)(1 - c_2 y^2)}}. \quad (120)$$

As expected, from these derivatives, we can see that these functions also invert the same integral functions that Jacobi was interested on [1, 4].

The second derivatives are

$$pn''(u) - pn(u)[c_3 + 2ma^2 pn^2(u)] = 0, \quad (121)$$

$$mn''(u) - mn(u)[c_3 + 2mb^2 mn^2(u)] = 0, \quad (122)$$

$$fn''(u) - fn(u)[c_1 + 2m fn^2(u)] = 0, \quad (123)$$

$$gn''(u) - gn(u)[c_4 + 2m gn^2(u)] = 0, \quad (124)$$

$$rn''(u) + 2rn(u)[c_3 - rn^2(u)] = 0, \quad (125)$$

$$nf''(u) - nf(u)[c_1 - 8abc_2nf^2(u)] = 0, \quad (126)$$

$$ng''(u) - ng(u)[c_4 + 8ab ng^2(u)] = 0, \quad (127)$$

$$nr''(u) - 2nr(u)[c_2 nr^2(u) - c_3] = 0. \quad (128)$$

where

$$c_1 = 1 - 8mab, \quad c_2 = 1 - 4mab, \quad c_3 = 1 - 2mab, \quad (129)$$

$$c_4 = 1 + 4mab. \quad (130)$$

Then, the functions that we have just introduced are solutions of nonlinear second-order differential equations with the one-dimensional Gross-Pitaevskii equation form, for a constant potential and real functions.

Additionally, the energy or Liapunov functions are given by

$$pn'(u)^2 - pn(u)^2[c_3 + ma^2 pn^2(u)] = mb^2, \quad (131)$$

$$mn'(u)^2 - mn(u)^2[c_3 + mb^2 mn^2(u)] = ma^2, \quad (132)$$

$$fn'(u)^2 - fn(u)^2[c_1 + m fn^2(u)] = -4abc_2, \quad (133)$$

$$gn'(u)^2 - gn(u)^2[c_4 + m gn^2(u)] = 4ab, \quad (134)$$

$$rn'(u)^2 + 2rn(u)^2[c_3 - rn^2(u)] = c_2, \quad (135)$$

$$nf'(u)^2 - nf(u)^2[c_1 - 4abc_2nf^2(u)] = m, \quad (136)$$

$$ng'(u)^2 - ng(u)^2[c_4 + 4ab ng^2(u)] = m, \quad (137)$$

$$nr'(u)^2 - nr(u)^2[-2c_3 + c_2 nr^2(u)] = 1, \quad (138)$$

where we have made use of the relationships between the squares of the functions. Note that, the functions  $nf$  and  $ng$  have the same energy, whereas that the functions  $pn(u)$  and  $mn(u)$  would have the same energy if  $b = a$ .

Some particular cases are the following. When  $4mab = 1$  or  $2mab = 1$ , we can write down explicit expressions of  $u$  in terms of trigonometric, hypergeometric, and exponential functions of  $x$ . When  $4mab = 1$ , we get

$$u = \int_0^x \frac{\sqrt{4ab} dx}{(ae^{2x} + be^{-2x})} = 2 \left[ \tan^{-1} \left( \sqrt{\frac{a}{b}} e^x \right) - \tan^{-1} \left( \sqrt{\frac{a}{b}} \right) \right], \quad (139)$$

and when  $2mab = 1$ , we obtain

$$\begin{aligned}
 u &= \sqrt{2ab} \int_0^x \frac{dt}{\sqrt{a^2 e^{2t} + b^2 e^{-2t}}} \\
 &= \frac{1}{\sqrt{2abab}} \\
 &\quad \times \left\{ e^{-2x} \sqrt{b^2 e^{-2x} + a^2 e^{2x}} \left[ b^2 - e^{2x} (b^2 e^{-2x} + a^2 e^{2x}) {}_2F_1 \left( \frac{3}{4}, 1; \frac{1}{4}; -\frac{a^2 e^{4x}}{b^2} \right) \right] \right. \\
 &\quad \left. - \sqrt{a^2 + b^2} \left[ b^2 - (a^2 + b^2) {}_2F_1 \left( \frac{3}{4}, 1; \frac{1}{4}; -\frac{a^2}{b^2} \right) \right] \right\}, \tag{140}
 \end{aligned}$$

where  ${}_2F_1$  is the hypergeometric function.

When  $a = b = 1$ , the nonlinear functions reduce to Jacobi's elliptic functions with complex argument:

$$u = \int_0^x \frac{1}{\sqrt{1 + 4m \sin^2(t)}} dt = -iF(ix|4m), \tag{141}$$

where  $F$  is elliptic integral of the first kind.

This is the minimum set of properties of the exponential-type nonlinear functions.

## 5. Remarks

Thus, we were able to obtain three sets of nonlinear functions which are solutions to the Gross-Pitaevskii equation. With these functions, we have the nonlinear versions of the trigonometric, real, and complex exponential functions and their linear combinations, and a complete set of functions as in the linear counterpart.

Due to the method of solution, which makes use of elliptic functions, these functions will expand the set of solutions that can be given to polynomial nonlinear equations, in general [8, 12–25].

For instance, a well-known optical phenomenon is the nonlinear dispersion in parabolic law medium with Kerr law nonlinearity [24]. This system is described by a nonlinear Schrödinger equation:

$$i\Psi_t + a\Psi_{xx} + b|\Psi|^2\Psi + c|\Psi|^4\Psi + d\left(|\Psi|^2\right)_{xx}\Psi = 0, \tag{142}$$

where a subindex indicates a derivative with respect to that index. The second term of the above equation represents the group velocity dispersion, the third and fourth terms are the parabolic law nonlinearity, and the last term is the nonlinear dispersion. Some solutions of Eq. (142) were found in Ref. [24]. A solution is the traveling wave, with Jacobi's sn function profile, given by

$$\Psi(x, t) = A \operatorname{sn}[B(x - vt), m] e^{i\phi}, \tag{143}$$

$$B = \left( \frac{-bA^2}{am(1+m) - 2d(m^2 + m + 2)A^2} \right)^{1/2}, \tag{144}$$

$$\omega = B^2(2dA^2 - a(1+m)). \tag{145}$$

where  $v = -2ak$  is the velocity,  $k$  is the soliton frequency,  $\omega$  is the soliton wave number,  $\theta$  is the phase constant, and  $0 < m < 1$  is the modulus of Jacobi's elliptic function.

A second solution was given as

$$\Psi(x, t) = A \operatorname{cn}[B(x - vt), l] e^{i\phi}, \quad (146)$$

$$B = \left( \frac{b}{4d} \right)^{1/2}, \quad (147)$$

$$\omega = B^2(2dA^2 - a) - ak^2. \quad (148)$$

Since the functions that we have introduced in these chapters comply with differential and algebraic equations similar to the ones for Jacobi's elliptic functions, we can give additional solutions in terms of these new functions, giving rise to new sets of soliton waves.

## Author details

Gabino Torres Vega  
Physics Department, Cinvestav, México City, México

\*Address all correspondence to: [gabino@fis.cinvestav.mx](mailto:gabino@fis.cinvestav.mx)

## IntechOpen

© 2018 The Author(s). Licensee IntechOpen. This chapter is distributed under the terms of the Creative Commons Attribution License (<http://creativecommons.org/licenses/by/3.0>), which permits unrestricted use, distribution, and reproduction in any medium, provided the original work is properly cited. 

## References

- [1] Cayley A. An Elementary Treatise on Elliptic Functions. 2nd ed. N.Y: Dover Publications, Inc; 1961
- [2] Abramowitz M, Stegun I. Handbook of Mathematical Functions. New York: Dover; 1964
- [3] Khare A, Sukhatme U. Linear superposition in nonlinear equations. *Physical Review Letters*. 2002;**88**: 244101
- [4] Markushevich AI. Introduction to the Classical Theory of Abelian Functions, Series Translations of Mathematical Monographs. Vol. 96. Providence, Rhode Island: American Mathematical Society; 1992
- [5] Carr LD, Clark CW, Reinhardt WP. Stationary solutions of the one-dimensional nonlinear Schrödinger equation. I. Case of repulsive nonlinearity. *Physical Review A*. 2000; **62**:063610
- [6] Carr LD, Clark C,W, Reinhardt WP. Stationary solutions of the one-dimensional nonlinear Schrödinger equation. II. Case of attractive nonlinearity. *Physical Review A*. 2000; **62**:063611
- [7] Mahmud KW, Kutz JN, Reinhardt WP. Bose-Einstein condensates in a one-dimensional double square well: Analytical solutions of the nonlinear Schrödinger equation. *Physical Review A*. 2002;**66**:063607
- [8] Zayed EME, Alurrfi KAE. A new Jacobi elliptic function expansion method for solving a nonlinear PDE describing pulse narrowing nonlinear transmission lines. *Journal of Differential Equations*. 2015;**28**:128
- [9] D'Agosta R, Malomed BA, Presilla C. Stationary solutions of the gross-Pitaevskii equation with linear counterpart. *Physics Letters A*. 2000;**275**:424-434
- [10] Torres-Vega G. Some real, periodic stationary solutions of the one-dimensional nonlinear Schrödinger equation for constant potentials. *Journal of Physics: Conference Series*. 2017;**792**: 012054
- [11] Torres-Vega G. Decaying steady states of the one-dimensional nonlinear Schrödinger equation with a constant potential. *Journal of Physics: Conference Series*. 2017;**792**:012031
- [12] Ma H-C, Zhang Z-P, Deng A-P. A new periodic solution to Jacobi elliptic functions of MKdV equation and BBM equation. *Acta Mathematicae Applicatae Sinica (English Series)*. 2012;**28**:409. DOI: 10.1007/s10255-012-0153-7
- [13] Zayed EME, Alurrfi KAE. A new Jacobi elliptic function expansion method for solving a nonlinear PDE describing the nonlinear low-pass electrical lines. *Chaos, Solitons and Fractals*. 2015;**78**:148. DOI: 10.1016/j.chaos.2015.07.018
- [14] Zayed EME, Al-Nowehy A-G. New extended auxiliary equation method for finding many new Jacobi elliptic function solutions of three nonlinear Schrödinger equations. *Waves in Random and Complex Media*. 2017;**27**: 420. DOI: 10.1080/17455030.2016.1259690
- [15] Sonmezoglu A. Exact solutions for some fractional differential equations. *Advances in Mathematical Physics*. 2015;**2015**:567842
- [16] Zhou Q, Zhu Q, Savescu M, Bhrawy A, Biswas A. Optical solitons with nonlinear dispersion in parabolic law medium. *Proceedings of the Romanian Academy, Series A*. 2015;**16**:152

- [17] Feng Q, Meng F. Explicit solutions for space-time fractional partial differential equations in mathematical physics by a new generalized fractional Jacobi elliptic equation-based sub-equation method. *Optik*. 2016;**127**:7450
- [18] Feng Q. Jacobi elliptic function solutions for fractional partial differential equations. *International Journal of Applied Mathematics*. 2016; **46**:121
- [19] Kudryashov NA, Sinelshchikov DI. On the connection of the quadratic Lienard equation with an equation for the elliptic functions. *Regular and Chaotic Dynamics*. 2015;**20**:486. DOI: 10.1134/S1560354715040073
- [20] Zhang Z-Y. Jacobi elliptic function expansion method for the modified Korteweg-de Vries-Zakharov-Kuznetsov and the Hirota equations. *Romanian Journal of Physics*. 2015;**60**: 1384
- [21] Aslan EC, Tchier F, Inc M. On optical solitons of the Schrödinger-Hirota equation with power law nonlinearity in optical fibers. *Superlattices and Microstructures*. 2017; **105**:48. DOI: 10.1016/j.spmi.2017.03.014
- [22] Aslan EC, Inc M, Baleanu D. Optical solitons and stability analysis of the NLSE with anti-cubic nonlinearity. *Superlattices and Microstructures*. 2017; **109**:784. DOI: 10.1016/j.spmi.2017.06.003
- [23] Tasbozan O, Çenesiz Y, Kurt A. New solutions for conformable fractional Boussinesq and combined KdV-mKdV equations using Jacobi elliptic function expansion method. *European Physical Journal Plus*. 2016; **131**:244. DOI: 10.1140/epjp/i2016-16244-x
- [24] Tchier F, Aslan EC, Inc M. Optical solitons in parabolic law medium: Jacobi elliptic function solution. *Nonlinear Dynamics*. 2016;**85**:2577. DOI: 10.1007/s11071-016-2846-6
- [25] Triki H, Wazwaz A-M. New solitons and periodic wave solutions for the (2+1)-dimensional Heisenberg ferromagnetic spin chain equation. *Journal of Electromagnetic Waves and Applications*. 2016;**30**:788. DOI: 10.1080/09205071.2016.1153986



# Hydrodynamic Methods and Exact Solutions in Application to the Electromagnetic Field Theory in Medium

*Sergey G. Chefranov and Artem S. Chefranov*

## Abstract

The new Vavilov-Cherenkov radiation theory which is based on the relativistic generalization of the Landau theory for superfluid threshold velocity and Abraham theory of the electromagnetic field (EMF) in medium is represented. The new exact solution of the Cauchy problem in unbounded space is obtained for the  $n$ -dimensional Euler-Helmholtz (EH) equation in the case of a nonzero-divergence velocity field for an ideal compressible medium. The solution obtained describes the inertial vortex motion and coincides with the exact solution to the  $n$ -dimensional Hopf equation which simulates turbulence without pressure. Due to the introduction of a fairly large external friction or by introducing an arbitrary small effective volume viscosity, a new analytic solution of the Cauchy problem for the three-dimensional Navier-Stokes (NS) equation is obtained for compressible flows. This gives the positive solution to the Clay problem ([www.clamath.org](http://www.clamath.org)) generalization on the compressible NS equation. This solution also gives the possibility to obtain a new class of regular solutions to the  $n$ -dimensional modification of the Kuramoto-Sivashinsky equation, which is ordinarily used for the description of the nonlinear propagation of fronts in active media. The example for potential application of the new exact solution to the Hopf equation is considered in the connection of nonlinear geometrical optics with weak nonlinear medium at the nonlocality of the small action radii.

**Keywords:** hydrodynamics, compressibility, viscosity, turbulence, vorticity, EMF waves, Abraham theory, photon in medium

## 1. Introduction

The main subject of the nonlinear optic theory is a nonlinear activity of a medium where electromagnetic field (EMF) is propagated.

In this connection, the analogy between electromagnetic and hydrodynamic phenomena, which was noted yet by Helmholtz and Maxwell [1], is considered. In more recent papers, also different types of this analogy are used [2–4] and give possibility to open new ways for the solution of some nonlinear hydrodynamic problems on the basis of this analogy.

However up to now, there are only a few examples of the direct mathematical correspondence between hydrodynamics and EMF theory, which gives resolution of the EMF problems on the basis of hydrodynamics [5, 6].

Thus in [5] there is an exact mathematical correspondence between the solutions for the point electric dipole potential and velocity potential obtaining for the rigid sphere moving with constant speed in the ideal incompressible fluid.

In [6] an exact correspondence is established between the mathematical description of the single vortex velocity on the sphere and the Dirac magnetic monopole (DMM) [7] vector potential. Similar analogy with DMM was noted also for the vortices in quantum superfluid He-3A [8–11].

Moreover, in [6], it was proved that the hydrodynamic equations do not allow the existence of a solution in the form of a single isolated vortex on sphere, but allow the exact solution in the form of two antipodal point vortices (which have the same value but different signs of circulation and located on the sphere on the maximal possible distance from each other). This result gives the first theoretical base for the proposition that DMM also cannot exist in the single form, but they must be included in the structure of point magnetic dipole, which is confirmed by all observations and experiment data.

Here we consider some examples of the application of hydrodynamic methods for the problems of EMF interaction with medium which may be important in the field of nonlinear optics.

In Part 1 of the chapter, we give the example for demonstration of the new mechanism of the Vavilov-Cherenkov radiation (VCR), which is obtained only on the basis of relativistic generalization to the Landau theory of superfluid threshold velocity [12]. In analogy with the Landau criterion its relativistic generalization is deduced for the determination of threshold conversion of medium Bose-condensed excitation into Cherenkov's photon. Thus, the VCR arises only due to the reaction of medium on the electric charge moving with super threshold velocity [13–15]:

$$V_0 > V_{th} = c/n_*, n_* = n + \sqrt{n^2 - 1}, n > 1; n_* = (1 + \sqrt{1 - n^2})/n, n < 1 \quad (1)$$

In (1),  $c$  is the light speed in vacuum and  $n$  is the medium refractive index.

In contraposition to the classic VCR theory [16–18], the new VCR theory in [13–15] and (1) admits the conditions for effective and direct VCR realization even for high-frequency transverse waves of EMF in isotropic plasma when  $n < 1$  in (1). This is possible in the new VCR theory only because it is based on the Abraham theory for EMF in a medium where photons have nonzero real mass of rest, which determines necessary (in energy balance equation) energy difference for the medium when the medium emits photon VCR only for the condition (1).

In the second part of this chapter, we consider a new exact solution of nonlinear hydrodynamic equations. This gives corresponding possibility of its application to the problems of nonlinear EMF and other wave propagation in active and dissipative medium, where the Kuramoto-Sivashinsky equation [19–21] is used, giving the generalization of the Korteweg-de Vries (KdV) equation. Indeed, in nonlinear optic the KdF equation may describe the EMF wave propagation (for the case when electric wave  $E$  is propagating along axis  $x$ ):

$$\frac{\partial E}{\partial t} + \sigma E \frac{\partial E}{\partial x} + \sigma_0 \frac{\partial^3 E}{\partial x^3} = 0 \quad (2)$$

On the other side, the problem of the propagation of a flame front (generated by a self-sustained exothermal chemical reaction) may be considered on the basis of the simplified version of the Sivashinsky equation  $\nabla$  [21]:

$$\frac{\partial f}{\partial t} - \frac{1}{2} U_s \left( \vec{\nabla} f \right)^2 = \gamma_0 f \quad (3)$$

In the one-dimensional case, (3) is the same as (2) if  $E = \partial f / \partial x$ ;  $U_s = -\sigma$  and if we replace (for the case  $\gamma_0 < 0$ )  $\sigma_0 \partial^3 E / \partial x^3 \rightarrow -\gamma_0 E$ .

In Eq. (3), the function  $x_3 = f(x_1, x_2, t)$  determines the flame front which represents the interface between a combustible matter ( $x_3 > 0$ ) and the combustion products ( $x_3 < 0$ );  $U_s$  and  $\gamma_0$  are constant positive quantities which characterize the front velocity and the combustion intensity, respectively. For  $\gamma_0 = 0$  Eq. (3) coincides with the Hamilton-Jacobi equation for a free nonrelativistic particle. In the two-dimensional case (more exactly, in its modification with account for the external friction with the coefficient  $\mu$  when  $\mu = -\gamma_0$ ), the exact solution of the n-dimensional Hopf equation modification with  $\mu \neq 0$

$$\frac{\partial u_i}{\partial t} + u_k \frac{\partial u_i}{\partial x_k} = -\mu u_i; i, k = 1, \dots, n \quad (4)$$

(for the inertial motion of compressible medium with velocity  $u_i$ ) gives also the exact solution of Eq. (3) when the velocity of compressible medium  $\vec{u} = -U_s \vec{\nabla} f$ .

The common solution of 1D, 2D, and 3D equations (4) in Euler variables is first time obtained in [22–26]. On the basis of this solution, we give the positive answer to the generalization of the Clay problem [27] on the case of compressible medium motion with nonzero divergence of velocity field [23–26]. The existence and smoothness of this solution for all time may take place only for super threshold friction  $\mu > \mu_{th} = 1/t_0$  (here  $t_0$  is the minimal finite time of singularity realization for solution of the Hopf equation (4)) or for any finite volume viscosity [22–26]. This gives the possibility to obtain also exact solutions in nonlinear optic when equations of Kuramoto-Sivashinsky type are used for EMF wave propagation in nonlinear medium.

### 1.1 New theory of the Vavilov-Cherenkov radiation (VCR)

The Vavilov-Cherenkov radiation (VCR) phenomenon has justly become an inherent part of modern physics. The VCR in a refractive medium was experimentally discovered by Cherenkov and Vavilov [28] more than half a century ago. This was also the time when Tamm and Frank [16, 17] developed the electromagnetic macroscopical theory of this phenomenon, which, as well as the VCR discovery, was marked later by a Nobel Prize. The Tamm-Frank theory appeared to be very similar to the Heaviside theory, which had been forgotten for a century [29].

The Heaviside-Tamm-Frank (HTF) theory demonstrated that the cylindrically symmetrical EMF, created in a medium by an electron, which moves rectilinearly with the constant velocity  $V_0$ , does not exponentially reduce only in the case of the super threshold electron velocity  $V_0 \geq c/n$ . According to the HTF theory, this field must be identical to the VCR field, observed in the experiment [28].

However, such direct identification is not in agreement with the basic microscopical conception that VCR photons are radiated by a medium and not by an electron itself [16, 30]. The latter can serve only for the initiation of such radiation

by the medium. The phenomenological quantum theory of the VCR, developed by Ginzburg [18] on the basis of the Minkowski EMF theory in medium, still does not take into consideration the changes of the radiating medium energy state, which might be necessary for the VCR realization. As we show the latter, this is so because, in contrast to the Abraham EMF theory, for the momentum of photon in the Minkowski EMF theory, the corresponding photon mass of rest in medium always has only exact imaginary (with zero real part) value and cannot be taken into account in the energy balance equation for the VCR.

Thus, the classic theory of the VCR phenomenon leaves a question of the energy mechanism of the VCR effect open. Indeed, to elaborate this mechanism, we need to find out the necessary possible changes of the energy state of the medium itself, which ensure the VCR effect realization.

The suggested theory is based on directly using the Abraham momentum of photon:

$$\vec{p}_A = \frac{\varepsilon_{ph}}{cn} \vec{k}, n > 1; \vec{p}_A = \frac{\varepsilon_{ph}n}{c} \vec{k}, n < 1; \vec{k} = \frac{\vec{V}_{ph}}{|\vec{V}_{ph}|} \quad (5)$$

In (5)  $\varepsilon_{ph}$  is the photon energy and  $\vec{V}_{ph}$  its velocity in medium.

For the Minkowski EMF theory, the momentum of photon in medium with  $n > 1$  has the form:  $\vec{p}_M = \frac{\varepsilon_{ph}n}{c} \vec{k}$

For (5), the real nonzero photon rest mass  $m_{ph}$  is determined from the known relativistic equation  $m_{ph}^2 c^2 = \frac{\varepsilon_{ph}^2}{c^2} - p_A^2$ , and from (5), we have

$$m_{ph} = \frac{\varepsilon_{ph}}{c^2 n} \sqrt{n^2 - 1}, n > 1; m_{ph} = \frac{\varepsilon_{ph}}{c^2} \sqrt{1 - n^2}, n < 1 \quad (6)$$

In the new VCR quantum theory [13–15], the energy  $\Delta E_m = m_{ph}c^2$  may correspond to the energy of a medium long-wave Bose excitation which can transform into the VCR photon only when the super threshold condition (1) takes place. Thus, the value  $\Delta E_m$  must be taken into account in the energy balance equation for VCR realization possibility (when medium must lose this energy when the VCR photon is arising from it), and this new VCR theory is provided in [13, 14]. In [15] we also give examples where it is easy to obtain experimental and observational evidence of the difference between Abraham's and Minkowski's EMF theories when the VCR may be observed during the electron beam transfer through the medium which is the light of intense laser or when high-energy cosmic rays go through the relict background radiation.

To obtain a relativistic generalization of the Landau criterion [12] for the VCR realization, it is necessary to use the energy balance equation for the VCR (including in it the value of medium energy loss  $\Delta E_m = m_{ph}c^2$ , where  $m_{ph}$  may be taken from (6)) in the coordinate system moving with the initial electron velocity  $\vec{V}_0$  [13, 14]:

$$m_e c^2 \left[ 1 - \Gamma_0 \Gamma_1 \left( 1 - \frac{(\vec{V}_0 \vec{V}_1)}{c^2} \right) \right] = \varepsilon_{ph} \Gamma_0 \left[ 1 - \frac{(\vec{V}_0 \vec{V}_{ph})}{c^2} - \frac{m_{ph}c^2}{\varepsilon_{ph}} \right] \quad (7)$$

where  $\vec{V}_1$  is the velocity of electron after VCR photon arising. In (7)  $\Gamma_\alpha = 1/\sqrt{1 - \frac{V_\alpha^2}{c^2}}$ , where  $\alpha = 0$  or  $\alpha = 1$  and  $m_{ph}c^2/\varepsilon_{ph} = \sqrt{1 - \frac{V_{ph}^2}{c^2}}$  according to (6).

For example, in the case  $n > 1$  in (7), we have  $V_{ph} = c/n$  and in the right-hand side

$$\text{of (7) } A = 1 - \frac{(\vec{V}_0 \vec{V}_{ph})}{c^2} - \frac{m_{ph} c^2}{\epsilon_{ph}} = 1 - \frac{V_0}{c} \cos \theta - \frac{\sqrt{n^2 - 1}}{n}.$$

The left-hand side of (7) is always negative (it is zero only for the case when the initial and finite velocity of the electron are the same  $\vec{V}_0 = \vec{V}_1$ ).

In the nonrelativistic limit when  $V_0 \ll c$ ;  $V_{ph} \ll c$  from (7) for  $\epsilon_p > 0$ , the Landau criterion [12] may be obtained:  $\epsilon_V - (\vec{p} \vec{V}_0) < 0$ ;  $\epsilon_V = \epsilon_p \left( 1 - \sqrt{1 - \frac{V_p^2}{c^2}} \right) \cong \frac{\epsilon_p V_p^2}{2c^2}$ .

Then  $\epsilon_V = \frac{V_p p}{2}$  is the only kinetic energy of excitation (in [12] these are vorton elementary excitations).

Thus for the possibility of arising VCR photon with positive energy  $\epsilon_{ph} > 0$ , it is necessary to have in the right-hand side of (7) the negative value of  $A < 0$  or inequality:

$$\cos \theta > \frac{c}{V_0 n_*} \quad (8)$$

where the value  $n_*(n) > 1$  for any cases of  $n > 1$  or  $n < 1$  as it shown in (1). From the condition  $|\cos \theta| \leq 1$  in (8), the value of threshold velocity in (1) is obtained.

The conditions (8) and (1) give the necessary condition for arising VCR, and from (8) it is possible to obtain the maximal angle of the VCR cone of rays. The classic VCR theory gives good correspondence to experiment only in the determination of position for the maximum of intensity in the VCR cone of rays, but not to the maximal angle of this cone. In [13, 14] it is shown that the new VCR theory gives a better agreement with the experiment [28] than classical VCR theory when describing the threshold edge of the VCR cone of rays.

According to [28] the VCR effect is observed in the whole region of angles  $0 \leq \theta \leq \theta_{\max}^{A,B}$  with the maximum of radiation intensity  $I(\theta)$  at the angle  $\theta = \theta_0^{A,B} < \theta_{\max}^{A,B}$ . Here Index A corresponds to gamma rays of  $ThC''$ , and the Index B corresponds to the VCR induced by  $Ra$ . Thus,  $I(\theta) = 0$  when  $\theta > \theta_{\max}^{A,B}$ . In the [31] the same result was also obtained for VCR realization through the direct use of high-energy electron beam.

In the classic VCR theory in (1) and (8), the value  $n_*$  must be replaced with the value  $n$  for the case with  $n > 1$ .

Let us introduce the values  $\beta_*^A$ ;  $\beta_*^B$  which correspond to  $\theta_{\max}^{A,B}$  of experiment [28] when (8) is used for evaluation of parameter  $\beta = V_0/c$  and the analogy values  $\beta^A$ ;  $\beta^B$  for the classic VCR theory.

For example, when the medium where the VCR arising is water ( $H_2O$ ), where  $n = 1.333$ ,  $n_* = 2.247$ , and for the values  $\cos \theta_{\max}^A = 0.6691$ ;  $\cos \theta_{\max}^B = 0.7431$  from (8), we obtain  $\beta_*^A = 0.6718$ ;  $\beta_*^B = 0.6049$  which are smaller than 1, as they need from the relativity theory. For the classic VCR theory, the result is not corresponding to the inequality  $\beta = V_0/c < 1$  of the relativity theory because from the classic VCR theory,  $\beta^A = 1.1177$ ;  $\beta^B = 1.0064$  may be obtained. The same results obtained for all other media are considered in the experiment [28, 31] (see [13, 14]).

Thus, the classic VCR theory gives good correspondence with experiment [28] only in the determination of angle  $\theta_0^{A,B}$ , but not of the angle  $\theta_{\max}^{A,B}$ . In this connection the classic VCR theory tied only with interference maximum at  $\theta = \theta_0^{A,B}$  and does not consider at all the energetic base for threshold arising of this coherent VCR. Actually, this is clearer for the case of plasma with  $n < 1$ , where the classic VCR theory total excludes the possibility of the VCR in the form of transverse

high-frequency EMF waves. The present new VCR theory gives this possibility due to the transformation of a longitudinal Bose-condensed plasmon into transverse VCR photon, during the scattering of a plasmon on the relativistic electron [14, 37].

Moreover in this new VCR theory, the VCR phenomenon has the same nature as for numerous physical systems where dissipative instability is realized when corresponding excitations in a medium become energetically favorable at some super threshold conditions [12, 32–36].

## 1.2 Exact solution of hydrodynamic equations

Fundamental turbulence problem was unsolved during many years by virtue of the absence of analytical, time-dependent, smooth-at-all-time solutions of the nonlinear hydrodynamic equations. A few exact solutions are known in hydrodynamics, but none of these solutions is time-dependent and defined in unbounded space or in space with periodic boundary conditions [38–40].

The importance of this problem is determined by stability and predictability problems in all fields of science where solutions and methods of hydrodynamics are used. In this connection in 2000, the problem of the existence of smooth time-dependent hydrodynamic solutions was stated as one of the seven Millennium Prize Problems (MPPs) by the Clay Institute of Mathematics [27]. MPPs relate only to incompressible flows “since it is well known that the behavior of compressible flows is abominable” [41].

Here we show that even for a compressible case, it is possible to obtain exact analytical, time-dependent, smooth-at-all-time solutions of Hopf equation (4) (which gives also new class solution also for vortex typ. 2D and 3D Euler equation) when any viscosity of super threshold friction is taken into account [22–26].

With the aim to introduce effective volume viscosity (in addition to external friction in (4)), let us consider the  $n$ -dimensional Hopf equation (4) in the moving with velocity  $V_i(t)$  coordinate system, where  $V_i(t)$  is a random Gaussian delta-correlated in-time velocity field for which the relations hold:

$$\begin{aligned} \langle V_i(t)V_j(\tau) \rangle &= 2\nu\delta_{ij}\delta(t - \tau) \\ \langle V_i(t) \rangle &= 0 \end{aligned} \quad (9)$$

In (9)  $\delta_{ij}$  is the Kronecker delta,  $\delta$  is Dirac-Heaviside delta function, and the coefficient  $\nu$  characterizes the action of the viscosity forces. In the general case, the coefficient  $\nu$  can be a function of time when describing the effective turbulent viscosity, but also it can coincide with the constant kinematic viscosity coefficient when the random velocity field considered corresponds to molecular fluctuations. We will restrict our attention to the consideration of the case of constant coefficient  $\nu$  in (9).

Thus, the initial equation (4) (for the case  $\mu = 0$ ) takes the form:

$$\frac{\partial u_i}{\partial t} + (u_j + V_j(t)) \frac{\partial u_i}{\partial x_j} = 0 \quad (10)$$

As shown in Appendix, in the case of an arbitrary dimensionality of the space ( $n = 1, 2, 3$ , etc.), Eq. (10) has the following exact solution (see also [22–26]):

$$u_i(\vec{x}, t) = \int d^n \xi u_{0i}(\vec{\xi}) \delta(\vec{\xi} - \vec{x} + \vec{B}(t) + t\vec{u}_0(\vec{\xi})) \det \hat{A} \quad (11)$$

where  $B_i(t) = \int_0^t dt_1 V_i(t_1)$ ,  $\hat{A} \equiv A_{nm} = \delta_{nm} + t \frac{\partial u_{0n}}{\partial \xi_m}$ ,  $\det \hat{A}$  is the determinant of the matrix  $\hat{A}$ , and  $u_{0i}(\vec{x})$  is an arbitrary smooth initial velocity field. The solution (11)

satisfies Eq. (10) only at such times for which the determinant of the matrix  $\hat{A}$  is positive for any values of the spatial coordinates  $\det \hat{A} > 0$ .

In the case of the potential initial velocity field, the solution (11) is potential for all successive instants of time, corresponding to a zero-vortex field. On the contrary, in the case of nonzero initial vortex field, the solution also determines the evolution of velocity with a nonzero vortex field. In [42] the potential solution to the two-dimensional Hopf equation (4) (or when  $\vec{B} = 0$  in (12)) was obtained only in the Lagrangian representation which also exactly follows from (11) for  $n = 2$ . It is important to understand that here in (11) we have a solution in Euler variables, which is firstly obtained in [22] for  $n = 2$  and  $n = 3$ . From the solution of (10) or (4) in Lagrangian variables, it is unreal to obtain a solution of (4) or (10) in Euler variables. From the other side, it is easy to obtain a solution in Lagrangian variables if we have a solution in Euler variables as in (11).

For example, in the one-dimensional case ( $n = 1$ ) in (11), we have  $\det \hat{A} = 1 + t \frac{du_{01}}{d\xi_1}$ , and the solution (11) coincides exactly with the solutions obtained in [43, 44]. The solution (11) can be obtained if we use the integral representation for the implicit solution of Eq. (10) in the form  $u_k(\vec{x}, t) = u_{0k}(\vec{x} - \vec{B}(t) - t \vec{u}(\vec{x}, t))$  with the use of the Dirac delta function (see Appendix or [22, 23]).

After averaging over the random field  $B_i(t)$  (with the Gaussian probability density), from (11) we can obtain the exact solution in the form:

$$\langle u_i \rangle = \int d^n \xi u_{0i}(\vec{\xi}) |\det \hat{A}| \frac{1}{(2\sqrt{\pi t})^n} \exp \left[ -\frac{(\vec{x} - \vec{\xi} - t\vec{u}_0(\vec{\xi}))^2}{4t} \right] \quad (12)$$

As distinct from (11), the average solution (12) of Eq. (10) is already arbitrarily smooth on any unbounded time interval and not only providing the positiveness of the determinant of the matrix  $\hat{A}$ .

If, on the other side, we neglect the viscosity forces when  $\vec{B}(t) = 0$  in (11), the smooth solution (11) is defined, as was already noted, only under the condition  $\det \hat{A} > 0$  [22–26] (see Appendix). This condition corresponds to a bounded time interval  $0 \leq t < t_0$ , where the minimum limiting time  $t_0$  of existence of the solution can be determined from the solution to the following  $n$ th-order algebraic equation (and successive minimization of the expression obtained, which depends on the spatial coordinates, with respect to these coordinates):

$$\begin{aligned} \det \hat{A}(t) &= 1 + t \frac{du_{01}(x_1)}{dx_1} = 0, n = 1 \\ \det \hat{A}(t) &= 1 + t \operatorname{div} \vec{u}_0 + t^2 \det \hat{U}_{012} = 0, n = 2 \\ \det \hat{A}(t) &= 1 + t \operatorname{div} \vec{u}_0 + t^2 (\det \hat{U}_{012} + \det \hat{U}_{013} + \det \hat{U}_{023}) + t^3 \det \hat{U}_0 = 0, n = 3 \end{aligned} \quad (13)$$

where  $\det \hat{U}_0$  is the determinant of the  $3 \times 3$  matrix  $U_{0nm} = \frac{\partial u_{0n}}{\partial x_m}$ , and  $\det \hat{U}_{012} = \frac{\partial u_{01}}{\partial x_1} \frac{\partial u_{02}}{\partial x_2} - \frac{\partial u_{01}}{\partial x_2} \frac{\partial u_{02}}{\partial x_1}$  is the determinant of a similar matrix in the two-dimensional case for the variables  $(x_1, x_2)$ . In this case  $\det \hat{U}_{013}$ ,  $\det \hat{U}_{023}$  are the determinants of the matrices in the two-dimensional case for the variables  $(x_1, x_3)$  and  $(x_2, x_3)$ , respectively.

In the two-dimensional case, the condition in the form of Eq. (13) exactly coincides with the collapse condition obtained in [42] in connection with the problem of propagation of a flame front investigated on the basis of the Kuramoto-Sivashinsky Eq. (3). In this case for exact coincidence, it is necessary to replace  $t \rightarrow b(t) = \frac{U_s(\exp(\gamma_0 t) - 1)}{\gamma_0}$  in (13).

In the one-dimensional case, when  $n = 1$ , from Eq. (13) we can obtain the minimum time of appearance of the singularity  $t_0 = \frac{1}{\max \left| \frac{d u_{01}(x_1)}{d x_1} \right|} > 0$ . In particular,

for the initial distribution  $u_{01}(x_1) = a \exp\left(-\frac{x_1^2}{L^2}\right)$ ,  $a > 0$ , it follows that  $t_0 = \frac{L}{a} \sqrt{\frac{e}{2}}$  obtained for the value  $x_1 = x_{1\max} = \frac{L}{\sqrt{2}}$ . In this case the singularity itself can be implemented only for positive values of the coordinate  $x_1 > 0$  when Eq. (13) has a positive solution for time.

This means that the singularity (collapse) of the smooth solution can never occur when the initial velocity field is nonzero only for negative values of the spatial coordinate  $x_1 < 0$ .

Similarly, we can also determine the vortex wave burst time  $t_0$  for  $n > 1$ . For (13) in the two-dimensional case (when the initial velocity field is divergence-free) for the initial stream function in the form  $\psi_0(x_1, x_2) = a \sqrt{L_1 L_2} \exp\left(-\frac{x_1^2}{L_1^2} - \frac{x_2^2}{L_2^2}\right)$ ,  $a > 0$ , we obtain that the minimum time of existence of the smooth solution is equal to  $t_0 = \frac{e \sqrt{L_1 L_2}}{2a}$ .

In the example considered, this minimum time of existence of the smooth solution is implemented for the spatial variables corresponding to points on the ellipse  $\frac{x_1^2}{L_1^2} + \frac{x_2^2}{L_2^2} = 1$ .

In accordance with (13), the necessary condition of implementation of the singularity is the condition of existence of a real positive solution to a quadratic (when  $n = 2$ ) or cubic (when  $n = 3$ ) equation for the time variable  $t$ . For example, in the case of two-dimensional flow with the initial divergence-free velocity field  $\text{div } \vec{u}_0 = 0$ , in accordance with (13), the necessary and sufficient condition of implementation of the singularity (collapse) of the solution in finite time is the condition:

$$\det U_{012} < 0 \tag{14}$$

For the example considered above from (14), there follows the inequality  $\frac{x_1^2}{L_1^2} + \frac{x_2^2}{L_2^2} > \frac{1}{2}$ . When this inequality is satisfied, for  $n = 2$  there exists a real positive solution to the quadratic equation in (13) for which the minimum collapse time  $t_0 = \frac{e \sqrt{L_1 L_2}}{2a} > 0$  given above is obtained.

On the contrary, if the initial velocity field is defined in the form of a finite function which is nonzero only in the domain  $\frac{x_1^2}{L_1^2} + \frac{x_2^2}{L_2^2} \leq \frac{1}{2}$ , then the inequality (14) is violated, and the development of the singularity in a finite time turns out already to be impossible, and the solution remains smooth in unbounded time even regardless of the viscosity effects.

The condition of existence of a real positive solution of Eq. (13) (e.g., see (14)) is the necessary and sufficient condition of implementation of the singularity (collapse) of the solution, as distinct from the sufficient but not necessary integral criterion which was proposed in [45] (see formula (38) in [45]) and has the form:

$$\left(\frac{dI}{dt}\right)_{t=0} = - \int d^3x \operatorname{div} \vec{u}_0 \det^2 \hat{U}_0 > 0; I = \int d^3x \det^2 \hat{U} \quad (15)$$

In fact, in accordance with this criterion proposed in [45], the collapse of the solution is not possible in the case of the initial divergence-free velocity field, i.e., when  $\operatorname{div} \vec{u}_0 = 0$ . However, in this case the violation of criterion (15) does not exclude the possibility of the collapse of the solution by virtue of the fact that the criterion (15) does not determine the necessary condition of implementation of the collapse. Actually, in the example considered above (in determination of the minimum time of implementation of the collapse  $t_0 = \frac{\varepsilon\sqrt{L_1 L_2}}{2a}$ ) for two-dimensional compressible flow, the initial condition corresponded just to the initial velocity field with  $\operatorname{div} \vec{u}_0 = 0$  in (13) when  $n = 2$ .

On the basis of the solution (11), using (13) and the Lagrangian variables  $\vec{a}$  (where  $\vec{x} = \vec{x}(t, \vec{a}) = \vec{a} + t\vec{u}_0(\vec{a})$ ), we can represent the expression for the matrix of the first derivatives of the velocity  $\hat{U}_{im} = \frac{\partial u_i}{\partial x_m}$  in the form:

$$\hat{U}_{im}(\vec{a}, t) = \hat{U}_{0ik}(\vec{a}) A_{km}^{-1}(\vec{a}, t) \quad (16)$$

In this case the expression (16) exactly coincides with the formula (30) given in [45] for the Lagrangian time evolution of the matrix of the first derivatives of the velocity which must satisfy the three-dimensional Hopf equation (10) (when  $\vec{B}(t) = 0$  in (10)). In particular, in the one-dimensional case when  $n = 1$ , in the Lagrangian representation from (11) and (13), we obtain a particular case of the formula (16):

$$\left(\frac{\partial u(x, t)}{\partial x}\right)_{x=x(a, t)} = \frac{\frac{du_0(a)}{da}}{1 + t \frac{du_0(a)}{da}} \quad (17)$$

where  $a$  is the coordinate of a fluid particle at the initial time  $t = 0$ .

The solution (17) also coincides with the formula (14) in [45] and describes the catastrophic process of collapse of a simple wave in a finite time  $t_0$  whose estimate is given above on the basis of the solution to Eq. (13) in the case  $n = 1$  with the use of the Euler variables.

Let us take into account only the external friction. For this purpose it is necessary to consider the case with  $\mu > 0$  in Eq. (4). In this case we can also obtain the exact solution from the expression (11) (for the case when in (11)  $\vec{B} = 0$ ) changing in them the time variable  $t$  by the variable  $\tau = \frac{1 - \exp(-t\mu)}{\mu}$  (see (31) in Appendix and [22, 23]). The new time variable  $\tau$  now varies within the finite limits from  $\tau = 0$  (when  $t = 0$ ) to  $\tau = \frac{1}{\mu}$  (as  $t \rightarrow \infty$ ). This leads to the fact that in the case of fulfillment of the inequality

$$\mu > \frac{1}{t_0} \quad (18)$$

for given initial conditions, the quantity  $\det \hat{A} > 0$  for all times since the necessary and sufficient condition of implementation of the singularity (13) will be not satisfied because the change  $t \rightarrow \tau(t)$  must also be carried out in the condition (13).

Providing (18), the solution to the  $n$ -dimensional EH equation is smooth on an unbounded interval of time  $t$ . The corresponding analytic vortical solution to the three-dimensional Navier–Stokes equation also remains smooth for any  $t \geq 0$  if the condition (18) is satisfied [22–26].

Note that under the formal coincidence of the parameters  $\mu = -\gamma_0$  (see the Sivashinsky equation (3) in Introduction), the equality  $\tau(t) = b(t)$  takes place providing the implementation of the singularity (13) when  $n = 2$  and in accordance with the solution of the Kuramoto–Sivashinsky equation in [42] and the regularization of this solution for all times if (18) takes place.

Moreover the example of interesting prosperity for the direct application for solution (11) (see also (12)–(18)) may be done in the connection of the results [46], where the description of light propagation in a nonlinear medium on the basis of the Burgers–Hopf equation is done.

Indeed, in [46], the model of light propagation in weak nonlinear 3D Coul–Coul’s medium with small action radii of nonlocality is represented. In [46], it was stated that in the geometric optic approach, this model is integrated and described by the Veselov–Novikov equation which has a 1D reduction in the form of the Burgers–Hopf equation. The last equation is considered in connection with nonlinear geometrical optics when 1D reduction is made for the case when the refractive index has no dependence on one of the space coordinates. It is important when the property of nonlinear wave finite-time breakdown for Burgers–Hopf solutions is considered in the application to the case of nonlinear geometrical optics. These solutions are useful for modeling of dielectrics which have impurities which induced sharp variations of the refractive index. Indeed, in the points of breakdown, the curvature of the light rays obtained discontinues property as it takes place at the boundary between different media [46].

In [46], the only hodograph method is used for the Burgers–Hopf (or Hopf equation which is obtained from the Burgers’ equation in the limit of zero viscosity) equation solution in this connection. Thus the direct analytical description of the 1D–3D solutions to the Hopf equation in the form (11) gives the new possibility also for the nonlinear optic problem which is considered in [46]. For example, according to this solution, it is possible to obtain the important effect of avoidance of finite-time singularities when viscosity or friction forces are taken into account (when condition (18) takes place for the case of external friction).

## **2. Conclusions**

Here we represent some examples where hydrodynamic methods and solutions may be useful for different problems in nonlinear optics. In these examples, the medium itself has the first degree of importance in realization of all mentioned phenomena. Indeed, the main future of the Vavilov–Cherenkov radiation is that the medium is the source of this radiation instead of any kinds of bremsstrahlung radiations by moving charged particles. The VCR theory presented here for the first time takes into account the real mechanism of VCR by the medium itself, excited by a sufficiently fast electron. It can also be shown only from the microscopic theory, but not from the macroscopic one stated in [16]. The first step in this direction was made in [47] also on the basis of the Abraham theory where it is proposed that the Vavilov–Cherenkov radiation is emitted by the medium in a nonequilibrium polarization state which is arising due to the parametric resonance interaction of the medium with a fast-charged particle.

The second example, which is represented here, also gives new perspectives on the basis of the new exact solution (in the Euler variables) for n-dimensional Hopf equation because this equation is known as the possible model for weak nonlinear optic problems [46]. The importance of the new solution is connected with its Euler form in dependence from space variables, which are not represented in the solution of the Burgers-Hopf equation well known before (see [45] and others).

### A. Exact solution of n-D Hopf equation (n = 1, 2, 3)

The Appendix presents a procedure for deriving the exact solution of the 3D Hopf equation.

The Hopf equation in the n-dimensional space (n = 1..3) is as follows:

$$\frac{\partial u_i}{\partial t} + u_l \frac{\partial u_i}{\partial x_l} = 0 \quad (19)$$

When the external friction coefficient tends to zero in Eq. (4),  $\mu \rightarrow 0$ , Eq. (4) also coincides with the Hopf equation (19).

In the unbounded space, the general Cauchy problem solution for Eq. (19) under arbitrary smooth initial conditions  $\vec{u}_0(\vec{x})$  may be obtained as follows (see also in [22, 23]):

Eq. (19) may be represented in an implicit form as follows:

$$u_i(\vec{x}, t) = u_{0i}(\vec{x} - t \vec{u}(\vec{x}, t)) = \int d^n \xi u_{0i}(\vec{\xi}) \delta(\vec{\xi} - \vec{x} + t \vec{u}(\vec{x}, t)) \quad (20)$$

In (20),  $\delta$  is the Dirac delta function. Using known (see farther) properties of the delta function, it is possible to express the delta function in (20) with the help of an identity true for the very velocity field meeting Eq. (19):

$$\delta(\vec{\xi} - \vec{x} + t \vec{u}(\vec{x}, t)) \equiv \delta(\vec{\xi} - \vec{x} + t \vec{u}_0(\vec{\xi})) |\det \hat{A}| \quad (21)$$

In (21), the matrix  $\hat{A}$  depends only on the initial velocity field and is as follows:

$$\hat{A} \equiv A_{km} = \delta_{km} + t \frac{\partial u_{0k}(\vec{\xi})}{\partial \xi_m} \quad (22)$$

To infer (21), it is necessary to use the following delta-function property that is true for any smooth function  $\vec{\Phi}(\vec{\xi})$ :

$$\delta(\vec{\Phi}(\vec{\xi})) = \frac{\delta(\vec{\xi} - \vec{\xi}_0)}{\left| \det \left( \frac{\partial \Phi_k}{\partial \xi_m} \right)_{\vec{\xi} = \vec{\xi}_0} \right|} \quad (23)$$

In (23), the values  $\vec{\xi}_0$  are defined from the solution of the equation

$$\vec{\Phi}(\vec{\xi}_0) = 0 \quad (24)$$

To prove (23), it is necessary to use Taylor series decomposition wrt  $\vec{\xi}$  near  $\vec{\xi} = \vec{\xi}_0$  for the argument of the delta function  $\vec{\Phi}(\vec{\xi})$  when in the limit  $\vec{\xi} \rightarrow \vec{\xi}_0$  taking into account (24), we get

$$\delta\left(\Phi_k(\vec{\xi}_0) + \left(\frac{\partial\Phi_k}{\partial\xi_m}\right)_{\vec{\xi}=\vec{\xi}_0}(\xi_m - \xi_{0m}) + O\left(\vec{\xi} - \vec{\xi}_0\right)^2\right) = \delta\left(\left(\frac{\partial\Phi_k}{\partial\xi_m}\right)_{\vec{\xi}=\vec{\xi}_0}(\xi_m - \xi_{0m})\right) \quad (25)$$

Using variable substitution in the argument of the right-hand side of (25) (of the type  $\hat{A}\vec{x}=\vec{y}$  and taking into account that  $d\vec{x} = \frac{d\vec{y}}{|\det\hat{A}|}$  [48]), we get from the right-hand side of (25) the right-hand side of (23).

When in (23),  $\vec{\Phi}(\vec{\xi}) \equiv \vec{\xi} - \vec{x} + t\vec{u}_0(\vec{\xi})$  and  $\det \frac{\partial\Phi_k}{\partial\xi_m} = \det A_{km}$  where  $A_{km}$  is from (22); then Eq. (24) is reduced to the following equation:

$$\vec{\xi}_0 - \vec{x} + t\vec{u}_0(\vec{\xi}_0) = 0 \quad (26)$$

The solution of Eq. (26) is as follows:

$$\vec{\xi}_0 = \vec{x} - t\vec{u}(\vec{x}, t) \quad (27)$$

This can be verified substituting (27) into (26) and taking into account that the general implicit solution of the equation (19) can be represented as

$$\vec{u}(\vec{x}, t) = \vec{u}_0(\vec{x} - t\vec{u}(\vec{x}, t)) \text{ that is used in (20).}$$

Let us use a known property of the delta function that for any smooth function  $\vec{f}(\vec{x})$ , the following equality  $\vec{f}(\vec{x})\delta(\vec{x} - \vec{x}_0) = \vec{f}(\vec{x}_0)\delta(\vec{x} - \vec{x}_0)$  holds. That is

why, in the general case, it is possible to multiply both sides of (23) by  $\left|\det \frac{\partial\Phi_k(\vec{\xi})}{\partial\xi_m}\right|$  getting the following:

$$\delta(\vec{\xi} - \vec{\xi}_0) = \delta(\vec{\Phi}(\vec{\xi})) \left|\det \frac{\partial\Phi_k(\vec{\xi})}{\partial\xi_m}\right| \quad (28)$$

From (28) and (27), identical holding of the equality (21) follows.

Taking into account (21), from (20), we get an exact general (for any smooth initial velocity fields) solution of the Cauchy problem for Eq. (19) as

$$u_i(\vec{x}, t) = \int d^n\xi u_{0i}(\vec{\xi})\delta(\vec{\xi} - \vec{x} + t\vec{u}_0(\vec{\xi})) \det \hat{A}, \quad (29)$$

where  $\det \hat{A} = \det\left(\delta_{mk} + t\frac{\partial u_{0m}(\vec{\xi})}{\partial\xi_k}\right)$ . That solution of Eq. (19) is considered under the following condition:

$$\det \hat{A} > 0 \quad (30)$$

That is why, sign of  $\det \hat{A}$  is absent in (29). The condition (30) provides smoothness of the solution only on the finite-time interval defined above from (13).

We can check that the very (29) under condition (30) exactly satisfies Eq. (19) by direct substitution of (29) in (19). The solution (29) describes not only potential but also vortex solutions of Eq. (19) in two- and three-dimensional cases for any smooth initial velocity field  $\vec{u}_0(\vec{x})$  that was not known earlier for the solutions of Eq. (19) [22–26].

The solution (29) of Eq. (19) allows getting an exact solution of Eq. (10) if in (29) to make a substitution:  $\vec{x} \rightarrow \vec{x} - \vec{B}(t)$  that yields Eq. (10) representation as in (11).

The solution (29) also can be described as an exact solution of Eq. (4) for  $\mu > 0$  if in (29) to substitute:

$$t \rightarrow \frac{1 - \exp(-t\mu)}{\mu} \quad (31)$$

### A.1 The direct validation of the solution

To verify the solution (29) satisfies Eq. (19), let us substitute (29) in Eq. (19). Then we get from (19):

$$\int d^n \xi \left[ u_{0i}(\vec{\xi}) \frac{\partial \det \hat{A}}{\partial t} \delta(\vec{\xi} - \vec{x} + t\vec{u}_0(\vec{\xi})) - u_{0i} u_{0m} \det \hat{A} \frac{\partial \delta(\vec{\xi} - \vec{x} + t\vec{u}_0(\vec{\xi}))}{\partial x_m} \right] + \int d^n \xi \int d^n \xi_1 F = 0 \quad (32)$$

where

$$F \equiv u_{0m}(\vec{\xi}_1) \det \hat{A}(\vec{\xi}_1) \delta(\vec{\xi}_1 - \vec{x} + t\vec{u}_0(\vec{\xi}_1)) u_{0i}(\vec{\xi}) \det \hat{A}(\vec{\xi}) \frac{\partial \delta(\vec{\xi} - \vec{x} + t\vec{u}_0(\vec{\xi}))}{\partial x_m}.$$

To transform sub-integral expression in (32), the following identities shall be used:

$$\frac{\partial \delta(\vec{\xi} - \vec{x} + t\vec{u}_0(\vec{\xi}))}{\partial x_m} = -A_{km}^{-1} \frac{\partial \delta(\vec{\xi} - \vec{x} + t\vec{u}_0(\vec{\xi}))}{\partial \xi_k} \quad (33)$$

$$\frac{\partial \det \hat{A}}{\partial t} \equiv \frac{\partial u_{0m}}{\partial \xi_k} A_{km}^{-1} \det \hat{A} \quad (34)$$

$$\frac{\partial}{\partial \xi_k} (A_{km}^{-1} \det \hat{A}) \equiv 0 \quad (35)$$

The identity (33) is obtained from the relationship (obtained by differentiating the delta function having argument as a given function of  $\vec{\xi}$ )

$\frac{\partial \delta(\vec{\xi} - \vec{x} + t\vec{u}_0(\vec{\xi}))}{\partial \xi_k} = - \frac{\partial \delta(\vec{\xi} - \vec{x} + t\vec{u}_0(\vec{\xi}))}{\partial x_l} A_{lk}$  after multiplying it both sides by the inverse matrix  $A_{km}^{-1}$  (where  $A_{lk} A_{km}^{-1} = \delta_{lm}$  and  $\delta_{lm}$  is the unity matrix or the Kronecker delta).

The validity of the identities (34) and (35) is proved by the direct checking. In the one-dimensional case, when  $\hat{A} = 1 + t \frac{du_{01}}{d\xi_1} = \det \hat{A}; \hat{A}^{-1} = (\det \hat{A})^{-1}$ , it obviously follows directly from (34) and (35). Further, in Item 3, the proof of the identities (34) and (35) of the two- and three-dimensional cases is given.

Taking into account (33)–(35), from (32), we get

$$\int d^n \xi \delta(\vec{\xi} - \vec{x} + t\vec{u}_0(\vec{\xi})) A_{km}^{-1} \det \hat{A} \left( u_{0i} \frac{\partial u_{0m}}{\partial \xi_k} - \frac{\partial}{\partial \xi_k} (u_{0i} u_{0m}) \right) + \int d^n \xi \int d^n \xi_1 F_1 = 0 \quad (36)$$

where the sub-integral expression in the second term of the left-hand side of (36) is as follows:

$$F_1 = u_{0m}(\vec{\xi}_1) \frac{\partial u_{0i}(\vec{\xi})}{\partial \xi_k} \det \hat{A}(\vec{\xi}_1) \det \hat{A}(\vec{\xi}) A_{km}^{-1}(\vec{\xi}) \delta(\vec{\xi} - \vec{x} + t\vec{u}_0(\vec{\xi})) \delta(\vec{\xi}_1 - \vec{x} + t\vec{u}_0(\vec{\xi}_1)) \quad (37)$$

To transform (37), it is necessary to use the following identities:

$$\begin{aligned} & \delta(\vec{\xi} - \vec{x} + t\vec{u}_0(\vec{\xi})) \delta(\vec{\xi}_1 - \vec{x} + t\vec{u}_0(\vec{\xi}_1)) \\ & \equiv \delta(\vec{\xi} - \vec{x} + t\vec{u}_0(\vec{\xi})) \delta(\vec{\xi}_1 - \vec{\xi} + t(\vec{u}_0(\vec{\xi}_1) - \vec{u}_0(\vec{\xi}))) \end{aligned} \quad (38)$$

$$\delta(\vec{\xi}_1 - \vec{\xi} + t(\vec{u}_0(\vec{\xi}_1) - \vec{u}_0(\vec{\xi}))) \equiv \frac{\delta(\vec{\xi}_1 - \vec{\xi})}{\det \hat{A}} \quad (39)$$

In (39), as it is noted above,  $\det \hat{A} > 0$ , and that is why the sign is not used in the denominator of (39).

The identity (38) is a consequence of the noted above property of the delta function (see discussion before the formula (28)).

To infer the identity (39), it is necessary to consider in the argument of the delta function a Taylor series decomposition of the function

$$u_{0k}(\vec{\xi}_1) = u_{0k}(\vec{\xi}) + \left( \frac{\partial u_{0k}}{\partial \xi_m}(\vec{\xi}) \right)_{\vec{\xi}_1 = \vec{\xi}} (\xi_{1m} - \xi_m) + O(\xi_1 - \xi)^2 \text{ near the point}$$

$\vec{\xi}_1 = \vec{\xi}$ . Then the left-hand side of (39) has the form  $\delta(\hat{A}(\vec{\xi}_1 - \vec{\xi}))$  similar to that of the right-hand side of (25), and according to (23), we get from here the identity (39).

After the application of the identity (39) to the expression (37), defining the form of the second term in (36), from (36), we get

$$\int d^n \xi \delta(\vec{\xi} - \vec{x} + t\vec{u}_0(\vec{\xi})) A_{km}^{-1} \det \hat{A} \left[ u_{0i} \frac{\partial u_{0m}}{\partial \xi_k} - \frac{\partial}{\partial \xi_k} (u_{0i} u_{0m}) + u_{0m} \frac{\partial u_{0i}}{\partial \xi_k} \right] = 0 \quad (40)$$

Equality (40) holds identically due to the identical equality to zero of the expression in the brackets in the sub-integral expression in (40).

Thus, we have proved that (29) exactly satisfies the Hopf equation (19) for any smooth initial velocity fields on the finite-time interval under condition  $\det \hat{A} > 0$  in (13).

## A.2 The validation of identities (34) and (35)

In the two-dimensional case, the elements of the inverse matrix  $A_{km}^{-1}$  and the determinant of the matrix  $\hat{A}$  are

$$A_{11}^{-1} = \frac{1 + t \frac{\partial u_{02}}{\partial \xi_2}}{\det \hat{A}}; A_{12}^{-1} = -\frac{t \frac{\partial u_{01}}{\partial \xi_2}}{\det \hat{A}}; A_{21}^{-1} = -\frac{t \frac{\partial u_{02}}{\partial \xi_1}}{\det \hat{A}}; A_{22}^{-1} = \frac{1 + t \frac{\partial u_{01}}{\partial \xi_1}}{\det \hat{A}} \quad (41)$$

$$\det \hat{A} = 1 + t \left( \frac{\partial u_{01}}{\partial \xi_1} + \frac{\partial u_{02}}{\partial \xi_2} \right) + t^2 \left( \frac{\partial u_{01}}{\partial \xi_1} \frac{\partial u_{02}}{\partial \xi_2} - \frac{\partial u_{01}}{\partial \xi_2} \frac{\partial u_{02}}{\partial \xi_1} \right) \quad (42)$$

Here, (42) corresponds to the formula (13) for  $n = 2$ .

Using (41), it is possible to show that the following equality holds (in the left-hand side of (43), summation is assumed on the repeating indices from 1 to 2):

$$\frac{\partial u_{0m}}{\partial \xi_k} A_{km}^{-1} \det \hat{A} = \frac{\partial u_{01}}{\partial \xi_1} + \frac{\partial u_{02}}{\partial \xi_2} + 2t \left( \frac{\partial u_{01}}{\partial \xi_1} \frac{\partial u_{02}}{\partial \xi_2} - \frac{\partial u_{01}}{\partial \xi_2} \frac{\partial u_{02}}{\partial \xi_1} \right) \quad (43)$$

From (42), it follows that the right-hand side of (43) exactly matches  $\frac{\partial \det \hat{A}}{\partial t}$  obtained when differentiating over time in (42). This proves the identity of (34) in the two-dimensional case.

To prove the identity (35), let us introduce

$$B_m = \frac{\partial}{\partial \xi_k} \left( A_{km}^{-1} \det \hat{A} \right) \quad (44)$$

Using (41), one gets from (44)

$$B_1 = \frac{\partial}{\partial \xi_1} \left( 1 + t \frac{\partial u_{02}}{\partial \xi_2} \right) - \frac{\partial}{\partial \xi_2} \left( t \frac{\partial u_{02}}{\partial \xi_1} \right) \equiv 0 \quad (45)$$

$$B_2 = \frac{\partial}{\partial \xi_1} \left( -t \frac{\partial u_{01}}{\partial \xi_2} \right) + \frac{\partial}{\partial \xi_2} \left( 1 + t \frac{\partial u_{01}}{\partial \xi_1} \right) \equiv 0 \quad (46)$$

The identities (45) and (46) confirm the truth of the identity (35) in the two-dimensional case.

Similarly, the identity (35) is proved in the three-dimensional case. For that, we need the following representation of the entries of the inverse matrix  $\hat{A}^{-1}$  [49]:

$$\begin{aligned} A_{11}^{-1} &= \frac{1}{\det \hat{A}} \left[ \left( 1 + t \frac{\partial u_{02}}{\partial \xi_2} \right) \left( 1 + t \frac{\partial u_{03}}{\partial \xi_3} \right) - t^2 \frac{\partial u_{02}}{\partial \xi_3} \frac{\partial u_{03}}{\partial \xi_2} \right]; \\ A_{12}^{-1} &= \frac{1}{\det \hat{A}} \left[ t^2 \frac{\partial u_{01}}{\partial \xi_3} \frac{\partial u_{03}}{\partial \xi_2} - t \left( 1 + t \frac{\partial u_{03}}{\partial \xi_3} \right) \frac{\partial u_{01}}{\partial \xi_2} \right]; \\ A_{13}^{-1} &= \frac{1}{\det \hat{A}} \left[ t^2 \frac{\partial u_{01}}{\partial \xi_2} \frac{\partial u_{02}}{\partial \xi_3} - t \left( 1 + t \frac{\partial u_{02}}{\partial \xi_2} \right) \frac{\partial u_{01}}{\partial \xi_3} \right]; \\ A_{21}^{-1} &= \frac{1}{\det \hat{A}} \left[ t^2 \frac{\partial u_{02}}{\partial \xi_3} \frac{\partial u_{03}}{\partial \xi_1} - t \left( 1 + t \frac{\partial u_{03}}{\partial \xi_3} \right) \frac{\partial u_{02}}{\partial \xi_1} \right]; \\ A_{22}^{-1} &= \frac{1}{\det \hat{A}} \left[ \left( 1 + t \frac{\partial u_{01}}{\partial \xi_1} \right) \left( 1 + t \frac{\partial u_{03}}{\partial \xi_3} \right) - t^2 \frac{\partial u_{01}}{\partial \xi_3} \frac{\partial u_{03}}{\partial \xi_1} \right]; \\ A_{23}^{-1} &= \frac{1}{\det \hat{A}} \left[ t^2 \frac{\partial u_{01}}{\partial \xi_3} \frac{\partial u_{02}}{\partial \xi_1} - t \left( 1 + t \frac{\partial u_{01}}{\partial \xi_1} \right) \frac{\partial u_{02}}{\partial \xi_3} \right]; \\ A_{31}^{-1} &= \frac{1}{\det \hat{A}} \left[ t^2 \frac{\partial u_{02}}{\partial \xi_1} \frac{\partial u_{03}}{\partial \xi_2} - t \left( 1 + t \frac{\partial u_{02}}{\partial \xi_2} \right) \frac{\partial u_{03}}{\partial \xi_1} \right]; \\ A_{32}^{-1} &= \frac{1}{\det \hat{A}} \left[ t^2 \frac{\partial u_{01}}{\partial \xi_2} \frac{\partial u_{03}}{\partial \xi_1} - t \left( 1 + t \frac{\partial u_{01}}{\partial \xi_1} \right) \frac{\partial u_{03}}{\partial \xi_2} \right]; \\ A_{33}^{-1} &= \frac{1}{\det \hat{A}} \left[ \left( 1 + t \frac{\partial u_{01}}{\partial \xi_1} \right) \left( 1 + t \frac{\partial u_{02}}{\partial \xi_2} \right) - t^2 \frac{\partial u_{01}}{\partial \xi_2} \frac{\partial u_{02}}{\partial \xi_1} \right] \end{aligned} \quad (47)$$

From (44), in the three-dimensional case, we get on the basis of (47) that all three components of the vector  $B_m \equiv 0$ . For each  $m = 1, 2, 3$ , we get identical zeroing separately for the sum of terms proportional to  $t$  and separately for the sum of the terms proportional to  $t^2$ .

For example, in the expression for  $B_1$  the sum of terms proportional to the first degree of time has the form  $t \left[ \frac{\partial}{\partial \xi_1} \left( \frac{\partial u_{02}}{\partial \xi_2} + \frac{\partial u_{03}}{\partial \xi_3} \right) - \frac{\partial^2 u_{02}}{\partial \xi_2 \partial \xi_1} - \frac{\partial^2 u_{03}}{\partial \xi_3 \partial \xi_1} \right] \equiv 0$ , and similarly we can show the vanishing of the sum of twelve terms proportional to the square of time. Thus, the identity (35) is also proved in the three-dimensional case.

Proof of the identity (34) also is possible in the 3D case on the basis of (47) and (13) but is related to the cumbersome transformations.

## Author details

Sergey G. Chefranov<sup>1,2\*</sup> and Artem S. Chefranov<sup>1</sup>

1 Obukhov Institute of Atmospheric Physics of Russian Academy of Sciences, Moscow, Russia

2 Plasma Physics and Pulse Power Research Laboratory, Technion-Israel Institute of Technology, Haifa, Israel

\*Address all correspondence to: [schefranov@mail.ru](mailto:schefranov@mail.ru); [csergei@technion.ac.il](mailto:csergei@technion.ac.il)

## IntechOpen

© 2018 The Author(s). Licensee IntechOpen. This chapter is distributed under the terms of the Creative Commons Attribution License (<http://creativecommons.org/licenses/by/3.0>), which permits unrestricted use, distribution, and reproduction in any medium, provided the original work is properly cited. 

## References

- [1] Maxwell G. Selected Works on the Electro-Magnetic Field Theory. Moscow, Mir, 1952
- [2] Kambe T. Fluid Dynamics Research. 2010;**42**:055502
- [3] Kuznetsov AP, Kuznetsov SP, Trubetskov DI. *Isvestia Vusov*, PND. 2015;**23**:5
- [4] Kambe T. New scenario of turbulence theory and wall-bounded turbulence: Theoretical significance. arXiv. Jun 2017. 1610.05975v2 (Physics > Fluid Dynamics)
- [5] Feinman R, Leiton R, Sands M. Feinman Lectures in Physics. Vol. 5. Moscow, Mir, 1964
- [6] Chefranov SG, Mokhov II, Chefranov AG. The hydrodynamic singular vortex on the sphere and the Dirac monopole. arXiv. 2017. 1711.04124v1 (Physics > Fluid Dynamics )
- [7] PAM D. *Proceedings of the Royal Society A*. 1931;**133**:60
- [8] Blaha S. *Physical Review Letters*. 1976;**36**:874
- [9] Volovik GE, Mineev VP. *Soviet Physics. JETP Letters*. 1976;**23**:647
- [10] Volovik GE et al. arXiv. 1999. cond-mat/9911486v2
- [11] Volovik GE. *Proceedings of the National Academy of Sciences of the United States of America*. 2000;**97**:2431
- [12] Landau LD. *Soviet Physics. JETP Letters*. 1941;**11**:592
- [13] Chefranov SG. *Physical Review Letters*. 2004;**93**:254801
- [14] Chefranov SG. *JETP*. 2004;**99**:296
- [15] Chefranov SG. *JETP*. 2016;**123**:12
- [16] Tamm IM. *Journal de Physique*. 1939;**1**:139
- [17] Frank IM. *Physics Review*. 1943;**75**:1862
- [18] Ginzburg VL. *Journal de Physique*. 1940;**2**:441
- [19] Kuramoto Y, Tsuzuki T. *Progress in Theoretical Physics*. 1976;**55**:356
- [20] Sivashinsky GI. *Physica D: Nonlinear Phenomena*. 1982;**4**:227
- [21] Sivashinsky GI. *Annual Review of Fluid Mechanics*. 1983;**15**:179
- [22] Chefranov SG. *Soviet Physics – Doklady*. 1991;**36**(4):286
- [23] Chefranov SG, Chefranov AG. Exact time dependent solution to the 3D Euler-Helmholtz and Riemann-Hopf equations for the vortex flow of compressible medium and the Sixth Millennium Prize Problem. arXiv. 2017. 1703.07239v3 (Physics > Fluid Dynamics)
- [24] Chefranov SG, Chefranov AG. *Cardiometry*. 2017. 10 [www.cardiometry.net](http://www.cardiometry.net)
- [25] Chefranov SG, Chefranov AG. The 6th International Conference 10th Anniversary Program “Turbulent Mixing and Beyond”. Abdus Salam International Centre for Theoretical Physics; 14–18 August 2017; Trieste, Italy
- [26] Chefranov SG, Chefranov AG. *Proceedings of Euromech/Ercoftac Colloquium 589 “Turbulent Cascades*

II"; 5–7 December 2017. Lyon, France: Ecole Central de Lyon Ecully

[27] Feffermann CB. Existence and Smoothness of the Navier-Stokes Equation, The Millennium Prize Problems. Vol. 57. Cambridge, MA: Clay Mathematics Institute; 2006. www.claymath.org

[28] Cherenkov PA. Physical Review. 1937;**52**:378

[29] Bolotovskiy BM. Oliver Heaviside. Moscow: Nauka; 1985

[30] Landau LD, Lifshitz EM. Electrodynamics of Continuous Mediums. Moscow: Nauka; 1982. p. 553. republished by Pergamon Press, Oxford, 1984

[31] Collins GB, Reiling. Physical Review. 1938;**54**:499

[32] Tailor JB. Physical Review Letters. 1974;**33**:1133

[33] Chefranov SG. JETP Letters. 2001; **73**:274

[34] Chefranov SG, Chefranov AG. JETP. 2014;**146**:373

[35] Chefranov SG, Chefranov AG. Doklady Physics. 2015;**60**:327

[36] Chefranov SG, Chefranov AG. JETP. 2016;**122**:925

[37] Ryazanov MI. Soviet Physics – Doklady. 1964;**18**:238

[38] Monin AS, Yaglom AM. Statistical Hydromechanics. Saint-Petersburg: Gidrometeoizdat; 1992

[39] Batchelor GK. An Introduction to Fluid Dynamics. Cambridge: Cambridge University Press; 1970

[40] Landau LD, Lifshitz EM. Fluid Mechanics. 2nd ed. Oxford: Pergamon Press; 1987

[41] Stewart I. The Great Mathematical Problems. Profile Boobs, Joat Enterprise; 2013

[42] Kuznetsov EA, Mineev VP. Physics Letters A. 1996;**221**:187

[43] Pelinovskii EN. Izvestiya Vuzov, Radiophysics. 1976;**19**:373

[44] Chefranov SG. Soviet Physics - JETP. 1989;**69**(1):94

[45] Kuznetsov EA. Physica D: Nonlinear Phenomena. 2003;**184**:266

[46] Konopelchenko BG, Moro A. Theoretical and Mathematical Physics. 2005;**144**(1):968

[47] Chefranov SG. The new microscopic Vavilov-Cherenkov radiation theory. arXiv. 2012. 1204.0002v1 (Physics > General Physics)

[48] Gel'fand IM, Vilenkin NY. Generalize Functions. Vol. 4. Moscow; 1961. p. 317

[49] Cramer H. Mathematical methods of Statistics, Stockholm, 1946. p. 128 (In Russian-Moscow, Mir, 1975)

---

Section 3

# Optical Generation Processes

---



# Polarization Properties of the Solitons Generated in the Process of Pulse Breakup in Twisted Fiber Pumped by ns Pulses

*Ariel Flores Rosas, Orlando Díaz Hernández, Roberto Arceo, Gerardo J. Escalera Santos, Sergio Mendoza Vázquez, Elizeth Ramírez Álvarez, Christian I. Enriquez Flores and Evgeny Kuzin*

## Abstract

Common optical fibers are randomly birefringent, and solitons forming and traveling in them are randomly polarized. However, it is desirable to have solitons with a well-defined polarization. With pump relatively long pulses, the nonlinear effects of modulation instability (MI) and stimulated Raman scattering (SRS) are dominant at the initial stage of the process of supercontinuum (SC) generation; modulation instability results in pulse breakup and formation of short pulses that evolve finally to a bunch of solitons and dispersive waves. We do the research of the polarization of solitons formed by the pulse breakup process by the effect of modulation instability with pump pulses of nanoseconds in standard fiber (SMF-28) with circular birefringence introduced by fiber twist, and the twisted fiber mitigates the random linear birefringence. In this work, we found that polarization ellipticity of solitons is distributed randomly; nevertheless, the average polarization ellipticity is closer to the circular than the polarization ellipticity of the input pulse. In the experimental setup, 200 m of SMF-28 fiber twisted by 6 turns/m was used. We used 1 ns pulse to pump the fiber. The results showed that at circular polarization of the input pulse solitons at the fiber output have polarizations close to the circular, while in the fiber without twist, the soliton polarization was random.

**Keywords:** fiber optic, nonlinear optics, pulse propagation and temporal solitons, birefringence and polarization, stimulated Raman scattering

## 1. Introduction

One of the important mechanisms for the generation of supercontinuum (SC) is the formation of solitons by the nonlinear effect of modulation instability. One feature of the common optical fibers is that they are randomly birefringent, and therefore the generation of solitons and the transition of them by these fibers generated by the nonlinear effects are randomly polarized. Solitons with a well-defined

polarization are necessary for some applications like supercontinuum generation. The propagation of a pulse in a low birefringence fiber using coupled nonlinear Schrödinger equations was considered in [1–3]. In these works, the investigation concludes that the fractional pulses in each of the two polarizations trap each other and move together as one unit which is called a vector soliton. The frequency of each pulse is shifted to compensate the difference in group velocities caused by birefringence. It has been reported the experimental observation of vector solitons [4]. The vector solitons have attracted more attention in applications with linearly birefringent fibers. For the case of fibers with circular birefringence, a special case is when circular birefringence is induced when the fibers are twisted. These twisted fibers can present special advantages for some laser applications. The especial characteristic of twisted fiber is that it induces circular birefringence and eliminates the random linear birefringence [5]. An important consequence of this result is that twisted fiber is less sensitive to environmental conditions and with this we can find new useful features for nonlinear applications [6]. This helps us make the twisted fiber less sensitive to environmental conditions and provides new useful features for nonlinear applications [6]. In [7], it has been analyzed the polarization behavior of vector solitons in a circularly birefringent fiber. In this work, for analysis, we used the two coupled propagation equations in a circularly birefringent fiber that include self-phase modulation, cross phase modulation, and the soliton self-frequency shift [8]. We consider the polarization dependence of the Raman amplification unlike the previously published works [9]. We work on the equations to make a transformation to reduce them to a form of perturbed Manakov task. For our case, the equations were considered as a perturbation unlike the Manakov integrable case. For the case of the perturbation method, we can get the equations for the analysis of the development of evolution of the polarization state of pulses. An important result when analyzing the equations shows that for circularly birefringent fiber (twisted fiber), the cross-polarization Raman term leads to unidirectional energy transfer from the slow circularly polarized component to the fast one. The product of the birefringence and the amplitudes of both polarization components determine the importance of this effect. From all of the above, we can conclude that solitons with any initial polarization state will eventually develop circularly stable polarized solitons.

The split-step Fourier method was used for the numerical analysis of the two coupled nonlinear Schrödinger equations. The parameters of a standard fiber (SMF-28) were used with delay between left- and right-circular polarizations of 1 ps/km that corresponds to circular birefringence in a twisted fiber by 6 turns/m. Furthermore, by the numerical analysis, it is possible to analyze the polarization of solitons generated by the modulation instability effect. An input pulse of 30 ps with 40 W of power was used with a noise imposed which was launched to the fiber input. The input pulses had different polarization ellipticity from circular to linear. From the results, it was found that polarization ellipticity of solitons does not coincide with the polarization of the input pulses. An important result that was also found is that polarization ellipticity of solitons is distributed randomly, but the average polarization ellipticity is mostly circular compared to polarization ellipticity of the input pulse. In the experimental and numerical analysis, SMF-28 standard fiber twisted with 60 y 200 m of length with a pump pulse of 1–10 ns in a wavelength of about 1550 nm was used. The output signal at the fiber end is separated in circular-right and circular-left polarization. The ellipticity of the pulses is calculated with the ratio between the output pulses. The experimental results show that circularly polarized pulses in a fiber with circular birefringence (twisted fiber) are promising for the generation of supercontinuum with stable polarization and confirm the principal conclusions of the modeling propose in [8]; the polarization properties of supercontinuum are also an important issue for application [9–13].

## 2. Equations to analyze

The equations that describe self-frequency shift of picosecond pulses with linear polarization can be written as follows [14]:

$$\partial_z A_x = i\gamma \left[ T_R \partial_T |A_x|^2 \right] A_x \quad (1)$$

the terms  $A_x$ ,  $\gamma$ , and  $T_R$  in Eq. (1) are the envelope of the pulse with linear polarization on the x-axis, the nonlinearity, and the Raman response time, respectively. If the pulse has elliptical polarization, two polarization components have to be included if the input pulse has elliptical polarization, for this case the nonlinear effect of self-frequency shift is considered as dependent on the sum of the powers of the orthogonal components [9]. From the above, it can be said that the value of the parallel Raman gain is equal to the orthogonal Raman gain; the parallel Raman gain is when the pump and Stokes have the same linear polarization, and the orthogonal Raman gain is when the pump and Stokes are polarized orthogonally. The experimental results show that the Raman gain caused by the perpendicular component has a value of 0.3 of the Raman gain for parallel component for a small Stokes shift [15]. For this reason, we used the following equations for the self-frequency shift effect:

$$\partial_z A_x = i\gamma \left[ T_R \partial_T |A_x|^2 \right] A_x + i\alpha\gamma \left[ T_R \partial_T |A_y|^2 \right] A_x \quad (2)$$

$$\partial_z A_x = i\gamma \left[ T_R \partial_T |A_x|^2 \right] A_x + i\alpha\gamma \left[ T_R \partial_T |A_y|^2 \right] A_x \quad (3)$$

here  $\alpha = \alpha_{\perp}/\alpha_{\parallel}$ , where  $\alpha_{\perp}$  and  $\alpha_{\parallel}$  denote, respectively, the perpendicular and parallel Raman gains.

Using circularly polarized components, we can obtain the equation for the right- and left-circularly polarized state as follows:

$$\partial_z A_+ = \frac{i\gamma T_R}{2} \left\{ \frac{1+\alpha}{2} \partial_t (|A_+|^2 + |A_-|^2) A_+ + (1-\alpha) \partial_t [\text{Re}(A_+ A_-^*)] A_- \right\} \quad (4)$$

$$\partial_z A_- = \frac{i\gamma T_R}{2} \left\{ \frac{1+\alpha}{2} \partial_t (|A_+|^2 + |A_-|^2) A_- + (1-\alpha) \partial_t [\text{Re}(A_+ A_-^*)] A_+ \right\} \quad (5)$$

Eqs. (4) and (5) are the coupling equations describing the self-frequency shift. Adding group velocity dispersion (GVD) and walk-off between circularly polarized components, self-phase modulation (SPM), and cross-phase modulation (XPM) terms to these equations, we have coupling equations that we analyzed analytically and numerically:

$$\begin{aligned} \partial_z A_+ + \beta_1 \partial_t A_+ + \frac{i\beta_2}{2} \partial_t A_+ &= \frac{2i\gamma}{3} (|A_+|^2 + 2|A_-|^2) A_+ \\ &- \frac{i\gamma T_R}{2} \left\{ \frac{1+\alpha}{2} \partial_t (|A_+|^2 + |A_-|^2) A_+ + (1-\alpha) \partial_t [\text{Re}(A_+ A_-^*)] A_- \right\} \end{aligned} \quad (6)$$

$$\begin{aligned} \partial_z A_- - \beta_1 \partial_t A_- + \frac{i\beta_2}{2} \partial_t A_- &= \frac{2i\gamma}{3} (|A_-|^2 + 2|A_+|^2) A_- \\ &- \frac{i\gamma T_R}{2} \left\{ \frac{1+\alpha}{2} \partial_t (|A_+|^2 + |A_-|^2) A_- + (1-\alpha) \partial_t [\text{Re}(A_+ A_-^*)] A_+ \right\} \end{aligned} \quad (7)$$

To describe the above equations, the last two terms on the left side are the effects of Walk-off and Group Velocity Dispersion (GVD) respectively, the terms

in parenthesis of right side are the effects of Self Phase Modulation (SPM) and Cross Phase Modulation (XPM), and finally the terms in key of right side are the Stimulated Raman Scattering effect.

The vector soliton can be approximated by the next equations (not taking into account phases),

$$|A_+(z)| = A \cos(\theta) \operatorname{sech} \left[ A(t - t_0) / \sqrt{|\beta_2|} \right], \quad (8)$$

$$|A_-(z)| = A \cos(\theta) \operatorname{sech} \left[ A(t - t_0) / \sqrt{|\beta_2|} \right]. \quad (9)$$

And finally applying the perturbation method [16] to Eqs. (6) and (7), we can define the ratio between powers of circularly left- and right-polarized components as follows [7]:

$$\frac{|A_-(z)|}{|A_+(z)|} = \tan(\theta(0)) \exp \left[ \frac{2(1 - \alpha)}{3} \gamma A^2 \frac{T_R \beta_1}{|\beta_2|} z \right]. \quad (10)$$

From Eq. (10), we can see that the change of the polarization ellipticity of the vector soliton along the fiber may occur only in the presence of circular birefringence (twisted fiber,  $\beta_1$  is not equal to 0).

### 3. Numerical results

The split-step Fourier method is used for solving Eqs. (6) and (7) [14]. The values of using parameters are the following:  $\beta_1 = 1$ ,  $\beta_1 = -1$  ps/km;  $\beta_1 = 0$ ;  $\beta_2 = -25$  ps<sup>2</sup>/km,  $\alpha = 0.3$ ,  $\gamma = 1.6$  1/(W-km),  $T_R = 3$  fs. The value of  $\beta_1 = 1$  corresponds to the twisted fiber with 6 turns/m. The meaning of the change of the sign of the constant  $\beta$  is for representing the change of the twist direction. For simulations, the 30 ps input pulse with 40 W power in the input fiber was used, and the Gaussian noise was added on the pulse. Modulation instability (MI) effect breaks up the pulse generating a set of solitons; the highest soliton were traced in this set [8].

When a linearly polarized pulse is introduced to the fiber input, we can see the influence of the walk-off effect between circularly right- and left-polarized components on ellipticity, see **Figure 1**. The fiber optic length used varies from 1 to 1.5 km. The results for the simulations are present in **Figure 1**, the result for  $\beta_1 = 1$  is shown by open circles, for  $\beta_1 = -1$  is shown by closed circles, and for  $\beta_1 = 0$  is shown by squared. The important result for the dependence of polarization behavior can be observed clearly. The polarization behavior with  $\beta_1 = 1$ , but in this special case, we consider  $\alpha = 1$ , that is, the parallel Raman gain is equal to the perpendicular,  $\alpha = 1$ , see **Figure 2**. It can be seen that in this case, the effect of the ellipticity change of the soliton along the fiber is not presented. The results obtained are based on Eq. (10), and these results show that some ellipticity change must be presented on the circular birefringence and difference between Raman parallel and perpendicular gain. It can be observed that the ellipticity of the highest soliton does not coincide with the ellipticity of the input pulse (there is an exception for the case where  $\beta_1 = 0$ ).

For the special case when using elliptical input polarization, the results show a similar behavior of the polarization ellipticity to make the energy transform from the slow to fast circularly polarized component. With these results, it can be said that the soliton with a fast circular polarization component propagates in the fiber with stable polarization. From the case of Eq. (10), we can say that this equation describes the polarization evolution of the soliton, but it is not applicable for

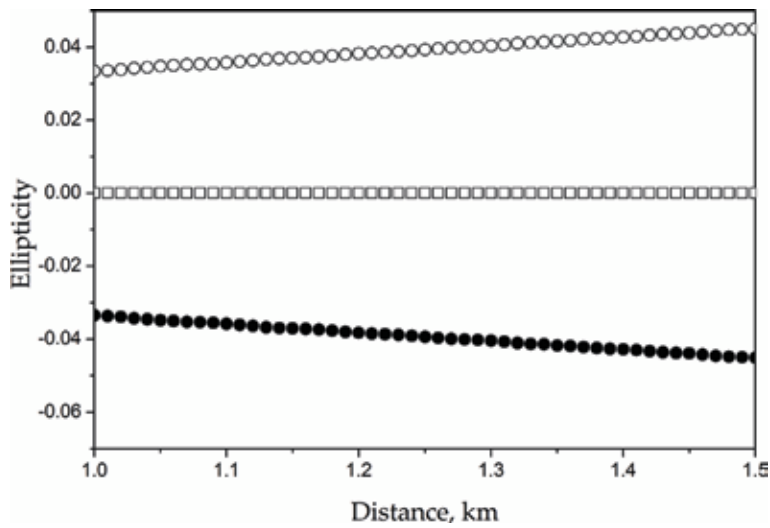


**Figure 1.** Ellipticity vs. fiber length for a soliton with linearly polarized pulse at the entrance for  $\beta_1 = 1$  (closed circles),  $\beta_1 = -1$  (open circles), and  $\beta_1 = 0$  (squared).

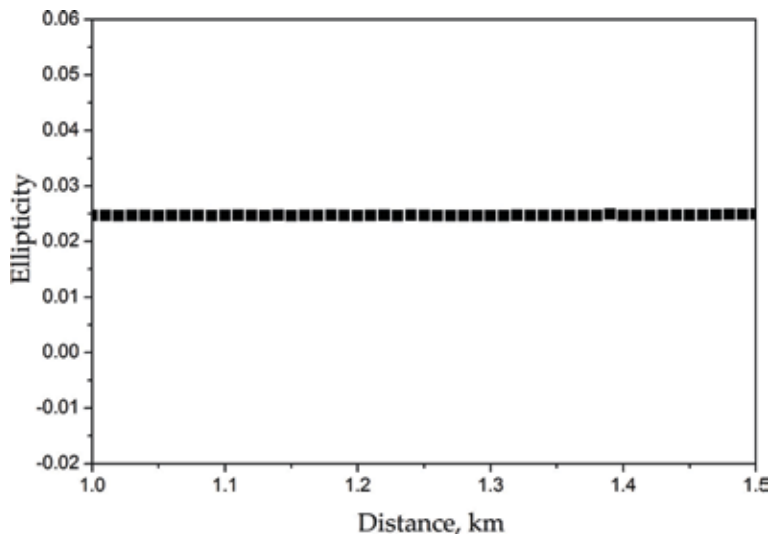


**Figure 2.** Ellipticity vs. fiber length for linear input pulse, particularly for the case when parallel Raman gain is equal to perpendicular Raman gain.

development of the process of the soliton formation. As we can see from the previous results, the polarization of the soliton at the end of the soliton formation process does not coincide with the polarization of the input pulse. The process of generation of solitons by the effect of modulation instability is complex, and the stochastic process depends on the noise. It was calculated by the ellipticity of solitons generated in the process of the effect of modulation instability for different noise imposed on the input pulse. The ellipticity of the highest solitons was found to be randomly distributed. In **Figure 3**, the number of solitons that were generated with different ellipticity when linearly polarized input pulse was used is showed; the total of number of calculation was 150. As you can see, the polarizations of solitons are mostly concentrated close to the linear one; however, solitons with a wide range of the polarization ellipticity can also appear. **Figure 3** shows that the

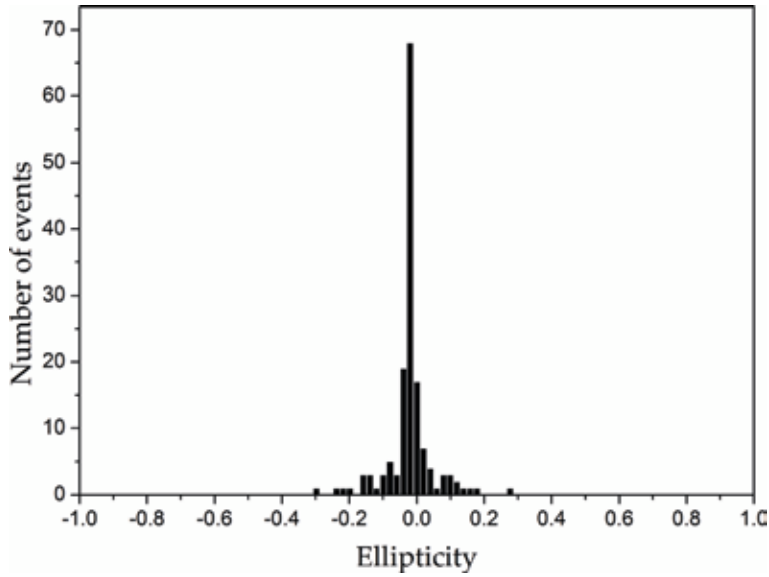


**Figure 3.** The number of solitons with different ellipticity generated by the effect of modulation instability at linear polarization of the input pulse.

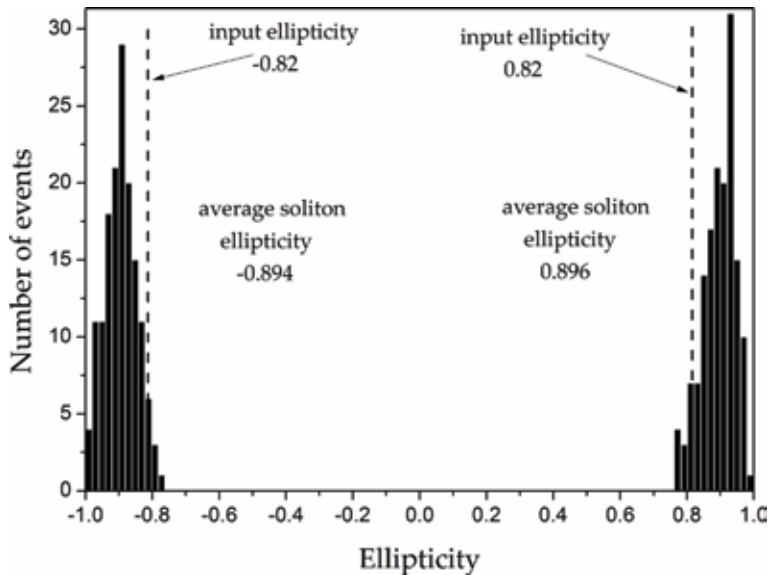


**Figure 4.** The number of solitons with different ellipticity generated by modulation instability at polarization of the input pulse of 0.82 and  $-0.82$ .

average polarization ellipticity of solitons is  $-0.02$ . The maximum ellipticity found in this set of calculations was 0.3.

The distribution of polarization of solitons when the input pulse has ellipticity of 0.82 is showed in **Figure 4**. From **Figure 4**, it can be observed that the average soliton polarization moves toward circular polarization. For the case when the polarization of the input pulse is close to the circular polarization, the dispersion of the polarization ellipticity of solitons becomes much less, see **Figure 5**. For **Figure 5**, the polarization ellipticity of the input pulse used was equal to 0.906 and  $-0.906$ . It

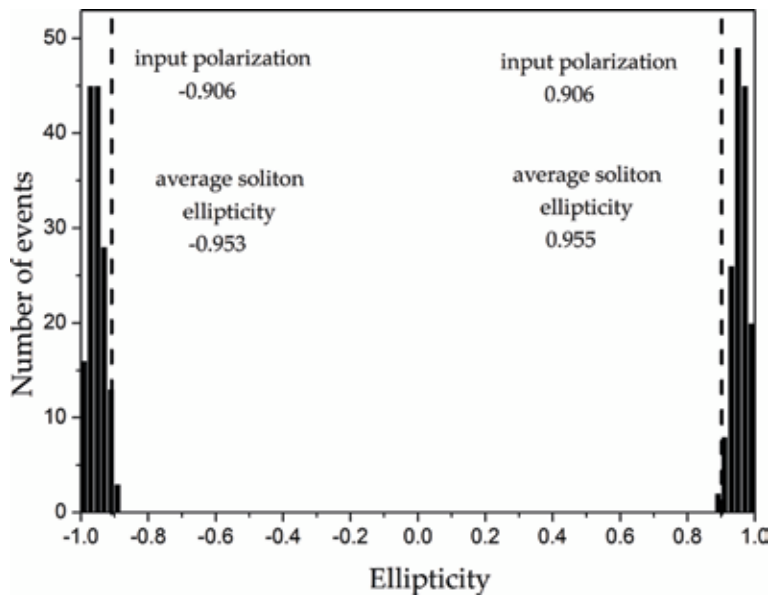


**Figure 5.**  
 The number of solitons with different ellipticity generated by modulation instability at polarization of the input pulse of 0.906 and  $-0.906$ .

can be seen that most of the solitons have the ellipticity closer to the circular polarization than the input pulse. Average ellipticity of solitons in this case was found to be about 0.95.

#### 4. Experimental setup

In **Figure 6**, the experimental setup is showed. For the source of signal, a continuous wave distributed feedback semiconductor laser with a wavelength of 1550 nm was used. The continuous wave signal was gated and amplified by the erbium doped fiber amplifier (EDFA) from which you can get pulses with 1–10 ns duration and a maximum peak power of about 150 W. To assure the stable polarization state, the pulses from the EDFA pass through a polarization controller (PC) and a polarizer. With the rotation of quarter wave retarder (QWR1), we can change the polarization ellipticity to be able to control the input polarization on the fiber. The output of the fiber under the test (twisted fiber) is connected to a quarter wave retarder (QWR2) and polarization beam splitter (PBS). The QWR2 and PSB convert the right and left circularly polarized component at the output fiber to orthogonally polarized linear components at the output PBS. The output of PSB (linearly polarized component) is separated in time by a delay line (10 m of SMF-28 fiber), and they come together using a 50/50 coupler to launch the same monochromator input. The output pulses are detected and monitored by an oscilloscope. A typical

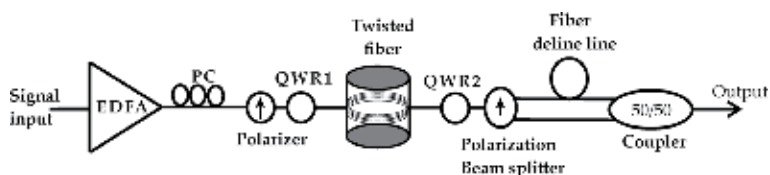


**Figure 6.**  
 Experimental setup.

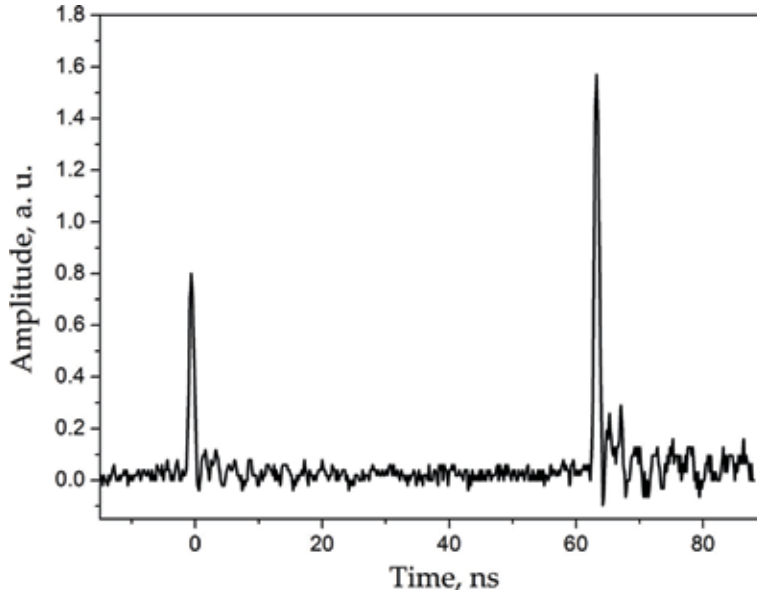


**Figure 7.**  
A typical oscilloscope trace.

oscilloscope trace is shown in **Figure 7**. The first pulse is that traveling from a port 1 of the polarization beam splitter, and second pulse travels from a port 2 of the polarization beam splitter through the delay line (10 m of SMF-28 fiber). With this experimental setup, we can measure the amplitudes of left and right circularly polarized component at any wavelength using one single shot in the oscilloscope [17]. The ellipticity is calculated using the next equation:

$$\rho = \tan^{-1} \left( \frac{\sqrt{P_+} - \sqrt{P_-}}{\sqrt{P_+} + \sqrt{P_-}} \right) \quad (11)$$

where  $P_+$  and  $P_-$  are the pulse amplitudes at the monochromator output. A disadvantage of this method is that we measure the average ellipticity of the bundle of solitons.

We used span of SMF-28 fiber with different lengths, twisted, and without twist. To calibrate the ellipticity measurement system, the ellipticity was measured at the polarizer output. The results of measurements are presented in **Figure 8**. The angle 0 on the position of the QWR1 corresponds to linearly polarized signal at the QWR1 output. Taken into account that the ellipticity of the signal at the QWR1 output is equal to the angle of the rotation of QWR1 in the range  $-45^\circ + 45^\circ$  [18]. The maximum ellipticity measured was  $35^\circ$ . At this ellipticity, 97% of the power is in one circularly polarized component and only 3% is in orthogonal component. In our setup, the measurement of the higher ellipticity is restricted by the possibility of the measurement of low power pulse. In the experiment, it was used 1-ns pump pulse with a maximum power of 150 W and a wavelength of 1550 nm. Linearly polarized pump pulses passed through QWR1. The angle of QWR1 defined the polarization state of the input pulse that is launched to the fiber. In the experiment, the span of SMF-28 fibers was used with lengths of 65 and 218 m. The fibers under the test were twisted with a twist of 6 turn/m and they were put on the cylinder with diameters of 25 and 50 cm. From the experimental results, it can be observed that both fibers conserved the polarization ellipticity along the fiber at low powers. **Figure 8** shows the ellipticity of the low power continuous wave (CW) radiation at the output of

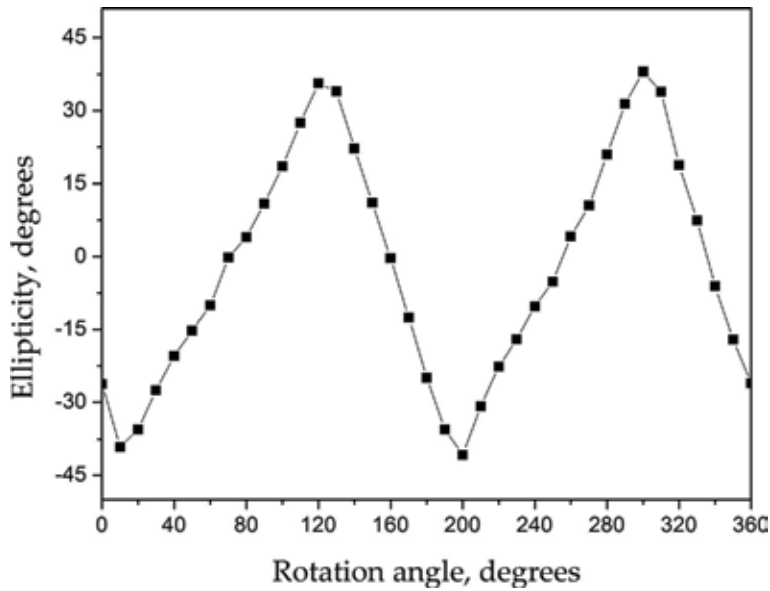


**Figure 8.**  
*Ellipticity at the QWR1 output measured by our setup.*

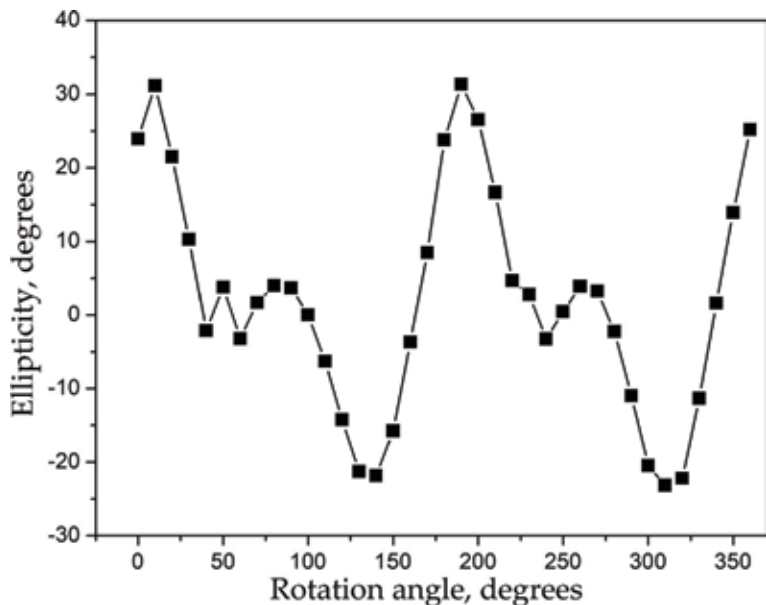


**Figure 9.**  
*The ellipticity at the output of the 218-m fiber without twist.*

the 65-m SMF-28 fiber. It can be observed that the dependence is the same as the dependence of the ellipticity on the QWR1 angle at the fiber input.

Next step was the measurements of the ellipticity at the fiber output at low power. These measurements show the effect of residual linear birefringence in the fiber. In **Figure 9**, we show the ellipticity at the output of the 218-m fiber without twist. As another example, **Figure 10** shows the ellipticity at the output of the 218-m twisted fiber wound on the cylinder with a diameter of 25 cm (squares); **Figure 10** shows the ellipticity at the output of the same fiber however wound on the cylinder with a diameter of 50 cm (circles). **Figure 10** (for fiber wound on the

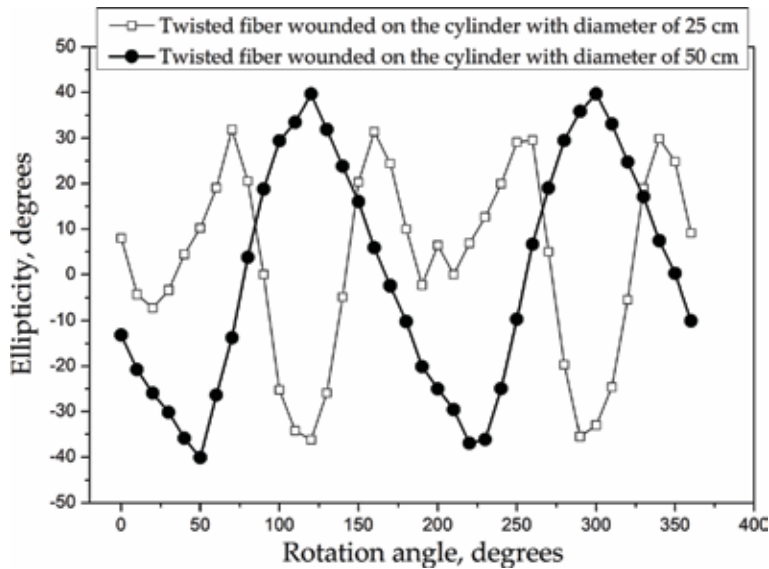


**Figure 10.** The ellipticity at the output of the 218-m fiber: squares—on 25-cm cylinder and circles—on the 50-cm cylinder.

cylinder with a diameter of 50 cm) shows the ellipticity at the fiber output is the same as at the fiber input. It means that there is no effect of linear birefringence. However, for the 25-cm diameter cylinder, the effect of the linear birefringence can be clearly seen.

When the pulses with the power of 150 W were launched to the input fiber, the pulse breakup occurred followed by the soliton formation and soliton self-frequency shift; see **Figure 11**. The polarization ellipticity was measured at the output of the 218-m twisted fiber on the 50-cm cylinder and also at the output fiber with the same length but without twist. The measurements were done for high power wavelengths of 1560, 1570, and 1580 nm. The results for these wavelengths are presented in **Figures 12–14**, for 1560, 1570, and 1580 nm, respectively. For these results, it can be seen that solitons at the output of twisted fiber present a high grade of polarization at least when the input polarization has circular polarization, for the angle of QWR1 of about 50°. We can use Eq. (11) to calculate that about 90% of output power is in the same circular polarization as in the output and only about 10% in the orthogonal polarization. With this technique used, we can measure the averaged polarization, and so if measured ellipticity is close to 0, it does not imply that solitons have linear polarization, it just means that powers of all solitons in the selected spectral range in both circularly polarized components are equal. For the case of the fibers without twist, the polarization is chaotic. It can be seen that for the wavelengths of 1570 and 1580 nm, where the measured ellipticity is very close to 0 [17]. There are no physical reasons for the linear polarization at any input polarization; so we can think that the polarization ellipticity of solitons most probably is random.

The slope of the dependencies of the output ellipticity on the input at the input ellipticity equal to 0 is equal to 1.9 for wavelengths 1570 and 1580 nm and 0.9 for 1560 nm. The fact that the slope is higher than in 1570 and 1580 nm can show that the output ellipticity tends to be higher than the input ellipticity. The ellipticity of the highest soliton generated in the process of pulse breakup at different noise imposed on the pulse was also calculated. The equations and the procedure described before were used [7]. The equations are taken into account the difference of group velocity of orthogonal circularly polarized components and vectorial nature of the Raman

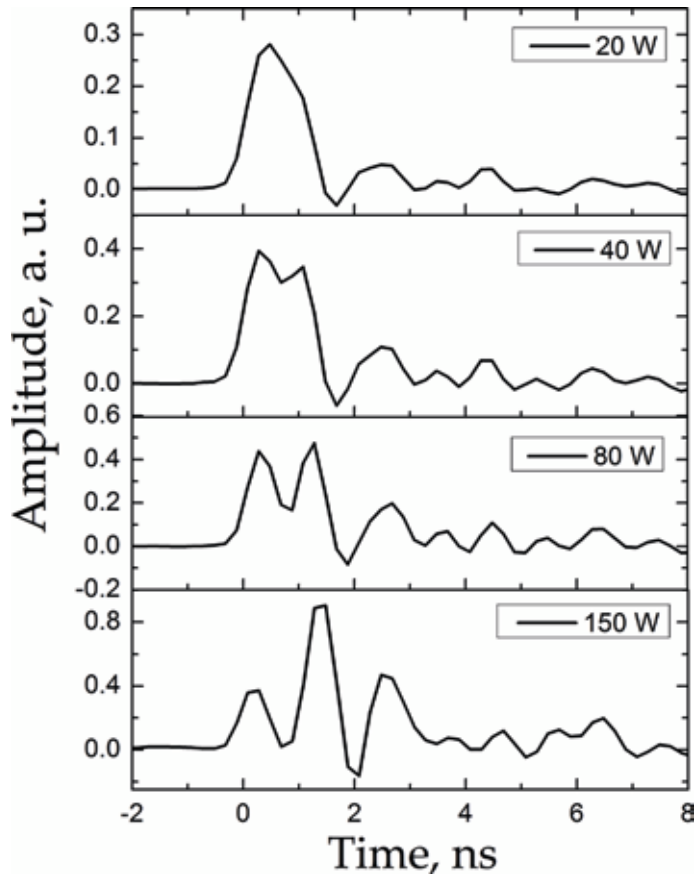


**Figure 11.**  
*The process of the pulse breakup.*

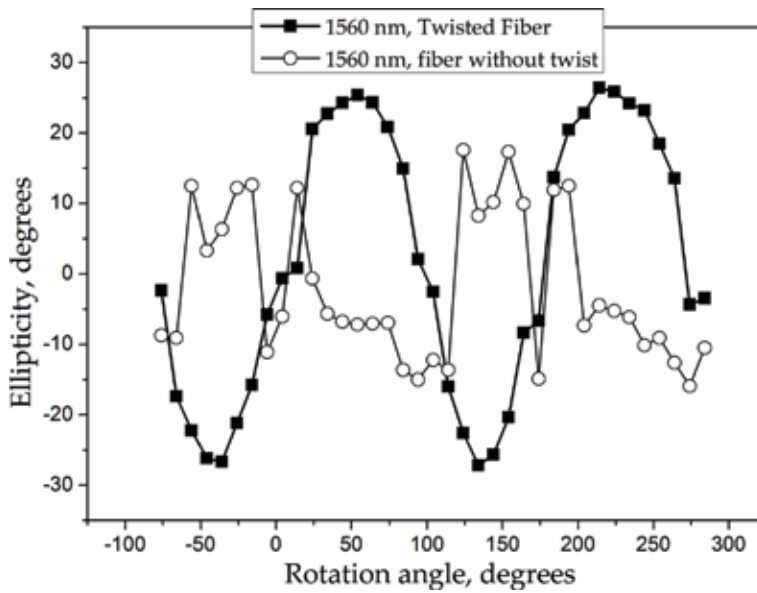


**Figure 12.**  
*The ellipticity at the output of the 218-m fiber for 1560 nm: squares for the twisted fiber and circles for the fiber without twist on the 50 cm cylinder.*

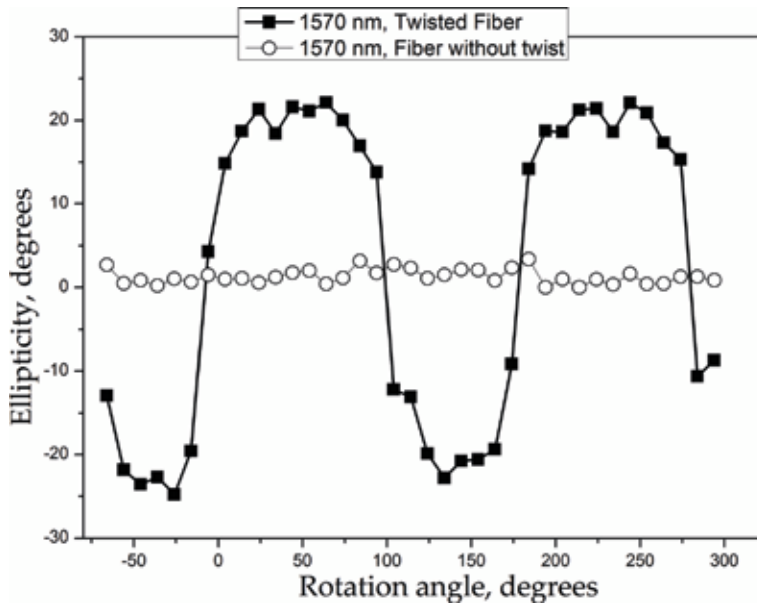


**Figure 13.** The ellipticity at the output of the 218-m fiber for 1570 nm: squares for the twisted fiber and circles for the fiber without twist on the 50 cm cylinder.

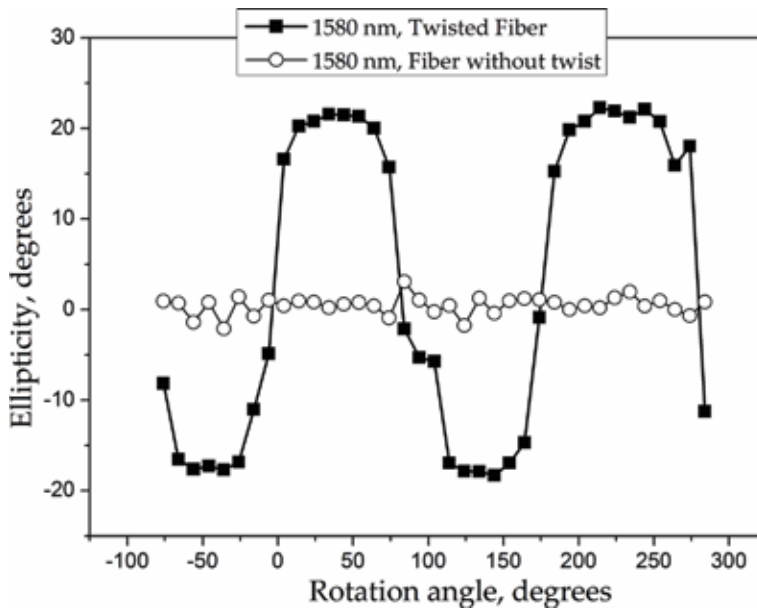


**Figure 14.** The ellipticity at the output of the 218-m fiber for 1580 nm: squares for the twisted fiber and circles for the fiber without twist on the 50-cm cylinder.

effect in the optical fiber. Like in **Figure 15**, we have examples of the 50 calculations with 30 ps input pulse with 40 W of power. For the numerical calculation, the following parameters were used:  $\beta_1 = 0.2$  ps/km and  $\beta_2 = 25$  ps<sup>2</sup>/km. The input polarizations were equal to 0.4 (equal to 21.8°) and 0.9 (equal to 42°). As we can see in most of the realizations, the output ellipticity of the solitons was greater than the ellipticity of the input pulse. For the case when input ellipticity is equal to 0.4, the

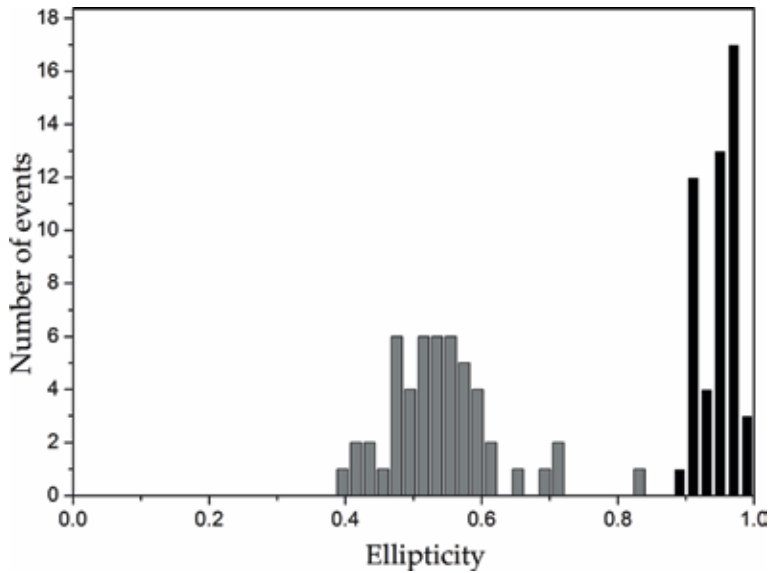


**Figure 15.**  
 Statistics of the ellipticity of the highest soliton.

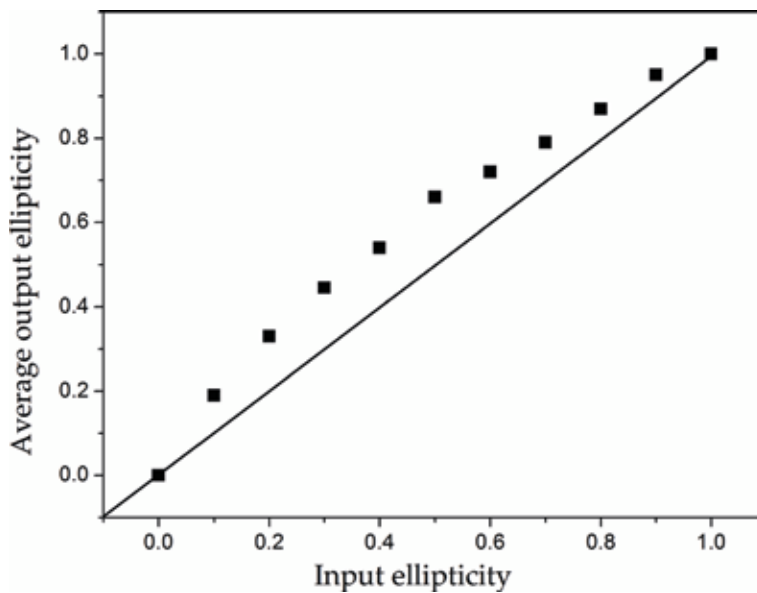


**Figure 16.**  
 Average output polarization vs. input polarization.

average output ellipticity is equal to 0.54, and the case for input ellipticity is equal to 0.9, the average output ellipticity is equal to 0.95, see **Figure 15** [18].

Numerical calculations were done for different input polarizations. The dependence of the average output soliton ellipticity on the input ellipticity is showed in **Figure 16**. The simulations corroborate the measured tendency of soliton to have the higher ellipticity than the input pulse. Simulations show that the fluctuations of the soliton polarization get to be smaller when the input polarization approaches to the circular. We also made calculations for  $\beta_1 = 0$ , that is, for ideal fiber without any birefringence and found similar statistic for the polarization of solitons.

## 5. Conclusions

Finally, it can be concluded that the solitons generated in the nonlinear process of pulse breakup for the special case when the twisted standard fiber is used can present a high degree of polarization for the case when the polarization of the input pulse is circular. The numerical calculations agree with the experimental results show that the polarization ellipticity of solitons tends to be greater than the polarization of the input pulse (for the case when the polarization of the input pulse is circular). We can say that according to the results, this effect does not depend on the circular birefringence, so, in this particular case, the twisted fiber plays a role of the ideal fiber without birefringence.

## Acknowledgements

The authors thank the Mexican Council for Science and Technology (CONACyT) for providing financial support for the realization of this project and the Publication funded with PFCE 2018 resource (Program for Strengthening Educational Quality).

## Author details

Ariel Flores Rosas<sup>1\*</sup>, Orlando Díaz Hernández<sup>1</sup>, Roberto Arceo<sup>1</sup>, Gerardo J. Escalera Santos<sup>1</sup>, Sergio Mendoza Vázquez<sup>1</sup>, Elizeth Ramírez Álvarez<sup>1</sup>, Christian I. Enriquez Flores<sup>2</sup> and Evgeny Kuzin<sup>3</sup>

<sup>1</sup> Faculty of Sciences in Physics and Mathematics, Autonomous University of Chiapas, Tuxtla Gutiérrez, Chiapas, México

<sup>2</sup> Conacyt Chairs Program, National Council of Science and Technology, México City, México

<sup>3</sup> Department of Optics, National Institute of Astrophysics, Optics and Electronics (INAOE), Puebla, México

\*Address all correspondence to: ariel.flores@unach.mx

## IntechOpen

© 2018 The Author(s). Licensee IntechOpen. This chapter is distributed under the terms of the Creative Commons Attribution License (<http://creativecommons.org/licenses/by/3.0>), which permits unrestricted use, distribution, and reproduction in any medium, provided the original work is properly cited. 

## References

- [1] Menyuk CR. Stability of solitons in birefringent optical fibers. I: Equal propagation amplitudes. *Optics Letters*. 1987;**12**(8):614-616
- [2] Menyuk CR. Stability of solitons in birefringent optical fibers. II. Arbitrary amplitudes. *Journal of the Optical Society of America B: Optical Physics*. 1988;**5**(2):392-402
- [3] Christodoulides DN, Joseph RI. Vector solitons in birefringent nonlinear dispersive media. *Optics Letters*. 1988; **13**(1):53-55
- [4] Islam MN, Poole CD, Gordon JP. Soliton trapping in birefringent optical fibers. *Optics Letters*. 1989;**14**(18): 1011-1013
- [5] Tsao C. *Optical Fiber Waveguide Analysis*. New York: Oxford University Press; 1999
- [6] Tanemura T, Kikuchi K. Circular-birefringence fiber for nonlinear optical signal processing. *Journal of Lightwave Technology*. 2006;**24**(11):4108-4119
- [7] Korneev N, Kuzin EA, Villagomez-Bernabe BA, Pottiez O, Ibarra-Escamilla B, González-García A, et al. Raman-induced polarization stabilization of vector solitons in circularly birefringent fibers. *Optics Express*. 2012;**20**(22): 24289
- [8] Kuzin EA, Flores-Rosas A, Peralta-Hernandez JI, Villagomez-Bernabe BA, Ibarra-Escamilla B, Gonzalez-Garcia A, et al. Polarization properties of vector solitons generated by modulation instability in circularly birefringent fibers. In: *Nonlinear Optics and Applications VII*. Vol. 8772. Prague, Czech Republic: SPIE Optics + Optoelectronics. 2013. p. 877218
- [9] Tu H, Liu Y, Liu X, Turchinovich D, Lægsgaard J, Boppart SA. Nonlinear polarization dynamics in a weakly birefringent all-normal dispersion photonic crystal fiber: Toward a practical coherent fiber supercontinuum laser. *Optics Express*. 2012;**20**(2): 1113-1128
- [10] Lehtonen M, Genty G, Ludvigsen H, Kaivola M. Supercontinuum generation in a highly birefringent microstructured fibre. *Applied Physics Letters*. 2003;**82**: 2197-2199
- [11] Xiong C, Wadsworth WJ. Polarized supercontinuum in birefringent photonic crystal fiber pumped at 1064 nm and application to tunable visible/UV generation. *Optics Express*. 2008;**16**: 2438-2445
- [12] Zhu Z, Brown TG. Polarization properties of supercontinuum spectra generated in birefringent photonic crystal fibers. *Journal of the Optical Society of America B: Optical Physics*. 2004;**21**:249-257
- [13] Zhu Z, Brown TG. Experimental studies of polarization properties of supercontinua generated in a birefringent photonic crystal fiber. *Optics Express*. 2004;**12**:791-796
- [14] Agrawal GP. *Nonlinear Fiber Optics*. San Diego, CA, USA: Academic Press; 2001. pp. 48-49
- [15] Mandelbaum I, Bolshtyansky M, Heinz F, Hight R. Method for measuring gain tensor in optical fibers. *Journal of the Optical Society of America B: Optical Physics*. 2006;**23**(4):621-627
- [16] Midrio M, Wabnitz S, Franco P. Perturbation theory for coupled nonlinear Schrödinger equations. *Physical Review E*. 1996;**54**(5):5743-5751
- [17] Flores-Rosas A, Mendoza-Vazquez S, Posada-Ramirez B, Kuzin EA,

Ibarra-Escamilla B. Polarization properties of solitons generated in process of pulse breaking-up in a fiber with circular birefringence. In: Latin America Optics and Photonics Conference, Paper LTu4A47

[18] Flores-Rosas A, Peralta-Hernandez JI, Villagomez-Bernabe BA, Bracamontes- Rodríguez YE, Beltran-Perez G, Pottiez O, et al. Observation of a high grade of polarization of solitons generated in the process of pulse breakup in a twisted fiber. *Journal of the Optical Society of America B: Optical Physics.* **31**:821-826

# Towards Enhancing the Efficiency of Nonlinear Optical Generation

*Padma Nilaya J. and Dhruba J. Biswas*

## Abstract

The chapter dwells on two novel approaches towards enhancing the efficiency of nonlinear optical generation. The former is to enable the unabsorbed pump beam to pass through the crystal repeatedly. Integration of an unstable cavity containing the crystal with the stable pump cavity made this possible. The Q of the unstable cavity could be maintained high as the output coupler of the pump laser, itself served as the entrance mirror of this cavity. The unstable nature of the cavity kept the crystal from being exposed to high flux while ensuring longer interaction length. Although this scheme demonstrated in mid-IR region its advantage should persist across UV, visible, and near-IR regions too. The enhancement of conversion efficiency is effected in the second scheme by way of illuminating the crystal with alternate high and low regions of intensity along its length as against the uniform illumination case maintaining the same average intensity as in the conventional operation. The advantage is attributed to the square dependence of the second harmonic on the intensity of the pump. A simple modification of the existing experimental setup involving integration of an additional optical element with the pump cavity allowed exploitation of interference effect to realise such a non-uniform illumination condition.

**Keywords:** non-linear optical conversion, unstable cavity, interference, CO<sub>2</sub> laser, dichroic optics

## 1. Introduction

There has been a constant endeavour to increase the number of available coherent sources allowing wider coverage of the electromagnetic spectrum. To this end, nonlinear optical conversion of the emission of a laser inside an appropriate nonlinear crystal by ensuring that the fundamental and generated waves are phase matched has emerged as one of the most attractive methods across UV [1], visible [2], infrared [3], and mid-infrared [4] regions of the electromagnetic spectrum. As the non-linearity of the crystal is responsible for effecting this conversion, an increase in the intensity of the pump radiation to which the crystal is subjected to increases the conversion efficiency too albeit in a non-linear fashion. Single crystals, specifically grown to provide a reasonable interaction length, invariably suffer from low optical damage threshold. This thus puts an upper limit on the pump intensity to which the crystal can be exposed to causing a corresponding reduction in the conversion efficiency. A significant under-utilisation of the pump beam is thus the end result. The crystals employed for the conversion in the mid infrared region have

inherently high refractive index and the problem thus gets further compounded as the entrance and the exit faces of the crystals need to be essentially anti-reflection coated to arrest losses due to Fresnel reflection. The pump intensity therefore, needs to be further reduced as the optical damage threshold of dielectric coatings is usually lower than the crystal bulk. This drawback can be surmounted by increasing the interaction length of the pump beam with the nonlinear medium giving due consideration to the thermal de-phasing effect that occurs along the length of the crystal [5]. Increasing the length of the crystal brings about a steep rise in its cost and therefore is not an economically viable option. Attempts have been made to use a number of crystals instead, either in tandem [6] or in parallel [7] to circumvent this problem. These schemes however, suffer from an inherent disadvantage as they present too many crystal surfaces off which the pump photons escape through Fresnel reflections. To be noted here that the same crystal has also been used in the past to enhance the interaction length by allowing the pump beam to make two [8] or multiple passes [9] through it. These methods have not gained much popularity as the cavity configuration employed in the former case limited the operation to a non-collinear phase matched mode while in the latter case it resulted in enhancing the second harmonic (SH) conversion of the SH wave itself. In case of frequency doubling of near infrared cw pump to the visible, the schemes that have gained importance use the crystal in the intra-cavity mode [10] or external cavity resonant enhancement mode [11]. Ring cavity configuration that has an inherent advantage of blocking any feedback into the pump cavity has generally been employed here. The applicability of these schemes for pulsed second harmonic conversion (SHG) is challenging due to the high intra-cavity flux that prevails in a pulsed laser. Literature on similar schemes for SHG in the mid infrared region is scanty primarily due to the possibility of thermal lensing effect that may lead to crystal damage. This has restricted the operation to quasi-cw regime with adequate precautions to forbid Q-switched lasing [12] while in the case of pulsed operation, the intra-cavity flux has been brought down by using appropriate attenuators [13].

Another approach has been to increase the intensity of the pump beam itself. That the generated SH output increases in a non-linear fashion with the intensity of the pump radiation to which the crystal is exposed is a fact known since the time SHG was reported more than half a century ago [14]. A direct consequence of this fact is that if the crystal can in some way be subjected to alternate high and low regions of pump intensity along its conversion length that results in an average intensity  $I_{av}$  there would be a net gain with respect to SHG as compared to the conventional situation where the same crystal is subjected to a uniform pump intensity of  $I_{av}$ . These two cases are illustrated in **Figure 1**. In the first case (**Figure 1a**) the crystal of length ' $l$ ' is illuminated by a pump beam of uniform intensity ' $I$ ' along its length. In the second case the incident pump intensity ' $I$ ' is redistributed as alternate periodic intensity packets of ' $2I$ ' and ' $0$ ' longitudinally along the crystal thus maintaining the same average intensity ' $I$ ' as before (**Figure 1b**). The square dependence of second harmonic conversion on the incident pump intensity can be represented mathematically for the two cases as follows:

For the case of **Figure 1a**:  $SH(\text{output}) \propto l \times I^2$ .

For the case of **Figure 1b**:  $SH(\text{output}) \propto [(l/2) \times 0] + [(l/2) \times (2I)^2] \propto 2l \times I^2$ .

This clearly suggests that the generated SH, in the second case, is enhanced by a neat 100% as against the first case when the crystal is illuminated uniformly. A non-linear crystal placed inside a Fabry-Perot or a bidirectional ring cavity experiences flux from both ends and therefore is one of the most obvious ways of creating such a situation of non-uniform illumination. The interference of the forward and reverse beams creates alternate high (anti-nodal) and low (nodal) regions of intensity in the crystal and therefore should result in an enhancement of the SHG.

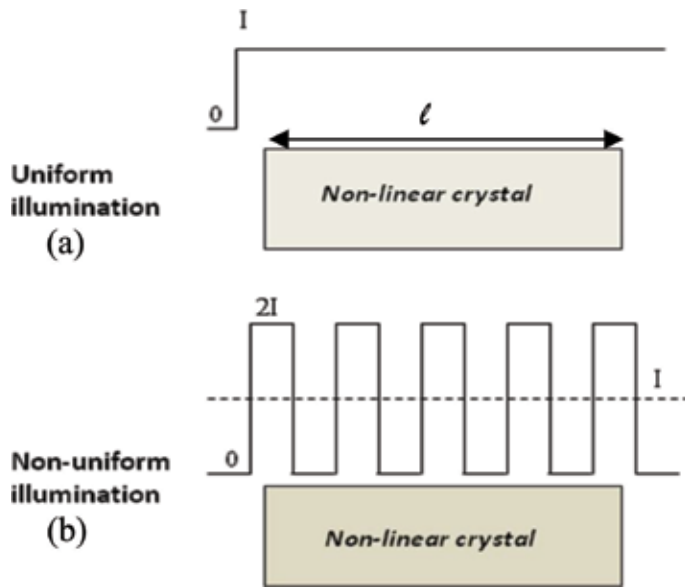


**Figure 1.** A non-linear crystal exposed to the pump radiation. (a) Uniform illumination of intensity  $I$ . (b) Periodic illumination with intensity packets of  $2I$  and  $0$  thus maintaining the same average intensity  $I$  as before.

This chapter dwells on the recent advances made by our group in these two areas viz., enhancing the conversion efficiency by way of (a) increasing the interaction length between the pump and the non-linear medium and, (b) exploiting the effect of non-uniform illumination of the non-linear medium.

## 2. Enhancing the SH conversion efficiency by increasing the interaction length between the pump and the non-linear medium

By way of constructing a coupled plano-convex cavity external to the pump laser (Figure 2) that allowed to and fro passes of the unabsorbed pump through the crystal, we conceived a novel way to increase the effective interaction length between the non-linear medium and the pump beam [15]. An ideal situation demands that the coupling optics offers high transmission at the pump wavelength and high reflection too at the same wavelength to enable multiple passes through the crystal; a conflicting requirement indeed that is inherently taken care of in the above

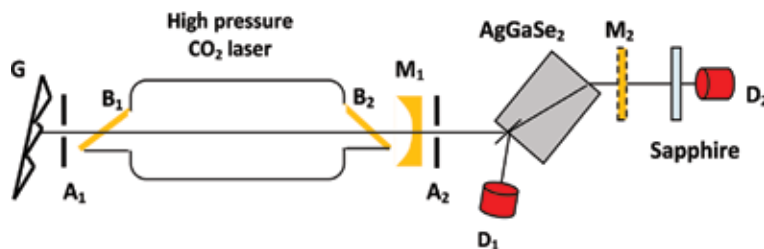


**Figure 2.** Schematic diagram of the experimental setup for second harmonic conversion of the emission of a  $\text{CO}_2$  laser in a  $\text{AgGaSe}_2$  crystal. G: Plane blazed grating,  $A_1$  and  $A_2$ : Adjustable apertures,  $B_1$  and  $B_2$ : ZnSe Brewster plates,  $M_1$ : 70% R ZnSe concave mirror,  $D_1$  and  $D_2$ : Energy/power detectors,  $M_2$ : Dichroic mirror. (a) In case of single pass second harmonic generation, dichroic mirror  $M_2$  is absent. (b) In case of multi-pass second harmonic generation, dichroic mirror  $M_2$  in conjunction with pump laser output coupler  $M_1$ , forms the unstable external cavity.

scheme. As the output coupler of the pump laser itself functioned as the entrance mirror of the external cavity, its quality factor could be maintained high allowing at the same time, efficient transportation of the pump beam into it. Further, the intra-cavity photon flux could be maintained within acceptable level due to the unstable nature of the external cavity. This reduced the risk of optical flux induced crystal damage besides eliminating the possibility of feed back into the pump cavity.

## 2.1 Experimental

The experimental demonstration of this scheme was effected in the second harmonic generation of the 10 micron emission of a pulsed CO<sub>2</sub> laser. A commercial uncoated 17 mm thick AgGaSe<sub>2</sub> crystal served as the non-linear medium for this conversion process. A rise in the energy conversion efficiency by ~300% and even higher peak power conversion efficiency has been achieved by making the unconverted pump go through the crystal time and again. The increase in the effective length of the crystal should in principle, allow the performance of a thin crystal in such a cavity configuration to match that of a thick crystal in the conventional operation although at a lower level of optical flux, that in turn, precludes the possibility of its damage even in the pulsed operation.

The schematic of the experimental lay out is depicted in **Figure 2**. In the first set of experiments (**Figure 2a**), the pulsed emission of a commercial multi-atmosphere TE-CO<sub>2</sub> laser was made use of to affect SHG in an uncoated AgGaSe<sub>2</sub> crystal (cross-section 10 × 10 mm and length 17 mm). A plane master grating (150 lines/mm) and a concave (7 m ROC) 70%R ZnSe output coupler separated by 105 cm formed the passively stabilised pump laser cavity. For this experiment, the laser was operated on 10P (34) line for which the second harmonic phase matching occurred at an external angle of incidence of ~34°. Usage of an intra-cavity adjustable aperture A<sub>1</sub> allowed the operation of the pump laser on the TEM<sub>00</sub> mode. The energy incident on the crystal was controlled by varying the charging voltage of the laser. An external adjustable aperture 'A<sub>2</sub>' allowed maintaining the pump beam cross-section on the crystal entrance to ~4.5 mm diameter so as to ensure its clear passage through the non-linear medium. Monitoring of both the energy and the power of the incident pump pulse was possible by probing its Fresnel reflection off the incident face of the crystal. The energy and power profile of the generated SH beam were measured after blocking the unconverted pump beam that also emerged along with the SH beam through the crystal by means of a sapphire plate. The CO<sub>2</sub> laser, by virtue of its multi-atmosphere operation, possessed inherently very high gain and thus emitted pulses of relatively short duration (FWHM ~110 nsec, **Figure 3**). In the present experiment, the maximum intensity was restricted to ~2.5 MW/cm<sup>2</sup>.

## 2.2 Results and discussion

In order to find the efficiency of the single pass non-linear conversion process as a function of the input pump energy, we gradually increased the input and measured the corresponding SH energy and the dependence is as shown in **Figure 4**. The parabolic nature of this dependence clearly reveals the square proportionality of the SH intensity on the pump intensity. As would be seen, ~8.46% is the maximum internal SH energy conversion efficiency that was obtained maintaining the pump intensity below the damage threshold of the crystal. Understandably therefore, significant fraction of the pump photons stays unconverted and emerge together with the SH beam and the same was measured using detector D<sub>2</sub> when the sapphire plate is removed. Effective utilisation of the pump beam is possible by making it to pass through the crystal time and again. To this end, a Fabry-Perot cavity was constructed

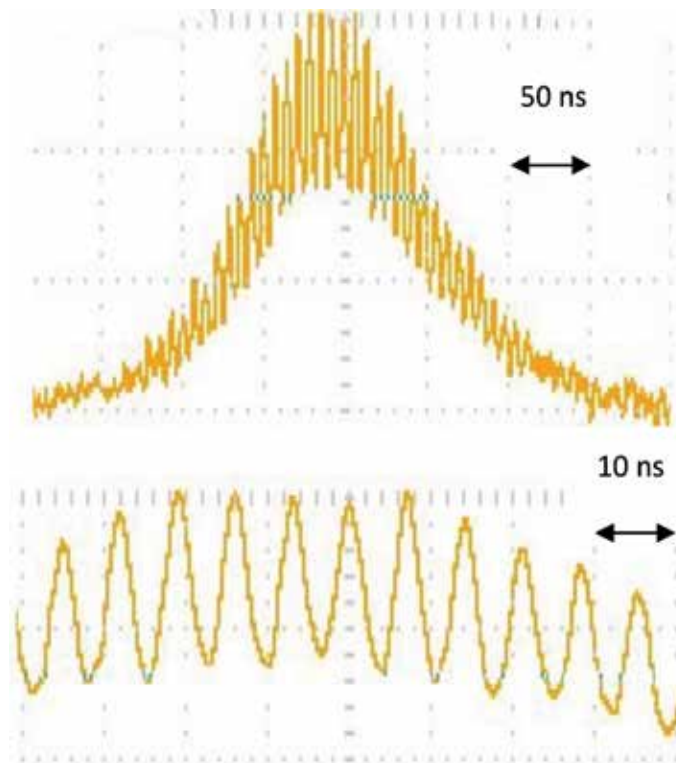


**Figure 3.** Typical temporal profile of the emission of the pump  $\text{CO}_2$  laser. FWHM value of  $\sim 110$  ns is evident from the upper trace. The beating of two longitudinal modes at a period of  $\sim 7$  ns is apparent from the lower trace. Absence of any beat at a longer period indicates operation on multi-longitudinal modes belonging to the same transverse family.

that contained the crystal and comprised of the output coupler ( $M_1$ ) of the pump laser of plano-concave geometry [plane surface AR coated @  $10.6 \mu\text{m}$  and the concave

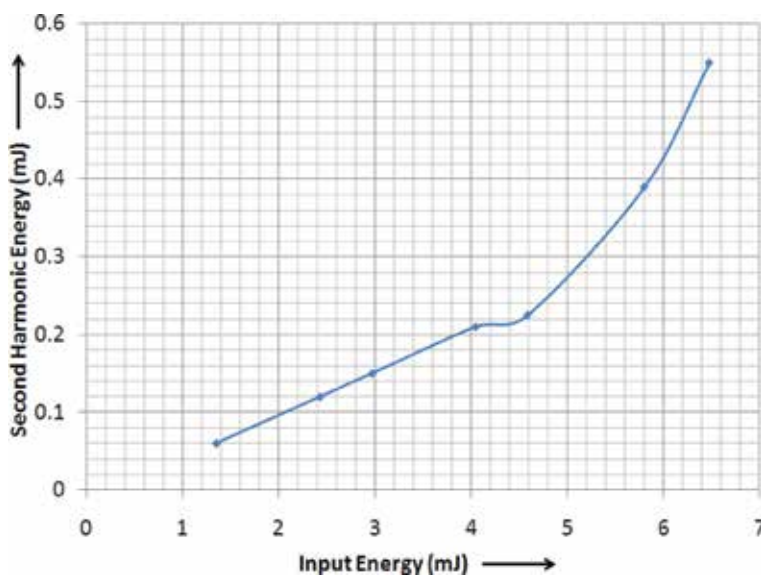


**Figure 4.** Dependence of single-pass SH output on the energy of the pump pulse.

surface (7 m ROC) dielectric coated for 70% R @ 10.6  $\mu\text{m}$ ] and a plane ZnSe dichroic mirror  $M_2$  (R > 90% @ 10.74  $\mu\text{m}$ , T > 90% @ 5.37  $\mu\text{m}$ ) (refer to **Figure 2b**). The length of this external cavity ( $\sim 1.21$  m) was such as to push the  $g_1 \times g_2$  value viz., 1.17 beyond the region of stability. There was a remarkable enhancement in the generation of SH output when  $M_2$  was fine tuned to ascertain its parallelism with the convex face of mirror ' $M_1$ '. Performance of this multi-pass cavity with respect to the generation of SH was characterised by varying the pump energy incident on the crystal and measuring the corresponding energy of the SH beam emerging through ' $M_2$ ' (**Figure 5**). When the cavity is perfectly aligned, the pump photons coming through the Mirror  $M_1$  are in phase, at every instant, with the fraction of the unconverted pump that is reflected off it. This increases the effective energy input to the crystal and that, in turn, results in a correspondingly increased SH output. This fact is amply clear from **Figure 4** in conjunction with **Figure 5**. It is apparent that for a maximum input pump energy of  $\sim 6.5$  mJ, the single pass SH output is  $\sim 0.55$  mJ (**Figure 4**) while according to **Figure 5**, the same input of 6.5 mJ gets enhanced to  $\sim 9.2$  mJ due to cavity effect. The corresponding SH multi pass output is  $\sim 1.625$  mJ, almost a three-fold increase when compared to the single pass case. Considering 9.2 mJ as the input energy, the SHG efficiency can be estimated to be  $\sim 17.66\%$  - a clear  $\sim 209\%$  improvement as against the single pass case. To be noted here that the pump energy has actually been maintained at  $\sim 6.5$  mJ and therefore the conversion efficiency has risen by  $\sim 295\%$  as a matter of fact. In these experiments, both pump and SH beams suffered significant Fresnel reflection losses during their repeated back and forth passage through the crystal that was not anti-reflection coated. Further, as the pump laser output coupler  $M_1$  is only 23% reflective at 5.35  $\mu\text{m}$ , a major part of the SH generated in the reverse direction escapes through this mirror. The dramatic improvement in the SH conversion efficiency that has been obtained in the multi-pass case is thus by no means an optimised one. Increasing the reflectivity of the rear mirror at the SH wavelength in addition to employing a crystal with broadband anti reflection coating on both its entrance and exit faces should be able to fully exploit the decided advantage of a multi-pass case. We also note here that this scheme does not suffer from the conventional single pass walk off [16] between the pump and the SH beams as mirror  $M_2$  is almost transparent to the SH beam thereby providing feedback only to the pump beam. As the second

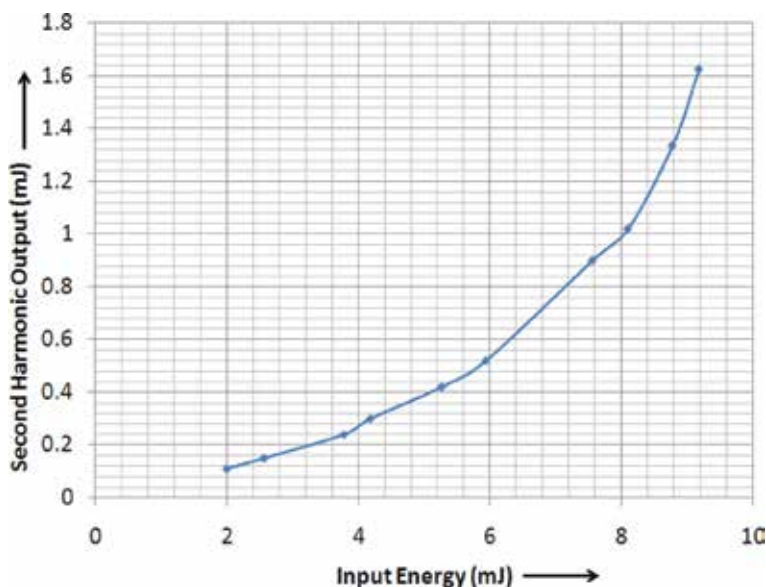


**Figure 5.** Dependence of multi-pass second harmonic output on the effective input pump energy following cavity effect.

harmonic beam generated in the forward direction alone is extracted in this configuration, its spatial quality is practically same as that of a single pass case. Therefore no special effort was expended to monitor the spatial quality of the SH beam. However, the visual observation of a clear well defined spot when the generated beam was focussed by a 10 cm focal length CaF<sub>2</sub> lens on a graphite plate bore testimony to its satisfactory spatial character.

Towards comparing the SH power conversion efficiency in the single and multi-pass cases, we monitored the temporal profiles of the pump and the corresponding SH pulses with the external cavity in aligned and misaligned conditions. In order to obtain smooth temporal profiles devoid of mode beating, we captured the power profiles in all the four cases with oscilloscope set in bandwidth limited mode and the same are displayed in the traces of **Figure 6** from where the single pass internal peak power SH conversion efficiency can be readily estimated to be ~10.48%. The power conversion efficiency is thus greater than the energy conversion efficiency (8.45%) of the SHG process. This is because the peak power always exceeds the average intra-pulse power of the pump beam and higher is the intensity at the pump wavelength, better is the SH conversion. This observation is in general concurrence with the finding of several researchers [13, 17, 18]. When the cavity is perfectly aligned, the photon flux at the entrance face of the crystal comprises of two components at any point of time; (i) the photons constituting the output of the pump laser and (ii) the photons constituting the fraction of the unconverted pump beam that is reflected off the convex surface of the output coupler of the pump laser. When the cavity is aligned, these two components fall in step and an overall rise in the power level of the input pulse is thus the end result. A comparison of the input power profile traces for aligned and misaligned conditions as recorded in **Figure 6** clearly substantiates this fact. The rise in the input power level, in turn, leads to an enhanced SH conversion yielding a peak power conversion efficiency of ~22.36%, more than twice that is possible by single-pass conversion. Actually though, since the pump laser output has remained the same for both the aligned and misaligned cases, the effective SH peak power conversion efficiency stands at 35.8%, a neat enhancement of 341% due to the cavity effect.

In the next set of experiments, we captured the temporal profiles of the pump and the corresponding cavity enhanced second harmonic pulses by setting the oscilloscope at its highest bandwidth (Tektronix MSO 3054) and the same are depicted in **Figure 7a**. That the emission of the pump laser is on multimode is evidenced by the rich modulation present in the temporal profile of the pump as well as the corresponding SH pulses. The lower trace of **Figure 7b** depicts the time expanded temporal profile of the pump pulse where an oscillation of period ~7 ns arising out of the beating of two longitudinal modes, matching with the round trip

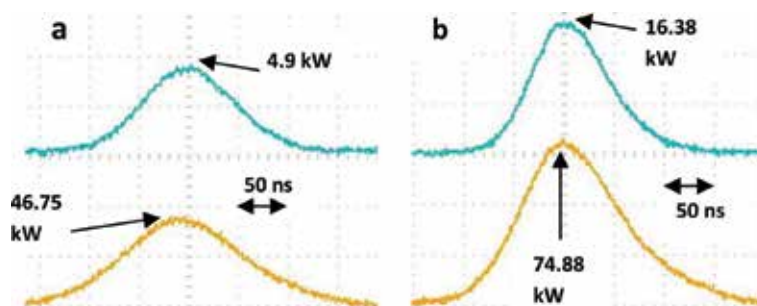


**Figure 6.** Temporal profiles of the fundamental (bottom trace) and the corresponding second harmonic (top trace) captured in bandwidth limited mode; a: Single pass conversion, b: Multi-pass conversion.

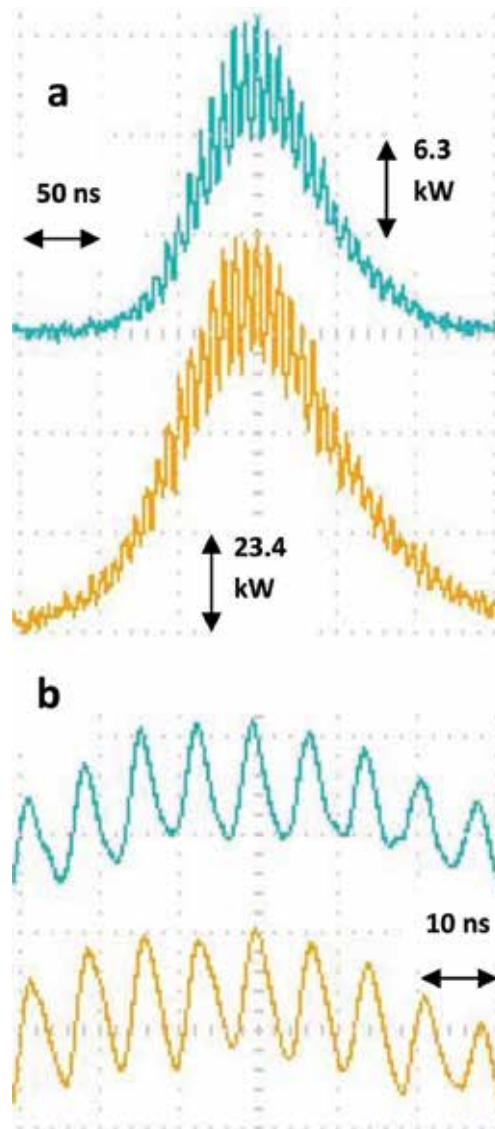


**Figure 7.** (a) Temporal profiles of the pump (lower trace) and the cavity enhanced SH (upper trace). Mode beating is reflected in the SH emission also. (b) 7 ns beat period indicates operation of the pump laser on two longitudinal modes (lower trace), the same is also reflected in the SH pulse (upper trace).

of 105 cm long cavity, is seen. Upon comparison with the typical temporal profile of the emission of the pump laser (**Figure 3**), it becomes obvious that the integration of the pump laser with this external unstable cavity does in no way bring in any new feature in its temporal profile or alter the beat period. This clearly implies that the coupling of the external cavity with the pump cavity has no effect on the dynamics of the pump laser. A comparison of the time expanded second harmonic temporal profile (upper trace of **Figure 7b**) with that of the temporal profile of the pump (lower trace of **Figure 7b**) readily establishes their phase and amplitude synchronisation: a signature of the instantaneous nature of the SHG process.

### 2.3 Conclusion

A thoughtful integration of a stable pump cavity with an unstable external Fabry-Perot cavity has resulted in remarkable enhancement in the SH conversion efficiency

even in case of pulsed operation of the laser. Although coupled external resonant enhancement has found application for the non-linear conversion process in the cw operation of the pump laser over visible region, it has not gained popularity in the mid-infrared (MIR) region owing to the possibility of damage to the MIR crystals that are not only expensive but also scarce. An unstable cavity that has the intrinsic ability to limit the intra-cavity flux there by safe-guarding the crystal from optical damage even in case of pulsed operation has been shown to offer a practical solution to this problem. We note here that the performance of this scheme can be further improved by employing a crystal with its end faces broad band AR coated, appropriate choice of the cavity parameters and control of cavity lengths. Although feasibility of this scheme has been demonstrated in the case of SHG in the MIR region, the same should, in principle, be valid for application across the near IR, visible and the UV regions of the electromagnetic spectrum as well for both cw and pulse operations.

### **3. Enhancing the SH conversion efficiency by non-uniform illumination of the non-linear medium**

As explained in the introduction to this chapter, if a non-linear crystal can in some way be subjected to alternate high and low regions of pump intensity along its conversion length the conversion efficiency can be shown to increase 100% as against the case of conventional uniform illumination maintaining the same average intensity. We provide experimental validation of this hypothesis wherein a significant enhancement in the SH conversion efficiency has been achieved by subjecting the crystal to non-uniform illumination. Such a situation could be realised by shining the crystal from both ends as against the conventional operation of illuminating it from one end. This was readily possible by placing the crystal inside a Fabry Perot cavity wherein the interference of the forward and the reverse beams creates a periodic intensity modulation along its length. The coherent input beam was derived from the emission of a high pressure CO<sub>2</sub> laser while an AgGaSe<sub>2</sub> crystal was made use of to affect its frequency doubling. Subjecting the crystal to alternate high and low intensity of coherent pump radiation requires placing it inside a high 'Q' cavity that, at the same time, should allow significant transport of the pump energy into it. As in the previous case, integration of the pump laser cavity with the external Fabry-Perot cavity allowed efficient transport of the pump beam into the crystal while at the same time maintaining high Q of the external cavity at the pump wavelength. The only work that we came across and that explicitly connects SHG with cavity interference, albeit with a totally different central theme, is of Wu and Kimble [19] wherein two fundamental beams generate one or two SH coherent beams under non-collinear phase matched condition and the focus has been to study the phase dependence of the pump and the generated waves.

#### **3.1 Experimental**

The experimental system utilised here is identical to the one used towards increasing the interaction length between the pump and the non-linear medium and the same would therefore, not be repeated here, and the reader may refer to **Figure 2** of Section 2.1 and its description therein instead. To be noted here that **Figure 2a** depicts the case of uniform illumination while **Figure 2b** represents the case of non-uniform illumination. The CO<sub>2</sub> laser was tuned to the 10P(32) line giving rise to emission at 10.72  $\mu\text{m}$  and consequently phase matching for frequency doubling was found to occur for an external angle of incidence of  $\sim 36^\circ$ . The cross-section of the pump beam on the crystal entrance face was restricted to  $\sim 5.0$  mm diameter that allowed its clear passage through the crystal. Although the crystal

was AR coated over broad range covering 5–10 micron on both input and exit faces for normal angle of incidence (AOI), the small Fresnel reflection from the entrance face of the crystal, that was inevitable at oblique AOI, was utilised to monitor both energy and temporal profile of the pump pulse. The energy and temporal profile of the SH beam were monitored after blocking the residual pump beam, that also emerged with it through the exit face of the crystal, by a sapphire plate. By virtue of its multi-atmosphere operation, the CO<sub>2</sub> laser possessed intrinsically very high gain and thus delivered a pulse of relatively short duration (FWHM ~110 nsec).

### 3.2 Results and discussion

Towards finding the efficiency of the SHG process as a function of the pump energy for the conventional case of uniform illumination (**Figure 2a**), we gradually increased the input and monitored the corresponding SH energy and the dependence is as shown in **Figure 8**. The maximum SH energy conversion efficiency can be estimated from this figure as ~8.0%.

In the next set of experiments we subjected the crystal to alternate regions of high and low intensities along its length. This was readily possible by constructing a Fabry-Perot cavity comprising of the output coupler of the pump laser ‘M<sub>1</sub>’ (R ~80%@10.72 μm, T ~20%@5.36 μm) and a plane dichroic mirror ‘M<sub>2</sub>’ (R > 90%@10.72 μm, T > 90%@5.36 μm) located at the exit end of the crystal (refer to **Figure 2b**). The pump energy incident on the crystal, as measured by Detector D<sub>1</sub>, showed a dramatic increase as ‘M<sub>2</sub>’ was fine tuned to establish its parallelism with ‘M<sub>1</sub>’, resulting, in turn, in a corresponding improvement in the measured SH output. In effect, there are now two inputs to the crystal; (a) Forward Input: the actual input on the entrance face in the forward direction that comes directly from the pump laser and (b) Reverse Input: the pump, that stays unconverted after its passage through the crystal, gets reflected off ‘M<sub>2</sub>’ and shines on the exit face of the crystal from the opposite direction. When the cavity is perfectly aligned, the interference of these two components creates alternating nodal and anti-nodal intensity regions inside the cavity and partly contributes towards the observed dramatic enhancement of SH conversion by the crystal. At every instant, the reverse

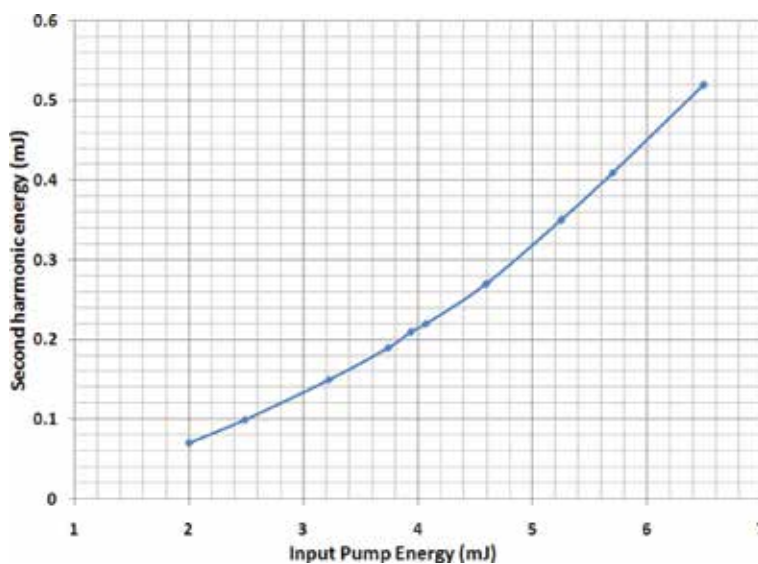


**Figure 8.** Second harmonic output as a function of the input pump energy in the conventional operation wherein the crystal is uniformly illuminated by the pump beam along its conversion length.

component, after traversing through the crystal, is reflected off  $M_1$  and falls in step with the pump photons emerging through it resulting in an effective increase in the energy incident on the entrance face of the crystal as measured by the detector  $D_1$ . At this point, towards gaining a deeper insight into this process, we gradually varied the pump (forward) input and measured both, the corresponding reverse input and the generated SH. The difference in the energy measured by  $D_1$  with  $M_1$  aligned and misaligned gives the measure of the reverse input. **Figure 9** depicts the dependence of the reverse input on the forward input to the crystal while **Figure 10** shows the SH output as a function of the total effective input to the crystal which is now the sum total of the forward and the corresponding reverse components. It is apparent from **Figure 9** that the reverse input does not exactly bear a linear relationship with the forward input and this behaviour owes its origin to the square dependence of the SH output on the intensity of the input at the fundamental wavelength as is evident from **Figure 8**. The square dependence basically means that as the pump intensity rises, increasingly higher fraction of it gets converted into SH and thus less of it is left to constitute the reverse input to the crystal. This explains the observed departure from the linear dependence of the reverse input on the forward input to the crystal.

The increase in the effective input to the crystal in case of an aligned cavity due to addition of forward and reverse components leads to the generation of higher SH output as revealed in **Figure 10**. For instance, the maximum pump input of 6.5 mJ in case of uniform illumination (**Figure 8**) gets enhanced to 10.34 mJ (**Figure 10**) in the aligned cavity condition giving rise to almost 2.54 fold increase in the SH conversion efficiency. However a closer examination of **Figure 10**, in conjunction with **Figure 8**, reveals a wealth of information, hitherto unexplored, that constitutes the central theme of this study and is captured in the traces of **Figure 11**. It is clearly evident from this figure that SH output in case of non-uniform illumination of the crystal is significantly higher compared to the case of its uniform illumination even when the total input to the crystal is maintained the same. Let us consider a typical input of 4.1 mJ that in case of uniform illumination generates 0.22 mJ (refer to **Figure 8**) of SH at a conversion efficiency of  $\sim 5.36\%$ . It can be readily estimated from **Figure 9** that this input of 4.1 mJ in case of non-uniform illumination comprises of a forward component of 2.5 mJ and a reverse component of 1.6 mJ. Thus,

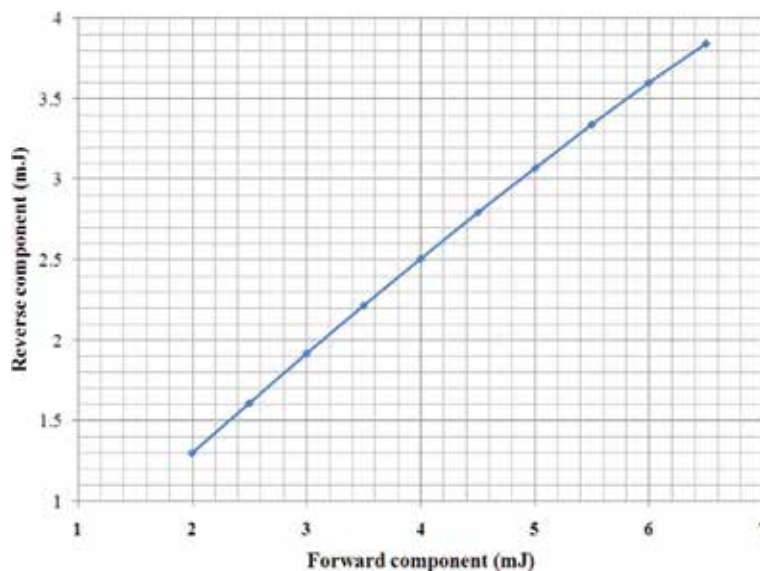


**Figure 9.**  
*Dependence of the reverse input to the crystal as a function of the forward component.*

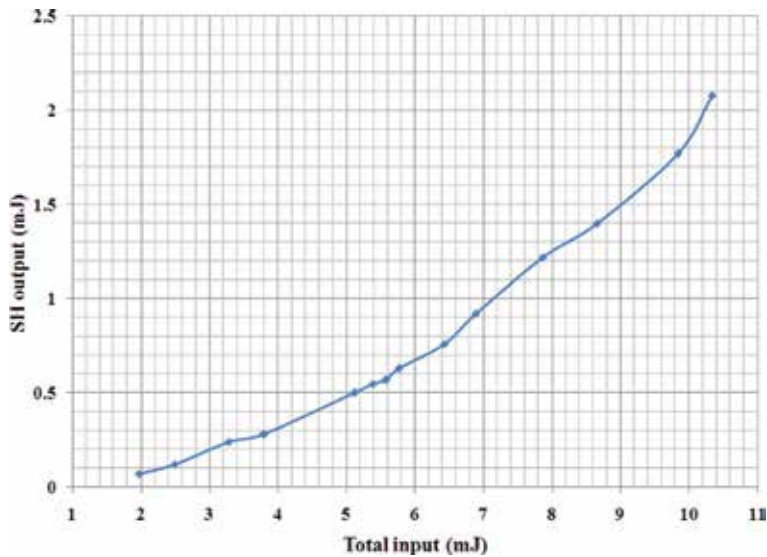


**Figure 10.** Dependence of second harmonic output on the effective input pump energy in case of non-uniform illumination.

when the same total input of 4.1 mJ is made to shine on the crystal as two separate beams of 2.5 and 1.6 mJ from opposite directions by taking advantage of a cavity, a SH output of 0.325 mJ (refer to **Figure 10**) is generated at an efficiency of 7.93%; a clear advantage of ~48% in the SH conversion efficiency by going for non-uniform illumination. As discussed before this is attributed to the alternate high and low intensity regions seen by the crystal as a result of the interference of the forward and reverse beams travelling through the crystal in the latter case.

In order to estimate the expected advantage of the situation when the crystal is non-uniformly illuminated over the case of uniform illumination, we used the

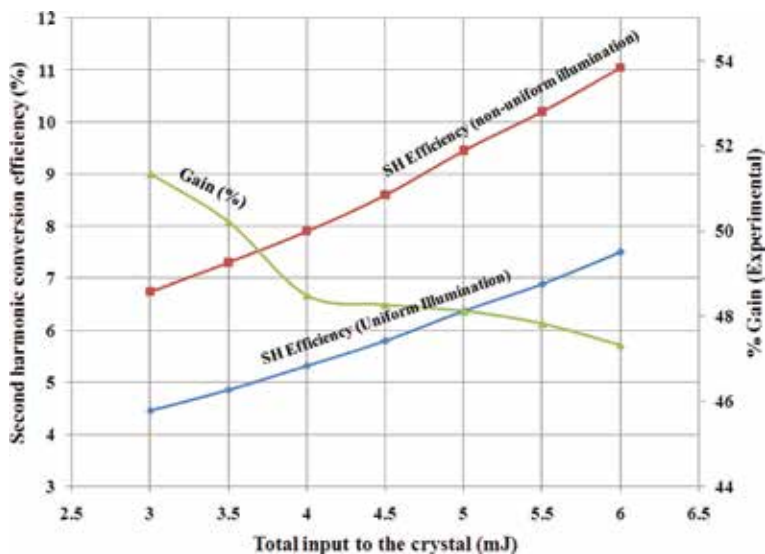


**Figure 11.** Experimental SH conversion efficiency as a function of the total input to the crystal is shown for both uniform and non-uniform illumination cases. The % gain of SH conversion in case of non-uniform illumination over the uniform illumination case, defined as  $[(SH_{NUI-EFF} - SH_{UI-EFF}) / SH_{UI-EFF}] \times 100$ , is also shown here as a function of the overall input to the crystal.

Uniform illumination		Non-uniform illumination				Overall Estimated Gain (%) <sup>*</sup>	
Input (E <sub>UI</sub> ) (mJ)	Estimated SH SH <sub>UI-EST</sub> α E <sub>UI</sub> <sup>2</sup>	Forward input (E <sub>F</sub> ) (mJ)	Reverse input (E <sub>R</sub> ) (mJ)	Total input (E <sub>NUI</sub> = E <sub>F</sub> + E <sub>R</sub> ) (mJ)	Standing Wave Intensities Anti-node (E <sub>AN</sub> = E <sub>F</sub> + E <sub>R</sub> + 2√(E <sub>F</sub> × E <sub>R</sub> )) Node (E <sub>N</sub> = E <sub>F</sub> + E <sub>R</sub> - 2√(E <sub>F</sub> × E <sub>R</sub> ))		Estimated SH SH <sub>NUI-EST</sub> α [E <sub>AN</sub> <sup>2</sup> + E <sub>N</sub> <sup>2</sup> ]/2
3.33	11.09	2.0	1.33	3.33	6.59	21.72	95.85
4.14	17.11	2.5	1.64	4.14	8.18	33.46	95.6
4.61	21.25	2.8	1.81	4.61	9.11	41.50	95.29
4.94	24.40	3.0	1.94	4.94	9.76	47.64	95.23
5.9	34.81	3.6	2.3	5.9	11.65	67.87	94.97
6.53	42.64	4.0	2.53	6.53	12.89	83.09	94.86

<sup>\*</sup> Estimated overall gain (%) = [(SH<sub>NUI-EST</sub> - SH<sub>UI-EST</sub>) / SH<sub>UI-EST</sub>] × 100.

To be noted that the total input to the crystal in the two cases viz., uniform and non-uniform illumination has been always maintained same.

**Table 1.**

Estimation of the % gain obtainable in case of non-uniform illumination over the uniform illumination through reconstruction of the standing wave parameters from the experimental data recorded in Figures 2, 3 and 4.

data available from **Figures 8** and **10** in conjunction with the dependence of reverse input on forward input (**Figure 9**) for the reconstruction of the standing wave parameters. This is recorded in the **Table 1** above. It would be seen from this table that the advantage expected for the non-uniform illumination shows a definite reduction, although very marginal, with increasing input intensity. This reduction is because, with increasing intensity,  $E_R/E_F$  gradually reduces as is evident from **Figure 9** and discussed earlier. The experimentally measured advantage also recorded in **Figure 11** as a function of input intensity shows the same trend. The experimentally measured advantage of the non-uniform illumination, however, is seen to be considerably lower than the estimated value. This is due to the fact that a major fraction of the SH generated in the reverse direction escapes through the output coupler 'M<sub>1</sub>' of the pump laser. Usage of a coupler that offers high reflectivity at both fundamental and generated wavelengths will help square the full advantage of the non-uniform illumination case.

To be noted here that the enhancement in the second harmonic conversion efficiency achieved by way of placing the non-linear medium inside a cavity, basically comprises of two components arising out of: (i) increased effective length of interaction between the pump and the non-linear medium and, (ii) non-uniform illumination of the non-linear medium. The above study helps decouple these two components. In the above example where the input was maintained at 4.1 mJ for both uniform illumination (meaning  $E_F = 4.1$  mJ and  $E_R = 0$ ) and non-uniform illumination (meaning  $E_F = 2.5$  mJ and  $E_R = 1.6$  mJ), the added advantage arising out of increased interaction length has been annulled. Thus the enhancement in the SH conversion efficiency (viz., ~70%) is entirely attributable to the modulation of intensity arising out of interference of forward and reverse beams. In case of a non-uniform illumination with  $E_F = 4.1$  mJ, the corresponding  $E_R = 2.6$  mJ as evident from **Figure 9**. The SH output now is 0.85 mJ as against 0.22 mJ for uniform illumination and the advantage gained here comprises of both the above components. From the discussion above it is amply clear that the component of gain due to increase in interaction length between the pump beam and the non-linear medium is ~126%. The modest gain obtained due to non-uniform illumination of the active medium is attributable to the inequality of the forward and the reverse components in the present study.

#### 4. Conclusion

In conclusion, we conceived the advantage in SH generation by a nonlinear crystal when it is illuminated with alternate high and low regions of intensity along its length as against the conventional case of its uniform illumination with the same average intensity. Exploitation of interference effect by placing the crystal inside a Fabry Perot cavity has allowed the imposition of such a non-uniform illumination condition on to the crystal along its conversion length. The decided advantage of the non-uniform illumination over uniform illumination has been experimentally established under conditions of equal intensity exposure in the two cases. We believe that this advantage was always present in intra-cavity or resonantly enhanced frequency doubling generation processes but stayed unrecognised as the motivation of these works was to enhance the conversion efficiency by increasing the effective interaction length of the crystal and the advantage gained was thus automatically attributed in totality to this. Carefully planned experiment here has allowed us to decouple the advantage due to interference (as seen in **Figure 11**) from the total advantage as recorded in the data of **Figure 10** that also included the gain due to increased interaction length. While we have achieved the spatial variation of intensity by the exploitation of interference effect, we do not rule out the

possibility of achieving the same effect by some other means, e.g., a train of ps or fs mode locked pulses will manifest as spatial intensity variations in the sub mm to sub-micron scale appropriate to derive this advantage in a crystal of finite length. Advantage can be derived from even chaotic pulse trains wherein the temporal oscillations occur in the similar time scales as above. However, it is to be noted that the restriction on the maximum period of the spatial variation of the intensity is imposed by the crystal thickness while there is no restriction on the minimum period. As a matter of fact smaller is the periodicity of bright and dark intensity regions, better will be the heat diffusion and thus will be preferred from the point of view of handling higher intensity.

## Author details

Padma Nilaya J. and Dhruba J. Biswas\*  
Laser and Plasma Technology Division, Bhabha Atomic Research Centre, Mumbai,  
India

\*Address all correspondence to: [dhruba8biswas@gmail.com](mailto:dhruba8biswas@gmail.com)

## IntechOpen

---

© 2018 The Author(s). Licensee IntechOpen. This chapter is distributed under the terms of the Creative Commons Attribution License (<http://creativecommons.org/licenses/by/3.0>), which permits unrestricted use, distribution, and reproduction in any medium, provided the original work is properly cited. 

## References

- [1] Chen C, Lu J, Togashi T, Suganuma T, Sekikawa T, Watanabe S, et al. Second-harmonic generation from a  $\text{KBe}_2\text{BO}_3\text{F}_2$  crystal in the deep ultraviolet. *Optics Letters*. 2002;**27**:637
- [2] Herskind P, Lindballe J, Clausen C, Sorensen JL, Drewsen M. Second-harmonic generation of light at 544 and 272 nm from an ytterbium-doped distributed-feedback fiber laser. *Optics Letters*. 2007;**32**:268
- [3] Samanta GK, Kumar SC, Mathew M, Canalias C, Pasiskevicius V, Laurell F, et al. High-power, continuous-wave, second-harmonic generation at 532 nm in periodically poled  $\text{KTiOPO}_4$ . *Optics Letters*. 2008;**33**:2955
- [4] Zondy J, Bielsa F, Douillet A, Hilico L, Acef O, Petrov V, et al. Frequency doubling of  $\text{CO}_2$  laser radiation at 10.6  $\mu\text{m}$  in the highly nonlinear chalcopyrite  $\text{LiGaTe}_2$ . *Optics Letters*. 2007;**32**:1722
- [5] Samanta GK, Kumar SC, Devi K, Ebrahim-Zadeh M. Multicrystal, continuous-wave, single-pass second-harmonic generation with 56% efficiency. *Optics Letters*. 2010;**35**:3513
- [6] Kumar SC, Samanta GK, Devi K, Ebrahim-Zadeh M. High-efficiency, multicrystal, single-pass, continuous-wave second harmonic generation. *Optics Express*. 2011;**19**:11152
- [7] Li DJ, Guo J, Lang GL, Meng FJ, Zhang LM, Xie JJ, et al. High power 4.65  $\mu\text{m}$  single-wavelength laser by second-harmonic generation of pulsed TEA  $\text{CO}_2$  laser in  $\text{AgGaSe}_2$  and  $\text{ZnGeP}_2$ . *Laser Physics*. 2012;**22**:725
- [8] Harimoto T, Yo B, Uchida K. A novel multipass scheme for enhancement of second harmonic generation. *Optics Express*. 2011;**19**:22692
- [9] Chatterjee U, Gangopadhyay S, Ghosh C, Bhar GC. Large enhancement in second-harmonic generation by optical feedback. *Applied Physics Letters*. 2006;**88**:171102; Indian Patent No: 221735 granted on 03-07-2008
- [10] McDonagh L, Wallenstein R. Low-noise 62 W CW intracavity-doubled  $\text{TEM}_{00}$  Nd:  $\text{YVO}_4$  green laser pumped at 888 nm. *Optics Letters*. 2007;**32**:802
- [11] Jensen OB, Petersen PM. Generation of single-frequency tunable green light in a coupled ring tapered diode laser cavity. *Optics Express*. 2013;**21**:6076
- [12] Petukhov VO, Gorobets VA, Kozlov KV, Ya Tochitsky S. Intracavity second harmonic generation of a cw  $\text{CO}_2$  laser in  $\text{AgGaSe}_2$ . In: *Lasers and Electro-Optics Europe, 2000. Conference Digest. Nice: IEEE. Date of Conference: 10-15 Sept. 2000. ISBN: 0-7803-6319-1 INSPEC Accession Number: 6970334. DOI: 10.1109/CLEOE.2000.910221*
- [13] Petukhov VO, Gorobets VA, Tochitsky SY, Kozlov KV. Efficient intracavity frequency doubling of  $\text{CO}_2$  laser in nonlinear crystals. *Proceedings of SPIE*. 2001;**4351**:171-175
- [14] Franken PA, Hill AE, Peters CW, Vfeinreich G. Generation of optical harmonics. *Physical Review Letters*. 1961;**7**:118
- [15] Nilaya JP, Biswas DJ. Exploitation of an external unstable multi-pass cavity to enhance the second harmonic conversion efficiency. *Optics Communication*. 2015;**341**:155
- [16] New G. Introduction to Non-linear Optics. New York, Chapter 3: Cambridge University Press. p. 55
- [17] Eckardt RC, Fan YX, Byer RL, Route RK, Feigelson RS, van der Laan J. Efficient second harmonic generation

of 10 $\mu$ m radiation in AgGaSe<sub>2</sub>. *Applied Physics Letters*. 1985;47:786

[18] Russel DA, Ebert R. Efficient generation and heterodyne detection of 4.75- $\mu$ m light with second-harmonic generation. *Applied Optics*. 1993;32:6638

[19] Wu L, Kimble HJ. Interference effects in second harmonic generation within an optical cavity. *Journal of the Optical Society of America B: Optical Physics*. 1985;2:697



---

Section 4

Nonlinear Optical  
Processes in Micro- and  
Nanostructures

---



# Widely Tunable Quantum-Well Laser: OPO Diode Around 2 $\mu\text{m}$ Based on a Coupled Waveguide Heterostructure

*Alice Bernard, Jean-Michel Gérard,  
Ivan Favero and Giuseppe Leo*

## Abstract

We present the design of a widely tunable monolithic source on GaAs/AlGaAs. It consists of a quantum-well distributed feedback (DFB) laser vertically coupled with a waveguide engineered for nonlinear frequency conversion. No regrowth or alignment is necessary, and all the structure stems from a single epitaxy step. Light is emitted by the 0.98  $\mu\text{m}$  DFB laser and transmitted to the underlying waveguide by an adiabatic taper, where it can undergo parametric down-conversion, providing signal and idler beams around 2  $\mu\text{m}$ . Transfer rates and tolerances for transfer and conversion efficiency are calculated to be compatible with the tolerances of current fabrication processes. We estimate that an OPO threshold can be reached in the underlying waveguide for a laser emitted power of 20–100 mW, if high-reflectivity distributed Bragg reflectors (DBRs) are used.

**Keywords:** quantum well, laser diode, near infrared, AlGaAs, tunable source, optical parametric oscillator (OPO), active-passive integration, adiabatic coupling, vertical coupling

## 1. Introduction

Five decades after the first demonstrations of a laser diode [1, 2], current integrated laser sources include diodes, quantum cascade lasers, and interband cascade lasers. These sources span a wide range from the visible spectrum to the far infrared. However, they present to this day a limited tunability, up to a few tens of nm at the most excluding external cavity setups. This is a limitation in particular in the field of spectroscopy, in demand of coherent and widely tunable sources. In parallel to the development of integrated lasers, optical parametric oscillators (OPOs) have undergone a wide progress, spanning the electromagnetic spectrum from ultraviolet to infrared and providing largely tunable outputs, but they are not yet widely adopted on integrated platforms. This is mostly due to the difficulty of adjusting the phase mismatch in situ and historically to the lack of nonlinear materials in semiconductor platforms. However, GaAs/AlGaAs provides high nonlinear conversion efficiencies, and fabrication efforts have resulted in a diminution of losses in this material system [3, 4]. Optically, pumped OPOs have been demonstrated

in micrometric GaAs/AlGaAs waveguides through orientation patterning [5] and artificial birefringence [6].

In addition to providing high nonlinear conversion efficiencies, AlGaAs are also a mature platform for laser diodes. As a consequence, a few proposals of all-in-one laser diode/OPO have been made [7, 8], without experimental demonstration to this day. In these proposals, the laser and OPO cavity are one and the same. This configuration reduces fabrication complexity and allows one to harness high intracavity fields. However, the best design parameters for efficient laser behavior tend to degrade nonlinear light conversion and vice versa. More precisely, the main bottleneck in this case is related to the dopant-induced FCA propagation losses. Indeed, in order to achieve an efficient electric injection in the laser, the dopant concentration should be high in the cladding layers. But this introduces FCA losses for the signal and idler beams, hence reducing the conversion efficiency and generated power. As a result, dopant-induced losses are an obstacle to reach the OPO threshold. Another limitation of this configuration is the adjustment of phase mismatch, as the only available in situ tool is temperature, which may degrade laser efficiency if high temperatures are needed.

The main alternative to this approach is heterogeneous integration, a cumbersome and time-intensive method. We propose here an original approach where laser and OPO cavities are distinct but grown on the same wafer. No subsequent alignment or epitaxy regrowth is necessary. This device is based on vertical coupling: laser and OPO cavities are grown on vertically separated layers and coupled so that light can pass from one to the other. Vertical couplers have been widely described for the integration of lasers or detectors on an underlying chip [9]. At the upper level, a material of smaller gap is used for light generation or detection, while the lower levels comprise a material of higher gap for light transmission and analysis. This scheme is also used for the integration of III-V laser on silicon chips [10]. Both systems are analogous to our proposal: a laser is coupled to another waveguide, which provides a secondary function (light modulation, transmission, or in our case conversion). Here, however, design is not straightforward since the fundamental laser mode needs to be coupled to a higher order mode in the underlying waveguide. The use of this higher order mode enables modal phase matching in the buried waveguide, which is optimized for parametric conversion.

We base our design on the growth sheet of a 0.98- $\mu\text{m}$  AlGaAs laser and engineer the OPO cavity to provide down-conversion toward a signal/idler range between 1.8 and 2.2  $\mu\text{m}$ . We rely on modal phase matching between a TE-polarized higher order mode at the pump wavelength and fundamental cross polarized modes at signal/idler wavelengths. As a consequence, the fundamental mode in the laser cavity is transferred to a higher order mode in the OPO cavity. In situ adjustment of the phase mismatch can be achieved through modifications of laser wavelength and temperature of the OPO cavity.

## **2. General description of the device**

In order to provide the best fabrication tolerance, we base our design on an adiabatic taper (instead of, e.g., a resonant coupler that would provide a shorter transfer length). Before detailing the device, we single out here some points critical to its operation. These aspects dictate design choices for the rest of the device.

The first “hard point” is spectral stability. To achieve a lower OPO threshold, we choose a doubly resonant OPO (DR-OPO) configuration. Concerning the laser, to avoid mode competition and instability, the pump should not return into the laser cavity after having explored the OPO region. This requires DBR with

high reflectivities at signal/idler wavelengths and low reflectivities at the pump wavelength, as present, for example, in [6]. Furthermore, stability of the device is improved by in situ control of the phase mismatch, through shift of the pump wavelength or of the OPO cavity temperature. These two factors can be tuned independently if the laser and OPO temperatures are set separately. This is possible if the two areas are separated by at least 100  $\mu\text{m}$  and are controlled by individual heaters.

Thermal behavior and contact geometry are also expected to be critical. III/V on Si laser typically emits powers in the 10 mW range [11], while the pump power for OPO threshold is a few tens of mW in our case. The laser should be single mode for stable OPO operation, which imposes a maximal ridge width and thus a minimum optical power density. Furthermore, high-power single-mode lasers are usually shallowly etched (for single-mode operation) and mounted epi-down to limit thermal resistance [12]. In our case, these two aspects cannot be implemented at the same time. Indeed, if the laser is grown on top, the insulating section between laser and doped substrate makes it necessary to use lateral contacts, which requires deep lateral etching and compromises laterally monomode operation. On the opposite, if the laser is grown under the nonlinear (NL) waveguide, shallow etches are possible but epi-down mounting is impossible.

We also carefully examine fabrication tolerances in the region of parametric conversion and assess their impact on conversion efficiency.

## 2.1 Choice of geometry

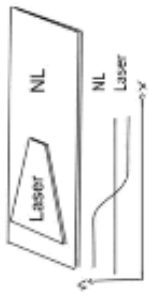
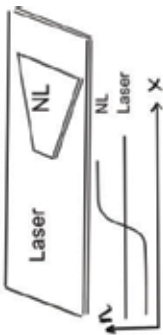
To reduce fabrication complexity, we limit ourselves to a single level of etching. This implies that the bottom waveguide geometry is invariant in the direction of propagation and that the top waveguide is narrowed. Keeping in mind the points presented in the previous section, we summarize the advantages of different geometries in **Table 1**. The waveguide where parametric light conversion takes place is called “NL waveguide” (for nonlinear).

We explore the range of possibilities opened by the GaAs/AlAs/InAs system, and we base the design of the laser part on already-existing, high-performance AlGaAs lasers at 1  $\mu\text{m}$  [13]. The detail of layer's thickness and composition is not shown here for confidentiality reasons. In this structure, the fundamental mode at 0.98  $\mu\text{m}$  has an effective index of about 3.36. Regarding the waveguide where parametric conversion is to take place, modal phase matching is more readily achieved if the pump mode is of order 2 in the vertical direction. Additionally, high conversion efficiency is favored by high cladding/core index contrasts. This, coupled with the fact that we have to work with a higher order mode, sets the maximum value of effective index in the waveguide at approximately 3.2. We therefore choose the “laser on top” geometry for its compatibility with effective indices in our project.

This choice has two important consequences. To keep the underlying waveguide undoped, contact for the bottom part of the laser must be taken laterally instead of under the substrate. This implies that the gain region should be deeply etched to clear access to the contacts. This is obviously at odds with a single-mode laser operation, since the important index contrast between air and semiconductor (in the absence of a regrowth step) will cause the laser to oscillate on several transverse modes, unless it is extremely narrow, which is not desirable given the target optical power. As a solution, we propose to etch deeply only one side of the ridge. Single-mode operation can then be achieved with a contact on one side.

## 2.2 Proposed design

Given the constraints presented earlier, we propose a general design. A general view of the structure is shown in **Figure 1**. On the left, we choose a DFB cavity for the

	Laser on top	NL waveguide on top
		
Contacts	Lateral contacts necessary Single-mode operation of the laser is hindered	Lateral contacts not necessary
Thermal control	Epi-up and epi-down possible	Epi-down impossible
Laser multimodality	The laser must start in single-mode operation in a zone in shallow etching; then, it should taper down in the transfer zone (longer total length)	The laser is buried, and single-mode emission is easily achieved
Effective indices	Transition from a high index in the laser to a low index in the NL guide	The laser index should be lower than the indices in the NL waveguide, which are already low (~3.2)

**Table 1.** Advantages and drawbacks of different coupling geometries.

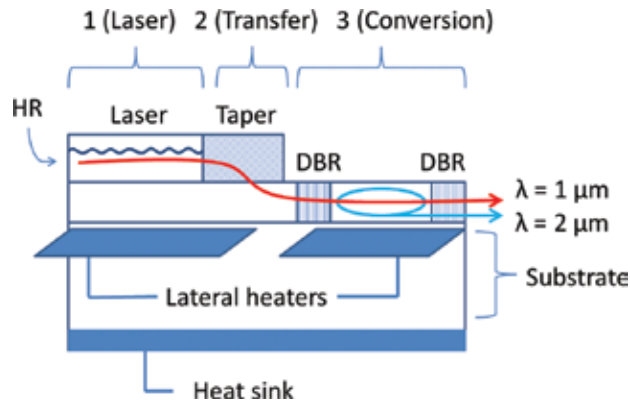


**Figure 1.**  
 General view of the proposed coupled-cavity design.

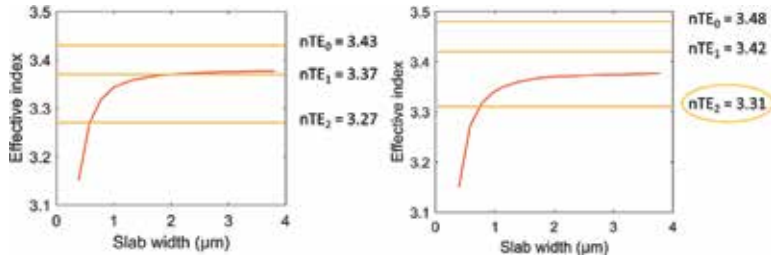
laser in order to provide longitudinal as well as transversal single-mode operation. The upper waveguide narrows in the transfer region, where the mode moves to the bottom waveguide. On the right, parametric conversion takes place in the bottom waveguide, where distributed Bragg reflectors (DBRs) provide a high reflectivity at the signal and idler wavelengths. We will describe the device step-by-step, starting from the end because the zone of parametric conversion is the most sensitive to geometry variations.

### 2.3 Choice of material

To reach phase matching and a high conversion efficiency, we simulated various waveguide geometries before settling on high index contrasts and a pump of order 2 in the direction of growth. To maximize index contrast in the vertical direction, the waveguide is surrounded by  $\text{Al}_{0.8}\text{Ga}_{0.2}\text{As}$  in the bottom cladding and by air above. However, in the region of transfer, the top cladding will be provided by whatever material separates laser and underlying waveguide core. We set this material to be  $\text{Al}_{0.3}\text{Ga}_{0.7}\text{As}$ , since it is already used as cladding in GaAs lasers. This layer structure is summarized in **Table 2**. It is identical to a standard laser data sheet, apart from the modified separation layer and added nonlinear waveguide and cladding. In the region of frequency conversion, all layers are etched, except for the last three: nonlinear waveguide, bottom cladding, and substrate.

Layer type	Material
Top cladding	AlGaAs
Optical confinement (laser core)	InGaAsP
Quantum well	InGaAs
Optical confinement (laser core)	InGaAsP
Separation layer	$\text{Al}_{0.3}\text{Ga}_{0.7}\text{As}$
Nonlinear waveguide	GaAs
Bottom cladding	$\text{Al}_{0.8}\text{Ga}_{0.2}\text{As}$
Substrate	GaAs

**Table 2.**  
 Layer structure proposed for the coupled-cavity design. In the region of conversion, all layers are etched except the last three.


**Figure 2.**

Effective indices of guided modes in the structure. (Red) Index of the laser mode as a function of guide width. (Orange) Indices of guided modes in the buried waveguide, assuming a planar waveguide of  $Al_{0.1}Ga_{0.9}As$  (left) or  $GaAs$  (right) surrounded by  $Al_{0.3}Ga_{0.7}As$  on one side and  $Al_{0.8}Ga_{0.2}As$  on the other.

The waveguide core should hold as little aluminum as possible in order to increase its nonlinear susceptibility. We set the exact Al fraction by comparing the effective index of guided modes in the upper waveguide to the effective index of the lower waveguide as taper width is reduced (**Figure 2**). For 10% Al composition, the laser mode index crosses the index of  $TE_1$  in the buried waveguide. We can thus expect the mode to couple to  $TE_1$ . Using pure  $GaAs$ , the laser mode crosses only the  $TE_2$  index, which is the desired configuration. Absorption in  $GaAs$  at 1 μm is expected to be negligible [14]. Setting a pure  $GaAs$  waveguide has another advantage: it eliminates the uncertainty on the Al fraction.

### 3. Nonlinear characteristics

#### 3.1 Conversion efficiency and OPO threshold

We calculate conversion efficiencies with a code developed in the team, based on the work presented in [15]. **Table 3** shows the nonlinear conversion efficiency at several ridge widths for a waveguide of thickness 0.95 μm surrounded by  $Al_{0.8}Ga_{0.2}As$  and air. The corresponding pump powers necessary for an OPO threshold are presented in **Figure 3**. Propagation losses are assumed to be  $0.1 \text{ cm}^{-1}$ . The threshold pump power lies in the 10–100 mW range.

#### 3.2 Tolerances

**Figure 4** shows the SPDC normalized efficiency as a function of ridge width and thickness. The FWHM of efficiency is 200 nm for a variation in width, a value compatible with the current state of fabrication technology. The FWHM for a variation in thickness is much smaller, around 3 nm. The typical precision of thickness achieved by molecular beam epitaxy is approximately 2%, corresponding to a variation of 2 nm in a 0.95 μm waveguide. Depending on growth systems, this value can be further increased by inhomogeneities along the wafer.

Ridge width (μm)	Conversion efficiency ( $\text{W}^{-1} \text{ cm}^{-2}$ )
2	600
3	380
4	230

**Table 3.**

SPDC efficiency vs. ridge width in a 0.95-μm-thick waveguide surrounded by  $Al_{0.8}Ga_{0.2}As$  and air.

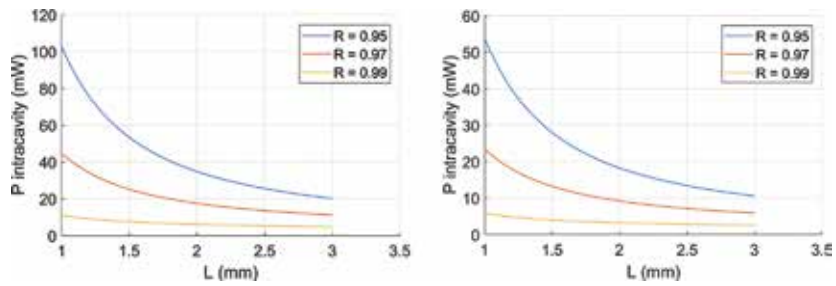


**Figure 3.** OPO pump power threshold for a ridge width of  $4 \mu\text{m}$  (left) and  $2 \mu\text{m}$  (right) as a function of length and signal/idler reflectivity. Guide thickness is  $0.95 \mu\text{m}$ .

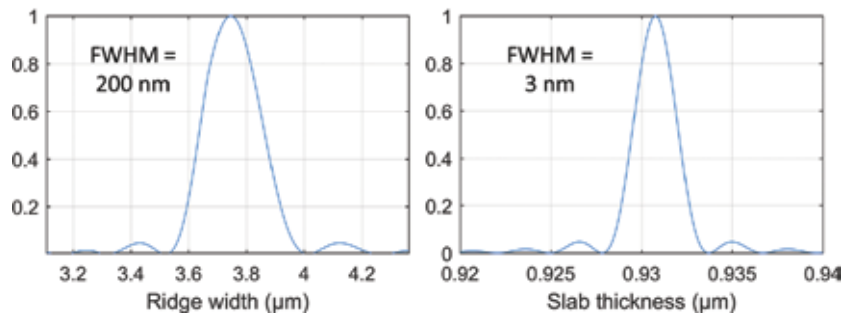


**Figure 4.** Normalized SPDC efficiency as a function of ridge width and thickness.

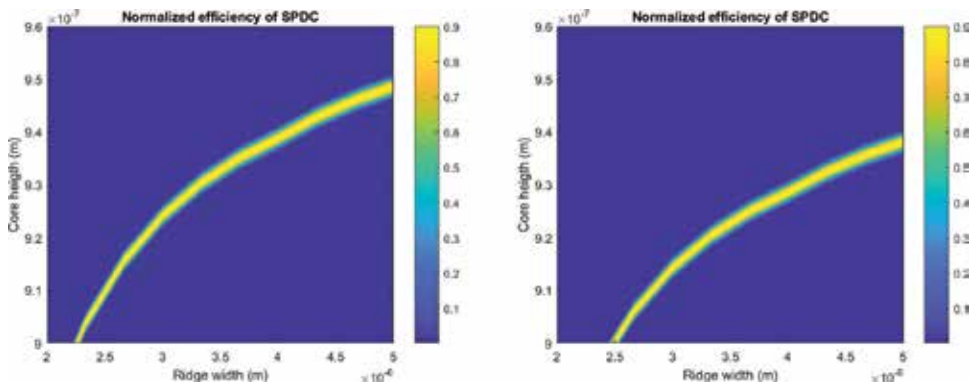


**Figure 5.** Normalized SPDC efficiency as a function of ridge width and thickness, for a waveguide temperature of  $20^\circ\text{C}$  (left) and  $50^\circ\text{C}$  (left). Pump wavelength is  $1 \mu\text{m}$  in both cases.

Fortunately, two tools allow us to shift the efficiency curve: temperature and pump wavelength. **Figure 5** shows the normalized SPDC efficiency as a function of ridge width and thickness, for waveguide temperatures of  $20$  and  $50^\circ\text{C}$ . A temperature shift of  $30^\circ\text{C}$  can compensate for a  $10\text{-nm}$  variation of the waveguide core thickness. We stress here that the temperatures of laser and parametric conversion regions can be set separately and that an increase of  $30^\circ\text{C}$  in the SPDC area has a negligible impact on the laser temperature, assuming that the two regions are separated by  $300 \mu\text{m}$  (a typical distance for adiabatic transfer).

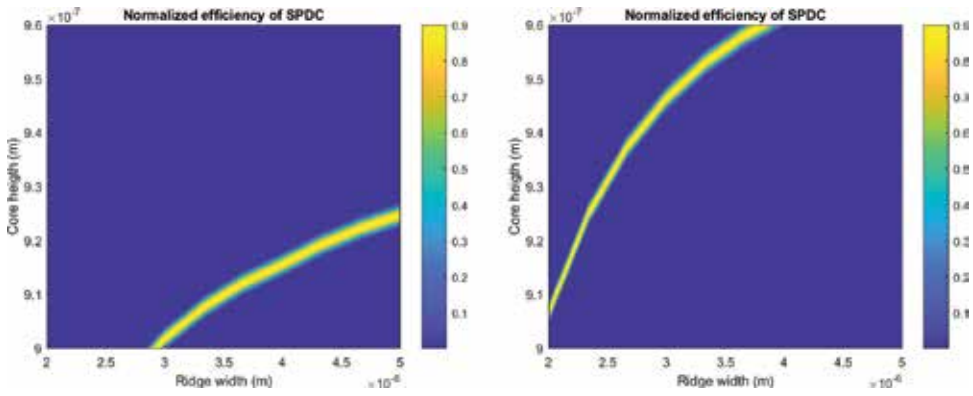


**Figure 6.** Normalized SPDC efficiency as a function of ridge width and thickness, for pump wavelengths of 990 nm (left) and 1010 nm (right). Temperature is 20°C in both cases.

**Figure 6** presents the normalized spontaneous down-conversion (SPDC) efficiency as a function of ridge width and thickness, at pump wavelengths of 990 and 1010 nm. A wavelength shift of  $\pm 10$  nm can compensate for a variation of 40 nm of the waveguide core thickness. This variation is typically accessible to a single-mode DFB laser.

As a conclusion, while efficient parametric down-conversion is only encountered in a narrow window of parameters, it can realistically be achieved by compensating variations in fabrication with a shift in temperature and pump wavelength.

### 3.3 DBR design

The DBRs should provide a reflectivity above 95% at both signal and idler wavelengths (see **Figure 3**) and nearly null reflectivity at pump wavelength. As mentioned earlier, this has already been demonstrated with dielectric stacks deposited on the waveguide facets [6]. While the outer mirror can be fabricated in this fashion, the inner one needs to be etched at an interface. Let us estimate now the DBR coupling constants in the approximation of weak perturbations. For a DBR length of 100  $\mu\text{m}$ , the coupling constant should be 220  $\text{cm}^{-1}$  in order to achieve 95% reflectivity. **Table 4** presents the coupling constants of the fundamental TE and TM modes at 2  $\mu\text{m}$  for a grating depth of 200 nm. The grating is supposed to be perfectly rectangular, with a filling factor of one-half. Whether the grating is formed by etching the top interface (air/GaAs) or by etching the underlying cladding and restarting epitaxy (GaAs/ $\text{Al}_{0.8}\text{Ga}_{0.2}\text{As}$  interface), an etch depth of at least 200 nm is necessary to achieve reflectivity over 95% with a DBR smaller than 100  $\mu\text{m}$ .

Grating depth (nm)	Grating at the top interface (air/GaAs)		Grating at the lower interface (GaAs/ $\text{Al}_{0.8}\text{Ga}_{0.2}\text{As}$ )	
	$\kappa_{\text{TE}}$ ( $\text{cm}^{-1}$ )	$\kappa_{\text{TM}}$ ( $\text{cm}^{-1}$ )	$\kappa_{\text{TE}}$ ( $\text{cm}^{-1}$ )	$\kappa_{\text{TM}}$ ( $\text{cm}^{-1}$ )
200	214.5	242.5	277	180.9

**Table 4.** Coupling constants for fundamental TE and TM modes at 2  $\mu\text{m}$ , given a rectangular grating of depth 200 nm and duty cycle 50%.

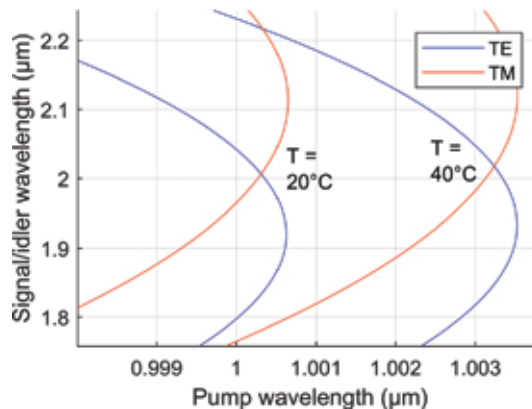


**Figure 7.**  
*Tunability curves of the waveguide supporting frequency conversion.*

### 3.4 Tunability

We show in **Figure 7** the tunability curves of the waveguide at temperatures 20 and 40°C. Outside of degeneracy, a signal/idler wavelength range of 300 nm is accessible for a pump wavelength variation of a few nm.

## 4. Waveguide coupling

### 4.1 2D approximation for the effective index

A transverse view of the structure is shown in **Figure 8**. The two waveguides are separated by 300 nm of  $\text{Al}_{0.3}\text{Ga}_{0.7}\text{As}$ . **Figure 9** presents a simulation of light propagation along the structure by a beam propagation method (BPM), which has been carried out with the commercial software RSoft. To reduce calculation time and quickly converge on an intuitive model, we first make a 2D effective-index approximation, whose validity will be checked in the next section. The injected mode, visible on the right-end side of **Figure 9a**, is the eigenmode presenting the highest overlap with the active region. As is visible from **Figure 9b**, 90% of the guided power is contained in the laser core layer at  $Z = 0$ , that is, before the taper. Thus, modal gain is expected to not suffer from the presence of the underlying GaAs layer. From  $Z = 0$  to  $Z = 300 \mu\text{m}$ , the two top layer widths are reduced from 4  $\mu\text{m}$  to 0. From  $Z = 300 \mu\text{m}$  to  $Z = 500 \mu\text{m}$ , the separation layer ( $\text{Al}_{0.3}\text{Ga}_{0.7}\text{As}$ ) width is reduced in the same way. Over 95% of the power is transferred to the GaAs waveguide. To estimate the robustness of the design to a limited resolution in lithography, we simulate the same transfer with widths ending at 0.4  $\mu\text{m}$  instead of 0: the transfer of power to the underlying waveguide is 85%. While a more detailed set of tests would be necessary to account for fabrication-induced deviations, these results are encouraging.

In order to find out if the power in the slab is in the desired  $\text{TE}_2$  mode, we calculate the overlap of the BPM-simulated field with the GaAs waveguide eigenmodes. The result, reported in **Figure 10**, is that 97% of the power is in the  $\text{TE}_2$  mode after one transfer length.

### 4.2 3D simulations

In the 2D-effective index approximation made in the previous section, we assumed single-mode behavior in the lateral direction. The geometry chosen in 3D

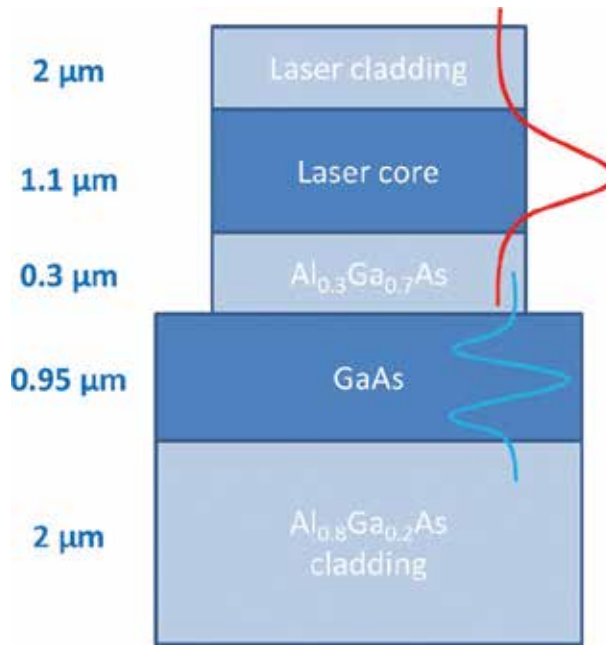


**Figure 8.** Transverse view of the structure. The fundamental mode of the top waveguide is shown in blue. Second-order mode of the lower waveguide is shown in red. The three top layers (laser cladding, laser core, and  $\text{Al}_{0.3}\text{Ga}_{0.7}\text{As}$  separation) have widths varying from 4 to 0  $\mu\text{m}$ . The GaAs waveguide and inferior cladding have infinite width.

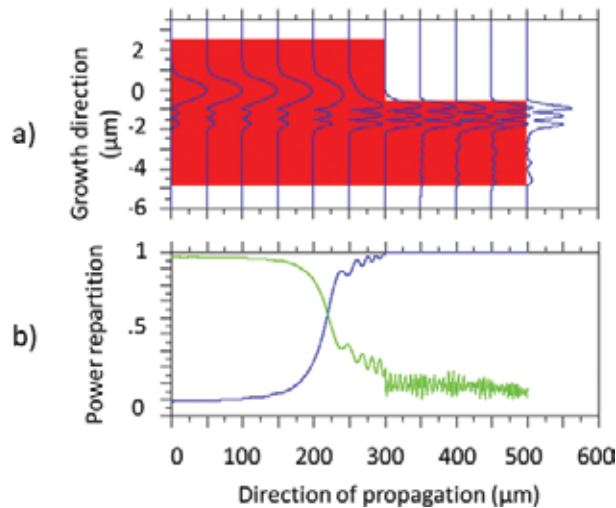


**Figure 9.** (a) BPM simulation of light propagation in the structure. (b) Normalized guided power along  $z$ , in the upper (laser, blue) and the lower (OPO, green) waveguide.

must balance two conditions in order to give a high transfer to the  $\text{TE}_{20}$  mode. On the one hand, the lateral confinement of the buried waveguide should be minimal so that the single-mode approximation is satisfied, and coupling to higher order modes in the lateral direction is minimized. On the other hand, the buried waveguide should be confined enough to prevent the field from escaping.

**Figure 11** shows the proposed taper design. From  $Z = 0$  to  $Z = 300 \mu\text{m}$ , the width of laser cladding, top half of the laser core and QW, is reduced from 4  $\mu\text{m}$  to

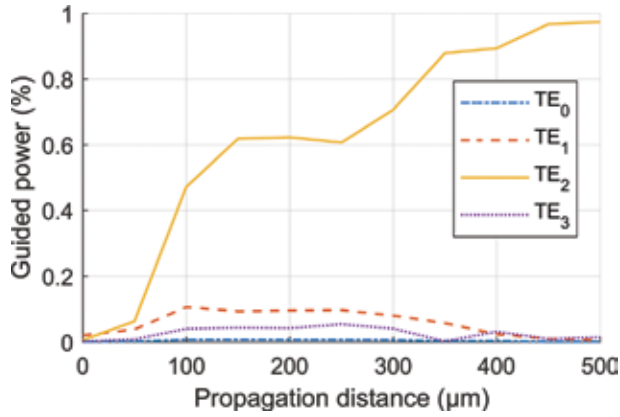


**Figure 10.** Modal decomposition of the BPM-simulated field in **Figure 9** on the eigenmodes of the GaAs waveguide.

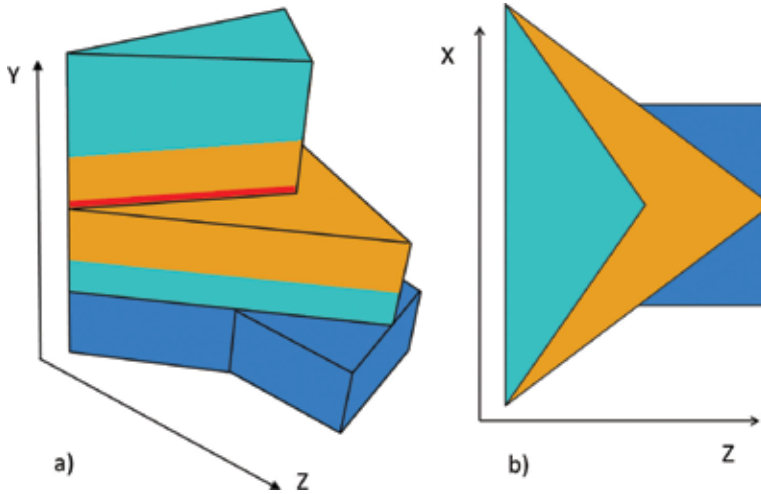


**Figure 11.** Side (a) and top (b) view of the proposed taper geometry. Green,  $\text{Al}_{0.3}\text{Ga}_{0.7}\text{As}$ ; orange, laser core layer; dark blue, GaAs; red, quantum well. Dimensions are not to scale.

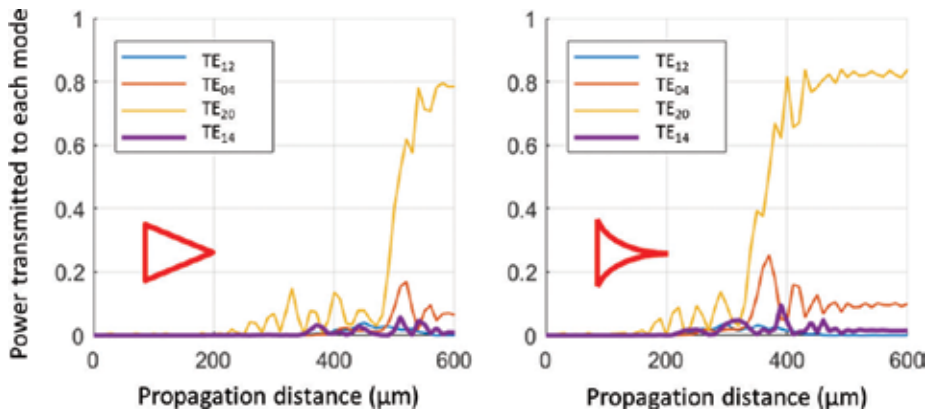


**Figure 12.** Power transmitted to the eigenmodes in **Figure 13**. (Left) Triangular tapers. (Right) Quadratic tapers.

0. From  $Z = 300 \mu\text{m}$  to  $Z = 600 \mu\text{m}$ , the width of the bottom half of laser core and separation layer ( $\text{Al}_{0.3}\text{Ga}_{0.7}\text{As}$ ) is reduced in the same way. The width of the final GaAs waveguide is  $2 \mu\text{m}$ . For this design, the calculated transfer efficiency into the  $\text{TE}_{20}$  mode is as large as 80%.

**Figure 12** shows the power transmitted to the eigenmodes of the  $2 \mu\text{m}$  wide and air clad GaAs ridge waveguide that are plotted in **Figure 13**. For the sake of clarity, among all the eigenmodes supported by the waveguide, we only show those that are the most likely to sustain a transfer (because they have a similar effective index, the same polarization, and the same horizontal parity as the laser mode).

Modifying the taper shape affects the effective index and thus the position of transfer. A  $-0.02$  shift in the laser core and cladding refractive indices accelerates the transfer without affecting the total transmission. An opposite shift ( $+0.02$ ), which can be caused by a  $30^\circ\text{C}$  temperature increase, makes the transfer drop to 30–40% depending on the taper shape.

These values must be compared to the estimated OPO thresholds (**Figure 3**): depending on the OPO cavity length and mirror reflectivity, its threshold can range from 20 to 100 mW. Transmission of 30–80% thus sets the target optical power at 25–300 mW. Since AlGaAs laser diodes at 980 nm can emit powers in excess of 10 W in broad area configurations [13] and 700–1500 mW in narrow, laterally single-mode configurations [12], our target power seems within reach.

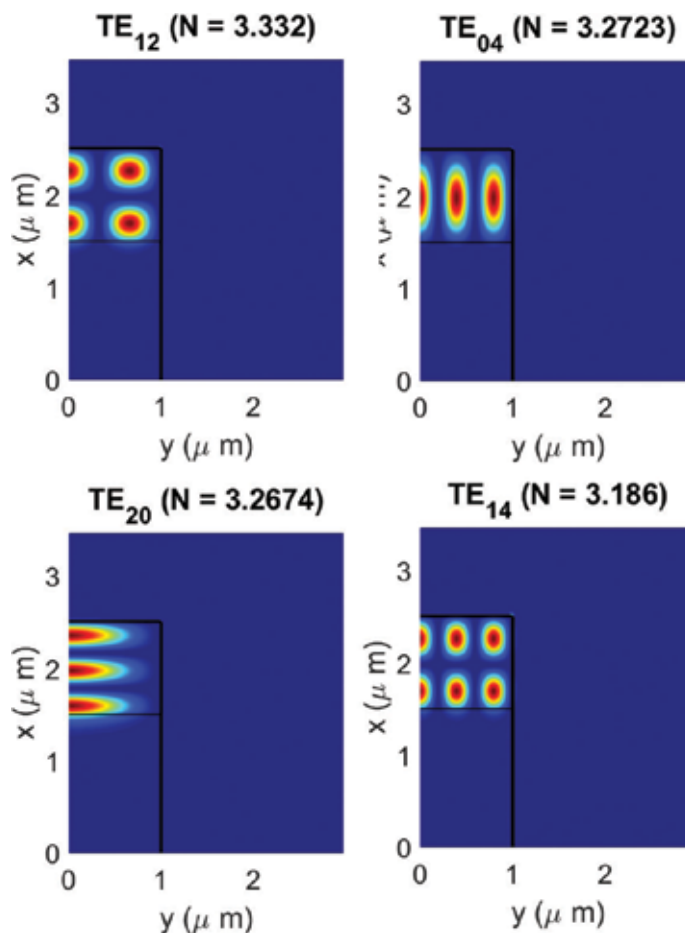


**Figure 13.** Four eigenmodes of the ridge GaAs waveguide of width  $2 \mu\text{m}$ . The pump mode for SPDC is  $\text{TE}_{20}$  (bottom left). Only half of the waveguide is represented in the lateral direction for symmetry reasons.

## 5. Laser

We propose here a preliminary description of the laser cavity. While the laser design is unconventional, we show that its key parameters (confinement in the QW, reflectivity, estimated differential efficiency) fall in a typical range of values for AlGaAs lasers. Active properties are not investigated, although they could be undertaken in the future on the basis of this work.

### 5.1 Thermal behavior

As mentioned earlier, thermal behavior is a critical point for the operation of the DOPO source. Given a maximal ridge width for single-mode operation, an epi-up geometry, and a target optical power, we can estimate the temperature rise in the laser.

The laser ridge width is taken to be 5  $\mu\text{m}$ , as this size provides single-mode operation for an index contrast of 0.005 [12]. Assuming a target optical power of 100 mW and a wall-plug efficiency of 16%, the emitted power in the form of heat is 500 mW. We simulate a crude model of the temperature rise with the software COMSOL. The heat is assumed to escape fully from the junction of size 5  $\mu\text{m} \times 0.1 \mu\text{m} \times L$  (1, 2, or 3 mm) (Figure 14). The latter is set inside 10  $\mu\text{m}$  of  $\text{Al}_{0.3}\text{Ga}_{0.7}\text{As}$ , and the underlying material is GaAs. Figure 15 shows the junction temperature calculated as a function of the substrate thickness for three different lengths ( $L = 1, 2, \text{ or } 3 \text{ mm}$ ).

To stay under 40°C, we find that the laser should be at least 2 mm long and the wall-plug efficiency should be over 16% at the target power.

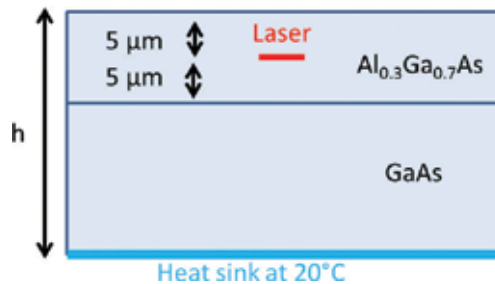


Figure 14.  
Model used to estimate the laser temperature rise.

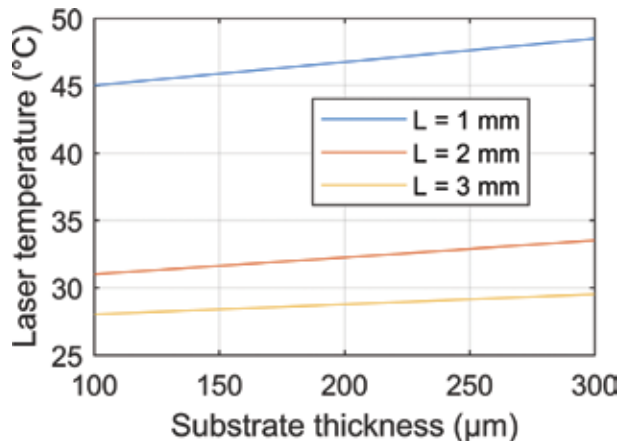


Figure 15.  
Junction temperature as a function substrate thickness, for three laser lengths.

## 5.2 Key parameters

To limit its temperature rise, the laser should be at the least 2 mm long. This size is above the average for common sources in integrated optics, which often favor compactness. Large DFB grating lengths increase modal reflectivity, not only lowering threshold but also degrading differential efficiency. Furthermore, the laser mode is only partially confined before the taper, so we estimate the impact of confinement on the modal gain.

In order to achieve high optical powers and single-mode operation, we propose a DFB laser with low grating reflectivity and high reflectivity (HR) coating on the external facet. We assume that the DFB grating is etched at the interface between laser core and top cladding. To avoid regrowth, gratings can also be etched on the surface [16]. However, optimization of surface gratings depends on the top contact geometry, which has not been defined yet. Therefore, we present only the buried grating case.

If the laser is 1–2 mm long to limit temperature rise, an etch depth of 10–20 nm is necessary to provide a  $\kappa L$  product of  $\sim 0.5$  (where  $\kappa$  is the coupling constant of the fundamental mode). This value is realistically achievable with a shallow etch and epitaxy regrowth.

For a laser of length 2 mm with a coating of reflectivity 90% on the external facet, assuming a  $\kappa L$  product of 0.5, total output coupling losses are  $9 \text{ cm}^{-1}$  [17]. If parasitic losses are  $10 \text{ cm}^{-1}$  and internal efficiency is 80%, external differential efficiency is 0.38. The modal gain needed to reach laser oscillation is  $19 \text{ cm}^{-1}$  [17]. QW lasers at 980 nm commonly achieve modal gains in excess of this value [18]; however, the threshold is also affected by the confinement factor. For a single QW of thickness (10 nm), we find that the confinement of lasing mode in the well is 1.2%, which corresponds to a material gain of  $1600 \text{ cm}^{-1}$  at threshold. This is achieved under a carrier density of  $2.5 \times 10^{18} \text{ cm}^{-3}$  in the well [19]. Assuming a recombination time of 3 ns, the threshold current density is then expected to be  $130 \text{ A/cm}^2$ , comparable to the range of  $120\text{--}150 \text{ A/cm}^2$  measured in similar lasers [13, 18].

In conclusion, we have shown that the key parameters (threshold and efficiency) of this laser are not affected by its unusual design and that they are compatible with operation in excess of 100 mW.

## 6. Conclusion

We have defined the main conditions required for a diode-OPO structure based on a vertical coupler, and we have described the passive properties of this source. Phase matching can be dynamically controlled through wavelength and temperature tuning. We achieve transfer to a higher order mode of the structure, with sufficient efficiency. The taper layout can still be improved via further optimization.

Overall, this design predicts promising results for the fabrication of an integrated diode-OPO based on GaAs. Unlike all-in-one DOPO configurations, this device does not require record-low propagation losses in the laser diode.

While fabrication of this device is complex, epitaxy regrowth can be avoided completely if the laser DFB grating can be defined at the surface. Most of the technological complexity occurs in the various etching levels necessary to define the structure, from tapers to DFB grating to DBRs.

To ensure feasibility of this project, future work should focus on laser design, particularly on expected optical power and impact of doping on the transfer.

## Acknowledgements

This work is supported by a public grant overseen by the French National Research Agency (ANR) as part of the project DOPO. The authors thank the Commissariat à l'Énergie Atomique and Direction Générale de l'Armement for the PhD funding. We thank Michel Krakowski and Bruno Gérard for their information and stimulating discussions.

## Author details

Alice Bernard<sup>1,2</sup>, Jean-Michel Gérard<sup>2</sup>, Ivan Favero<sup>1</sup> and Giuseppe Leo<sup>1\*</sup>

1 Laboratoire Matériaux et Phénomènes Quantiques, UMR 7162, Université Paris Diderot–CNRS, Paris, France

2 Université Grenoble-Alpes, CEA, INAC-PHELIQS, CEA-CNRS Nanophysics and Semiconductors Joint Group, Grenoble, France

\*Address all correspondence to: [giuseppe.leo@univ-paris-diderot.fr](mailto:giuseppe.leo@univ-paris-diderot.fr)

## IntechOpen

© 2018 The Author(s). Licensee IntechOpen. This chapter is distributed under the terms of the Creative Commons Attribution License (<http://creativecommons.org/licenses/by/3.0>), which permits unrestricted use, distribution, and reproduction in any medium, provided the original work is properly cited. 

## References

- [1] Nathan MI, Dumke WP, Burns G, Dill FH, Lasher G. Stimulated emission of radiation from GaAs p-n junctions. *Applied Physics Letters*. Nov. 1962;**1**(3):62-64
- [2] Hall RN, Fenner GE, Kingsley JD, Soltys TJ, Carlson RO. Coherent light emission from GaAs junctions. *Physical Review Letters*. Nov. 1962;**9**(9):366-368
- [3] Grisard A, Gutty F, Lallier E, Gérard B. Compact fiber laser-pumped mid-infrared source based on orientation-patterned Gallium Arsenide. In: *Technologies for Optical Countermeasures VII*. Vol. 7836; 2010. p. 783606
- [4] Boitier F et al. Electrically injected photon-pair source at room temperature. *Physical Review Letters*. May 2014;**112**(18):183901-1-183901-5
- [5] Oron MB, Blau P, Pearl S, Katz M. Optical parametric oscillation in orientation patterned GaAs waveguides. In: *Nonlinear Frequency Generation and Conversion: Materials, Devices, and Applications XI*. Vol. 8240; 2012. p. 82400C
- [6] Savanier M. et al. Near-infrared optical parametric oscillator in a III-V semiconductor waveguide. *Applied Physics Letters*. Dec. 2013;**103**(26):261105
- [7] Zareian N, Helmy AS. Static and dynamic characteristics of integrated semiconductor optical parametric oscillators. *Journal of the Optical Society of America B*. Aug. 2013;**30**(8):2306
- [8] Andronico A, Gérard JM, Favero I, Ducci S, Leo G. Quantum dot parametric source. *Optics Communication*. Sep. 2014;**327**:27-30
- [9] Fengnian X, Menon VM, Forrest SR. Photonic integration using asymmetric twin-waveguide (ATG) technology: Part I-concepts and theory. *IEEE Journal of Selected Topics in Quantum Electronics*. Jan. 2005;**11**(1):17-29
- [10] Yariv A, Sun X. Supermode Si/III-V hybrid lasers, optical amplifiers and modulators: A proposal and analysis. *Optics Express*. 2007;**15**(15):9147-9151
- [11] Keyvaninia S et al. Demonstration of a heterogeneously integrated III-V/SOI single wavelength tunable laser. *Optics Express*. Feb. 2013;**21**(3):3784-3792
- [12] Wenzel H et al. Fundamental-lateral mode stabilized high-power ridge-waveguide lasers with a low beam divergence. *IEEE Photonics Technology Letters*. Feb. 2008;**20**(3):214-216
- [13] Krakowski M et al. Very high-power broad area laser diode with internal wavelength stabilization at 975 nm for Yb fibre laser pumping. In: *Novel In-Plane Semiconductor Lasers XIII*. Vol. 9002; 2014. p. 90021G
- [14] Beaudoin M, DeVries AJG, Johnson SR, Laman H, Tiedje T. Optical absorption edge of semi-insulating GaAs and InP at high temperatures. *Applied Physics Letters*. Jun. 1997;**70**(26):3540-3542
- [15] Ruan Z, Veronis G, Vodopyanov KL, Fejer MM, Fan S. Enhancement of optics-to-THz conversion efficiency by metallic slot waveguides. *Optics Express*. 2009;**17**(16):13502-13515
- [16] Dridi K, Benhsaien A, Akrouf A, Zhang J, Hall T. Narrow-linewidth three-electrode regrowth-free semiconductor DFB lasers with uniform surface grating. In: *Novel In-Plane Semiconductor Lasers XII*. Vol. 8640; 2013. p. 864009

[17] Coldren LA, Corzine SW, Mashanovitch ML. Diode Lasers and Photonic Integrated Circuits. Vol. 218. Hoboken, New Jersey: John Wiley & Sons; 2012

[18] Klopff F, Reithmaier JP, Forchel A. Highly efficient GaInAs/(Al)GaAs quantum-dot lasers based on a single active layer versus 980 nm high-power quantum-well lasers. Applied Physics Letters. Aug. 2000;77(10):1419-1421

[19] Corzine SW, Yan RH, Coldren LA. Theoretical gain in strained InGaAs/AlGaAs quantum wells including valence-band mixing effects. Applied Physics Letters. Dec. 1990;57(26):2835-2837



# Stimulated Raman Scattering in Micro- and Nanophotonics

*Maria Antonietta Ferrara and Luigi Sirleto*

## Abstract

Micro- and nanophotonics explore behavior of light on the micro-/nanoscale and the interaction of micro-/nanoobjects with light. The driving force for their development is the aim to go beyond the limit of photonics. Because of the diffraction limit, photonics components are not able to confine light to the microscale or nanoscale dimension; therefore, one of the key challenges for micro- and nanophotonics is a reduction in the size of integrated optical devices, while maintaining a high level of performance. As far as light amplifiers and laser sources based on stimulated Raman scattering (SRS) are concerned, important accomplishments have been achieved in the fields of fiber optics amplification and integrated photonics devices. In this chapter, the most interesting investigations in the field of stimulated Raman scattering in micro- and nanophotonics are reviewed. These findings provide promising perspectives for integrated micro-/nano-Raman lasers.

**Keywords:** nonlinear optics, stimulated Raman scattering, Raman laser, microphotonics, nanomaterials, nanophotonics

## 1. Introduction

Spontaneous Raman is an inelastic light scattering by which a fraction of the light incident upon a transparent material is shifted in frequency. Linear Raman scattering is a weak process (approximately 1 in  $10^7$  photons) involving the collective behavior of many atoms, behaving independently (see **Figure 1(a)**) and leading to nearly isotropic emission. Raman spectra, given by the superposition of stochastic totally independent vibrations from individual molecules, are unique to the material [1].

Stimulated Raman scattering (SRS) phenomenon occurs when there is a transfer of energy from a high power pump beam to a probe beam (copropagating or counterpropagating) through SRS. In particular, this energy exchange occurs when the frequency difference between the pump and the Stokes laser beams matches a given molecular vibrational frequency of the sample under test; the SRS effect occurs in the form of a gain of the Stokes beam power (stimulated Raman gain, SRG) and a loss of the pump beam power (stimulated Raman loss, SRL. See **Figure 1(b)**) [2]. Because of its coherent nature, the molecular bonds oscillate in phase and interfere constructively inside the focus area of the laser beam. As a consequence a SRS signal, which is orders of magnitude bigger than spontaneous Raman scattering, is generated (about 20–30% of the incident laser radiation can efficiently be converted into SRS) (see **Figure 1(c)**).

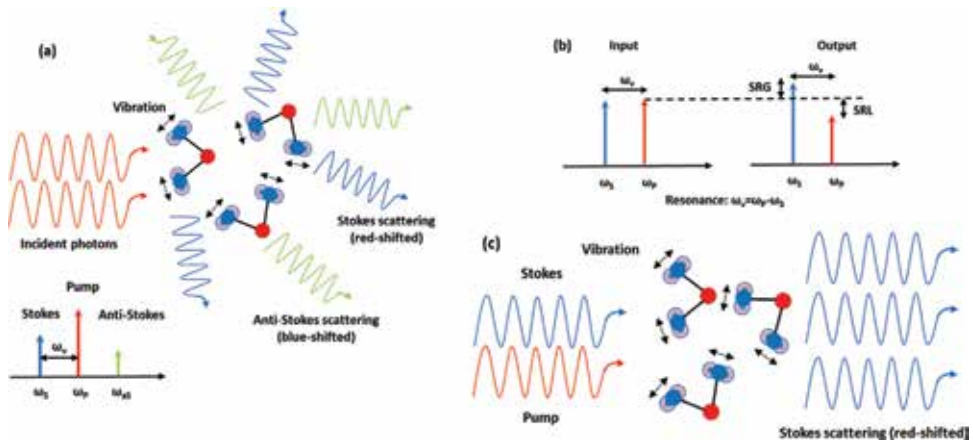


**Figure 1.**

(a) Spontaneous Raman scattering: incident photons inelastically scatter off spontaneously excited molecules, behaving independently. (b) Stimulated Raman scattering: two incident lights, a pump and a Stokes laser beams, whose energy difference matches a particular vibrational energy, drive the molecule at  $\omega_v = \omega_s - \omega_p$  producing coherent Raman signals at  $\omega_s = \omega_p + \omega_v$ . SRS modalities are: SRG, stimulated Raman gain; SRL, stimulated Raman loss. (c) Stimulated Raman scattering: inelastic scattering of probe photons off from vibrationally excited molecules that interfere coherently.

Due to its Raman-shifted output, SRS is a workable method for generating coherent radiation at new frequencies. SRS permits, in principle, the amplification in a wide interval of wavelengths, from the ultraviolet to the infrared. Since the Raman frequency of a medium is usually fixed, the tunability can be achieved by using a tunable pump laser. Raman lasing occurs when the Raman-active gain medium is placed between mirrors, reflecting the first Stokes wavelength. This is analogous to lasers, where the gain medium must be placed inside a cavity to achieve laser threshold. Raman lasers and traditional lasers differ in the wavelength of light required for pumping. In the case of Raman laser, it does not depend on the electronic structure of the medium, so the wavelength of pump laser can be chosen to minimize absorption.

In order to tailor Raman laser characteristics and performances, there are two main basic configurations. The first one, external-resonator Raman laser, the Raman crystal is placed inside a cavity, resonating the Stokes field (**Figure 2(a)**). This configuration is used for pump pulses that are longer than the transit time through the Raman crystal. The second one, the intracavity Raman laser (**Figure 2(b)**) combines both a Raman medium and the laser medium inside a single cavity, so that the fundamental and Stokes fields are both resonating within the cavity [3].

Raman amplification, demonstrated in the early 1970s, is a feasible approach for fiber optics amplification, being only restricted by the pump wavelength and Raman active modes of the gain medium [4]. In this case, optical fiber is used as Raman gain medium and both pump and signal waves are launched into it (**Figure 2(c)**). In the past century, fused silica has been the main material used for transmission of optical signals, because of its good optical properties and attractive trade-off between Raman gain and losses. The main disadvantage of the current silica fiber amplifiers is the limited usable bandwidth for Raman amplification (5 THz, approx.  $150 \text{ cm}^{-1}$ ). A development in fiber optics communications was achieved opening the communication range to span from 1270 to 1650 nm, corresponding to about 50 THz bandwidth [5]. For future amplification requirements, due to this significant increase in bandwidth, the use of existing Er-doped fiber amplifiers is kept out, while Raman gain becomes the key mechanism.

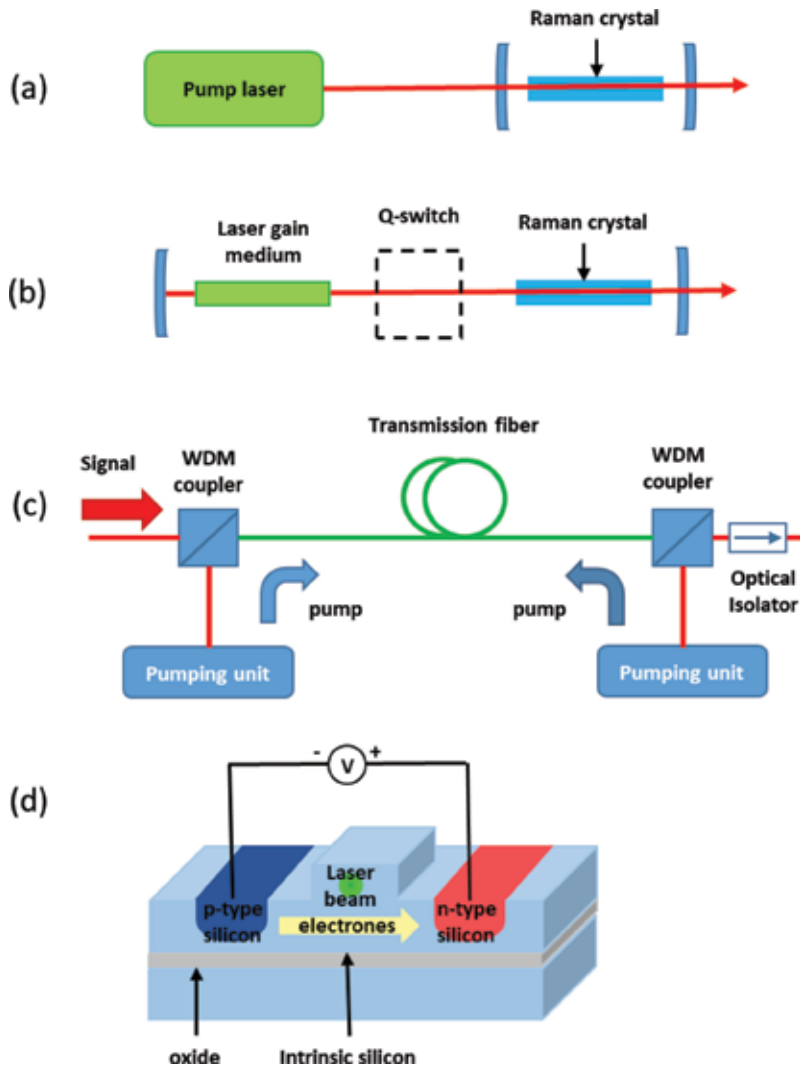


**Figure 2.** Basic configurations of Raman laser: (a) external-resonator Raman laser; (b) intracavity Raman laser; (c) fiber Raman amplifiers; and (d) silicon on insulator waveguide Raman laser.

Silicon photonics is an important player in the low-cost optical interconnect technology, as silicon-based optical components could be manufactured using the existing silicon fabrication techniques [6]. Silicon on insulator (SOI) waveguides allows to limit the optical field into an area 100 times smaller than the modal area of a typical single-mode optical fiber. In addition, the Raman gain in silicon is much stronger than in glass ( $\approx 10,000$  times), therefore allowing to reduce the length required from kilometers of fiber to centimeters of silicon waveguides [2]. The waveguide approach, schematically reported in **Figure 2(d)**, led to the demonstration of pulsed Raman silicon laser [7] and continuous-wave (CW) lasing [8]. The merit of this approach is the ability to use pure silicon without the need for Er doping; i.e. it is fully compatible with silicon microelectronics manufacturing. On the other hand, there are three main limitations. The first, Raman laser cannot be electrically excited and it requires an off-chip pump. The second, the narrow-band (105 GHz) of stimulated Raman gain makes it unsuitable for its use in WDM applications, unless expensive multi-pump schemes are implemented. The third,

Raman gain in Si at the wavelength of interest for telecommunications is reduced by two-photon absorption (TPA).

We note that as a general rule, in all laser gain bulk materials there is a tradeoff between gain and bandwidth: linewidth may be increased at the expense of peak gain. In nature, we have material with high Raman gain and small bandwidth (for example, silicon), and others with a large bandwidth but with small Raman gain (for example, silica). This trade-off is a fundamental limitation toward the realization of sources with high efficiency and large emission spectra. In this book chapter, a review of the most significant accomplishments in the field of SRS in micro- and nanophotonics is reported. From a theoretical point of view, the difference between micro- and nanostructures is significant. In microstructures, the measured SRS enhancement can be related to photons confinements effect and it can be quantified by a corresponding gain ( $g_{micro}$ ), given by:  $g_{micro} = f^* g_{bulk}$ , where  $f$  is the optical field enhancement due to the presence of microstructures and  $g_{bulk}$  is the gain of bulk material, making up the microstructures [2]. According to this formula, photonics microstructures allow an enhancement of Raman gain, but the bandwidth does not change, therefore the fundamental trade-off between gain and bandwidth of bulk materials cannot be overcome using microstructures. Concerning SRS in nanostructures, although a general theory on the relation between nanostructuring and Raman gain is not established, we expect that the Raman gain of nanomaterials  $g_{nano}$  should be related to the intrinsic properties of materials and for this reason different from bulk. Therefore, the fundamental trade-off between gain and bandwidth should be overcome, too.

The chapter is organized as follows. In Section 2, some the most successful applications areas of SRS in microstructures are described. In Section 3, a number of investigations concerning SRS in nanostructures are described. Finally, in the appendix, for the sake of completeness, the basic theory of SRS and experimental methods for measuring Raman gain are reported.

## **2. SRS in microphotonics**

In this section, in order to describe stimulated Raman scattering investigations in microstructures, two crucial parameters have been individuated: dimension of microstructure and order/disorder degree of microstructure distribution. As to regard dimension of microstructure, in order to point out its role, in Section 2.1, SRS investigations in microcavities are reported. Concerning the order/disorder degree of microstructure distribution, we note that interesting developments have been recently demonstrated, which point out that it is possible to make use of the intrinsic order/disorder in photonic materials to create useful optical functionality [9]. In order to highlight the role of order/disorder degree of microstructure distribution, we describe two limit cases: in Section 2.2 SRS in photonics crystals, i.e. in a completely ordered structure, is reported, while in Section 2.3 SRS in random laser, i.e. in a disordered structure is described.

### **2.1 SRS in microcavities**

In nonlinear optics devices, the use of microcavities allows to take advantage of both the micrometers dimension and the increasing of the local field, combining small modal volume with high optical quality-factors ( $Q$ ). One of the most important consequences for nonlinear optics applications is that strong resonant increase of energy in microscale volumes significantly reduces the power threshold at which nonlinear optical effects occur [10]. In the case of SRS, in agreement with the observed SRS for high- $Q$  cavities experimental results [10], the explicit

expression of the cavity-enhanced Raman gain shows that the improvement is inversely proportional both to the square of the radius of the spherical cavity and to the linewidth of the Raman process.

In Ref. [11], SRS from spherical droplets and microspheres, with diameters of the order of tens of micrometers and optically coupled by the use of a tapered optical fiber, has been observed. The threshold was measured whereas the coupling air gap between the taper and microsphere was changed, allowing to obtain a micrometer-scale, nonlinear Raman source with a pump threshold approximately 1000 times lower than reported before and a pump-signal conversion higher than 35% [2, 11].

Diamond as a possible material for compact, on-chip Raman lasers over a wide spectrum was introduced in Ref. [12]. A CW, low-threshold, tunable Raman laser operating at  $\sim 2 \mu\text{m}$  wavelengths based on waveguide-integrated diamond racetrack microresonators embedded in silica on a silicon chip was demonstrated.

## 2.2 SRS in photonics crystals

A high-quality-factor nanocavity using a photonic crystal with a triangular lattice structure realized by circular air holes in a suspended silicon membrane and without any p-i-n diodes, yielding a device with a cavity size of less than  $10 \mu\text{m}$ , has been demonstrated in Ref. [13]. The heterostructure nanocavity is obtained by introducing a line defect waveguide with two kinds of propagation modes inside the photonic bandgap, an odd-waveguide mode and an even-waveguide mode, which were used to confine pump light and Stokes-Raman-scattered light, respectively. A continuous-wave Raman silicon laser with an extraordinary low lasing threshold of  $1 \mu\text{W}$  was demonstrated. In fact, an optimized nanocavity design allows to produce a net Raman gain in the low-excitation range before TPA-induced free carrier absorption (FCA) becomes dominant, permitting a low lasing threshold [2, 13].

## 2.3 SRS in random laser

Multiple scattering is a well-known phenomenon, occurring in nearly all optical opaque materials. Random walk of light waves in disordered materials could carry out to a multiple scattering with a consequent strong localization of electric field. Wave character of multiply scattered light is not lost and the wave can interfere both during and after the scattering process. Considering that the scattering is elastic, optical information does not change. Furthermore, due to reciprocity, multiple scattering is, in theory, fully reversible [2]. Reciprocity means that waves following the same path in opposite directions can interfere. Interference between such counter-propagating waves is always constructive, which gives rise to the incredibly robust interference phenomenon of coherent backscattering (also called weak localization). The combination of weak localization together with reciprocity, leads to a series of interesting physical effects and to an enormous potential for new disorder-based optical applications [14].

The first experimental evidence of lasing via a Raman interaction in a bulk three-dimensional random medium was demonstrated taking advantage of barium sulfate ( $\text{BaSO}_4$ ) powder with particle diameters of  $1\text{--}5 \mu\text{m}$ . The pump energy threshold was  $1.05 \text{ mJ}$ ; at higher values, gain is stronger than losses and SRS dominates the conversion process, allowing to obtain random Raman lasing. A Raman signal of  $2.0 \text{ mJ}$  was measured at a maximum of  $11.5 \text{ mJ}$  of pump energy [2, 15]. The complicated dynamics of nonlinear pulse propagation in a turbid medium make a theoretical approach to describing this problem very challenging.

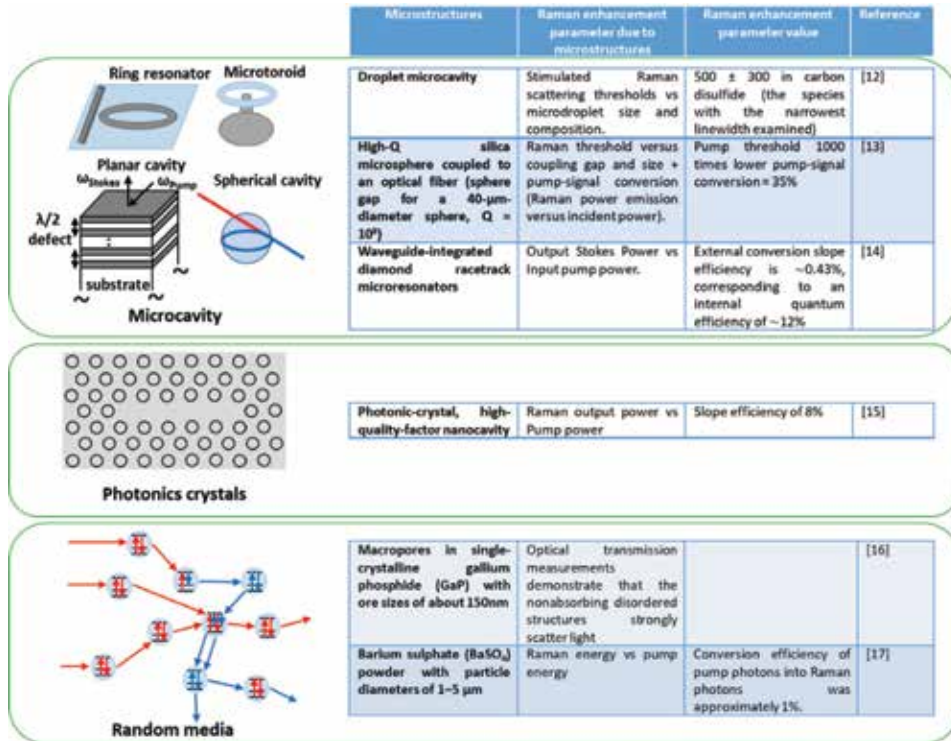


Figure 3. SRS enhancement reported in different kind of microstructures.

To have a rapid idea of the Raman enhancement reported by the different approaches in microstructures described in this section, in **Figure 3** we summarized them.

### 3. SRS in nanophotonics

In order to control a signal light, its intensity or phase has to be modified by a control signal. In a nonlinear optics device, a control light-wave is employed to modify the optical properties of the medium as seen by a signal light-wave. Of course, higher nonlinearity requires shorter interaction length  $L$ . In order to reduce  $L$  in a nonlinear device with physical dimensions greater than the wavelength, the efficiency of nonlinear effects can be enhanced taking advantage of optical resonators (see Section 2.1 for examples) [2]. In nanoscale devices, which should be able to control light with light in a nanoscale layer or in a nanoparticle of nonlinear material, the trick of using optical resonators cannot be used. Therefore, we have to develop nanostructured materials having enough large nonlinearities [16].

The search for new materials, from an experimental point of view, should satisfy a number of technological and economical requirements, while, from a theoretical point of view, it should be combined with a deep understanding of nonlinear polarization mechanisms, elucidating their relation to the structure of nanostructures (average radius, volume fraction and size dispersions) [17]. In the past few decades, a number of nanomaterials proved remarkable nonlinear optical (NLO) properties, which encourage the fabrication of ultra-compact, low-loss and high-performance nanoscale photonic devices [18].

Recent interest in the optical responses of metal nanoparticles and metamaterials is focused on enhancing local electromagnetic fields [19]. The significant enhancement factors of  $10^3$ – $10^6$ , predicted at a flat metal surface, are significant for nonlinear optical processes [19]. However, although plasmonics structures and metamaterials can provide substantial size reduction for optical components, their optical losses are often undesired [20]. Therefore, in order to control the flow of light, an all-dielectric platform is highly attractive. Although *resonant nonlinearities* are significant, they are not appealing for applications, due to their long response times. In addition, at resonance the incident radiation is absorbed by materials [17]. On the other hand, *nonresonant nonlinearities* take place at frequencies below the absorption edge (i.e. when the light linear absorption is negligible) and they are very fast (typical recovery times are of the order of picoseconds). Recently, third-order NLO properties of Si-nc have been widely investigated and a large variation of the nonlinear refractive index ( $n_2$ ) values has been reported, complicating the interpretation of experimental results [21].

As far as the investigation of SRS at the nanoscale is concerned, there have been a few number of fundamental investigations, both experimental and theoretical. In Ref. [22], a large Raman gain, measured by resonant Raman spectra excited at 632.8 nm, was obtained from individual single-walled carbon nanotubes. The theoretical interpretation takes in to account both the exceptional nonlinear properties and the efficient electron-phonon interaction in single-walled carbon nanotubes. In Ref. [23], SRS from GaP nanowires was measured by Raman spectra in backscattering configuration, using CW laser excitation (514.5 nm). Strong nonlinear SRS, obtained by crystalline nanowires with a diameter of 210 nm and with length of about 1 micron, were discussed in terms of theoretical results developed for dielectric cavities.

In the following, the observation of SRS in nanostructured silica-based materials (Section 3.1) and nanostructured silicon-based materials (Section 3.2) are reported and discussed.

### 3.1 SRS in nanocomposites silica-based materials

Among the innovative materials for Raman amplification, one of the most interesting classes is oxide glasses, above all silicon dioxide-based glasses due to their compatibility with the current optical fibers technology. To try to improve their SRS efficiency, a useful strategy is to add suitable dopants (heavy metal oxides as  $Ta_2O_5$ ,  $Bi_2O_3$ , and  $Nb_2O_5$ ) to silica [24–27]. We note that in other systems, such as niobium-phosphate glasses, characterized by a high concentration of niobium, a higher peak Raman gain (but in the best case of  $\approx 10$  times) and a broadening of the bandwidth with respect to silica glass has been demonstrated [28, 29].

In this paragraph, in order to increase SRS optical features of silica-based glasses, we propose an alternative approach: instead of to investigate new glass compositions, we change the glass arrangement. We note that a glass structural variations can be obtained as a result of an appropriate heat treatments made in the glass transition range, generating glass-ceramics with nanocrystals uniformly dispersed in the glass matrix (glass-crystals nanocomposites) [30]. We consider glasses, belonging to the  $K_2O-Nb_2O_5-SiO_2$  (KNS) system, forming transparent and stable glasses and showing interesting non-linear optical properties. For glasses in the class of the KNS glass-forming system, an interesting glass nanostructuring process has been considered. The process contains two partially overlapped processes, namely, phase separation and crystallization [31]. We note that a clear relationship between glass nanostructuring and Raman gain has not been proven yet, although, in our previous paper, a connection between local structure and SRS in bulk

nanostructured  $30\text{K}_2\text{O}\cdot 30\text{Nb}_2\text{O}_5\cdot 40\text{SiO}_2$  (KNS 30-30-40) glass was found [31]. It is worth noting that an appropriate choice of the annealing parameters, therefore of the degree of crystallization, can allow to obtain the best compromise between the highest Raman gain and the highest nonlinear coefficients for third order effects.

Moreover, Raman spectroscopy characterization of nanostructured  $20\text{K}_2\text{O}\cdot 25\text{Nb}_2\text{O}_5\cdot 55\text{SiO}_2$  (KNS 20-25-55) glasses are also reported. The optical and structural characteristics of the samples have been measured by the Raman set up reported in Ref. [31]. Due to dependence of the intensity of the Raman active modes on both the temperature and the frequency of the vibrational modes, the measured Stokes Raman intensity was reduced according to the procedure also described in our previous papers [28–32]. Then, in order to properly compare the Raman spectra of KNS glasses with the silica glass standard, the measured Raman spectra were modified also for the differences in reflection and angle of collection by using the procedure reported in Refs. [28–32]. Usually, due to the more extended electronic clouds, elements with high atomic number yields highest intensity Raman bands, making the polarizability more sensitive to bonds stretching. Adding niobium oxide to silica-based glasses induces an enhancement of Raman cross section respect to silica glass, being the polarizability of Nb-O bonds higher than Si-O bonds. In the studied glasses, niobium enters in the glass network creating  $\text{NbO}_6$  octahedra more or less distorted, namely with different NbO bond length, and produces several Raman bands over a wide wavenumbers range. Due to the typical glass disorder, a broadening of all Raman bands occurs and, therefore, Raman spectra of KNS glasses outcome from the strong overlapping of several broad bands.

In **Figure 4** the Raman gain respect to the Raman gain of silica is reported as a function of the Raman bandwidth for different materials. Inter alia, in **Figure 4** is evident that glasses at initial and at different times of heat-treatment show the same bandwidth, but different gain. Hence, the nanostructuring process is nearly complete in glasses at a time between 2 and 10 h and produces nanocrystalline inhomogeneities distributed in the glass matrix [30, 32].

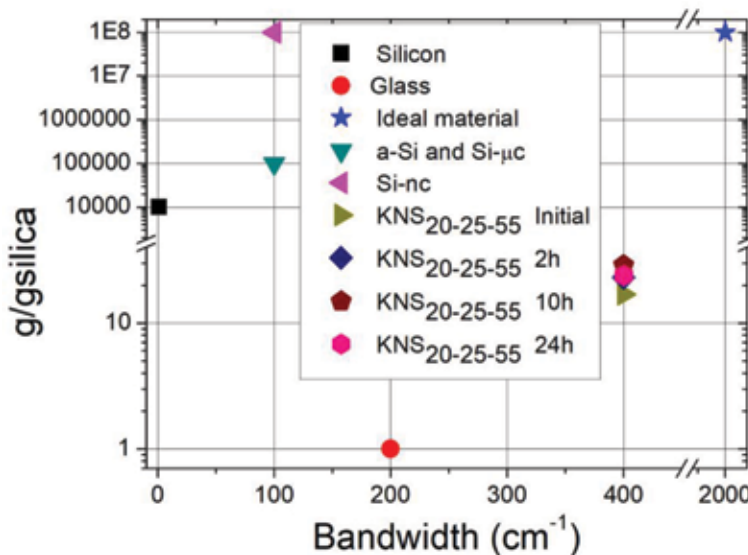


**Figure 4.** Raman gain coefficients and their bandwidth are reported for different material: silicon and silica (as ‘bulk material’), nanocomposite glasses (KNS) in different phases of the thermal treatment for the initial glass composition 20-25-55, silicon micro- and nano-particles (amorphous and crystalline). Features for ‘ideal materials’ for Raman amplification are reported, too.

### 3.2 SRS in nanostructured silicon-based materials

In our previous papers [2, 33–35] experimental results of spontaneous Raman scattering measurements in silicon nanostructures at the wavelength of interest for telecommunications (1.54  $\mu\text{m}$ ), were showed. Due to the phonon confinement model, two significant enhancements of the Raman spectra in silicon quantum dots respect to silicon were obtained: the broadening of spontaneous Raman emission and the tuning of the Stokes shift. In detail, in silicon quantum dots with a crystal size of 2 nm an important broadening of about  $65\text{ cm}^{-1}$  and a peak shift of about  $19\text{ cm}^{-1}$  were demonstrated. Taking into account that the width of C-band telecommunication is  $146\text{ cm}^{-1}$ , we have that more than the half of C-band could be covered using silicon quantum dots, without implementing the multi-pump scheme.

In this paragraph, comparison among experimental investigations of SRS in amorphous silicon nanoparticles and in silicon micro- and nano-crystals, at the wavelengths of interest for telecommunications, are reported. We considered three different samples:

1. Silicon nanocomposites dispersed in  $\text{SiO}_2$  matrix. The mean radius of the silicon dots and the dot density were of 49 nm and  $1.62 \times 10^8$  dots/ $\text{cm}^2$ , respectively [36, 37].
2. Amorphous silicon nanoclusters embedded in Si-rich nitride/silicon superlattice structures (SRN/Si-SLs). The structure of the sample consists of 10 SRN layers and 9 amorphous Si (a-Si) layers for a total thickness of 450 nm. Amorphous silicon nanoclusters size was 2 nm [38–40].
3. Silicon nanocrystals (Si-nc) with a size of about 4 nm embedded in a silica matrix layer about 7 cm long. The sample was realized with an increasing concentration of Si-nc varying along the longer dimension of the sample, allowing to distinguish seven areas.

Results obtained can be summarized as follows:

- I. In silicon nanocomposites, an amplification of Stokes signal up to 1.4 dB/cm at 1542.2 nm using a 1427 nm continuous-wavelength (CW) pump laser was reported. This result demonstrates a five-fold improvement of the Raman gain respect to bulk silicon. Furthermore, a threshold power reduction of about 60% is also reported [36, 37, 40, 41].
- II. In SRN/Si-SLs, a magnification of Stokes signal up to 0.87 dB/cm at 1540.6 nm by means of a 1427 nm CW pump laser was reported. This result demonstrates a four-fold enhancement of the Raman gain with respect to bulk silicon. Additionally, a threshold power reduction of about 40% is also reported [38–41].
- III. In Si-nc an enhancement of the Raman gain by increasing their concentration was measured, and, a remarkable improvement of the Raman gain in Si-nc respect to bulk silicon, by three to four orders of magnitude depending on the Si concentration, was proven. The amplification was carried out by using a probe signal at 1541.3 nm and a pump signal at 1427 nm [2, 42, 43].

The obtained results are summarized in **Figure 4** where the Raman gain is plotted as a function of the Raman bandwidth for the considered nanostructured

silicon-based materials. By combining our earlier results on the broadening of the Raman gain spectra [33–35] with the observation of higher Raman gain [2, 36–42], bring us to state that the traditional trade-off between gain and bandwidth is overcome in low dimensional materials [30].

#### 4. Conclusion(s)

In this book chapter, some of the most significant experimental investigations of SRS in micro- and nano-photonics are reported. The focuses are microstructures and nanostructures, which are able to enhance nonlinear interaction between light and matter based on SRS.

We try to highlight how the nonlinear interaction based on SRS can take advantage of micro- and nanostructure with respect to bulk structure in order to improve SRS efficiency. In addition, we try to discuss new perspectives for the realization of Raman lasers with ultra small sizes, which would increase the synergy between electronic and photonic devices.

#### A. Appendix

We note that pulsed lasers are often used in SRS experiment; therefore, we have to consider the time dependence of the output. If the pulsewidth is much longer than the relation time of the Raman excitation and the time required for light to traverse the medium, we can expect from physical argument that the output pulse will follow the temporal variation of the input pulse. This is the quasi-steady-state case. Otherwise, the output should exhibit a transient behavior. The transient effects are out of the scope of this chapter [44–46].

##### A.1 Theory: the classical approach

The wave equations for pump and Stokes laser pulses with electromagnetic field amplitude  $\vec{E}_P$  and  $\vec{E}_S$  at frequencies  $\omega_P$  and  $\omega_S$  ( $\omega_P > \omega_S$ ), are:

$$\begin{aligned} \nabla \times (\nabla \times \vec{E}_P) - \frac{\omega_P^2}{c^2} \epsilon_P \vec{E}_P &= \frac{4\pi\omega_P^2}{c^2} \vec{P}^{(3)}(\omega_P) \\ \nabla \times (\nabla \times \vec{E}_S) - \frac{\omega_S^2}{c^2} \epsilon_S \vec{E}_S &= \frac{4\pi\omega_S^2}{c^2} \vec{P}^{(3)}(\omega_S) \end{aligned} \quad (1)$$

where  $\vec{P}^{(3)}$  is the nonlinear polarizations,  $\epsilon$  is the dielectric constants and  $c$  is the light velocity.

In the case of SRS, the material interaction is classically treated through a third-order nonlinear susceptibility tensor  $\chi^{(3)}$  given by:

$$\chi^{(3)} = \chi^{(3)NR} + \chi^{(3)R} \quad (2)$$

which defines both electronic ( $\chi^{(3)NR}$ , ‘non-resonant’) and vibrational ( $\chi^{(3)R}$ , ‘resonant’) responses. When input laser pulse frequencies are different from electronic resonances, the first term  $\chi^{(3)NR}$  does not depend on frequency, i.e. it is linked to a flat spectral background that changes immediately with the excitation change; thus, it is a real quantity. The second term, the complex quantity  $\chi^{(3)R}$ , characterizes the nuclear response of the molecules and yields the intrinsic vibrational mechanism of SRS [2].

In order to simplify, we study the special case of an isotropic medium with  $E_P$  and  $E_S$  with the same polarization direction and propagation along  $z$ . The whole field amplitude is:  $E(z, t) = E_P e^{i(\omega_P t - k z)} + E_S e^{i(\omega_S t - k z)}$ . According to Eq. (2), the nonlinear polarizations take the form:

$$\begin{aligned} P^{(3)}(\omega_P) &= [\chi_P^{(3)NR} |E_P|^2 + \chi_P^{(3)R} |E_S|^2] E_P \\ P^{(3)}(\omega_S) &= [\chi_S^{(3)R} |E_P|^2 + \chi_S^{(3)NR} |E_S|^2] E_S \end{aligned} \quad (3)$$

The  $\chi_P^{(3)NR}$  and  $\chi_S^{(3)NR}$  terms in  $P^{(3)}$  only act to modify the dielectric constant  $\epsilon_P$  and  $\epsilon_S$  in Eq. (1). They are responsible for the field induced birefringence, self-focusing, etc., but have no direct effect on SRS. Therefore, in the following discussion, we neglect them. The  $\chi^{(3)R}$  terms in  $P^{(3)}$ , instead, effectively couple  $E_P$  and  $E_S$  in Eq. (1) and is the reason of energy transfer between the two fields. They are the cause of the stimulated Raman process and are called Raman susceptibilities. Eq. (1) can be solved with Eq. (3) by knowing  $\chi^{(3)R}$ .

A molecular vibration or optical phonon is the most common case of SRS. The optical radiation is assumed interacting with a vibrational mode of a molecule and this vibrational mode can be defined as a simple harmonic oscillator of resonance frequency  $\omega_0$ , damping constant  $\gamma$ . The analysis is one-dimensional, thus, each oscillator can be distinguished by its position  $z$  and normal vibrational coordinate  $q$  [2].

The key assumption of the theory is that the optical polarizability of the molecule (which is typically predominantly electronic in origin) is not constant, but depends on the internuclear distance according to the equation:

$$\alpha(t) = \alpha_0 + \left( \frac{\partial \alpha}{\partial q} \right)_0 q(t) \quad (4)$$

This quantity is a tensor, but to simplify the discussion we will consider it as a scalar. Here  $\alpha_0$  is the polarizability of a molecule in which the internuclear distance is held at its equilibrium value.

Starting from Eqs. (4) and (5), we obtain

$$-\omega^2 q(\Omega) - 2i\omega\gamma q(\Omega) + \omega_0^2 q(\Omega) = \frac{1}{m} \left( \frac{\partial \alpha}{\partial t} \right)_0 E_P E_S^* \quad (5)$$

where  $m$  represents the reduced nuclear mass and  $\Omega = \omega_P - \omega_S$ . This equation shows explicitly  $q(\Omega)$  as a material excitation resonantly driven by optical mixing  $E_P E_S^*$ . SRS by phonons can therefore be considered a result of coupling three waves  $E_P$ ,  $E_S$  and  $q(\Omega)$  governed by the wave equations (3) and (6). This system is essentially the wave equation coupled to an oscillator equation. Starting from Eq. (6) it is possible to calculate the resonant Raman susceptibility, which, for the steady-state case, is related to the Raman gain by the following relation:

$$g = \frac{4\pi\omega^2}{c^2 k^2} \text{Im}(\chi_S^{(3)R}) \quad (6)$$

When the depletion of the pump field  $|E_P|^2$  is negligible, being the Raman susceptibility  $\chi^{(3)R}$  a negative imaginary, we find that the evolution of the intensity of Stokes field is given by the exponentially growing solution of

$$[E_S]^2 = [E_S(0)]^2 \exp(g * [E_P]^2 * z - \alpha * z) \quad (7)$$

The Stokes wave is amplified if the gain exceeds the losses. We note that Raman amplification is a process for which the phase matching condition is automatically satisfied. In other words, Raman amplification is a pure gain process.

## A.2 Experiment: measurements of Raman gain

### A.2.1 Direct measurement

The theory developed in previous paragraph is a theory of Raman amplification. This means that to measure Raman gain, we should perform experiments on Raman amplifiers [47, 48]. Several materials, such as silicon, allow a direct measurement of SRS [49, 50]. In this case the Raman gain can be evaluated by measuring the Stokes amplification in a Raman amplifier having as active medium the material under test [2].

In the steady-state (no pump depletion) regime of SRS, assuming no losses at the Stokes frequency, the value of the gain coefficient  $g$  can be obtained by fitting Eq. (8), which is readily transformed into:

$$\text{SRS Gain} = 10 * \log_{10} \left( \frac{I_S(L)}{I_S(0)} \right) = 4.34 * g * L * I_P(0) \quad (8)$$

where  $I_S(0)$  is the intensity of the input Stokes radiation (Stokes seed),  $I_S(L)$  is the intensity of the output Stokes radiation,  $I_P(0) = \frac{P}{A}$  is the intensity of the input pump radiation,  $P$  is the power incident onto the sample,  $A$  as the effective area of pump beam and  $L$  is the effective length. Since the sample is transparent to the incident light,  $L$  is taken to be equal to the thickness of the sample along the path of the incident light.

As an example, in **Figure 5** a typical trend of the maxima of the signal power plotted as a function of the effective pump power at the exit of Raman amplifier is reported. As the laser power increases, the SRS gain is first constant and then grows approximately linear when the power is greater than the threshold value and so stimulated scattering begins to prevail. The threshold is usually defined as the power at which the linear behavior starts, while the slope of the line is proportional to the Raman gain coefficient  $g$ . The estimation of the Raman gain coefficient  $g$  is not straightforward due to the uncertainty in the effective focal volume inside the sample [36, 39, 42].

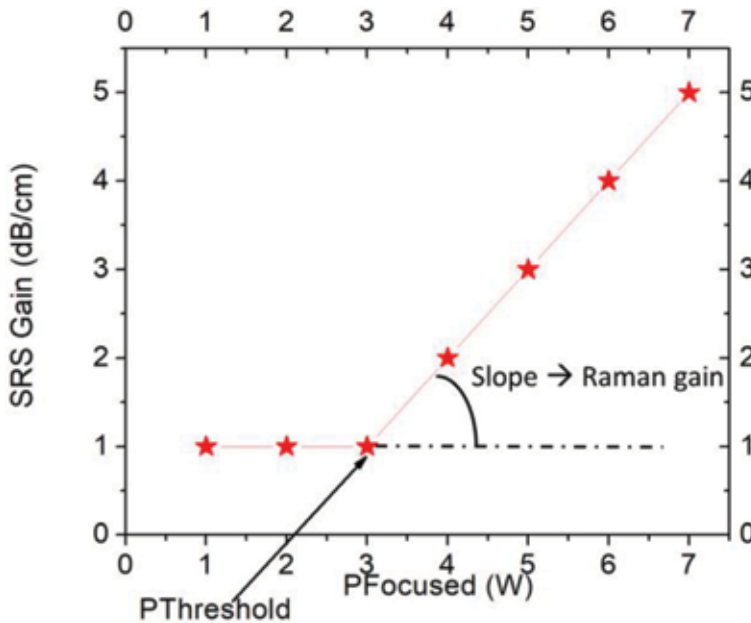


**Figure 5.** A typical trend of SRS signal plotted as a function of the effective pump power.

## A.2.2 Indirect measurement

If Raman gain is weak and the length of sample is small, Raman amplification is difficult to measure and an indirect measurement should be implemented. Frequently, this happens for glasses, for which the spontaneous Raman spectra is firstly measured by a standard Raman set up, then the Raman gain is estimated by a numerical procedure [2].

In order to eliminate in the measured Stokes Raman intensity  $I(\omega)$  its dependence on both the temperature and the frequency of the vibrational modes [51, 52], the following relation can be used:

$$R(\omega_S) = \frac{\omega_S}{[N(\omega_S, T) + 1] (\omega_P - \omega)^4} I(\omega_S) \quad (9)$$

where  $\omega_S$  is the Stokes Raman shift (in  $\text{cm}^{-1}$  units),  $\omega_P$  is the laser excitation frequency,  $N(\omega_S, T)$  is the Bose-Einstein mean occupation number and  $T$  is the temperature [31]. Afterwards, with the aim to properly relate the Raman spectra of investigated glasses with the standard silica glass, the measured Raman spectra can be adjusted also for the differences in reflection and angle of collection [26, 27, 31]. The relation between Raman gain spectrum and spectral and differential Raman cross section is expressed by the following equation:

$$g(\omega_S) = \frac{\lambda_S^3}{c^2 h n^2} \left( \frac{\partial^2 \sigma}{\partial \Omega \partial \omega_S} \right)_0 \quad (10)$$

where  $\left( \frac{\partial^2 \sigma}{\partial \Omega \partial \omega_S} \right)_0$  is the Raman cross section at  $T = 0$  K (i.e., corrected considering the thermal population factor),  $\lambda_S$  is the Stokes wavelength (in m),  $c$  is the velocity of light in vacuum and  $n$  is the refraction index at the excitation wavelength [24–27, 31].

## Conflict of interest

The authors declare that they have no competing financial interests.

## Author details

Maria Antonietta Ferrara\* and Luigi Sirteto  
National Research Council (CNR), Institute for Microelectronics and Microsystems (IMM), Napoli, Italy

\*Address all correspondence to: [antonella.ferrara@na.imm.cnr.it](mailto:antonella.ferrara@na.imm.cnr.it)

## IntechOpen

© 2018 The Author(s). Licensee IntechOpen. This chapter is distributed under the terms of the Creative Commons Attribution License (<http://creativecommons.org/licenses/by/3.0>), which permits unrestricted use, distribution, and reproduction in any medium, provided the original work is properly cited. 

## References

- [1] Popp J, Kiefer W. Raman scattering. In: Meyers RA, editor. *Fundamentals, Encyclopedia of Analytical Chemistry*. Chichester: John Wiley & Song Ltd; 2000. pp. 13104-13142
- [2] Sirleto L, Vergara A, Ferrara MA. Advances in stimulated Raman scattering in nanostructures. *Advances in Optics and Photonics*. 2017;**9**(1): 169-217. DOI: 10.1364/AOP.9.000169
- [3] Cern P, Jelínkov H, Zverevb PG, Basiev TT. Solid state lasers with Raman frequency conversion. *Progress in Quantum Electronics*. 2004;**28**:113
- [4] Stolen RH. In: Islam MN, editor. *Raman Amplifiers for Telecommunications 1*. New York: Springer-Verlag; 2004. p. 35
- [5] Rivero C, Richardson K, Stegeman R, Stegeman G, Cardinal T, Fargin E, et al. Quantifying Raman gain coefficients in tellurite glasses. *Journal of Non-Crystalline Solids*. 2004;**345** & **346**:396-401
- [6] Liang D, Bowers JE. Recent progress in lasers on silicon. *Nature Photonics*. 2010;**4**:511. DOI: 10.1038/nphoton.2010.167
- [7] Boyraz O, Jalali B. Demonstration of a silicon Raman laser. *Optics Express*. 2004;**12**:5269
- [8] Rong HS, Liu A, Jones R, Cohen O, Hak D, Nicolaescu R, et al. An all-silicon Raman laser. *Nature*. 2005;**433**:292
- [9] Wiersma DS. Disordered photonics. *Nature Photonics*. 2013;**7**:188
- [10] Lin H-B, Campillo AJ. Microcavity enhanced Raman gain. *Optics Communication*. 1997;**133**:287
- [11] Spillane SM, Kippenberg TJ, Vahala KJ. Ultralow-threshold Raman laser using a spherical dielectric microcavity. *Nature*. 2002;**415**:621-623
- [12] Latawiec P, Venkataraman V, Burek MJ, Hausmann BJM, Bulu I, Lončar M. On-chip diamond Raman laser. *Optica*. 2015;**2**:924. DOI: 10.1364/OPTICA.2.000924
- [13] Takahashi Y, Inui Y, Chihara M, Asano T, Terawaki R, Noda S. A micrometre-scale Raman silicon laser with a microwatt threshold. *Nature*. 2013;**498**:470-474
- [14] Schuurmans FJP, Vanmaekelbergh D, van de Lagemaat J, Lagendijk A. Strongly photonic macroporous GaP networks. *Science*. 1999;**284**:141
- [15] Hokr BH, Bixler JN, Cone MT, Mason JD, Beier HT, Noojin GD, et al. Bright emission from a random Raman laser. *Nature Communications*. 2014;**5**:4356. DOI: 10.1038/ncomms5356
- [16] Zheludev NI. Nonlinear optics on the nanoscale. *Contemporary Physics*. 2002;**43**:365. DOI: 10.1080/00107510110102281
- [17] Banfi G, De Giorgio V, Ricard D. Nonlinear optical properties of semiconductor nanocrystals. *Advances in Physics*. 1998;**47**:447
- [18] Suresh S, Arivuoli D. Nanomaterials for nonlinear optical applications: A review. *Reviews on Advanced Materials Science*. 2012;**30**:243-253
- [19] Chandra M, Das PK. Small-particle limit in the second harmonic generation from noble metal nanoparticles. *Chemical Physics*. 2009;**358**:203. DOI: 10.1016/j.chemphys.2009.02.003
- [20] Kawata S, Inouye Y, Verma P. Plasmonics for near-field nano-imaging and superlensing. *Nature Photonics*. 2009;**3**:388

- [21] Vildirim H, Bulutay C. Enhancement of optical switching parameter and third-order optical nonlinearities in embedded Si nanocrystals: A theoretical assessment. *Optics Communication*. 2008;**281**:4118
- [22] Zhang BP, Shimazaki K, Shiokawa T, Suzuki M, Ishibashi K, Saito R. Stimulated Raman scattering from individual single-wall carbon nanotubes. *Applied Physics Letters*. 2006;**88**(24):241101-241103
- [23] Wu J, Gupta AK, Gutierrez HR, Eklund PC. Cavity-enhanced stimulated Raman scattering from short GaP nanowires. *Nano Letters*. 2009;**9**(9):3252-3257
- [24] Galeener FL, Mikkelsen JC Jr, Geils RH, Mosby WJ. The relative Raman cross sections of vitreous SiO<sub>2</sub>, GeO<sub>2</sub>, B<sub>2</sub>O<sub>3</sub>, and P<sub>2</sub>O<sub>5</sub>. *Applied Physics Letters*. 1978;**32**:34-36
- [25] Irannejad M, Jose G, Jha A, Steenson P. Raman gain in modified tellurite glasses and thin films. *Optics Communication*. 2012;**285**:2646-2649
- [26] Manikandan N, Rysanyanskiy A, Toulouse J. Thermal and optical properties of TeO<sub>2</sub>-ZnO-BaO glasses. *Journal of Non-Crystalline Solids*. 2012;**358**:947-951
- [27] Lin A, Rysanyansky A, Toulouse J. Fabrication and characterization of a water-free mid-infrared fluorotellurite glass. *Optics Letters*. 2011;**36**:740-742
- [28] Sirleto L, Donato MG, Messina G, Santangelo S, Lipovskii AA, Tagantsev DK, et al. Raman gain in niobium-phosphate glasses. *Applied Physics Letters*. 2009;**94**:031105. DOI: 10.1063/1.3072354
- [29] Donato MG, Gagliardi M, Sirleto L, Messina G, Lipovskii AA, Tagantsev DK, et al. Raman optical amplification properties of sodium-niobium-phosphate glasses. *Applied Physics Letters*. 2010;**97**:231111. DOI: 10.1063/1.3525162
- [30] Ferrara MA, D'Arco A, Indolfi M, Sirleto L. Stimulated Raman scattering in nanostructured materials. In: *IEEE 15th International Conference on Nanotechnology (IEEE-NANO)*. 2015
- [31] Pernice P, Sirleto L, Vergara A, Aronne A, Gagliardi M, Fanelli E, et al. Large Raman gain in a stable nanocomposite based on niobosilicate glass. *Journal of Physical Chemistry C*. 2011;**115**(35):17314-17319. DOI: 10.1021/jp204353e
- [32] Sirleto L, Aronne A, Giofrè M, Fanelli E, Righini GC, Pernice P, et al. Compositional and thermal treatment effects on Raman gain and bandwidth in nanostructured silica based glasses. *Optical Materials*. 2013;**36**:408-413. DOI: 10.1016/j.optmat.2013.10.001
- [33] Sirleto L, Raghunathan V, Rossi A, Jalali B. Raman emission in porous silicon at 1.54 μm. *Electronics Letters*. 2004;**40**(19):121-122. DOI: 10.1049/el:20045284
- [34] Sirleto L, Ferrara MA, Rendina I, Jalali B. Broadening and tuning of spontaneous Raman emission in porous silicon at 1.5 μm. *Applied Physics Letters*. 2006;**88**:211105. DOI: 10.1063/1.2206123
- [35] Ferrara MA, Donato MG, Sirleto L, Messina G, Santangelo S, Rendina I. Study of strain and wetting phenomena in porous silicon by Raman scattering. *Journal of Raman Spectroscopy*. 2008;**39**(2):199-204. DOI: 10.1002/jrs.1846
- [36] Sirleto L, Ferrara MA, Rendina I, Nicotra G, Spinella C. Observation of stimulated Raman scattering in silicon nanocomposites. *Applied Physics Letters*. 2009;**94**:221106. DOI: 10.1063/1.3148669

- [37] Ferrara MA, Sirleto L, Nicotra G, Spinella C, Rendina I. Enhanced gain coefficient in Raman amplifier based on silicon nanocomposites. *Photonics and Nanostructures—Fundamentals and Applications*. 2011;**9**:1-7. DOI: 10.1016/j.photonics.2010.07.007
- [38] Sirleto L, Ferrara MA, Rendina I, Basu SN, Warga J, Li R, et al. Enhanced stimulated Raman scattering in silicon nanocrystals embedded in silicon-rich nitride/silicon superlattice structures. *Applied Physics Letters*. 2008;**93**:251104. DOI: 10.1063/1.3050109
- [39] Ferrara MA, Rendina I, Basu SN, Dal Negro L, Sirleto L. Raman amplifier based on amorphous silicon nanoparticles. *International Journal of Photoenergy*. 2012;**2012**:254946. DOI: 10.1155/2012/254946
- [40] Ferrara MA, Sirleto L. Experimental investigation of stimulated Raman scattering gain in silicon nanocomposite and in amorphous silicon nanoparticles. *Journal of Nonlinear Optical Physics and Materials*. 2012;**21**(3):1250039. DOI: 10.1142/S0218863512500397
- [41] Ferrara MA, D'Arco A, Indolfi M, Sirleto L. Study of Raman amplification in nanostructured materials. In: *AEIT International Annual Conference, IEEE Proceeding*. Article number 7415223. 2015. DOI: 10.1109/AEIT.2015.7415223
- [42] Sirleto L, Ferrara MA, Nikitin T, Novikov S, Khriachtchev L. Giant Raman gain in silicon nanocrystals. *Nature Communications*. 2012;**3**:1220. DOI: 10.1038/ncomms2188
- [43] Sirleto L, Ferrara MA, Vergara A. Toward an ideal nanomaterial for on-chip Raman laser. *Journal of Nonlinear Optical Physics and Materials*. 2017;**26**:1750039. DOI: 10.1142/S0218863517500394
- [44] Boyd RW. *Nonlinear Optics*. 2nd ed. USA: Academic Press; 2003
- [45] Shen YR. *The Principles of Nonlinear Optics*. New York: John Wiley & Sons, Inc; 2003
- [46] Yariv A. *Quantum Electronics*. New York: John Wiley & Sons, Inc; 1988
- [47] Levine BF, Shank CV, Heritage JP. Surface vibrational spectroscopy using stimulated Raman scattering. *IEEE Journal of Quantum Electronics*. 1979;**15**:1418
- [48] Levine BF, Bethea CG. Ultrahigh sensitivity stimulated Raman gain spectroscopy. *IEEE Journal of Quantum Electronics*. 1980;**16**:85
- [49] Ralston JM, Chang RK. Spontaneous Raman scattering efficiency and stimulated scattering in silicon. *Physical Review B*. 1970;**2**:1858
- [50] Owyong A. Sensitivity limitations for cw stimulated Raman spectroscopy. *Optics Communication*. 1977;**22**:323
- [51] Shuker R, Gammon RW. Raman-scattering selection-rule breaking and the density of states in amorphous materials. *Physical Review Letters*. 1970;**25**:222
- [52] Galeener FL, Sen PN. Theory for the first-order vibrational spectra of disordered solids. *Physical Review B*. 1978;**17**:1928





*Edited by Boris I. Lembrikov*

Nonlinear optics is a rapidly developing field of modern physics. Nonlinear optical phenomena such as self-focusing, self-phase modulation, soliton formation and propagation, higher harmonic generation, different types of stimulated light scattering, and four-wave mixing have attracted interest from the fundamental point of view of the investigation of light/matter interaction, and as a basis for applications in contemporary optical communications and optical signal processing.

*Nonlinear Optics—Novel Results in Theory and Applications* contains novel results concerning the mathematical methods of nonlinear optical phenomena analysis, soliton formation and propagation in optical fibers, and peculiarities of nonlinear optical phenomena in micro- and nanostructures.

The book may be interesting for researchers and engineers interested in nonlinear optics, lasers, and optical communications.

Published in London, UK

© 2019 IntechOpen  
© Scott Rodgerson / unsplash

**IntechOpen**

ISBN 978-1-83962-009-6

